Biophysical Journal

Best of 2012

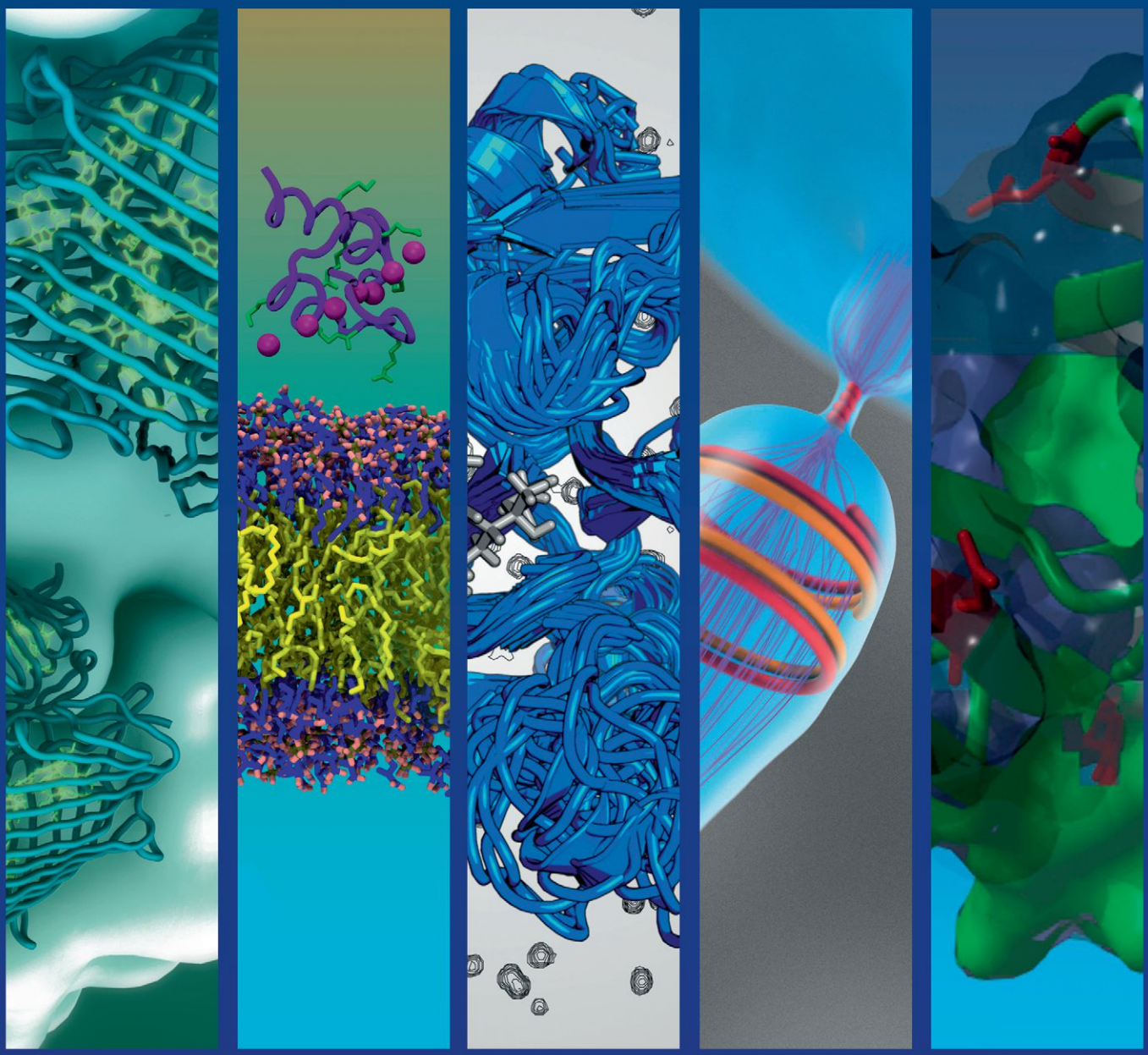

Volumes 102 & 103

Cell PRESS
www.cell.com

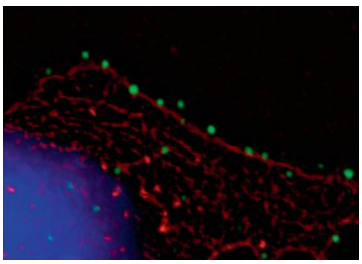

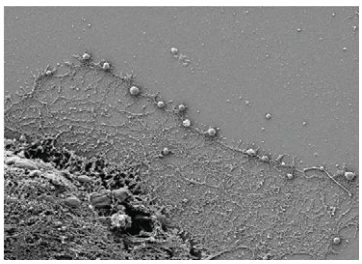

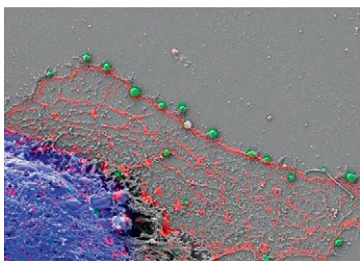

Visualize Beyond the 200nm Limit with Superresolution

ELYRA from Carl Zeiss incorporates up to two superresolution technologies, structured illumination and PALM/dSTORM, for twice the resolution power of confocal or single molecule resolution down to 20nm. Easily incorporate correlative studies and image the exact same area with superresolution as well as electron microscopy.

www.zeiss.com/superresolution

ZEISS

We make it visible.

When it comes to scan rates, the faster the better.

Think again!

Thermo Scientific Q Exactive identified more low abundance proteins than QTOF.

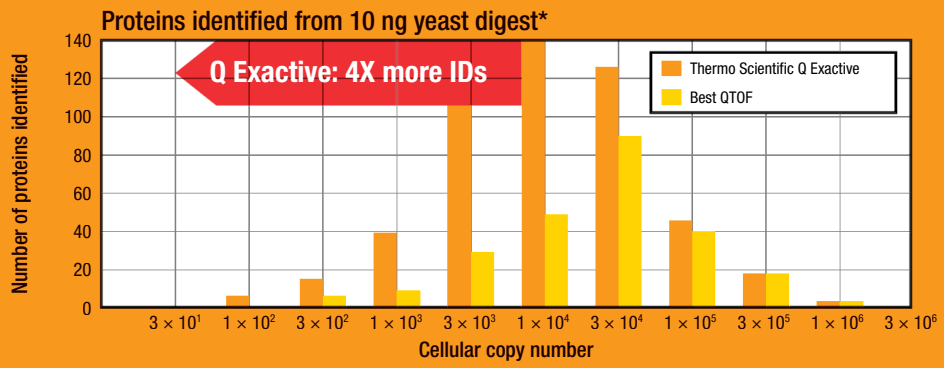


Exactive Plus LC-MS


Q Exactive LC-MS/MS


LTQ Orbitrap XL Hybrid FTMS


Orbitrap Velos Pro Hybrid MS


Orbitrap Elite Hybrid MS

Some manufacturers will try to convince you that you need to scan as fast as possible to obtain the most data from complex mixtures. The reality? Very fast scanning often leads to poor data quality. **Thermo Scientific Orbitrap mass spectrometers** deliver the highest effective scan rate for consistent, high quality spectra to access low-abundance proteins, making them the most desirable choice for complex samples. Learn about Orbitrap productivity and see how much more you can discover.

• visit haste makes waste at thermoscientific.com/scanspeed

* Hao Z, Zhang Y, Eliuk S, Blethrow J, Horn D, Zabrouskov V, Kellmann M, and Huhmer A. A Quadrupole-Orbitrap Hybrid Mass Spectrometer Offers Highest Benchtop Performance for In-Depth Analysis of Complex Proteomes; Thermo Scientific Application Note 552; April 2012.

Thermo SCIENTIFIC

What is Menkes?

Menkes is a fatal illness in which the intestines of male infants are unable to absorb copper, depriving the brain and other tissues of this essential mineral. The prognosis for individuals with Menkes is poor; death usually occurs within the first decade of life.

The purpose of The Menkes Foundation is to promote awareness and help diagnose children afflicted with Menkes disease. This is a rare genetic disease that is commonly missed by the medical community because the signs and symptoms at birth and in early infancy are subtle and often confused with other diseases. Early treatment of symptoms is crucial for these children to maintain a sense of normalcy during their infancy and early childhood. Our goal is to achieve improvements in health, education, and community involvement through medical conferences, fundraising events and other similar endeavors.

What are the symptoms?

There are variations ranging from mild to severe.
Distinctive symptoms begin at 2-3 months of age.

- Failure to meet developmental milestones
- Weak and "floppy" muscles
- Seizures
- Failure to thrive
- Kinky hair (short, sparse, coarse and twisted hair)
- Pudgy, rosy cheeks or sagging facial muscles
- Feeding difficulties
- Irritability
- Low body temperature
- Pale, pigmented skin color
- Frequent urinary tract infections (UTIs)
- Weak and/or brittle bones
- Respiratory difficulties

The Menkes Foundation

www.themenkesfoundation.org

Promoting awareness with hopes of finding a cure for Menkes Disease

Foreword

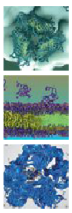

We are pleased to present this "Best of…" reprint collection, which provides a chance to reflect on what has caught the attention of *Biophyscial Journal* readers in 2012. This collection includes a selection of twelve of the most accessed articles across a range of topics. Article selection is primarily based on the number of requests for PDF and full-text HTML versions of a given article. We acknowledge that no single measurement can truly be indicative of "the best" research papers over a given period of time. This is especially true when sufficient time has not necessarily passed to allow one to fully appreciate the relative importance of a discovery. That said, we think it is still informative to look back at the scientific community's interests in what has been published over the past year.

In this collection, you will see a range of the exciting topics, including cell biophysics, motors and cytoskeleton, single-molecule microscopy, membrane biophysics, systems biophysics, biomolecular structure, biophysical methods, and channel electrophysiology, that have widely captured the attention and enthusiasm of our readers. They also represent several of the different types of papers that *BJ* publishes: one Biophysical Review, three Biophysical Letters, and eight regular articles.

We hope that you will enjoy reading this special collection and that you will visit http://www.cell.com/biophysj/home to check out the latest findings that we have had the privilege to publish. To stay on top of what your colleagues have been reading over the past 30 days, check out http://www.cell.com/biophysj/mostread. To find other high-quality papers published in the full collection of Cell Press journals, be sure to visit http://www.cell.com

Finally, we are grateful for the generosity of our sponsors, who helped make this reprint collection possible.

Biophysical *Journal*

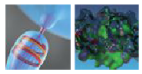

For information for the Best of Series, please contact:
Jonathan Christison
Program Director, Best of Cell Press
jchristison@cell.com
617-397-2893

Precision Instrumentation for the Sciences

MICROPIPETTE FABRICATION

Sutter Instrument, the recognized leader in micropipette fabrication technology, offers leading edge technology in the **P-1000** micropipette puller with an intuitive, full-featured interface. An extensive library of built-in programs is available through the color touch-screen display, taking the guesswork out of pipette pulling.

OPTICAL PRODUCTS

The latest in our expanding line of optical products is the **Lambda VF-5**™ tunable filter changer that allows access to any center wavelength from 330 to 800nm in nanometer increments. In addition to a full line of filter wheels and controllers, we design and build plasma and xenon light sources, and the **MOM** 2-photon microscope.

MICROMANIPULATION

Rock-solid precision and sub-micron accuracy. Whether your application requires the **MPC-200** for single-handed access to multiple manipulators, the programmable capabilities of the **MP-285**, the simplicity of the **MP-225**, or one of our traditional, manual style instruments, we have a manipulator to meet your needs.

MICROINJECTION

The **XenoWorks**™ microinjection system has been designed to meet the needs of a wide variety of applications that require the manipulation of cells and embryonic tissues including ICSI, ES Cell Microinjection, and Adherent Cell Microinjection. Highly-responsive movement and excellent ergonomics intuitively link the user with the micropipette, improving yield – saving time and resources.

SUTTER INSTRUMENT

ONE DIGITAL DRIVE, NOVATO, CA. 94949 PHONE: 415.883.0128 | FAX: 415.883.0572
EMAIL: INFO@SUTTER.COM | WWW.SUTTER.COM

Biophysical Journal
Best of 2012

Review

Biophysical Letters

Articles

High performance longpass edge filters . . .

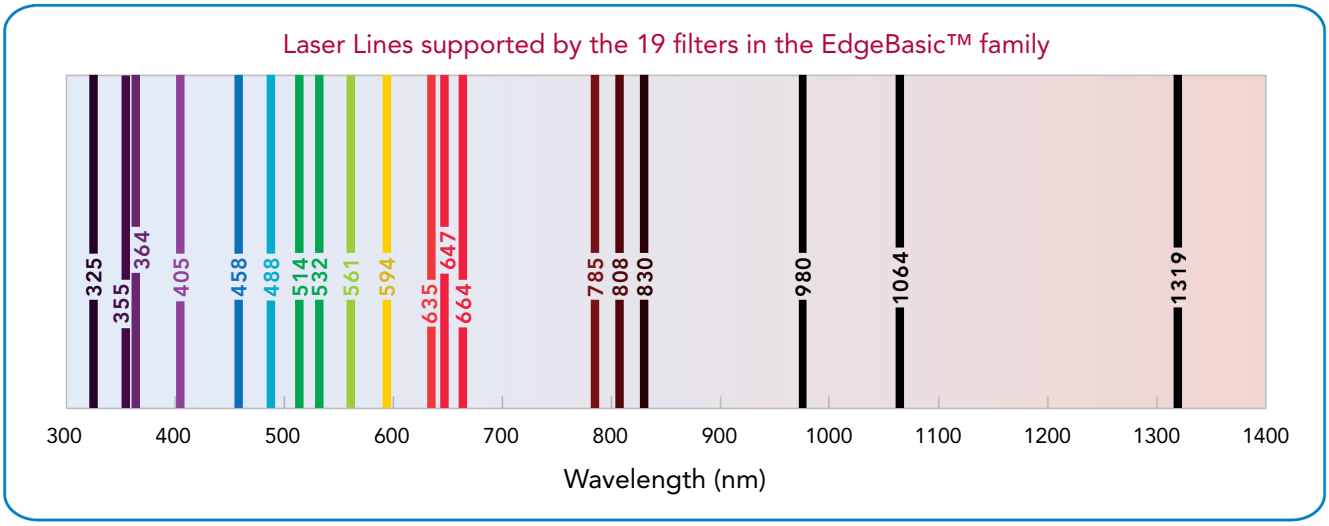

. . . now at more laser lines.

Now more laser wavelengths to choose from! Semrock has expanded our EdgeBasic™ longpass edge filters to offer a total of 19 filters, each optimized for a particular laser line. EdgeBasic™ filters provide a superb combination of very steep edge performance, extended blocking into the UV and high transmission beyond the laser line…all at an exceptional price point. Raman spectroscopy, fluorescence imaging, laser microscopy and metrology applications will all appreciate these EdgeBasic filter specifications and find the right filter, perfectly matched to your laser line.

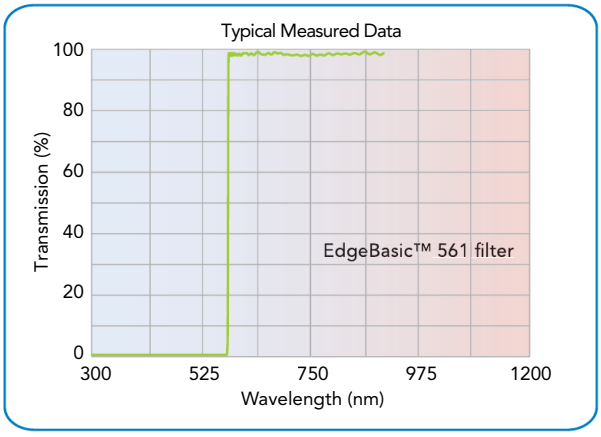

Visit Semrock.com for complete EdgeBasic™ filter specifications.

Semrock
The Standard in Optical Filters

The Right Filter. Right Now.

Seeing the Forest through the Trees: towards a Unified View on Physiological Calcium Regulation of Voltage-Gated Sodium Channels

Filip Van Petegem,[†*] Paolo A. Lobo,[†] and Christopher A. Ahern[‡*]
[†]The Department of Biochemistry and Molecular Biology, Vancouver, British Columbia, Canada; and [‡]Department of Molecular Physiology and Biophysics, University of Iowa, Iowa City, Iowa

ABSTRACT Voltage-gated sodium channels (Na_Vs) underlie the upstroke of the action potential in the excitable tissues of nerve and muscle. After opening, Na_Vs rapidly undergo inactivation, a crucial process through which sodium conductance is negatively regulated. Disruption of inactivation by inherited mutations is an established cause of lethal cardiac arrhythmia, epilepsy, or painful syndromes. Intracellular calcium ions (Ca^{2+}) modulate sodium channel inactivation, and multiple players have been suggested in this process, including the cytoplasmic Na_V C-terminal region including two EF-hands and an IQ motif, the Na_V domain III-IV linker, and calmodulin. Calmodulin can bind to the IQ domain in both Ca^{2+}-bound and Ca^{2+}-free conditions, but only to the DIII-IV linker in a Ca^{2+}-loaded state. The mechanism of Ca^{2+} regulation, and its composite effect(s) on channel gating, has been shrouded in much controversy owing to numerous apparent experimental inconsistencies. Herein, we attempt to summarize these disparate data and propose a novel, to our knowledge, physiological mechanism whereby calcium ions promote sodium current facilitation due to Ca^{2+} memory at high-action-potential frequencies where Ca^{2+} levels may accumulate. The available data suggest that this phenomenon may be disrupted in diseases where cytoplasmic calcium ion levels are chronically high and where targeted phosphorylation may decouple the Ca^{2+} regulatory machinery. Many Na_V disease mutations associated with electrical dysfunction are located in the Ca^{2+}-sensing machinery and misregulation of Ca^{2+}-dependent channel modulation is likely to contribute to disease phenotypes.

SODIUM CHANNEL ARCHITECTURE AND INACTIVATION

Na_Vs are large ~250-kDa membrane proteins comprised of four homologous domains (DI, DII, DIII, and DIV), each housing six α-helical transmembrane segments that form the voltage-sensing (Fig. 1 *A*: S1–S4, shown in *gray* and *red*) and the pore-forming (S5–S6, in *blue*) modules. The conductance of sodium ions through these channels is exquisitely sensitive to changes in voltage, where, upon opening, they allow the rapid inward flow of Na^+ ions which act to depolarize the cellular membrane. In mammals, at least nine different Na_V isoforms have been isolated ($Na_V1.1$–1.9). Within milliseconds of channel opening, the influx of Na^+ is reduced through a process known as "inactivation" (Fig. 1 *B*). This process is distinct from the normal "closing", and presents a way for the channel to minimize and regulate the depolarizing signal. Channels recover rapidly from inactivation under normal conditions within milliseconds, thus allowing for Na^+ influx during the next action potential. The inherent speed and efficiency of this opening/inactivating cycle is imperative for the electrical stability of the cell because small perturbations to the equilibrium among open, closed, and inactivated channel states can have devastating effects on electrical function.

Interestingly, Na_Vs can also inactivate directly from the closed conformation, as visible in the steady-state inactivation (SSI) curve (Fig. 1 *C*). The amount of SSI effectively controls the number of channels that are available for opening, and is directly dependent on the membrane voltage (1). In basal conditions near the resting membrane potential of excitable cells (~−90 mV), a considerable fraction of sodium channels are closed but ready to open upon depolarization, and the other half are inactivated and therefore unavailable to contribute to action potential firing. If the SSI curve is shifted only 10 mV to the right (a depolarizing shift), the number of available channels almost doubles. Thus, seemingly small changes in the steady-state inactivation properties can have significant effects on channel availability, and therefore on the rhythm and stability of the action potential.

The precise mechanism of Na_V inactivation is not known, but one possibility is that inactivation proceeds through a hinged-lid mechanism (2) whereby the ~50 amino-acid cytoplasmic linker between domains III and IV (DIII-IV) acts as the lid to rapidly occlude the permeation pathway (3). This scheme, albeit overly simplified, is likely accompanied by complementary motions within the pore region. In addition to the DIII-IV linker and its putative binding sites in the S4–S5 linker of domains III (4) and IV (5), the inactivation complex includes the C-terminus of the channel (6,7).

Submitted August 27, 2012, and accepted for publication October 18, 2012.

*Correspondence: chrisahern@gmail.com or filip.vanpetegem@gmail.com

Editor: Brian Salzberg.

0006-3495/12/12/2243/9 $2.00

http://dx.doi.org/10.1016/j.bpj.2012.10.020

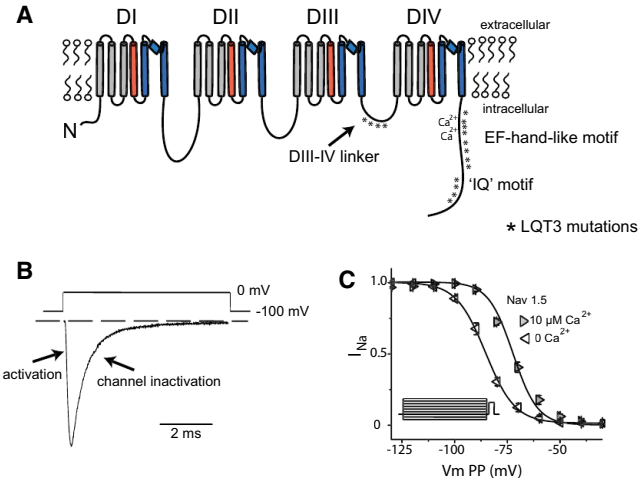

FIGURE 1 Sodium channel architecture, gating, and modulation by calcium. (*A*) Cartoon of a simplified sodium channel highlighting the four homologous domains (DI–DIV), with six transmembrane segments each (S1–S6). Voltage-sensing domain (*gray*, S1–S3 and *red*, S4); pore-forming domain (*blue*, S5–S6). Cytoplasmic regions implicated in Ca^{2+} modulation are indicated with inherited mutations (*Asterisks*). (*B*) Representative example of a rapid inward sodium current under patch-clamp conditions in response to a 15-ms depolarizing pulse from −100 mV to −20 mV, with the fast activation and inactivation indicated (*arrow*). (*C*) Steady-state inactivation curve for $Na_V1.5$ in the presence and absence of 10 μM free Ca^{2+} in the patch pipette. The data were generated with the protocol shown (*inset*) where a cell under voltage-clamp is held at −120 mV, stepped to a variable prepulse for 500 ms (to reach a new steady-state equilibrium) before a test pulse to −20 mV is employed to assay how many are available to open.

FUNCTIONAL EFFECT OF Ca^{2+} ON SODIUM CHANNEL GATING

The consensus of published data supports the observation that increased local cytoplasmic Ca^{2+} levels into the low micromolar range results in a ~10-mV depolarizing shift in the steady-state availability relationship for $Na_V1.5$ (6,8–12) (Fig. 1 *C*). Because the resting membrane potential is midway along the falling phase of this relationship, seemingly minor shifts in the equilibrium value can substantially increase the amount of available channels to open for the next action potential. However, a variety of effects mediated by cytoplasmic calcium has been reported, including effects on inactivation rate (6) and slow inactivation (12,13). There also seem to be isoform-specific differences, where shifts in the steady-state availability curve can also be observed upon coexpressing calmodulin or addition of short peptides, but there is no consensus on these effects (13). How is it possible that so many groups have reported conflicting results?

In addition to variable effects of EGTA and BAPTA, one potential culprit is the composition of the patch pipette solutions where CsF (typically >100 mM) is often used to produce very stable whole-cell patch-clamp recording conditions. However, fluoride avidly binds Ca^{2+} (K_{sp} ~ 3.45×10^{-11}) (http://pubchem.ncbi.nlm.nih.gov), thus effectively decreasing the free Ca^{2+} concentrations, especially in low buffering—suggesting that Ca^{2+} ion regulation measured under such conditions occurs at lower levels of free [Ca^{2+}]. Although Deschênes et al. (14) have reported no difference in modulation between CsF for CsCl, this outcome could differ among isoforms, and the precise amount of CsF used. Moreover, the regions known to support CaM binding and Ca^{2+} regulation, namely the DIII-IV linker and the IQ motif, are also home to phosphorylation sites (15,16), providing an intriguing form of additional regulation, but yet another confounding variable in the laboratory setting. Lastly, sodium channels expressed in different mammalian cell systems have yielded divergent results in terms of Ca^{2+} regulation (17).

Ca^{2+} regulation of sodium channels could act through a combination of mechanisms, including the direct interaction of ions with EF-hand motifs in the C-terminus of the channel, in addition to calmodulin-mediated effects. Calmodulin (CaM) is a ~17-kDa protein that is able to bind four Ca^{2+} ions through EF-hand motifs and the available data support a clear role for CaM in the Ca^{2+}-dependent modulation of sodium channel inactivation; however, considerable experimental variability exists. Coexpression of CaM has been shown to produce a Ca^{2+} dependent hyperpolarizing shift in the steady-state availability of skeletal muscle Na_V 1.4, but not of cardiac Na_V 1.5 (14). Chimeric ligation of CaM to the C-terminus of $Na_V1.4$ suggests that a single CaM is sufficient to shift the steady-state inactivation curve (18). The addition of a CaM inhibitory peptide via the patch pipette does not affect the Ca^{2+}-dependent shift in steady-state inactivation (10), leading some investigators to conclude that CaM is not essential to Ca^{2+} regulation. However, it is not known how effectively the inhibitory peptide competes with intact channels for binding to CaM, complicating the extrapolation of such results.

CALMODULIN AND THE IQ DOMAIN

Isoleucine-glutamine (IQ) domains are well-described motifs that were first reported for myosins as an interaction motif for CaM-like essential light chains (19) and neuromodulin (20). It is now clear that these motifs can form binding sites for CaM or CaM-like proteins, with Ca^{2+} dependencies and affinities differing in individual cases (21), and with a generalized IQ motif consisting of [I,L,V]QXXXR XXXX[R,K]. The C-terminal domain (CTD) of all Na_V isoforms encodes an IQ-like domain, first identified in the $Na_V1.1$–1.3 isoforms (22) (Fig. 2), and in some isoforms differs from the canonical IQ motif because it contains an extra fifth residue between the two positively charged residues of the consensus sequence. IQ motifs also occur in many other ion channels, including the closely related voltage-gated calcium channel, where several Ca^{2+}/CaM-IQ structures have been described in the literature (23–29).

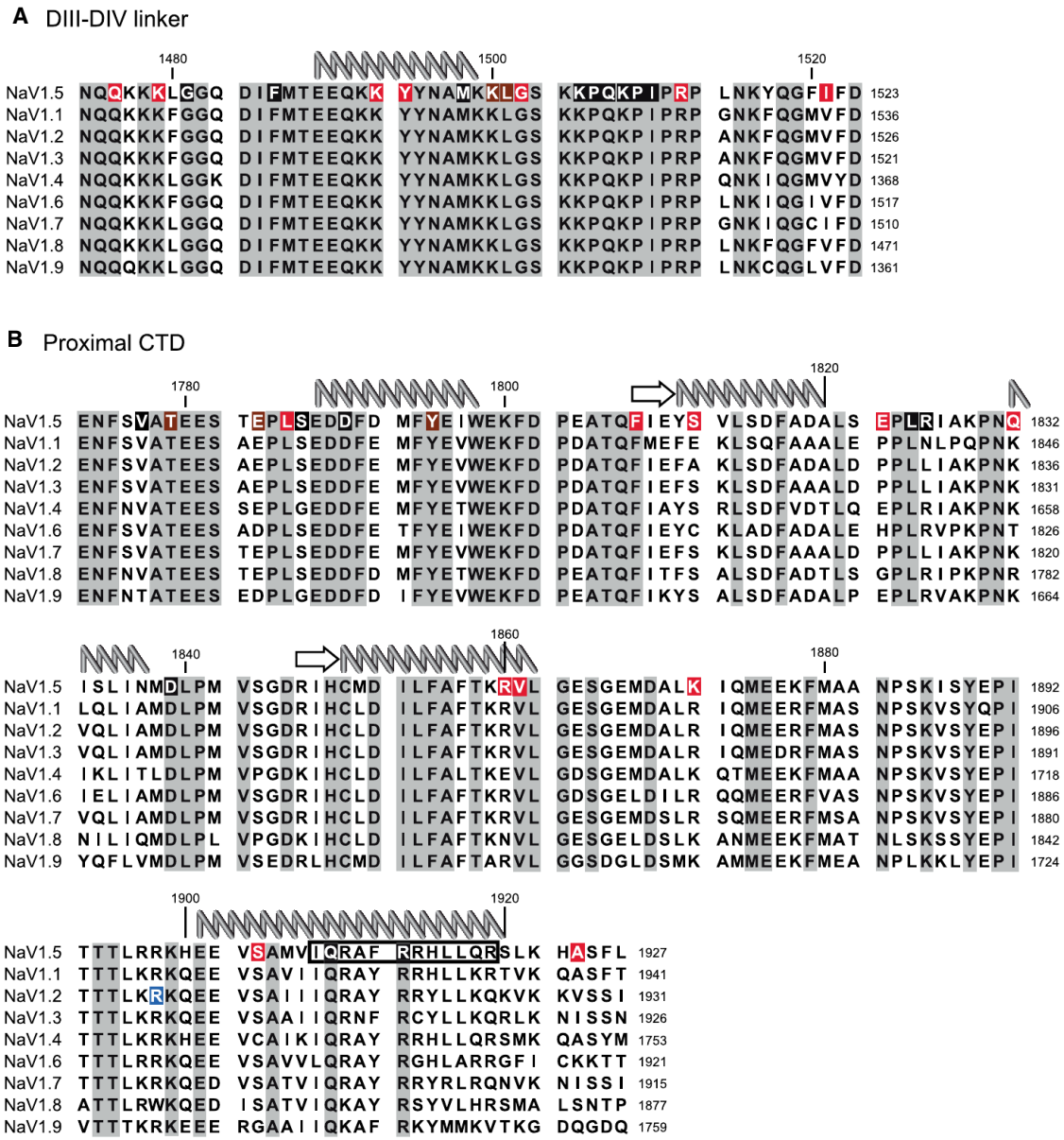

FIGURE 2 Conservation of calcium regulatory domains and the location of disease mutations. The DIII-DIV linker (*A*) and proximal CTD (*B*) sequences of $Na_V1.1$–1.9 are aligned against NaV1.5. (*Top*) Human $Na_V1.5$ numbering. (*Right-hand side*, *down*) Respective $Na_V1.1$–1.9 numbering. From published NMR and crystal structures, the available secondary structure elements are shown above the sequences: (*arrows*) β-strands; (*coils*) α-helices. Sites for disease mutations are highlighted: LQT3 (*black*), BrS (*red*), or both (*brown*). The R1902C mutation in $Na_V1.2$ is causative of GEFS+ (*blue*). The IQ consensus motif is indicated (*black box*) for $Na_V1.5$.

Early studies identified that mutants of CaM in *Paramecium tetraurelia* could impact voltage gated sodium currents in a lobe dependent manner (30,31). Numerous studies have since reported that CaM interacts with the Na_V IQ domain (6,8,12–14,18,32–34). Using intrinsic tyrosine fluorescence of CaM, the IQ motif peptide of $Na_V1.5$ was shown to bind apoCaM with ~160 nM K_d, and Ca^{2+}/CaM with ~2 μM K_d (35) with similar values obtained using isothermal titration calorimetry (8), suggesting that the Na_V IQ domain is primarily an apoCaM binding site. The interaction has been confirmed via FRET (12,18) yet co-immunoprecipitation experiments using GST fusion proteins of the CTD of some isoforms have failed to report an interaction with CaM (13). However, the folding and aggregation behavior for these constructs have not been sufficiently established.

NMR structures have been solved for apoC-lobe bound to the IQ domain of $Na_V1.2$ (36) and for apoCaM bound to the $Na_V1.5$ IQ domain (37) suggesting that the apoC-lobe is the primary binding partner for the IQ domain ($Na_V1.5$ residues 1901–1916), with major hydrophobic contacts made by residues I1908 and F1912. Some studies have shown that mutation of $Na_V1.5$ residues

I1908A/Q1909A (IQ/AA), as well as the analogous mutations in $Na_V1.2$ and $Na_V1.4$, disrupt IQ domain-CaM interactions (13,18,32). However, more quantitative biochemical approaches have shown that the IQ/AA mutation only weakly affects binding, with only a twofold lower affinity for both apoCaM and Ca^{2+}/CaM (35). In addition, the IQ/AA mutation alone causes a hyperpolarizing shift in the steady-state availability curve, and abolishes the calcium-dependent shift (35), in addition to an increase in sustained, noninactivating current (32). The IQ/AA mutation can also reduce current amplitudes (13), which is apparently the result of impaired channel trafficking (18).

Outright deletion of the IQ domain (stop-codon at amino acid (aa) 1885 in $Na_V1.5$) also reduces current amplitude, produces a −11 mV shift in steady-state availability (38) and increases the amount of noninactivating current (39) Interestingly, the IQ deletion mutant has been reported to retain a Ca^{2+}-dependent shift in steady-state inactivation, suggesting that other players participate in the regulation (12). However, overexpression of CaM or CaM_{1234} (a mutant that is no longer able to bind Ca^{2+} in a physiological range), in the absence of Ca^{2+}, can result in a depolarizing shift of the steady-state inactivation curve, and the deletion of the IQ domain abolishes this effect. This somewhat surprising set of results has been explained by a model whereby apoCaM/IQ domain association affects inactivation, independent of Ca^{2+}, and that the Ca^{2+}-dependence of inactivation does not require this interaction.

Thus, as with the variable macroscopic effects of Ca^{2+}/CaM on channel gating, the effects observed by different laboratories seem in direct conflict, with some suggesting the IQ motif is essential, whereas others concluding that it is peripheral. One potential explanation is that the IQ domain simply serves as a sink for a resident CaM molecule, where it serves to enrich CaM in the vicinity of the channel but is not directly involved in the mechanism of Ca^{2+}-dependent regulation. In this scenario, removing the sink can be overcome by overexpression of CaM, and thus different expression levels in the individual experiments, as well as different inherent affinities of Na_V isoforms for CaM, could result in functional discrepancies.

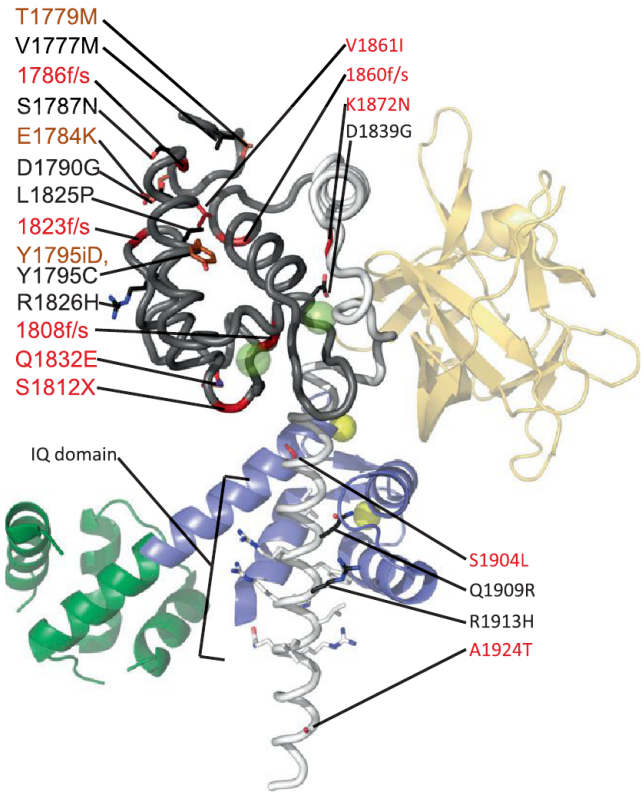

FIGURE 3 Structure of the human NaV1.5 C-terminal domain. Crystal structure of CaM bound to the NaV1.5 CTD (PDB:4DCK). Mg^{2+}-Calmodulin (*dark green N-terminus, blue C-terminus*) and fibroblast growth factor 13 (FGF13) (*orange*) are shown as part of a ternary complex from PDB:4DCK. (*Yellow spheres*) Magnesium ions. Mutations that cause LQT3 (*black*), BrS (*red*), or both (*brown*), are labelled. (*f/s*) Mutations that cause frame shifts. (*X*) Nonsense mutations. (Prefix *i*) Insertions. The NaV1.5 EF-hand domain, determined separately by NMR (PDB:2KBI), is highlighted (*dark gray*). It is clear that the portion C-terminal to this region forms interactions with the EF-hand domain. (*Transparent green spheres*) Calcium ions in the EF-hands, showing where they would bind based on structural superposition with Ca^{2+}-calmodulin. For clarity, only the side chains of the IQ domain as well as missense mutation sites are shown.

EF-HANDS

The function and role of the CTD proximal EF-hand domain has also been the subject of controversy. These two EF-hand motifs, initially thought to be formed by $Na_V1.5$ residues 1773–1852 (10), are actually encoded by $Na_V1.5$ residues 1788–1862 as shown by NMR (40) (Fig. 3). A similar structure has been reported simultaneously and independently for the $Na_V1.2$ EF-hand domain (41) which extends further toward the C-terminus (Na_V 1.2 residues 1777–1882 equivalent to $Na_V1.5$ residues 1773–1878), and includes a partially ordered fifth helix. The EF-hand domain is linked to the last transmembrane segment (IVS6; domain IV S6 segment) through a 13–15 aa flexible linker. As EF-hands typically form Ca^{2+}-binding motifs, it is possible that the Ca^{2+}-dependent effects on Na_V inactivation are due, in part, by direct Ca^{2+} ion binding to the EF-hands, absent of a CaM contribution.

However, based on the NMR structure, the EF-hands are predicted to bind, at most, one Ca^{2+} ion, as the second EF-hand lacks prerequisite acidic residues for Ca^{2+} ion coordination, thus it is has not been determined if the sodium channel EF-hands are functional or vestigial. However, using either 2 mM BAPTA to simulate Ca^{2+}-free conditions, or 20 mM $CaCl_2$, Shah et al. (35) showed distinct differences in ^{15}N- ^{1}H HSQC NMR spectra for a construct spanning Nav1.5 (1773–1865), and titrations yielded a K_d ~ 7.5 mM, suggesting that Ca^{2+} ions are capable of binding the EF-hands. Such a high K_d value would be

physiologically irrelevant, but larger constructs (1773–1920) yield a K_d between 1 and 6 μM, suggesting the affinity is strongly affected by the C-terminal region including the IQ domain binding to the EF-hands (10,35). Mg^{2+} was not found to have an effect. In contrast, Kim et al. (32) initially failed to detect any changes in Trp fluorescence of the EF-hands at varying Ca^{2+} concentrations, but then using ^1H,^{15}N chemical shifts during Ca^{2+} titrations of the $Na_V1.2$ and $Na_V1.5$ EF-hands, they also found low affinities for Ca^{2+} (K_d values between 1.6 and 3.3 mM) (41) However, the largest chemical shifts were found outside of the canonical EF-hand loop motifs, suggesting that Ca^{2+} binds weakly near the N-terminus of helix I, the linker between helices II and III, the C-terminus of helix IV, and the partially structured helix V.

In terms of functionality of expressed channels, a quadruple knock-out of Ca^{2+} binding to the EF-hands (E1788A, D1790A, D1792A, E1799A) effectively removes the Ca^{2+}-dependent shift in steady-state availability (10,12). Of note, the locations of these mutations were based on an early model of the EF-hands, and subsequent identification in the NMR structure shows, surprisingly, that none of these sites could be involved in coordinating Ca^{2+}. It is therefore puzzling that these mutations abolish Ca^{2+} binding, especially when both CD and NMR did not detect any structural changes (10). Further, the $Na_V1.5$ double-mutant D1802A/E1804A, which should knock out Ca^{2+} binding to the EF-hands based upon the NMR structure, disrupted Ca^{2+}-dependent shifts in the steady-state availability curve.

An additional level of complexity in Ca^{2+} regulation emerges from several reports that the EF-hands and the IQ domain can physically interact. NMR experiments indicate binding of $Na_V1.5$ residues 1897–1925 to an EF-hand construct (residues 1773–1865), thus helping to explain the difference in Ca^{2+} affinity between isolated EF-hands and longer constructs (35). Consistent with this, mutation of IQ/AA, which disrupts the EF-IQ interaction, lowers the affinity (K_d ~ 4 mM). Isothermal titration calorimetry (ITC) experiments between the EF-hands and IQ domain suggest a K_d ~ 27–38 μM, and using NMR, the IQ domain was mapped to bind between helices I and IV of the EF-hand domain (40) However, these experiments were performed on EF-hands as a distinct polypeptide from the IQ motif, and it is not clear whether the same interactions also occur in a physiological setting where both domains are within the same polypeptide.

Transition-metal FRET studies have been used to measure distances at three positions to a Trp residue within the EF-hand region, and these were used as restraints to build a model of the IQ domain bound to the EF-hands (42) Thus, one step of the mechanism is that Ca^{2+}/CaM could displace the EF-hands from the IQ domain, but as Ca^{2+}/CaM-IQ binding is not affected by the presence of the EF-hands (8), they could have the simple role of properly positioning the IQ domain relative to the rest of the channel.

These elements have been recently captured in a crystal structure of a near-full-length C-terminus, containing both the EF-hands and IQ domain of the $Na_V1.5$ isoform (residues 1776–1928) in complex with apo-CaM and the fibroblast growth factor homologous factor, FGF13 (43) (Fig. 3). This structure further confirms the preferred nature of the apo-C-lobe with the Na_V IQ motif and highlights the residues that support the interaction. Although considered an apo-CaM complex, Mg^{2+} is bound to the C-lobe. However, the C-lobe interactions with the IQ domain are very similar to the ones observed in the apoCaM-IQ domain NMR structures (36,37) In addition, no direct interaction between the EF-hands and the IQ motif was observed.

COUPLING INACTIVATION TO Ca^{2+}: INTERACTION BETWEEN CALMODULIN AND THE DIII-IV LINKER

Several studies have shown that CaM can interact with the isolated $Na_V1.5$ DIII-IV linker. Using both NMR and ITC, Potet et al. (11) showed binding of Ca^{2+}-loaded CaM to residues 1471–1523 of $Na_V1.5$, with a K_d of 0.6 μM and a 1:1 stoichiometry. In addition, a peptide corresponding to Na_V 1.5 1510–1530 binds Ca^{2+}/CaM with a K_d of ~8 μM and mutation of distal loop residues 1520–1522 FIF to AAA decreases the affinity of the latter peptide for Ca^{2+}/CaM.

In contrast, it has also been shown that Ca^{2+}/CaM can bind to the N-terminal portion of the DIII-IV linker (8,9). Here, ITC experiments yield a K_d of ~3 μM, and demonstrate that the interaction is driven by the Ca^{2+}/C-lobe, and importantly, no binding is measured in the absence of Ca^{2+}. Alanine scanning of several amino-acid residues suggests that the Ca^{2+}/C-lobe forms major contacts with a double Tyrosine motif (Na_V 1.5 residues 1494 and 1495), an observation that has been confirmed with a crystal structure that highlights intricate contacts between both tyrosines and the Ca^{2+}/C-lobe (8) (Fig. 4). There are additional energetically important contacts with M1498. Notably, no portion of the DIII-IV linker was found to interact with the Ca^{2+}/N-lobe, and whereas the isolated Ca^{2+}/N-lobe is able to interact with the DIII-IV linker in vitro, the affinity is extremely weak ($K_d > 500$ μM) and the binding site overlaps with the Ca^{2+}/C-lobe site. Thus, in the physiological setting the N-lobe is more likely to bind to a different site, such as the C-terminal IQ domain.

The two reports on Ca^{2+}/CaM binding to the DIII-IV linker are thus in conflict. However, full-length expressed $Na_V1.5$ channels containing the FIF/AAA or FIF/AIA mutations, that have been proposed to eliminate CaM N-lobe binding, still display a Ca^{2+}-dependent shift in steady-state inactivation, minimizing the role, if any, for the CaM N-lobe binding to the DIII-IV linker in Ca^{2+} regulation (8,11). This suggests that the 1510–1530 peptide

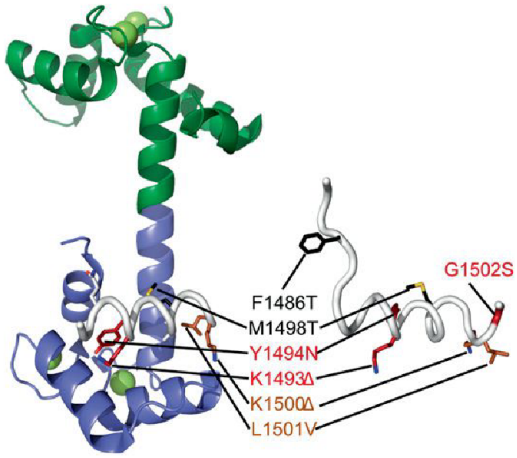

FIGURE 4 Structures of the sodium channel DIII-DIV linker alone and in complex with Ca^{2+}/CaM. Comparison between a Ca^{2+}/CaM-bound human $Na_V1.5$ DIII-DIV linker (PDB:4DJC) with the rat $Na_V1.2$ DIII-DIV linker (PDB:1BYY). The human $Na_V1.5$ numbering is used. Mutations that cause LQT3 (*black*), BrS (*red*), or both (*brown*), respectively. (Δ) Deletion mutations. (*Green*) N-lobe of calmodulin, (*blue*) C-lobe, and (*green spheres*) Ca^{2+} ions.

is not the functional binding site for Ca^{2+}/CaM within intact channels. Indeed, as the DIII-IV linker is likely to end around residue 1522 and become the transmembrane helix of DIV S1, a substantial portion of this site may not be available to cytoplasmic binding partners. Moreover, mutation of M1498 (highlighted in the Ca^{2+}/C-lobe interaction in the crystal structure) to alanine decreases the affinity as measured by ITC, and abolishes the Ca^{2+}-dependent shift in steady-state inactivation. In addition, introduction of a mutant that enhances the affinity of the DIII-IV linker for Ca^{2+}/CaM (E1489A/E1490A double mutant) also increases the Ca^{2+} sensitivity for shifting the steady-state availability curve. The correlation between loss of binding with loss of modulation, and gain of binding with gain of modulation, suggests that the Y1494/Y1495 motif as observed in the crystal structure is physiologically relevant, and although the distal DIII-IV linker FIF motif can bind CaM, these side chains are clearly not necessary for Ca^{2+} regulation.

A SIMPLIFIED MECHANISM FOR Ca^{2+} REGULATION OF SODIUM CHANNELS

In total, the in vitro and in vivo data using NMR, ITC, and crystallographic approaches suggest a simple yet dynamic lobe-switching mechanism for Ca^{2+}/CaM binding to intracellular channel domains, and provides a testable model biasing SSI inactivation in Na_Vs. In low Ca^{2+} levels, apoCaM is bound to the C-terminal IQ domain via the apoC-lobe, and as Ca^{2+} levels rise, Ca^{2+}/C-lobe gains affinity for the DIII-IV linker, opening access to the Ca^{2+}/N-lobe which now freely binds to the C-terminus IQ motif. The constrained configuration of the Ca^{2+}/C-lobe bound to the DIII-IV linker inherently destabilizes the interactions between the DIII-IV linker and the inactivation gate receptor. As the kinetics of inactivation of WT channels are unaffected by Ca^{2+}, CaM dissociation from the DIII-IV linker is not limiting. Indeed, the IFM motif known to be essential for inactivation lies well outside of the Ca^{2+}/C-lobe binding site. However, whether CaM does indeed bridge the DIII-IV linker and IQ domain within intact channels to form a tripartite complex remains to be fully visualized.

Even though the above model may be attractive, several additional complications remain. For one, mutations in both the DIII-IV linker and the CTD can affect inactivation in the absence of coexpressed CaM (44,45) For example, both the ΔKPQ in the $Na_V1.5$ DIII-IV linker, and a truncation of the CTD after the EF-hands (stop codon at aa 1885) result in an increased sustained current (39) suggesting that the DIII-IV linker and CTD may form a complex in the absence of CaM (32,39,46). Indeed, ITC experiments between isolated CTD and the DIII-IV linkers indicate a K_d of ~5 μM (46) and the interaction is only visible with longer CTD constructs containing both the EF-hands and IQ domain (39) However, other studies have failed to see a direct interaction between the DIII-IV linker and the CTD via ITC (8), a discrepancy that may be due to a different choice of constructs, as the positive ITC experiment made use of a longer CTD (ending at $Na_V1.5$ residue 1937 instead of 1924) and DIII-IV linker (ending at 1523 versus 1522).

A PHYSIOLOGICAL ROLE FOR CALCIUM ION REGULATION OF VOLTAGE-GATED SODIUM CHANNELS: USE-DEPENDENT FACILITATION OF CHANNEL AVAILABILITY

While the details of the mechanism of Ca^{2+} regulation continue to unfold, it is worth considering the role such a modulation might play in the physiological context. The consensus effect on Ca^{2+} regulation of Na_Vs is a destabilization of inactivation, which is manifest as an ~10-mV depolarizing shift in the steady-state availability relationship (8,10,11,18). Because this relationship is at equilibrium at physiological resting membrane potentials, roughly half of the channels are inactivated at resting conditions, and such a shift would significantly increase the number of channels that are available to fire for the next action potential.

How might this mechanism become relevant in an electrically excitable cell such as a cardiac myocyte? One might simply conclude that it would have little impact because the upstroke of the cardiac action potential, where Na_V channels are open, precedes the ensuing Ca^{2+} transient. However, a comprehensive synthesis of the available data points toward a different type of regulation that could, in

theory, take place on a rate-dependent basis to encode for a type of use-dependent facilitation. At low firing rates, Na^+ channels would sense diastolic, low Ca^{2+} levels and the DIII-IV linker would not engage significantly with the CaM-C-lobe. In addition, during the Ca^{2+} transient, interactions between calcium ions and CaM, an effector of Ca^{2+} regulation, would be functionally irrelevant as most channels are inactivated, and Ca^{2+} would have time to dissociate from CaM by the next upstroke of the action potential. However, as the firing rate increases, and in particular, when the rate of Ca^{2+} transient impinges upon the Ca^{2+}/C-lobe dissociation kinetics, then a type of Ca^{2+} memory would take place whereby Ca^{2+} ions would still be bound to the CaM C-lobe at the beginning of the next action potential. This would bias the steady-state availability relationship to more depolarized potentials and bring more Na_V channels to drive the upstroke of the action potential. Such a mechanism might not necessarily destabilize electrical signaling because it would only be employed transiently when having more channels would be efficacious. Moreover, the domains and specific residues that support the interaction between Na_Vs and Ca^{2+}/CaM are highly conserved among all nine sodium channel isoforms, and this mechanism would be expected to be widespread throughout the excitable cells of the cardiovascular and nervous systems.

SIMILARITIES WITH VOLTAGE-GATED CALCIUM CHANNELS

Voltage-gated calcium channels (Ca_Vs) share a fair amount of sequence identity with Na_Vs. Members of the Ca_V1 and Ca_V2 families are also modulated by CaM binding to the pore-forming α_1 subunit. CaM can mediate at least two Ca^{2+}-dependent feedback processes: Ca^{2+}-dependent inactivation and Ca^{2+}-dependent facilitation (for a limited set of examples, see Peterson et al. (48), Zülhke et al. (49), and Lee et al. (50)). Like Na_Vs, Ca_V1 and Ca_V2 family members encode EF-hands in the CTD, followed by an IQ domain that is able to bind both Ca^{2+}/CaM and apoCaM, suggesting that some of the mechanisms by which CaM alters inactivation may be conserved. However, there are some intrinsic differences. The Ca_V IQ domain favors Ca^{2+}/CaM binding, and both lobes contribute to binding of apoCaM and Ca^{2+}/CaM (23,24,26,28). In addition, a second CaM binding site is present between the EF-hands and the IQ domain (25,29). Although only a single CaM is required to mediate Ca^{2+}-dependent inactivation (51), this raises the possibility that multiple CaMs can associate with Ca_Vs. No binding has been detected between CaM and the Ca_V DIII-IV linker, although some Ca_V isoforms encode a CaM binding site in the N-terminal region (52). Thus, whereas some of the machinery seems conserved between Na_Vs and Ca_Vs, there are substantial discrepancies that mediate the different functional effects in both channels.

DISEASE MUTATIONS IN THE CA^{2+}-SENSING MACHINERY

Sodium channel mutations have been linked to a wide range of debilitating diseases, ranging from epilepsy (53) to myotonia (54), erythermalgia (55), cardiac arrhythmias (56) and migraine (57). Much attention has been given to mutations in the $Na_V1.5$ isoform, where gain-of-function mutations which impair the inactivation process result in the Long QT syndrome variant 3 (LQT3), a rare inherited disorder that is associated with an increased propensity to arrhythmogenic syncope, polymorphous ventricular tachycardia, and sudden cardiac death (58,59). The first reported LQT3 mutation, a deletion of three amino acids (KPQ) in the inactivation gate, results in a small, but significant, sustained sodium current over the duration of the action potential (60), a phenotype displayed by many LQT3 mutations. An additional seven LQT3 mutations have since been found in the inactivation gate, with 10 in the EF-hand region, and two between the EF-hands and the end of the IQ domain (mutations available on www.fsm.it/cardmoc/). Thus, the domains known to be essential to the Na_V Ca^{2+} regulatory apparatus (DIII-IV linker, EF-hand, and IQ-motif) form hot-spot regions for LQT3 syndrome (61) (Figs. 2–4). Thus, it is possible that disruption of Ca^{2+} sensing may serve to compound the direct effects of mutations on channel gating.

Loss of function mutations that result in reduced sodium current of $Na_V1.5$, mostly due to trafficking defects, underlie Brugada syndrome (BrS) (62). As such, many of the reported mutations provide truncated proteins that likely do not fold. However, a number of point mutations not resulting in truncations are present in the Ca^{2+}-sensing machinery: eight within the inactivation gate, five in the EF-hand region, and three following the EF-hands until the end of the IQ domain (Figs. 2–4). It is likely that several of these simply result in decreased folding stability of the channels, and hence a decreased functional expression.

The $Na_V1.5$ A1924T Brugada syndrome mutation, located immediately C-terminal to the IQ domain, has been shown to affect gating and Ca^{2+} regulation (6,35). Additionally, the $Na_V1.5$ D1790G LQT3 mutation in the EF-hands, at the N-terminus of the first helix (Fig. 4) reduces the Ca^{2+}-dependent shift in steady-state inactivation, and Trp fluorescence experiments indicate a ~20-fold reduction in Ca^{2+} affinity (10,12). Compared to wild-type channels, this mutation also significantly speeds up entry into inactivation in high Ca^{2+} (12). The LQT3 $Na_V1.5$ S1904L mutation near the IQ motif may affect the interaction between the IQ domain and the EF-hands (42,46) and reduces the affinity of the CTD for the DIII-IV linker to a level that can no longer be quantified via ITC.

Inherited mutations in neuronal channels may also impact Ca^{2+} sensing. The $Na_V1.2$ R1902C mutation has been linked to the inherited seizure disorder Generalized

Epilepsy with Febrile Seizures Plus (GEFS+). Located near the IQ motif (Fig. 2), this mutation causes a threefold reduction in the affinity for Ca^{2+}/CaM (63). In the NMR structure of the $Na_V1.2$ IQ motif complexed to apoC-lobe, R1902 was not found to interact with CaM (36) However, chemical-shift analysis indicates that Ca^{2+}/CaM binding differs from apoCaM binding to the IQ domain, and R1902 may therefore contribute to Ca^{2+}/CaM interactions.

CONCLUDING COMMENTS

The mechanistic basis for Ca^{2+}/CaM regulation of Na_Vs has thus far been a difficult biological problem to solve. Seemingly contradictory observations may be due to variable experimental conditions and inherent differences between Na_V isoforms, in addition to overlapping, redundant signaling pathways within Na_V channels themselves. In addition, while a growing number of experimental approaches promise to bring clarity to a historically murky topic, much mystery remains regarding the molecular mechanism and physiological role of this potentially important regulatory process. Na_V mutations associated with inheritable excitability disorders are likely to also disrupt Ca^{2+} sensing, and alternatively, given that many pathological disorders have chronically high Ca^{2+} levels, such as in the failing heart or catecholaminergic polymorphic ventricular tachycardia, it is feasible that targeted modulation Ca^{2+}/CaM regulation of Na_Vs could be a novel therapeutic strategy for these largely untreatable diseases.

This work is funded by grant No. 259572 from the Canadian Institutes of Health Research (to C.A.A. and F.V.P.). C.A.A. is a Heart and Stroke Foundation of Canada New Investigator and a Michael Smith Foundation for Health Research Career Investigator. F.V.P. is a Canadian Institutes of Health Research New Investigator and a Michael Smith Foundation for Health Research Career Investigator.

REFERENCES

1. Horn, R., J. Patlak, and C. F. Stevens. 1981. Sodium channels need not open before they inactivate. *Nature.* 291:426–427.
2. Joseph, D., G. A. Petsko, and M. Karplus. 1990. Anatomy of a conformational change: hinged "lid" motion of the triosephosphate isomerase loop. *Science.* 249:1425–1428.
3. Stühmer, W., F. Conti, …, S. Numa. 1989. Structural parts involved in activation and inactivation of the sodium channel. *Nature.* 339: 597–603.
4. Smith, M. R., and A. L. Goldin. 1997. Interaction between the sodium channel inactivation linker and domain III S4-S5. *Biophys. J.* 73:1885–1895.
5. McPhee, J. C., D. S. Ragsdale, …, W. A. Catterall. 1998. A critical role for the S4-S5 intracellular loop in domain IV of the sodium channel α-subunit in fast inactivation. *J. Biol. Chem.* 273:1121–1129.
6. Tan, H. L., S. Kupershmidt, …, J. R. Balser. 2002. A calcium sensor in the sodium channel modulates cardiac excitability. *Nature.* 415: 442–447.
7. Kass, R. S. 2006. Sodium channel inactivation in heart: a novel role of the carboxy-terminal domain. *J. Cardiovasc. Electrophysiol.* 17(*Suppl 1*): S21–S25.
8. Sarhan, M. F., C. C. Tung, …, C. A. Ahern. 2012. Crystallographic basis for calcium regulation of sodium channels. *Proc. Natl. Acad. Sci. USA.* 109:3558–3563.
9. Sarhan, M. F., F. Van Petegem, and C. A. Ahern. 2009. A double tyrosine motif in the cardiac sodium channel domain III-IV linker couples calcium-dependent calmodulin binding to inactivation gating. *J. Biol. Chem.* 284:33265–33274.
10. Wingo, T. L., V. N. Shah, …, J. R. Balser. 2004. An EF-hand in the sodium channel couples intracellular calcium to cardiac excitability. *Nat. Struct. Mol. Biol.* 11:219–225.
11. Potet, F., B. Chagot, …, J. R. Balser. 2009. Functional interactions between distinct sodium channel cytoplasmic domains through the action of calmodulin. *J. Biol. Chem.* 284:8846–8854.
12. Biswas, S., D. DiSilvestre, …, G. F. Tomaselli. 2009. Calcium-mediated dual-mode regulation of cardiac sodium channel gating. *Circ. Res.* 104:870–878.
13. Herzog, R. I., C. Liu, …, T. R. Cummins. 2003. Calmodulin binds to the C terminus of sodium channels $Na_v1.4$ and $Na_v1.6$ and differentially modulates their functional properties. *J. Neurosci.* 23:8261–8270.
14. Deschênes, I., N. Neyroud, …, G. F. Tomaselli. 2002. Isoform-specific modulation of voltage-gated Na^+ channels by calmodulin. *Circ. Res.* 90:E49–E57.
15. Ahern, C. A., J. F. Zhang, …, R. Horn. 2005. Modulation of the cardiac sodium channel $Na_V1.5$ by Fyn, a Src family tyrosine kinase. *Circ. Res.* 96:991–998.
16. Huttlin, E. L., M. P. Jedrychowski, …, S. P. Gygi. 2010. A tissue-specific atlas of mouse protein phosphorylation and expression. *Cell.* 143:1174–1189.
17. Young, K. A., and J. H. Caldwell. 2005. Modulation of skeletal and cardiac voltage-gated sodium channels by calmodulin. *J. Physiol.* 565:349–370.
18. Biswas, S., I. Deschênes, …, G. F. Tomaselli. 2008. Calmodulin regulation of $Na_v1.4$ current: role of binding to the carboxyl terminus. *J. Gen. Physiol.* 131:197–209.
19. Cheney, R. E., and M. S. Mooseker. 1992. Unconventional myosins. *Curr. Opin. Cell Biol.* 4:27–35.
20. Alexander, K. A., B. T. Wakim, …, D. R. Storm. 1988. Identification and characterization of the calmodulin-binding domain of neuromodulin, a neurospecific calmodulin-binding protein. *J. Biol. Chem.* 263: 7544–7549.
21. Bähler, M., and A. Rhoads. 2002. Calmodulin signaling via the IQ motif. *FEBS Lett.* 513:107–113.
22. Rhoads, A. R., and F. Friedberg. 1997. Sequence motifs for calmodulin recognition. *FASEB J.* 11:331–340.
23. Van Petegem, F., F. C. Chatelain, and D. L. Minor, Jr. 2005. Insights into voltage-gated calcium channel regulation from the structure of the $Ca_V1.2$ IQ domain-Ca^{2+}/calmodulin complex. *Nat. Struct. Mol. Biol.* 12:1108–1115.
24. Kim, E. Y., C. H. Rumpf, …, D. L. Minor, Jr. 2008. Structures of Ca_V2 Ca^{2+}/CaM-IQ domain complexes reveal binding modes that underlie calcium-dependent inactivation and facilitation. *Structure.* 16:1455–1467.
25. Kim, E. Y., C. H. Rumpf, …, D. L. Minor, Jr. 2010. Multiple C-terminal tail Ca^{2+}/CaMs regulate $Ca_V1.2$ function but do not mediate channel dimerization. *EMBO J.* 29:3924–3938.
26. Fallon, J. L., D. B. Halling, …, F. A. Quiocho. 2005. Structure of calmodulin bound to the hydrophobic IQ domain of the cardiac $Ca_v1.2$ calcium channel. *Structure.* 13:1881–1886.
27. Halling, D. B., D. K. Georgiou, …, S. L. Hamilton. 2009. Determinants in Ca_V1 channels that regulate the Ca^{2+} sensitivity of bound calmodulin. *J. Biol. Chem.* 284:20041–20051.
28. Mori, M. X., C. W. van der Kooi, …, D. T. Yue. 2008. Crystal structure of the Ca_V2 IQ domain in complex with Ca^{2+}/calmodulin: high-resolution mechanistic implications for channel regulation by Ca^{2+}. *Structure.* 16:607–620.

29. Fallon, J. L., M. R. Baker, …, F. A. Quiocho. 2009. Crystal structure of dimeric cardiac L-type calcium channel regulatory domains bridged by Ca^{2+}* calmodulins. *Proc. Natl. Acad. Sci. USA.* 106:5135–5140.
30. Kink, J. A., M. E. Maley, …, C. Kung. 1990. Mutations in paramecium calmodulin indicate functional differences between the C-terminal and N-terminal lobes in vivo. *Cell.* 62:165–174.
31. Saimi, Y., and K. Y. Ling. 1990. Calmodulin activation of calcium-dependent sodium channels in excised membrane patches of Paramecium. *Science.* 249:1441–1444.
32. Kim, J., S. Ghosh, …, G. S. Pitt. 2004. Calmodulin mediates Ca^{2+} sensitivity of sodium channels. *J. Biol. Chem.* 279:45004–45012.
33. Mori, M., T. Konno, …, K. Nagayama. 2000. Novel interaction of the voltage-dependent sodium channel (VDSC) with calmodulin: does VDSC acquire calmodulin-mediated Ca^{2+}-sensitivity? *Biochemistry.* 39:1316–1323.
34. Theoharis, N. T., B. R. Sorensen, …, M. A. Shea. 2008. The neuronal voltage-dependent sodium channel type II IQ motif lowers the calcium affinity of the C-domain of calmodulin. *Biochemistry.* 47:112–123.
35. Shah, V. N., T. L. Wingo, …, W. J. Chazin. 2006. Calcium-dependent regulation of the voltage-gated sodium channel hH1: intrinsic and extrinsic sensors use a common molecular switch. *Proc. Natl. Acad. Sci. USA.* 103:3592–3597.
36. Feldkamp, M. D., L. Yu, and M. A. Shea. 2011. Structural and energetic determinants of apo calmodulin binding to the IQ motif of the $Na_V1.2$ voltage-dependent sodium channel. *Structure.* 19:733–747.
37. Chagot, B., and W. J. Chazin. 2011. Solution NMR structure of Apo-calmodulin in complex with the IQ motif of human cardiac sodium channel $Na_V1.5$. *J. Mol. Biol.* 406:106–119.
38. Cormier, J. W., I. Rivolta, …, R. S. Kass. 2002. Secondary structure of the human cardiac Na^+ channel C terminus: evidence for a role of helical structures in modulation of channel inactivation. *J. Biol. Chem.* 277:9233–9241.
39. Motoike, H. K., H. Liu, …, R. S. Kass. 2004. The Na^+ channel inactivation gate is a molecular complex: a novel role of the COOH-terminal domain. *J. Gen. Physiol.* 123:155–165.
40. Chagot, B., F. Potet, …, W. J. Chazin. 2009. Solution NMR structure of the C-terminal EF-hand domain of human cardiac sodium channel $Na_V1.5$. *J. Biol. Chem.* 284:6436–6445.
41. Miloushev, V. Z., J. A. Levine, …, A. G. Palmer, 3rd. 2009. Solution structure of the $Na_V1.2$ C-terminal EF-hand domain. *J. Biol. Chem.* 284:6446–6454.
42. Glaaser, I. W., J. D. Osteen, …, R. S. Kass. 2012. Perturbation of sodium channel structure by an inherited long QT syndrome mutation. *Nat. Commun.* 3:706.
43. Wang, C., B. C. Chung, …, G. S. Pitt. 2012. Crystal structure of the ternary complex of a Na_V C-terminal domain, a fibroblast growth factor homologous factor, and calmodulin. *Structure.* 20:1167–1176.
44. Viswanathan, P. C., C. R. Bezzina, …, J. R. Balser. 2001. Gating-dependent mechanisms for flecainide action in SCN5A-linked arrhythmia syndromes. *Circulation.* 104:1200–1205.
45. Mantegazza, M., F. H. Yu, …, T. Scheuer. 2001. Role of the C-terminal domain in inactivation of brain and cardiac sodium channels. *Proc. Natl. Acad. Sci. USA.* 98:15348–15353.
46. Bankston, J. R., K. J. Sampson, …, R. S. Kass. 2007. A novel LQT-3 mutation disrupts an inactivation gate complex with distinct rate-dependent phenotypic consequences. *Channels (Austin).* 1:273–280.
47. Reference deleted in proof.
48. Peterson, B. Z., C. D. DeMaria, …, D. T. Yue. 1999. Calmodulin is the Ca^{2+} sensor for Ca^{2+}-dependent inactivation of L-type calcium channels. *Neuron.* 22:549–558.
49. Zühlke, R. D., G. S. Pitt, …, H. Reuter. 1999. Calmodulin supports both inactivation and facilitation of L-type calcium channels. *Nature.* 399:159–162.
50. Lee, A., S. T. Wong, …, W. A. Catterall. 1999. Ca^{2+}/calmodulin binds to and modulates P/Q-type calcium channels. *Nature.* 399:155–159.
51. Mori, M. X., M. G. Erickson, and D. T. Yue. 2004. Functional stoichiometry and local enrichment of calmodulin interacting with Ca^{2+} channels. *Science.* 304:432–435.
52. Dick, I. E., M. R. Tadross, …, D. T. Yue. 2008. A modular switch for spatial Ca^{2+} selectivity in the calmodulin regulation of Ca_V channels. *Nature.* 451:830–834.
53. Kearney, J. A., N. W. Plummer, …, M. H. Meisler. 2001. A gain-of-function mutation in the sodium channel gene SCN2A results in seizures and behavioral abnormalities. *Neuroscience.* 102:307–317.
54. Yang, N., S. Ji, …, A. L. George, Jr. 1994. Sodium channel mutations in Paramyotonia congenita exhibit similar biophysical phenotypes in vitro. *Proc. Natl. Acad. Sci. USA.* 91:12785–12789.
55. Yang, Y., Y. Wang, …, Y. Shen. 2004. Mutations in SCN9A, encoding a sodium channel α-subunit, in patients with primary erythermalgia. *J. Med. Genet.* 41:171–174.
56. Keating, M. T., and M. C. Sanguinetti. 2001. Molecular and cellular mechanisms of cardiac arrhythmias. *Cell.* 104:569–580.
57. Kahlig, K. M., T. H. Rhodes, …, A. L. George, Jr. 2008. Divergent sodium channel defects in familial hemiplegic migraine. *Proc. Natl. Acad. Sci. USA.* 105:9799–9804.
58. Splawski, I., J. Shen, …, M. T. Keating. 2000. Spectrum of mutations in long-QT syndrome genes. KVLQT1, HERG, SCN5A, KCNE1, and KCNE2. *Circulation.* 102:1178–1185.
59. Napolitano, C., S. G. Priori, …, S. Leonardi. 2005. Genetic testing in the long QT syndrome: development and validation of an efficient approach to genotyping in clinical practice. *JAMA.* 294:2975–2980.
60. Wang, Q., J. Shen, …, M. T. Keating. 1995. SCN5A mutations associated with an inherited cardiac arrhythmia, long QT syndrome. *Cell.* 80:805–811.
61. Ruan, Y., N. Liu, and S. G. Priori. 2009. Sodium channel mutations and arrhythmias. *Nat. Rev. Cardiol.* 6:337–348.
62. Chen, Q., G. E. Kirsch, …, Q. Wang. 1998. Genetic basis and molecular mechanism for idiopathic ventricular fibrillation. *Nature.* 392: 293–296.
63. Weiss, L. A., A. Escayg, …, M. H. Meisler. 2003. Sodium channels SCN1A, SCN2A and SCN3A in familial autism. *Mol. Psychiatry.* 8:186–194.

Be the first...

to read the latest issue of *Biophysical Journal.*

Receive *Biophysical Journal* Email Alerts – FREE!

Register Now at www.biophysj.org

Imaging Protein Structure in Water at 2.7 nm Resolution by Transmission Electron Microscopy

Utkur M. Mirsaidov,[†‡△] Haimei Zheng,[§△] Yosune Casana,[‡] and Paul Matsudaira[†‡*]
[†]Mechanobiology Institute and [‡]Center for BioImaging Sciences, Department of Biological Sciences, National University of Singapore, Singapore; and [§]Materials Sciences Division, Lawrence Berkeley National Laboratory, Berkeley, California

ABSTRACT We demonstrate an in situ transmission electron microscopy technique for imaging proteins in liquid water at room temperature. Liquid samples are loaded into a microfabricated environmental cell that isolates the sample from the vacuum with thin silicon nitride windows. We show that electron micrographs of acrosomal bundles in water are similar to bundles imaged in ice, and we determined the resolution to be at least 2.7 nm at doses of ~35 e/Å^2. The resolution was limited by the thickness of the window and radiation damage. Surprisingly, we observed a smaller fall-off in the intensity of reflections in room-temperature water than in 98 K ice. Thus, our technique extends imaging of unstained and unlabeled macromolecular assemblies in water from the resolution of the light microscope to the nanometer resolution of the electron microscope. Our results suggest that real-time imaging of protein dynamics is conceptually feasible.

Received for publication 13 November 2011 and in final form 11 January 2012.

[△]Utkur M. Mirsaidov and Haimei Zheng contributed equally to this work.

*Correspondence: dbsmpt@nus.edu.sg

"The colder the better" is the common wisdom in structural biology, and thus data are conventionally collected at cryogenic temperatures for x-ray crystallography and transmission electron microscopy (TEM). Several decades of research have shown that radiation damage is reduced significantly at liquid nitrogen (1) or helium (2) temperatures. Typically, a high-resolution structure is degraded through bond breakage and rearrangements, as well as interactions with highly reactive free radicals from the surrounding solvent (3). It is believed these effects are minimized in cryoelectron microscopy by preserving structure in vitreous ice of either cells by high-pressure freezing or molecules by plunge freezing (4). However, one consequence is that structures are immobile and the mechanisms underlying function are inferred from static states. Although dynamic processes such as assembly and disassembly of proteins, and in vitro motility of motor proteins are easily detected at the single-molecule level by high-resolution fluorescence light microscopy, the molecular structure of proteins can only be achieved at nanometer resolution by EM, NMR, or x-ray methods.

Forty years after Matricardi et al.'s (5) report on the electron diffraction patterns of hydrated flat catalase crystals in the presence of water vapor, little progress has been made in the direct imaging of proteins in liquids. Recently developed techniques allow biological imaging of micron-scale objects or labeled specimens by scanning EM (SEM) and TEM in liquid (6–8). However, the direct imaging of nanometer-sized proteins has not been achieved yet. Here, we show that protein structures can be directly imaged in liquid water at ambient temperature by TEM, where radiation damage to protein structure in water is unexpectedly less significant than that observed at 98 K. To study proteins in their native environment, we adapt methods from material sciences for studying nanoparticle growth in solution at room temperature using a liquid environmental cell operating in a 120 keV transmission electron microscope (Tecnai T12; FEI, Hillsboro, OR) equipped with a 4096×4096 pixel camera (Ultrascan; Gatan, Warrendale, PA) (9) (Supporting Material). Other groups used a similar approach to image whole cells in liquid water by scanning transmission electron microscopy (STEM), which visualizes gold nanoparticle labels to provide structural information about cells with thicknesses of a few micrometers (7). In this work, we focus on the direct imaging of protein structures in liquid water by TEM without the use of labels. The technique involves a liquid cell that is microfabricated from silicon and has an electron translucent silicon nitride (Si_3N_4) membrane window with lateral dimensions of ~3 × 50 μm and a thickness of only 10 nm (Fig. 1 *A*). The use of ultrathin (~10 nm) Si_3N_4 membranes for developing liquid environmental cells has proven to be critical for direct TEM imaging of protein structures in liquid water. The protein solution is loaded into the liquid cell and forms a thin liquid film (80–300 nm depending on the thickness of the indium spacer) between the silicon nitride membranes (Supporting Material). In the electron microscope, the electron beam penetrates through the top and bottom Si_3N_4 membranes and the enclosed thin layer of liquid sample.

We imaged an acrosomal process (a crystalline bundle of actin filaments) in liquid water by TEM, because its structure

Editor: Shin'ichi Ishiwata.

doi: 10.1016/j.bpj.2012.01.009

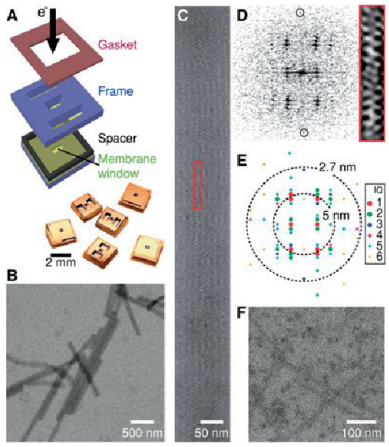

FIGURE 1 Imaging proteins in a liquid cell. (*A*) The liquid cell is assembled and a protein solution is loaded through two large reservoirs that are then sealed by a gasket. The protein solution is drawn by capillary force into the liquid cell and forms a thin film between two 10-nm-thick Si_3N_4 membranes. (*B*) Low-magnification image of 80-nm-diameter acrosomal bundles in liquid. (*C*) An acrosomal bundle in *h0l* orientation. The unit cell is boxed. (*D*) Fourier transform pattern from a portion of the image of the acrosomal bundle in *C*. The meridional reflection at 2.7 nm is circled. Red box: Unit cell reconstructed from reflections with S/N ratio > 1.2. (*E*) *IQ* plot of the Fourier transform and the resolution shells at 5 and 2.7 nm. (*F*) MAP-assembled microtubules show rod-shaped structures (enhanced contrast), whereas the protofilament substructure is not resolved.

can be preserved to >7 Å in vitreous ice under a transmission electron microscope (10), and we previously characterized its radiation hardiness extensively at liquid nitrogen temperatures (11). Initially, we were unable to detect the acrosomes in liquid cells with a 0.5- to 1.0-μm gap and 50- to 100-nm-thick windows due to scatter and absorption from water and Si_3N_4. However, when the thicknesses of water and membranes were reduced, we were able to clearly detect the acrosomes and identify the characteristic view along the *h0l* projection with $a = b = 147$ Å, $c = 762$ Å (10,11). Fig. 1, *B* and *C*, show the familiar patterns of bands and stripes and well-defined zigzag features from actin subunits in the filaments (10). Compared with images in vitreous ice, the image contrast of the acrosomes in liquid water is lower because of the additional thickness of the Si_3N_4 windows.

To assess the quality and resolution of the images, we measured the intensity of reflections from their Fourier transforms (Fig. 1 *D*), displayed by an *IQ* plot (11,12) (Fig. 1 *E*). The *IQ* values shown in Fig. 1 range from 1 (signal/noise (S/N) ratio $\geq$ 7) to 6 (S/N ratio > 1.1) (12). The highest-resolution reflection (S/N ratio > 2) detected is the 2.7-nm meridional arising from the helical rise of the actin subunits in filaments. Thus, at this resolution, when imaging at 120 keV, actin structure is qualitatively preserved to a similar extent in room-temperature water as in ice. Similarly, MAP-stabilized microtubules (diameter: 25 nm) are also imaged in 80-nm-thick water (Fig. 1 *F*). However, we are unable to see the protofilament substructures, which are visible at higher magnifications in ice. These images demonstrate the feasibility of imaging proteins in water, but immediately show that resolution is limited.

One major limit to resolution is the significant scattering from the window that reduces the S/N ratio (Si_3N_4: Z = 10.6; water: Z = 4.8). As the membrane thickness increases, we find that the contrast and resolution of the acrosome images degrade. Here, we define the image resolution to be the largest extent of the Fourier transform of the image with amplitude with S/N ratio > 2. Thus, we obtained resolutions of 2.7 nm, 5.1 nm, and 12.4 nm corresponding to membrane thicknesses of 10 nm, 14 nm, and 25 nm, respectively (with the same water thickness of ~300 nm; Supporting Material).

A second major limit to resolution is radiation damage caused by high-energy electrons. Radiation damage to a structure is first revealed by degradation or alteration of the highest-resolution features, which is more pronounced for organic polymers and biological specimens than for inorganic materials (13). At very high electron doses, the acrosomes in ice develop bubbles, whereas in water the structure dries and darkens (Supporting Material). For periodic structures and at lower electron doses, a more quantitative measure of radiation damage is defined by the decay of the Fourier peak amplitude. Our previous studies on imaging of acrosomal bundles indicate that the tolerable dose ($D_{1/e}$), at which the amplitude of Fourier peaks (A/A_0) drops by a factor of e, is ~25 e/Å^2 under 400 keV electron beam and at cryogenic temperature (11). It is noted that the tolerable electron doses for imaging powder samples and gelatin-encapsulated samples are several times lower at room temperature than in cryogenic conditions (1). To assess the extent of structural damage of the bundle in liquid water at room temperature, we measure the fall-off in intensity of reflection as a function of electron dose as the same acrosome is sequentially imaged. The amplitudes are normalized and arranged into two groups, (i.e., 27–50 Å and >50 Å) according to their reciprocal lattice sizes, and are plotted as a function of the electron dose (Fig. 2; also see Supporting Material). The plots are fitted to a simple exponential decay function for each case: $A/A_0 = \exp[-(D - D_0)/D_{1/e}]$, where D_0 is the electron dose delivered for the first image. For acrosomes imaged in ice at 120 keV, $D_{1/e}(98\ \mathrm{K}) = 31 \pm 3$ e/Å^2 for 27–50 Å and $D_{1/e}(98\ \mathrm{K}) = 68 \pm 4$ e/Å^2 for >50 Å. However, when imaging in liquid water, we find that contrary to expectations, the radiation damage is less in water than in ice: $D_{1/e}(293\ \mathrm{K}) = 35 \pm 2$ e/Å^2 for 27–50 Å and $D_{1/e}(293\ \mathrm{K}) = 110 \pm 5$ e/Å^2 for >50 Å. Because of the limit in resolution from the Si_3N_4 window, we are currently unable to measure radiation damage on the high-resolution features of the acrosome structure. Thus, it is not feasible to directly compare the radiation damage with our previous measurements for acrosomes imaged at 400 keV.

Previous studies reported increased radiation damage to dried or glucose-embedded biological specimens at

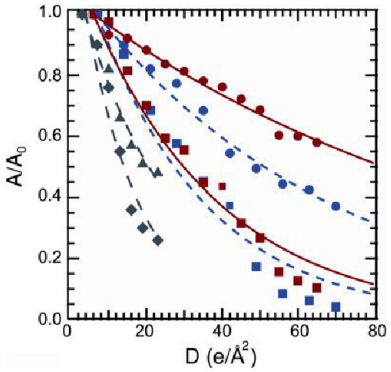

FIGURE 2 Radiation damage. A fall-off in resolution is shown at 293 K (aqueous) for resolution shells of 27–50 Å (*red square*) and >50 Å (*red circle*), 98 K (cryo) for resolution shells of 27–50 Å (*blue square*), and >50 Å (*blue circle*) at 120 keV for resolution shells of 27–50 Å and >50 Å (Fig. 1 *E*), compared with damage at 400 keV and at 98 K for resolution shells of 22–37 Å (*gray diamond*) and >37 Å (*gray triangle*; from Schmid et al. (11). Experimental data are fitted (*lines*) to exponential decay.

room versus cryogenic temperatures (1,4,14). The similarity between water and ice in tolerable electron dose for imaging proteins is contrary to the previous expectation. We suggest the difference lies in the mechanisms of radiation damage in water versus in ice caused by radicals generated during electron irradiation. Free radicals have slower reaction rates (15) and diffuse faster in 293 K water than in 98 K ice (16,17) (see Supporting Material). Additionally, specimen movements seen in ice are caused by two mechanisms: charging and gaseous hydrogen buildup induced during radiolysis of water inside the ice (18). These movements should be nonexistent in liquid water. The combination of the slower reaction rate, mobility of free radicals, and absence of distortion in water may account for the comparable tolerable dose of electrons. Another mechanism of damage is covalent bond breakage from inelastic scattering of electrons. However, this damage should be equivalent in aqueous and frozen water because the scattering cross section is determined by the atomic composition of protein and beam parameters. Thus, to our knowledge, our study provides the first direct comparison of radiation damage in water at room temperature versus in ice at liquid nitrogen temperature for biological TEM.

Our results illustrate that unlabeled protein structures can be imaged directly in water with a resolution of at least 2.7 nm, and the radiation tolerance of an acrosomal bundle is higher in liquid water than in frozen ice. Our ability to directly image proteins in water suggests that it may be possible to study protein dynamics (e.g., the assembly/disassembly or translocation of proteins) under physiologically relevant aqueous conditions with nanometer resolution. For decades, investigators have used biological labels to study these events with fluorescence light microscopy methods. This study provides the groundwork for future nanometer-scale dynamic imaging without labels, and opens what to our knowledge is a new avenue for biological TEM.

SUPPORTING MATERIAL

Supporting Methods, Discussion, eight figures, and references are available at http://www.biophysj.org/biophysj/supplemental/S0006-3495(12)00065-3.

ACKNOWLEDGMENTS

We thank Robert Glaeser and Wah Chiu for helpful discussions on radiation damage and Les Wilson for the gift of microtubules. H.Z. thanks the support from Laboratory Directed Research and Development of Lawrence Berkeley National Laboratory.

REFERENCES and FOOTNOTES

1. Hayward, S. B., and R. M. Glaeser. 1979. Radiation damage of purple membrane at low temperature. *Ultramicroscopy.* 4:201–210.
2. Chiu, W., E. Knapek, …, I. Dietrick. 1981. Electron radiation damage of a thin protein crystal at 4K. *Ultramicroscopy.* 6:291–295.
3. Glaeser, R. M. 2008. Retrospective: radiation damage and its associated "information limitations". *J. Struct. Biol.* 163:271–276.
4. Dubochet, J., M. Adrian, …, P. Schultz. 1988. Cryo-electron microscopy of vitrified specimens. *Q. Rev. Biophys.* 21:129–228.
5. Matricardi, V. R., R. C. Moretz, and D. F. Parson. 1972. Electron diffraction of wet proteins: catalase. *Science.* 21:268–270.
6. de Jonge, N., and F. M. Ross. 2011. Electron microscopy of specimens in liquid. *Nat. Nanotechnol.* 6:695–704.
7. de Jonge, N., D. B. Peckys, …, D. W. Piston. 2009. Electron microscopy of whole cells in liquid with nanometer resolution. *Proc. Natl. Acad. Sci. USA.* 106:2159–2164.
8. Thiberge, S., A. Nechushtan, …, E. Moses. 2004. Scanning electron microscopy of cells and tissues under fully hydrated conditions. *Proc. Natl. Acad. Sci. USA.* 101:3346–3351.
9. Zheng, H. R., R. K. Smith, …, A. P. Alivisatos. 2009. Observation of single colloidal platinum nanocrystal growth trajectories. *Science.* 324:1309–1312.
10. Schmid, M. F., J. Jakana, …, W. Chiu. 1993. Imaging frozen, hydrated acrosomal bundle from Limulus sperm at 7 A resolution with a 400 kV electron cryomicroscope. *J. Mol. Biol.* 230:384–386.
11. Schmid, M. F., J. Jakana, …, W. Chiu. 1992. Effects of radiation damage with 400-kV electrons on frozen, hydrated actin bundles. *J. Struct. Biol.* 108:62–68.
12. Henderson, R., J. M. Baldwin, …, F. Zemlin. 1986. Structure of purple membrane from *Halobacterium halobium*: recording, measurement, and evaluation of electron micrographs at 3.5Å resolution. *Ultramicroscopy.* 19:147–178.
13. Spence, J. C. H. 2003. High-Resolution Electron Microscopy (Monographs on the Physics and Chemistry of Materials), 3rd ed. Oxford University Press, New York.
14. Stark, H., F. Zemlin, and C. Boettcher. 1996. Electron radiation damage to protein crystals of bacteriorhodopsin at different temperatures. *Ultramicroscopy.* 63:75–79.
15. Vöhringer-Martinez, E., B. Hansmann, …, B. Abel. 2007. Water catalysis of a radical-molecule gas-phase reaction. *Science.* 315:497–501. Erratum in *Science* 2007;316:691.
16. Patten, F., and W. Gordy. 1960. Temperature effects on free radical formation and electron migration in irradiated proteins. *Proc. Natl. Acad. Sci. USA.* 46:1137–1144.
17. Symons, M. C. R. 1982. Radiation processes in frozen aqueous systems. *Ultramicroscopy.* 10:97–103.
18. Meents, A., S. Gutmann, …, C. Schulze-Briese. 2010. Origin and temperature dependence of radiation damage in biological samples at cryogenic temperatures. *Proc. Natl. Acad. Sci. USA.* 107:1094–1099.

Cell Press content is widely accessible

At Cell Press we place a high priority on ensuring that all of our journal content is widely accessible and on working with the community to develop the best ways to achieve that goal.

Here are just some of those initiatives...

Open archives

We provide free access to Cell Press research journals 12 months following publication

Access for developing nations

We provide free & low-cost access through programs like Research4Life

Open access journal

We launched Cell Reports - a new Open Access journal spanning the life sciences

Funding body agreements

We work cooperatively and successfully with major funding bodies

Public access

Full-text online via ScienceDirect is also available to the public via walk in user access from any participating library

Submission to PubMed Central

Cell Press deposits accepted manuscripts on our authors' behalf for a variety of funding bodies, including NIH and HHMI, to PubMed Central (PMC)

www.cell.com/cellpress/access

Cell PRESS

Mechanosensing in T Lymphocyte Activation

Edward Judokusumo,† Erdem Tabdanov,† Sudha Kumari,‡ Michael L. Dustin,‡ and Lance C. Kam†*
†Department of Biomedical Engineering, Columbia University, New York, New York; and ‡Program in Molecular Pathogenesis, Helen L. and Martin S. Kimmel Center for Biology and Medicine of the Skirball Institute of Biomolecular Medicine, New York University School of Medicine, New York, New York

ABSTRACT Mechanical forces play an increasingly recognized role in modulating cell function. This report demonstrates mechanosensing by T cells, using polyacrylamide gels presenting ligands to CD3 and CD28. Naive CD4 T cells exhibited stronger activation, as measured by attachment and secretion of IL-2, with increasing substrate elastic modulus over the range of 10–200 kPa. By presenting these ligands on different surfaces, this report further demonstrates that mechanosensing is more strongly associated with CD3 rather than CD28 signaling. Finally, phospho-specific staining for Zap70 and Src family kinase proteins suggests that sensing of substrate rigidity occurs at least in part by processes downstream of T-cell receptor activation. The ability of T cells to quantitatively respond to substrate rigidly provides an intriguing new model for mechanobiology.

Received for publication 19 July 2011 and in final form 7 December 2011.

*Correspondence: lk2141@columbia.edu

Cells have the remarkable ability to respond to the mechanical rigidity of the extracellular environment. This has been explored predominantly in anchorage-dependent cells and the specific context of integrin- and cadherin-based adhesion. As a complementary system, we demonstrate here mechanosensing by T lymphocytes, key modulators of adaptive immunity. T cells are activated through engagement of the T-cell receptor (TCR) by peptide-bearing major histocompatibility complex proteins on antigen presenting cells within a small (~70 μm^2) cell-cell contact area termed the immune synapse (1). This interface hosts additional receptor-ligand interactions; engagement of CD28 on the T cell surface provides a costimulatory signal that augments TCR function and is required for activation of naive T cells. The immune synapse is also characterized by a dynamic cytoskeleton (2) that transports clusters of signaling molecules, suggesting a role of physical forces in T cell activation. Indeed, recent studies show that the TCR is sensitive to forces (3,4), but the full impact and mechanism of mechanosensing in T cells remains unexplored.

In this report, the antigen presenting cell is replaced with polyacrylamide gels presenting two activating antibodies (see the Supporting Material), one against CD3 (epsilon subunit, which upon binding activates the TCR complex) and the other to CD28. Concurrent engagement of these two receptors by appropriate antibodies immobilized on rigid beads or planar surfaces is sufficient to induce T cell activation. Notably, activation is not induced by soluble anti-CD3 and anti-CD28. In this report, gel rigidity was controlled by varying the amount of bis-acrylamide cross-linker (5) yielding a core set of materials of bulk Young's moduli (E) between 10 and 200 kPa. Biotinylated anti-CD3 and anti-CD28 antibodies were tethered to the polyacrylamide using an acrylamide-modified streptavidin, yielding a thin (micrometers thick), layer of antibodies (Fig. S1 in the Supporting Material). The concentration of acrylamide-streptavidin was adjusted to produce a single, standard surface density of tethered proteins that will be used for this study across all substrates. Please see the Supporting Material for additional analysis of this approach.

Mouse naive CD4+ T cells were seeded onto polyacrylamide gels presenting a 1:1 mix of anti-CD3 and anti-CD28, and secretion of IL-2 over a 6-h period was compared across gels as a functional measure of activation using a fluorescence-based, surface capture method (6). IL-2 secretion was lowest on the softest ($E = 10$ kPa) gels, and increased with substrate rigidity (Fig. 1 *A*). A small, not statistically significant decrease was observed on the 200 kPa vs. 100 kPa gel, possibly reflecting lower T cell accessibility to the antibodies due to smaller gel pore size. IL-2 secretion was not detectable on surfaces containing either anti-CD3 or anti-CD28 alone (data not shown), reflecting the need for both signals in T cell activation. Cell attachment also responds to substrate rigidity, with a lower density of cells observed on the softest surface compared to the three stiffer preparations (Fig. 1 *A*). Decreasing the gel rigidity below 10 kPa presented no further change in either cell response (Fig. S2); the rest of this study focuses on the core range of 10–200 kPa. These results suggest that cell response can be divided into two ranges on the basis of Young's modulus; for rigidities of 25 kPa or higher, cells exhibit strong attachment and a positive (but saturating) correlation of IL-2 secretion with stiffness, whereas below this range, cells reduce both attachment and IL-2 secretion. An alternative interpretation of this data is that at the lower rigidities IL-2

Editor: Michael Edidin.

doi: 10.1016/j.bpj.2011.12.011

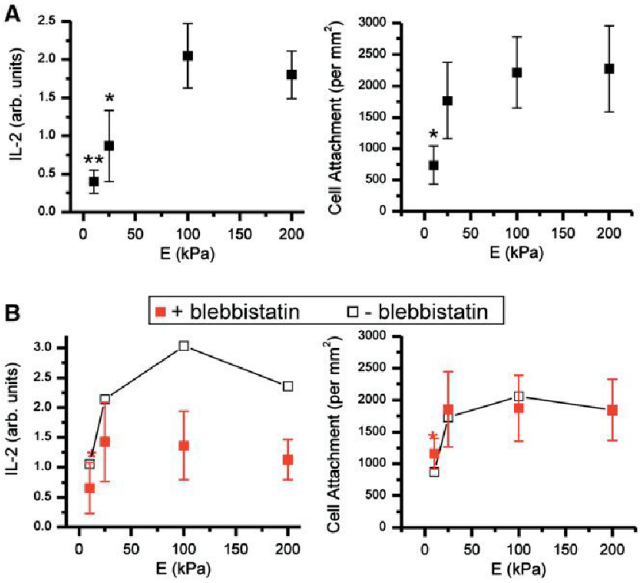

FIGURE 1 Rigidity-dependent activation of CD4+ T cells. (*A*) 6-h IL-2 secretion and cell attachment correlate with Young's modulus, *E*. * $P < 0.05$, ** $P < 0.005$ compared to 200 kPa surface. Data are mean ± SD, $n = 7$. (*B*) Inhibition of myosin-based contractility abrogates mechanosensing on surfaces of 25 kPa or greater. * $P < 0.05$ compared to 200 kPa surface, $n = 3$. Error bars for nonblebbistatin controls are omitted for clarity.

production is modulated by cell attachment density and not directly by elastic modulus. This was addressed by seeding cells at higher densities, as detailed in the Supporting Material. On the 10 kPa gels, an increase in cell attachment density to match that of the three stiffer gels resulted in a minor, not statistically significant increase in IL-2 secretion. Much larger increases in cell seeding density resulted in a minor statistically significant increase IL-2 secretion, but this was associated with a much larger increase in attachment density. Cooperativity between cells thus has an effect on cell activation that is small compared to mechanosensing.

Treatment of cells with blebbistatin (100 μM, Fig. 1 *B*) abrogated the sensitivity of IL-2 secretion across the three stiffest gels, indicating a role of cytoskeletal contractility in cell response. This builds upon an earlier study showing TCR signaling in response to B cells and anti-CD3 presenting bilayers is reduced by blebbistatin treatment (7). Notably, both IL-2 secretion and cell attachment on the 10 kPa gel remained lower than on the three stiffer gels, supporting the idea that cell interaction with the 10 kPa gel is fundamentally different than on the stiffer counterparts.

We next sought to determine whether mechanosensing is mediated by CD3 or CD28. For these experiments, one of the activating antibodies was tethered to the planar polyacrylamide gels while the other was immobilized onto rigid, 4-μm diameter polystyrene beads (Fig. 2 *A*). Varying the rigidity of gels presenting anti-CD3 modulated IL-2 secretion resembling that on surfaces presenting both anti-CD3 and anti-CD28 (Fig. 2 *B*). In contrast, cells on gels presenting

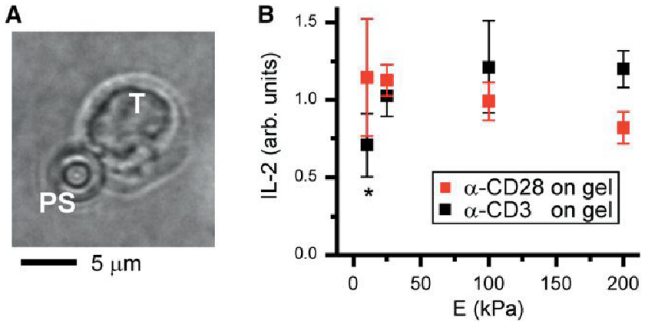

FIGURE 2 CD3-mediated mechanosensing. (*A*) T cell (T) interacting with an antibody-coated polystyrene (PS) bead and underlying gel. (*B*) 16-h secretion of IL-2. * $P < 0.05$ compared to 200 kPa gel. Data are mean ± SD, $n = 3$.

anti-CD28 showed only a small and statistically insignificant (analysis of variance (ANOVA), $\alpha = 0.05$, $n = 3$) decreasing trend in IL-2 secretion with increasing Young's modulus. A longer incubation time (16 h.) was required to obtain measurable IL-2 secretion from these cells. This delayed response may be related to the smaller surface presented by individual beads compared to a gel, or that CD3 and CD28 were engaged on different faces of the T cell, a configuration termed *trans*-costimulation that earlier studies show induces lower levels of activation than the *cis*- counterpart (8). We also note that a well-established method for activating T cells is to provide anti-CD3 on a solid support and anti-CD28 in solution. Surprisingly, soluble CD28 at concentrations of 2–20 μg/ml was ineffective in stimulating IL-2 secretion by cells on gels presenting anti-CD3. Together, these results suggest that T cell mechanosensing is associated with CD3 rather than CD28.

We next focused on proteins involved in T cell activation as potential mechanisms of mechanosensing. Phospho-specific antibodies were used to detect Zap70 (Tyr-493) and an activation loop that is conserved across many Src family kinase proteins (SFK) (9,10); available antibodies cannot distinguish between phosphorylated Lck (Tyr-394) and Fyn (Tyr-420), the two major SFK proteins involved in T cell signaling. By 2 min following seeding, both antibodies detected clusters of proteins in the cell-substrate interface on the three stiffest surfaces (Fig. 3). In contrast, cells on the 10 kPa gels were devoid of pZap70 and pSFK clusters within the interior of the cell-substrate interface, exhibiting only minor accumulations along the cell edge (Fig. 3 *A*). Whole-cell measurement of pZap70 and pSFK followed a similar pattern, being lower on the 10 kPa gel than the 200 kPa preparation (Fig. 3 *B*). The 2 min time point captures the early burst of Zap70 and SFK activity, but similar patterns were also observed for sustained signaling at 30 min (Fig. S3, *A* and *C*). Notably, cells on the three stiffest surfaces were more spread than on the 10 kPa preparation (Fig. S3 *A*). Application of blebbistatin did not affect the distribution or cellular levels of pZap70 and pSFK (Fig. S3, *B* and *C*; $\alpha = 0.05$, two-way ANOVA).

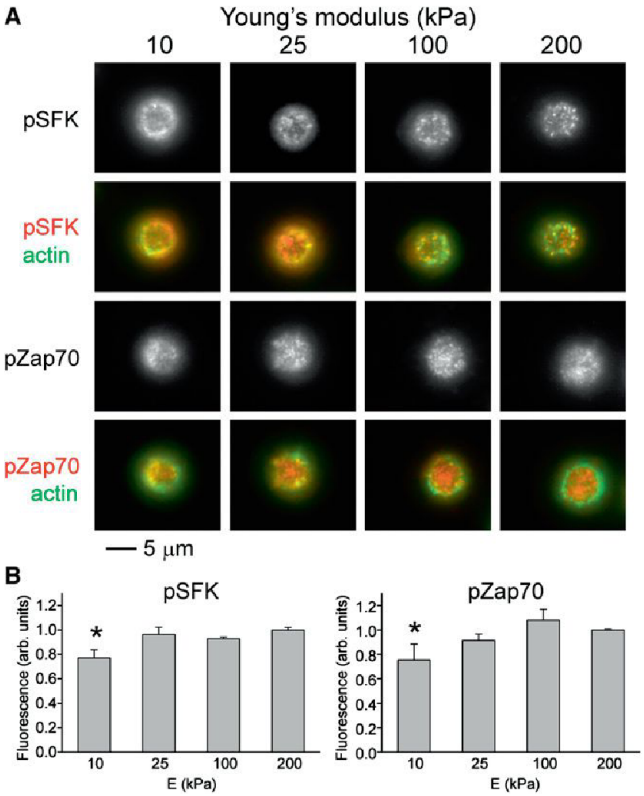

FIGURE 3 Rigidity-dependent early signaling. (*A*) Phospho-specific immunostaining 2 min after seeding. (*B*) Comparison of whole-cell phosphorylation of early signaling proteins. Data are mean ± SD, $n = 3$. * $P < 0.05$ compared to 200 kPa surface.

Together, these results suggest that loss of cell attachment and activation on the 10 kPa gel is associated with loss of early TCR signaling, whereas mechanosensing on the stiffest gels is mediated by mechanisms downstream of Lck/Fyn and Zap70. We note that for human cells interacting with B cells or lipid bilayers, blebbistatin reduces pZap70 at both the whole cell level and in microclusters at the cell-bilayer interface (7). This may reflect differences in species or ligand presentation, but the use of total internal reflection microscopy to probe the thin (200 nm) cell-bilayer interface (not possible at cell-gel contacts) may also explain these results. Finally, we followed phosphorylation of Pyk2 (Tyr-580), a protein related to focal adhesion kinase, which has additional roles in TCR signaling (11). Similar to SFK and Zap70, clusters of pPyk2 were found in the cell-substrate interface on the three stiffest gels, but were restricted to the interface edge on the 10 kPa preparations (Fig. S3, *A* and *B*). Unlike SFK and Zap70, whole-cell levels of pPyk2 were independent of rigidity (Fig. S3 *C*). However, blebbistatin induced a minor but statistically significant decrease in pPyk2 ($P < 0.01$, two-way ANOVA) across all substrates, suggesting that Pyk2 responds to cell contractility and may contribute to T cell mechanosensing.

Finally, we note that TCR and CD28 signaling is very distinct in mechanism than the integrin and cadherin pathways. Specifically, although CD3 and CD28 signaling influences cytoskeleton dynamics, direct mechanical connections between these structures have not been identified. Mechanosensing through these pathways is thus a new model in mechanobiology that sets a wider role of physical forces in biology.

SUPPORTING MATERIAL

Materials and Methods, three figures, and references (12,13) are available at http://www.biophysj.org/biophysj/supplemental/S0006-3495(11)05408-7.

ACKNOWLEDGMENTS

We thank E. U. Azeloglu (Mount Sinial School of Medicine, New York, NY) for assistance with mechanical testing of polyacrylamide gels.

This study was supported by National Institutes of Health grants PN2 EY016586 and R01AI088377.

REFERENCES and FOOTNOTES

1. Grakoui, A., S. K. Bromley, …, M. L. Dustin. 1999. The immunological synapse: a molecular machine controlling T cell activation. *Science.* 285:221–227.
2. Dustin, M. L. 2007. Cell adhesion molecules and actin cytoskeleton at immune synapses and kinapses. *Curr. Opin. Cell Biol.* 19:529–533.
3. Kim, S. T., K. Takeuchi, …, E. L. Reinherz. 2009. The alphabeta T cell receptor is an anisotropic mechanosensor. *J. Biol. Chem.* 284:31028–31037.
4. Li, Y. C., B. M. Chen, …, S. R. Roffler. 2010. Cutting Edge: mechanical forces acting on T cells immobilized via the TCR complex can trigger TCR signaling. *J. Immunol.* 184:5959–5963.
5. Pelham, Jr., R. J., and Y. Wang. 1997. Cell locomotion and focal adhesions are regulated by substrate flexibility. *Proc. Natl. Acad. Sci. USA.* 94:13661–13665.
6. Shen, K., V. K. Thomas, …, L. C. Kam. 2008. Micropatterning of costimulatory ligands enhances CD4+ T cell function. *Proc. Natl. Acad. Sci. USA.* 105:7791–7796.
7. Ilani, T., G. Vasiliver-Shamis, …, M. L. Dustin. 2009. T cell antigen receptor signaling and immunological synapse stability require myosin IIA. *Nat. Immunol.* 10:531–539.
8. Sanchez-Lockhart, M., and J. Miller. 2006. Engagement of CD28 outside of the immunological synapse results in up-regulation of IL-2 mRNA stability but not IL-2 transcription. *J. Immunol.* 176:4778–4784.
9. Chan, A. C., M. Dalton, …, T. Kurosaki. 1995. Activation of ZAP-70 kinase activity by phosphorylation of tyrosine 493 is required for lymphocyte antigen receptor function. *EMBO J.* 14:2499–2508.
10. Veillette, A., and M. Fournel. 1990. The CD4 associated tyrosine protein kinase p56lck is positively regulated through its site of autophosphorylation. *Oncogene.* 5:1455–1462.
11. Ostergaard, H. L., and T. L. Lysechko. 2005. Focal adhesion kinase-related protein tyrosine kinase Pyk2 in T-cell activation and function. *Immunol. Res.* 31:267–282.
12. Costa, K. D., and F. C. Yin. 1999. Analysis of indentation: implications for measuring mechanical properties with atomic force microscopy. *J. Biomech. Eng.* 121:462–471.
13. Sims, T. N., T. J. Soos, …, M. L. Dustin. 2007. Opposing effects of PKCtheta and WASp on symmetry breaking and relocation of the immunological synapse. *Cell.* 129:773–785.

UNCOVER NEW INSIGHTS TO HELP YOU IDENTIFY POTENTIAL BIOLOGICAL TARGETS

Target Insights is a support tool that helps users find important facts that other search tools may miss, because it is based upon an automated analysis of the full text of scientific articles. Target Insights gets you to the right target quicker and with more confidence than other tools.

Developed by Elsevier to meet increasing demands on speed and efficiency it enables target identification and validation teams to discover new insights and update their understanding of the disease model by revealing crucial information which is normally obscured and hard-to-find, in three steps… Identify, Prioritize, Validate.

targetinsights
IDENTIFY PRIORITIZE VALIDATE

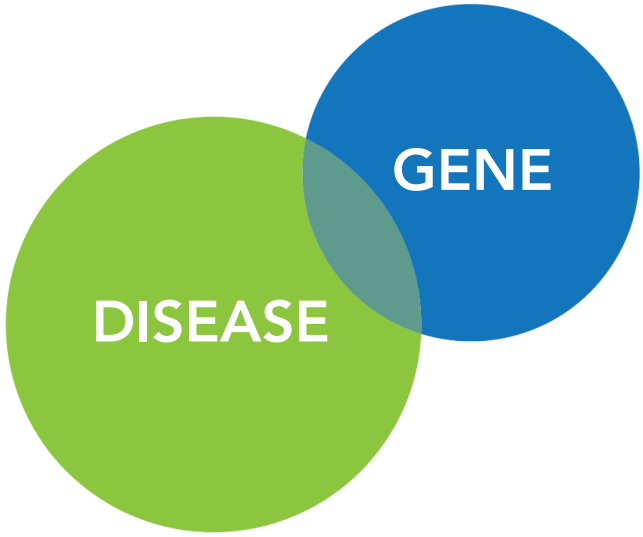

ELSEVIER

For the latest information visit
targetinsights.com/info

Direct Measurement of the Mechanical Properties of Lipid Phases in Supported Bilayers

Laura Picas, Felix Rico, and Simon Scheuring*
INSERM U1006, Institut Curie, Paris, France

ABSTRACT Biological membranes define not only the cell boundaries but any compartment within the cell. To some extent, the functionality of membranes is related to the elastic properties of the lipid bilayer and the mechanical and hydrophobic matching with functional membrane proteins. Supported lipid bilayers (SLBs) are valid biomimetic systems for the study of membrane biophysical properties. Here, we acquired high-resolution topographic and quantitative mechanics data of phase-separated SLBs using a recent atomic force microscopy (AFM) imaging mode based on force measurements. This technique allows us to quantitatively map at high resolution the mechanical differences of lipid phases at different loading forces. We have applied this approach to evaluate the contribution of the underlying hard support in the determination of the elastic properties of SLBs and to determine the adequate indentation range for obtaining reliable elastic moduli values. At ~200 pN, elastic forces dominated the force-indentation response and the sample deformation was <20% of the bilayer thickness, at which the contribution of the support was found to be negligible. The obtained Young's modulus (E) of 19.3 MPa and 28.1 MPa allowed us to estimate the area stretch modulus (k_A) as 106 pN/nm and 199 pN/nm and the bending stiffness (k_c) as 18 k_BT and 57 k_BT for the liquid and gel phases, respectively.

Received for publication 8 July 2011 and in final form 21 November 2011.

*Correspondence: simon.scheuring@inserm.fr

The concept that lipid bilayers are not just a simple passive beholder of membrane proteins is now well accepted. It is important to note that membranes are heterogeneous, with local associations of lipids (and proteins) in detergent-resistant membrane (DRM) domains or rafts (1,2).

In general, membrane dimensions and mechanical properties (i.e., bilayer thickness, bending and stretching stiffness, or membrane tension) modify the function not only of mechanosensitive proteins but of any membrane protein (3). In this framework, the mattress model is in favor of the importance of the lipid environment and provides an elastic model of lipid bilayer behavior (4). As a consequence of the established importance of bilayer compliance and lateral organization of membranes, a large number of techniques (including micropipette aspiration, surface force apparatus, biomembrane force probe or atomic force microscopy imaging, and force spectroscopy) have been employed to give insights into the structure and mechanical properties of biological membranes (5–8). Among them, atomic force microscopy (AFM) (9) in particular has been used to address fundamental questions on the nanomechanics of supported membranes (10).

Here, we introduce a novel, to our knowledge, AFM-based imaging technique, PeakForce-Quantitative Nano-Mechanics (PF-QNM), to probe the structural and mechanical properties of SLBs. PF-QNM allows simultaneous imaging and quantitative mechanical mapping of the sample, both at submolecular resolution (11), and, it is important to point out, improves acquisition time and spatial resolution compared to other AFM-based techniques, such as force volume. This is achieved by oscillating the sample in the z axis at a given amplitude (tens of nanometers) and frequency (2 kHz), thus providing cycles of force-distance (FνD) curves in which the tip intermittently contacts the sample surface. Each FνD plot is thereafter analyzed to determine the mechanical properties of the sample (Fig. S1 in the Supporting Material), thus coupling topography analysis with stiffness and deformation assessment at high resolution.

The aim of this study was to probe the mechanical properties of biological membranes in the elastic regime. We present measures of the elastic properties (i.e., Young's modulus) of different lipid phases, and characterize the effect of the underlying hard substrate.

Nanomechanical mapping of SLBs was performed on DOPC/DPPC (1:1, mol/mol) membranes (Fig. 1), which is one of the best-characterized SLBs and is commonly used as a straightforward model membrane for AFM studies (12,13). DOPC/DPPC bilayers display phase separation at room temperature between liquid (L_α) and gel (L_β) phase, as a consequence of the different transition temperatures of DOPC and DPPC (−20°C and 41°C, respectively) (14). The presence of two segregated domains was readily detected by means of AFM topography with heights for liquid and gel phases of 4.1 ± 0.2 nm and 5.3 ± 0.4 nm, respectively, over the mica support (see Fig. S2), which is in agreement with previous observations (12). It is worthy of note that DOPC has two 18C with one unsaturation (18:1) and DPPC has two 16C fully saturated hydrocarbon chains. These structural differences account not only for the different transition temperatures, more densely packed and gel-like ordered structure for

Editor: Peter Hinterdorfer.

doi: 10.1016/j.bpj.2011.11.4001

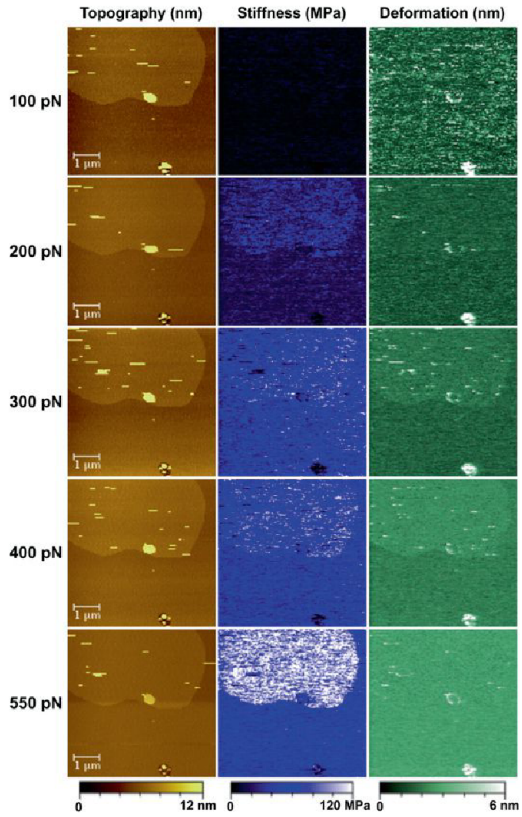

FIGURE 1 PF-QNM images showing the topography (nm) (*left*), stiffness (MPa) (*middle*), and deformation (nm) (*right*) at different peak loading forces (100 pN, 200 pN, 300 pN, 400 pN, and 550 pN). The false color scale is 12 nm for height, 120 MPa for apparent stiffness, and 6 nm for deformation.

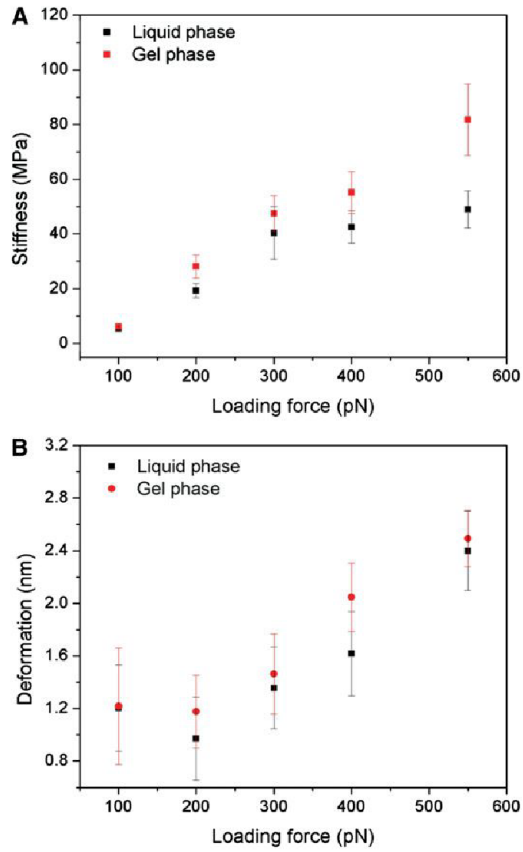

FIGURE 2 Graphical representation of stiffness (*A*) and deformation (*B*) as functions of the peak loading force for both fluid and gel phases. Data are shown as the mean ± SD.

DPPC, and liquidlike behavior for DOPC at room temperature, but also for other physicochemical properties, including differences in breakthrough forces, response to detergent addition, etc. (6,12). Indeed, using PF-QNM AFM imaging, we observed that the gel phase was systematically stiffer than the liquid phase (Figs. 1 and 2). Given the thinness of lipid bilayers, the contribution of the underlying hard mica substrate must be a matter of careful consideration. To address this sensible question, we employed PF-QNM at different loading forces (100 pN, 200 pN, 300 pN, 400 pN, and 550 pN). The Young's modulus of SLBs was determined by fitting the Hertz model to retracting curves at each applied force (Fig. S1). The resulting topography and nanomechanical maps document force-dependent height (nm), stiffness (MPa), and deformation (nm) behavior of the DOPC/DPPC SLBs (Fig. 1).

As expected, the obtained average stiffness values increased with increasing loading force, with the gel phase stiffer than the fluid phase at all loads (Fig. 2 *A*). The degree of deformation followed a similar trend (Fig. 2 *B*), except at very low loading forces (100 pN), where a high apparent deformation (1.2 nm) was observed as a result of long-range electrostatic forces that dominated the interaction over elastic forces (Table S1).

The force-indentation relationship of a parabolic tip indenting a thin layer has been developed and validated on thin layers of soft gels (15). According to this theoretical approach, the overestimation of E is small (<25%) when the indentation is <20% of the sample thickness. Thus, at forces of ~200 pN, where the deformation is ~1 nm, PF-QNM mapping provides reliable values of the actual bilayer elastic modulus of 19.3 MPa and 28.1 MPa for the liquid and gel phases, respectively (Table S1). Even though it is difficult to asses the validity of continuous models at the nanometer scale, and possible nonlinear strain hardening may occur, our values were also confirmed by determining E on supported lipid vesicles (Fig. S3). Moreover, our results show that gel-phase lipids are stiffer than fluid-phase lipids, though the former are thicker than the latter.

The measured Young's modulus on the gel- and fluid-phase bilayers allowed us to calculate the area stretch modulus (k_A) and bending stiffness (k_c), by invoking thin shell theory

$$k_A = Eh/\left(1-\nu^2\right) \text{ and } \kappa_c = Eh^3/24\left(1-\nu^2\right),$$

where ν is the Poisson ratio, assumed as 0.5, and h is the bilayer thickness (7). From our results, we estimated k_A at 106 pN/nm and 199 pN/nm and k_c at 18 k_BT and 57 k_BT for the liquid and gel phases, respectively. Previous estimations from micropipette aspiration and AFM-based methods were in quantitative agreement with our results (7,8,16). However,

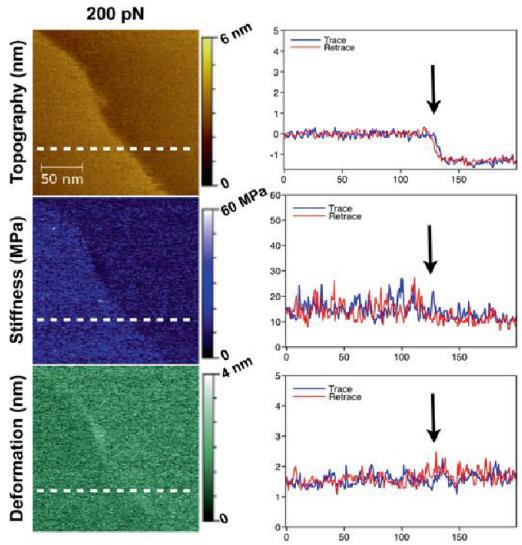

FIGURE 3 PF-QNM images at the lipid phase boundary showing the topography (nm), stiffness (MPa), and deformation (nm) at 200 pN peak loading force. The false color scale (from top to bottom) is 6 nm, 60 MPa, and 4 nm. Cross section of the trace (*blue line*) and retrace (*red line*) along the white dashed line for topography, stiffness, and deformation (average of three consecutive lines).

we found a considerably high bending stiffness in the case of the SLB in the gel phase, which to our knowledge has not been calculated before. The measured thickness and mechanical properties between the two phases allow us to estimate the energetic cost due to bilayer deformation to be 0.81 k_BT and 0.36 k_BT for DOPC and DPPC, respectively (see Supporting Material), which is in conceptual agreement with previous works (13,17). Thus, even though the energetic cost of mixing is low, it is sufficient for phase separation.

The improved time and lateral resolution of PF-QNM offered us more physical insight about SLB mechanical properties (Fig. 3). The stiffer gel-lipid phase can be understood by the lower mobility and tighter order of DPPC lipid tails. According to this interpretation, one could suggest that the edges between DOPC and DPPC would have intermediate stiffness, as lipids might be more disordered and mobile at phase edges. We observed slight changes in mechanics at phase edges on the order of ~10 nm, suggesting that the lateral range of this effect is short.

Our approach illustrates the suitability of PF-QNM AFM for the nanomechanical mapping of membrane models at high resolution and sufficient sensitivity to detect the properties of lipid phases. Our results suggest that at moderate indentations, determination of the stiffness is actually not perturbed by the solid support, thus providing reliable values of the Young's modulus. However, relative differences between lipid phases become more obvious at high applied forces. Accordingly, we propose that the high spatial resolution and sensitivity of the applied technique might be used to mechanically detect DRMs or rafts on cell surfaces before they can be directly visualized.

SUPPORTING MATERIAL

Materials and Methods, two figures, a table, and references are available at http://www.biophysj.org/biophysj/supplemental/S0006-3495(11)05352-5.

ACKNOWLEDGMENTS

The authors thank Pierre Sens for fruitful discussion.

This study was supported by a Fondation Pierre-Gilles de Gennes Fellowship (to L.P.) and a European Community Marie Curie Intra-European Fellowship for Career Development (to F.R.).

REFERENCES and FOOTNOTES

1. Lingwood, D., and K. Simons. 2010. Lipid rafts as a membrane-organizing principle. *Science.* 327:46–50.
2. Engelman, D. M. 2005. Membranes are more mosaic than fluid. *Nature.* 438:578–580.
3. Phillips, R., T. Ursell, …, P. Sens. 2009. Emerging roles for lipids in shaping membrane-protein function. *Nature.* 459:379–385.
4. Jensen, M. O., and O. G. Mouritsen. 2004. Lipids do influence protein function-the hydrophobic matching hypothesis revisited. *Biochim. Biophys. Acta.* 1666:205–226.
5. Dufrêne, Y. F., T. Boland, …, G. U. Lee. 1998. Characterization of the physical properties of model biomembranes at the nanometer scale with the atomic force microscope. *Faraday Discuss.* 111:79–94. discussion 111:137–157.
6. Garcia-Manyes, S., and F. Sanz. 2010. Nanomechanics of lipid bilayers by force spectroscopy with AFM: a perspective. *Biochim. Biophys. Acta.* 1798:741–749.
7. Rawicz, W., K. C. Olbrich, …, E. Evans. 2000. Effect of chain length and unsaturation on elasticity of lipid bilayers. *Biophys. J.* 79:328–339.
8. Das, C., K. H. Sheikh, …, S. D. Connell. 2010. Nanoscale mechanical probing of supported lipid bilayers with atomic force microscopy. *Phys. Rev. E.* 82:041920.
9. Binnig, G., C. F. Quate, and C. Gerber. 1986. Atomic force microscope. *Phys. Rev. Lett.* 56:930–933.
10. Gonçalves, R. P., G. Agnus, …, S. Scheuring. 2006. Two-chamber AFM: probing membrane proteins separating two aqueous compartments. *Nat. Methods.* 3:1007–1012.
11. Rico, F., C. Su, and S. Scheuring. 2011. Mechanical mapping of single membrane proteins at submolecular resolution. *Nano Lett.* 11:3983–3986.
12. Milhiet, P. E., F. Gubellini, …, D. Lévy. 2006. High-resolution AFM of membrane proteins directly incorporated at high density in planar lipid bilayer. *Biophys. J.* 91:3268–3275.
13. Leonenko, Z. V., E. Finot, …, D. T. Cramb. 2004. Investigation of temperature-induced phase transitions in DOPC and DPPC phospholipid bilayers using temperature-controlled scanning force microscopy. *Biophys. J.* 86:3783–3793.
14. Marsh, D. 2012. Handbook of Lipid Bilayers, 2nd ed. Taylor and Francis, New York.
15. Dimitriadis, E. K., F. Horkay, …, R. S. Chadwick. 2002. Determination of elastic moduli of thin layers of soft material using the atomic force microscope. *Biophys. J.* 82:2798–2810.
16. Dieluweit, S., A. Csiszár, …, R. Merkel. 2010. Mechanical properties of bare and protein-coated giant unilamellar phospholipid vesicles. A comparative study of micropipet aspiration and atomic force microscopy. *Langmuir.* 26:11041–11049.
17. Wallace, E. J., N. M. Hooper, and P. D. Olmsted. 2006. Effect of hydrophobic mismatch on phase behavior of lipid membranes. *Biophys. J.* 90:4104–4118.

In Vivo Imaging of the Actin Polymerization State with Two-Photon Fluorescence Anisotropy

Harshad D. Vishwasrao,[†‡] Pierre Trifilieff,[†§¶] and Eric R. Kandel[†‡‖*]

[†]Department of Neuroscience, Columbia University, New York, New York; [‡]Howard Hughes Medical Institute, New York, New York; [§]New York State Psychiatric Institute, New York, New York; [¶]Research Foundation for Mental Hygiene, New York, New York; and [‖]Kavli Institute for Brain Science, New York, New York

ABSTRACT Using two-photon fluorescence anisotropy imaging of actin-GFP, we have developed a method for imaging the actin polymerization state that is applicable to a broad range of experimental systems extending from fixed cells to live animals. The incorporation of expressed actin-GFP monomers into endogenous actin polymers enables energy migration FRET (emFRET, or homoFRET) between neighboring actin-GFPs. This energy migration reduces the normally high polarization of the GFP fluorescence. We derive a simple relationship between the actin-GFP fluorescence polarization anisotropy and the actin polymer fraction, thereby enabling a robust means of imaging the actin polymerization state with high spatiotemporal resolution and providing what to the best of our knowledge are the first direct images of the actin polymerization state in live, adult brain tissue and live, intact *Drosophila* larvae.

INTRODUCTION

Actin exists in cells in a dynamic equilibrium between monomeric and polymeric forms: g-actin and f-actin, respectively. Polymeric f-actin constitutes one of the principle components of the cytoskeleton and is involved in molecular scaffolding, cell motility, and myosin-based trafficking. Monomeric g-actin, on the other hand, exists as a cell-wide pool that serves as a ready source or sink of monomeric subunits to and from f-actin. The dynamic equilibrium between the two forms of actin is regulated by the cell locally, rapidly, and bidirectionally.

Given the central role for actin dynamics in a broad spectrum of cell function, it is of considerable interest to be able to image the polymerization state in live cells and tissues with high spatial and temporal resolution. Despite this need, there are few robust methods for directly imaging the actin polymerization state.

Methods for probing the actin polymerization state can be categorized either as indirect (utilizing a nonactin fluorescent probe that binds polymeric f-actin), or direct (utilizing fluorescently labeled actin). Phalloidin staining, an indirect probe, represents the gold-standard for labeling f-actin; however, it can only be applied to fixed cells and tissue, and therefore provides limited information about dynamics. A number of live cell indirect probes have been developed that we will return to in the Discussion.

Among the direct probes of actin polymerization, single-molecule-based techniques such as fluorescence speckle microscopy (1) and photoactivation localization microscopy (2) are most informative in cultured cells, but are computationally intensive and difficult to extend to live tissue.

The most broadly applicable approach to directly probe the actin polymerization state utilizes Förster resonance energy transfer (FRET) between coexpressed actin-CFP and actin-YFP. Incorporation of actin-CFP and actin-YFP into endogenous f-actin occasionally brings CFP and YFP into close proximity ($<$100 Å), resulting in FRET and an enhancement in the YFP/CFP fluorescence ratio. This approach has been applied in solutions of purified protein (3,4) as well as in tissue culture (5). For clarity, we will refer to the physical process of excitation energy transfer between any two molecules as "FRET" and the technique that utilizes energy transfer specifically between different fluorophores as "heteroFRET".

We present here an imaging method and analytical framework that utilizes energy migration FRET (6,7) (emFRET; also called homoFRET, homotransfer, energy migration) to directly probe the actin polymerization state quantitatively. EmFRET, like heteroFRET, is based on a resonant transfer of electronic excitation energy between two or more fluorophores. Unlike heteroFRET, emFRET occurs between fluorophores of the same type if the absorption and emission spectra overlap. Because the interacting fluorophores are identical, emFRET does not change the fluorescence color or lifetime ((7–10), and see Section S1 in the Supporting Material). However, because the emission dipoles of interacting fluorophores are seldom exactly parallel, emFRET does change the fluorescence polarization and can therefore be detected by polarization-sensitive modalities. The advantages of a single fluorophore technique such as emFRET over a dual fluorophore technique such as heteroFRET are numerous, including simplicity of experimental design, efficiency of FRET pair formation, and the potential for using already existing transgenic animals expressing actin-GFP. We will expand upon this comparison in the Discussion.

EmFRET has been used extensively to study the aggregation and structure of purified, labeled proteins. Its use in cells, although less common (for review, see Chan et al. (11)), has seen a number of promising applications and

Submitted October 5, 2011, and accepted for publication January 17, 2012.

*Correspondence: erk5@columbia.edu

Editor: Elizabeth Rhoades.

0006-3495/12/03/1204/11 $2.00

doi: 10.1016/j.bpj.2012.01.031

seminal developments of the experimental and theoretical tools necessary to derive information about intracellular molecular structure from images of emFRET-induced fluorescence depolarization (7,9–13). Much of the interest in these studies has been to extract oligomer structural parameters, for which time-resolved anisotropy measurements provide the most detailed information. Because a lifetime image typically requires minutes to acquire, this approach is of limited utility in imaging fast cellular dynamics (<10 s).

Our purpose is not to obtain structural details of f-actin, but rather to image the actin polymer fraction with a resolution sufficient to observe its characteristic rapid and highly localized dynamics in live cells, including neurons and their synapses. To this end, we employ steady-state two-photon anisotropy imaging to provide the requisite high spatiotemporal resolution. We also derive a relationship between anisotropy and the actin polymer fraction with which we can calculate images that are proportional to the actin polymer concentration. This relationship can be validated using f-actin specific stains. Although two-photon excitation is not necessary for anisotropy imaging, it provides a greater dynamic range for anisotropy due to enhanced excitation photoselection and it enables the technique to be easily extended from fixed cells to living tissue.

METHODS

See Sections S7–S12 in the Supporting Material.

RESULTS

Theoretical relationship between fluorescence anisotropy and the actin polymerization state

Actin-GFP fluorescence is highly polarized. This polarization is altered when actin-GFP incorporates into an endogenous actin polymer and undergoes FRET with other nearby incorporated molecules of actin-GFP. Although we empirically measure the fluorescence polarization anisotropy of actin-GFP, we are ultimately interested in its polymerization state. We must therefore derive the relationship between anisotropy and polymerization state.

Energy transfer between polymer-incorporated actin-GFP

Consider an actin polymer of sites *-M* to *N* with actin-GFP randomly incorporated into it (Fig. 1 *A*). Any two actin-GFP occupied sites *j*,*k* are capable of FRET with a rate F_{jk},

$$F_{jk} = \frac{3R_0^6}{2\tau}\frac{\kappa_{jk}^2}{|\vec{R}_{jk}|^6}, \qquad (1)$$

where $\vec{R}_{jk} = \vec{R}_k - \vec{R}_j$ is the vector between the two chromophores and the orientation factor,

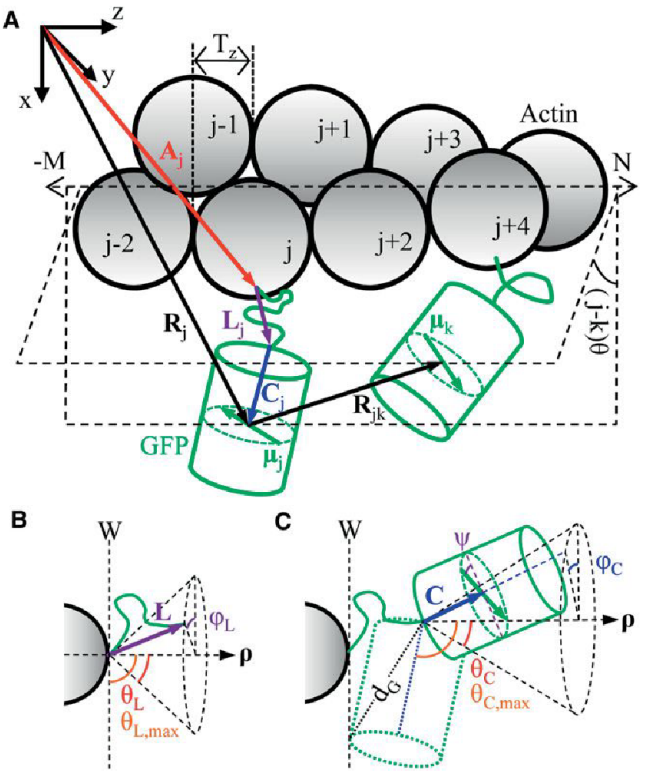

FIGURE 1 (*A*) Model of actin-GFP molecules randomly incorporated into an actin filament. (*B*) The long flexible linker (*green line*) connecting actin to GFP has an en-to-end vector **L** (*purple arrow*) with orientation angles θ_L and φ_L. (*C*) The GFP chromophore vector **C** (*blue arrow*) rotates freely at the end of the linker with orientation angles θ_C and φ_C. The orientation angles are with respect to the local helix radius vector at the actin N-terminus, **ρ**. The tangent plane *W* is a noninteracting wall; both the linker and chromophore vectors are allowed to move outside (to the right of) this wall. The GFP barrel drawn with the green dotted line in panel *C* represents the limit of motion for the GFP tag—the GFP semidiagonal d_G cannot cross *W*.

$$\kappa_{jk}^2 = \left(\left(\hat{\mu}_j \cdot \hat{\mu}_k\right) - 3\left(\hat{\mu}_j \cdot \hat{R}_{jk}\right)\left(\hat{\mu}_k \cdot \hat{R}_{jk}\right)\right)^2,$$

accounts for the relative orientation of the unit transition dipoles $\hat{\mu}_j$ and $\hat{\mu}_k$. For the GFP mutant used in most of the experiments presented here (Emerald-GFP), the fluorescence lifetime (τ) was found to be 2.49 ± 0.05 ns (see Section S1 in the Supporting Material) and the GFP-GFP Förster radius (R_0) was calculated to be 45.8 Å in tissue (refractive index 1.4), comparable to that for GFP-GFP (46.5 Å) and CFP-YFP (49.2 Å) in solution (14).

F-actin is a helix in which adjacent monomers are rotated by an angle $\theta = 166^\circ$ with respect to one another and axially offset by $A_z = 27.5$ Å. This well-defined structure relates the position of an actin N-terminus (where GFP is attached), $\vec{A}_j$, to its site index number *j* (3,15),

$$\vec{A}_j = A_{xy}\, cos(j\theta)\hat{x} + A_{xy}\, sin(j\theta)\hat{y} + A_z j\hat{z}, \qquad (2)$$

where $A_{xy} = 35$ Å is the radial distance of the N-terminus from the helix axis.

The actin N-terminus is attached to GFP by an 8 aa flexible linker. Moreover, the C-terminal 10 residues of Emerald-GFP have no secondary structure and are linked to the GFP β-barrel at a glycine residue (Gly^{229}). We therefore model actin-GFP as two rigid structures (actin and GFP(1–229)) linked by an 18-amino-acid, unstructured polypeptide chain (see Section S2 in the Supporting Material). An unstructured polypeptide chain whose contour length ($l_c = 68.4$ Å for 18 aa) greatly exceeds its persistence length ($l_p = 3.04$ Å (16)) can be modeled as a Gaussian chain with an end-to-end vector $\vec{L}_j$ whose magnitude follows the probability distribution

$$P(L_j) = P_{L0} L_j^2 \, exp\left(\frac{-3L_j^2}{4 l_p l_c}\right), \quad (3)$$

where P_{L0} is a normalization constant. Although the contour length of the linker is long, its high flexibility makes its trajectory in space a random walk, resulting in a relatively short mean end-to-end distance ($\langle L_j \rangle = 19$ Å). Finally, if $\vec{C}_j$ is the vector from the linker attachment point at Gly^{229} to the GFP chromophore ($|\vec{C}_j| = 24$ Å, Protein DataBank entry 1GFL), then the chromophore position vectors are $\vec{R}_{j,k} = \vec{A}_{j,k} + \vec{L}_{j,k} + \vec{C}_{j,k}$ and the vector between the chromophores is

$$\vec{R}_{jk} = \vec{R}_k - \vec{R}_j = \left(\vec{A}_k + \vec{L}_k + \vec{C}_k\right) - \left(\vec{A}_j + \vec{L}_j + \vec{C}_j\right). \quad (4)$$

We treat the tangent plane at the actin N-terminus as a noninteracting wall (*dashed line W*, Fig. 1, *B* and *C*) to simulate steric hindrance from the actin filament. The linker $(\vec{L})$ and chromophore $(\vec{C})$ vectors are permitted to move freely only in the half-space outside this wall (see Section S3 in the Supporting Material).

Fluorescence and FRET occur during the lifetime of the excited state (2.5 ns for Emerald GFP), substantially faster than the rotation time of GFP (15–20 ns). Hence, any single GFP has a nearly fixed position/orientation during the evolution of a single excitation. In a typical imaging experiment, however, the pixel dwell time (1–10 μs) is long in comparison to the timescale of molecular motion and involves many excitations, while the focal volume contains many GFPs (~10^2–10^3 at 1 μM GFP concentration). Therefore, the population of excited GFPs in a focal volume, over a pixel dwell time, can be considered to sample all possible positions/orientations with respect to their parent actin filaments. To account for this in the theory below, we perform an ensemble average ($\langle x \rangle$) of fluorescence-based quantities, defined as an average over all possible positions and orientations of the interacting GFP transition dipoles (that is, over all possible lengths and orientation angles of $\vec{L}_j$, $\vec{C}_j$, and $\hat{\mu}_j$), weighted by their respective probabilities of occurrence. The ensemble average is calculated using a Monte Carlo approach (see Section S4 in the Supporting Material) similar to that used by Blackman et al. (10) in modeling concentration dependent fluorescence depolarization.

For a lone pair of interacting GFPs on an actin filament, we suppose a single excitation begins on the donor at site 0. Then the probability that the emission occurs from the acceptor at site k is known as the fractional quantum yield of site k and is simply related to the FRET rate, $\Phi_k/\Phi_{total} = F_{0k}\tau/(1 + 2F_{0k}\tau)$ (17), where Φ_{total} is the fluorescence quantum yield (0.68 for Emerald-GFP). The ensemble average fractional quantum yield, as a function of the acceptor site index $|k|$, gives us a picture of how well a pairwise FRET interaction transfers energy directly between sites on an actin filament (Fig. 2 *A*, *red diamonds*). We use the absolute value of the site index here as the actin filament is symmetric about site 0. Energy transfer from the donor at site 0 is overwhelmingly to its next-to-nearest neighbors at $|k| = 2$ and becomes negligible beyond $|k| = 4$, a conclusion that we will utilize shortly.

Energy migration in an incompletely labeled polymer

Actin-GFP competes with endogenous g-actin to incorporate into f-actin, resulting in an actin filament sporadically labeled with GFP. To account for this incomplete labeling, we modify the theory of fluorescence depolarization due to energy migration between aggregated fluorophores as originally developed by Craver and Knox (17). We define the labeling (ℓ_j) of each site j as $\ell_j = 1$ if it is occupied by actin-GFP and $\ell_j = 0$ if it is occupied by endogenous actin.

Suppose a single excitation begins on an actin-GFP at an arbitrary site that we label "0". Then the probability of

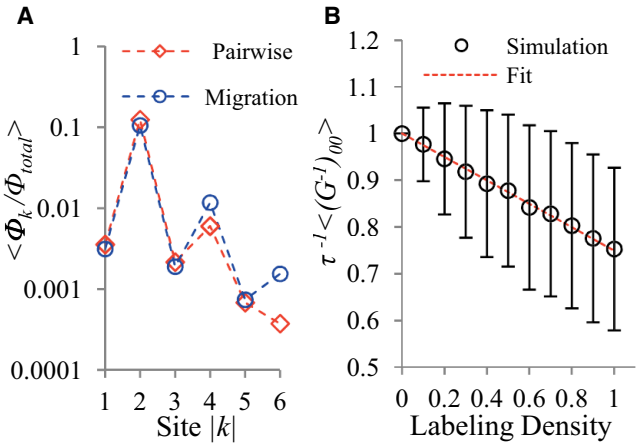

FIGURE 2 (*A*) Ensemble average fractional quantum yield as a function of site number $|k|$. Energy transfer from the initially excited site 0 directly (*Pairwise*, *red diamonds*) to another site is overwhelmingly to the $|k| = 2$ sites. On a fully labeled polymer (*Migration*, *blue circles*), the spread of excitation energy to even sites is facilitated by migration but is nonetheless restricted largely to $|k| = 2$ and 4 sites. (*B*) Simulation of a probabilistically labeled filament shows that $\tau^{-1}\langle (G^{-1})_{00} \rangle$ is linearly dependent on the labeling density ($\bar{\ell}$) of f-actin (each point is mean ± SD, 10^5 iterations).

finding an excited state at site j ($\rho_j(t)$) is governed by the master equation,

$$\frac{d\rho_j(t)}{dt} = \frac{-\rho_j(t)}{\tau} - \sum_{\substack{k=-M \\ k\neq j}}^{N} \ell_j\ell_k F_{jk}\rho_j(t) + \sum_{\substack{m=-M \\ m\neq j}}^{N} \ell_j\ell_m F_{mj}\rho_m(t), \quad (5)$$

with the temporal boundary conditions $\rho_0(t = 0) = 1$, $\rho_0(t = \infty) = 0$, and $\rho_{j\neq 0}(t = 0) = \rho_{j\neq 0}(t = \infty) = 0$. This is essentially the master equation of Craver and Knox (17) with additional $\ell_{j,k,m}$ terms to account for the incorporation of actin-GFP. The first term on the right side of the equation represents the rate of spontaneous decay, and the second and third terms, respectively, represent the FRET rate from and to site j. The summations are over all polymer sites; however, because FRET becomes negligible beyond a separation of four sites, the full summation can be approximated by a sum over k (and m) $= j-4$ to $j+4$, $\neq j$.

This system of linear differential equations can be rewritten as

$$\frac{d\rho_j(t)}{dt} = -\sum_{k=j-4}^{j+4} G_{jk}\rho_k(t), \quad (6)$$

where G_{jk} is the Craver-Knox matrix of coefficients, whose index j runs from -M to N to preserve the polymer site index notation,

$$G_{jk} = -\ell_j\ell_k F_{kj}\left(1 - \delta_{jk}\right) + \left(\frac{1}{\tau} + \sum_{\substack{m=j-4 \\ m\neq j}}^{j+4} \ell_j\ell_m F_{jm}\right)\delta_{jk}. \quad (7)$$

Once the G matrix is defined, the fractional quantum yield of site n is (8,17)

$$\frac{\Phi_n}{\Phi_{total}} = \frac{(G^{-1})_{0n}}{\tau}, \quad (8)$$

and the fluorescence anisotropy of the polymer is given by

$$\begin{aligned} r_p &= r_0\frac{\Phi_0}{\Phi_{total}} + r_{et}\left(1 - \frac{\Phi_0}{\Phi_{total}}\right) \\ &= r_0\frac{(G^{-1})_{00}}{\tau} + r_{et}\left(1 - \frac{(G^{-1})_{00}}{\tau}\right). \end{aligned} \quad (9)$$

Here r_0 is the anisotropy of the fluorescence arising from the initial directly excited site. Fluorescence from the initially excited site may directly follow excitation, or it may follow excitation and energy migration away from, and back to, that site. Because GFP is essentially motionless on the timescale of energy transfer, fluorescence following energy migration away from, and back to, the initially excited site will have the same polarization as if the energy had never left. Hence, the anisotropy of fluorescence from directly excited sites will be equal to that of a monomer ($r_0 \rightarrow r_m$). The value r_{et} is the anisotropy of the fluorescence from sites excited via FRET. It is generally held, and we confirm for polymer incorporated actin-GFP (see Section S5 in the Supporting Material), that even a single energy transfer is adequate to largely depolarize fluorescence, i.e., $r_{et} \rightarrow 0$ (8). Finally, because $(G^{-1})_{00}$ is defined for a specific configuration of fluorophores, the measured anisotropy from a real sample is related to the ensemble average $\langle(G^{-1})_{00}\rangle$. Equation 9 then simplifies to

$$r_p = r_m\tau^{-1}\left\langle\left(G^{-1}\right)_{00}\right\rangle. \quad (10)$$

To calculate the limits of energy migration from the initial site 0 of excitation, we simulated a seven-subunit-long polymer fully labeled on its positive sites ($\ell_j = 1$ for $0 \leq j \leq 6$) (Fig. 2 *A*, *blue circles*). By symmetry, these results apply to negative sites as well. The ensemble average fractional quantum yields for sites $|k| = 4$ and 6 on a fully labeled polymer are substantially higher than their corresponding values for direct (pairwise) FRET from the donor (Fig. 2 *A*, *red diamonds*). This indicates that energy migration (transfer via intermediary sites) to these sites can be a more efficient means of energy transfer than direct transfer. Nonetheless, energy migration was found to be highly local, with the ensemble average fractional quantum yield exceeding 1% only for sites $|k| = 2$ and 4. This acute localization of energy migration implies the anisotropy will be insensitive to the total length of the actin filament—typically hundreds of subunits or more (18,19).

Actin-GFP competes with endogenous g-actin to incorporate into actin filaments and so its incorporation probability will depend on its expression level. The probability that an actin-GFP is found at a filament site j (or the labeling density, $\overline{\ell}$) is

$$\begin{aligned} P(\ell_j = 1) &= \overline{\ell} \\ &= \frac{\mathrm{K}_{\mathrm{acGFP}}[actin - GFP]}{\mathrm{K}_{\mathrm{acGFP}}[actin - GFP] + [endogenous\ g\text{-}actin]}, \end{aligned} \quad (11)$$

where K_{acGFP} is the relative rate of incorporation of actin-GFP versus endogenous g-actin. We used a Monte Carlo simulation to average over all labeling configurations for a given labeling density (see Section S4 in the Supporting Material) to find the dependence of $\tau^{-1}\langle(G^{-1})_{00}\rangle$ and thereby the polymer anisotropy (Eq. 10), on the labeling density. Because energy transfer from the initially excited site 0 is largely restricted to the $|k| = 2$ and 4 sites even for a fully labeled polymer, we included only sites 0, ± 2, and ± 4 in the simulation. We find that the dependence of $\tau^{-1}\langle(G^{-1})_{00}\rangle$ on the labeling density (Fig. 2 *B*)

can be well fit by a straight line with a slope $m_\ell = 0.251 \pm 0.003$:

$$\tau^{-1}\left\langle \left(G^{-1}\right)_{00}\right\rangle = 1 - m_\ell \bar{\ell}. \tag{12}$$

We have fixed the intercept in the fit to be 1 because, for a negligible labeling density ($\bar{\ell} \to 0$), energy cannot transfer off site 0 and hence the fractional quantum yield of site 0 approaches the total quantum yield ($\Phi_0 \to \Phi_{total}$) and, therefore, by Eq. 8: $\tau^{-1}\langle (G^{-1})_{00}\rangle \to 1$.

Anisotropy of a mixture of monomer and polymer

For a fluorophore that exists as a mixture of monomeric and polymeric populations, the average anisotropy is simply the sum of the anisotropies of the monomer and the polymer weighted by their fractional concentrations:

$$r = \frac{C_m}{C_m + C_p} r_m + \frac{C_p}{C_m + C_p} r_p. \tag{13}$$

Here $C_{m,p}$ and $r_{m,p}$ are the concentrations and anisotropies of the monomer and polymer, respectively. Substituting the expressions for polymer anisotropy (Eq. 10) and $\tau^{-1}\langle (G^{-1})_{00}\rangle$ (Eq. 12) into Eq. 13 and solving for the polymer concentration, C_p, gives the final expression for the anisotropy of a monomer/polymer mixture,

$$\begin{aligned} C_p &= \left(\frac{1}{1 - \tau^{-1}\left\langle \left(G^{-1}\right)_{00}\right\rangle}\right)\left(1 - \frac{r}{r_m}\right) C_T \\ &= \frac{1}{m_\ell \bar{\ell}}\left(1 - \frac{r}{r_m}\right) C_T, \end{aligned} \tag{14}$$

where $C_T = C_m + C_p$ is the total actin-GFP concentration. Although $\tau^{-1}\langle (G^{-1})_{00}\rangle$ or m_ℓ can be explicitly calculated as we have shown above, for most experimental purposes it is enough to note from Eqs. 1–4, 7, and 11 that $\tau^{-1}\langle (G^{-1})_{00}\rangle$ is solely determined by three sets of parameters:

1. Fluorophore parameters: R_0, r_m, $|\vec{C}|$, and $|\vec{L}|$.
2. F-actin structure parameters: A_{xy}, A_z, θ, and filament length ($M + N + 1$).
3. Expression level: $\bar{\ell}$.

Because every term of G contains τ^{-1}, the explicit dependence of $\tau^{-1}\langle (G^{-1})_{00}\rangle$ on lifetime cancels out, leaving only an implicit dependence through the quantum efficiency term in R_0. Our analysis above indicates that $\tau^{-1}\langle (G^{-1})_{00}\rangle$ is minimally affected by the filament length. The other fluorophore parameters are constants for a given fluorescent fusion protein whereas the other f-actin structure parameters are generally constant. Finally, keeping actin-GFP expression roughly constant during an experiment is straightforward.

If its constituent parameters are constant, then $\tau^{-1}\langle (G^{-1})_{00}\rangle$ is a constant and Eq. 14 can be rewritten as a proportionality:

$$C_p \propto \left(1 - \frac{r}{r_m}\right) C_T. \tag{15}$$

Equation 15 relates the actin polymer concentration to the anisotropy under the constraint of constant expression level.

Imaging the anisotropy-derived actin polymerization state

Steady-state anisotropy in fixed and living HEK293 cells

Cultured HEK293 cells expressing actin-GFP (Fig. 3 *A*) were imaged either alive or after fixation. The actin-GFP anisotropy shows a region-specific variation (Fig. 3 *B*). In much of the central soma, the anisotropy is ~0.41 in both live and fixed cells (Fig. 3 *D*). Actively growing peripheral regions such as lamella/lamellipodia and filopodia exhibit a significantly reduced anisotropy. In comparison, the fluorescence anisotropy in cells expressing only GFP is spatially

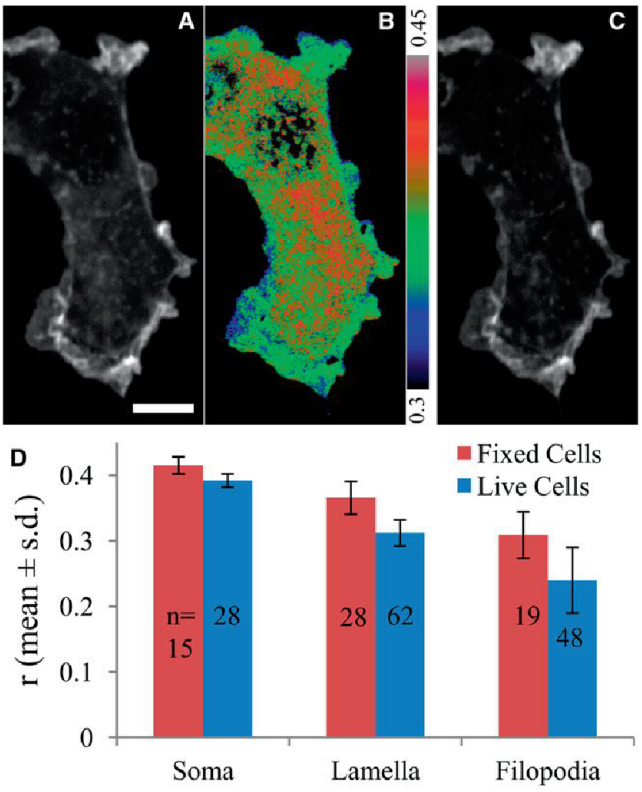

FIGURE 3 Total fluorescence intensity (*A*), anisotropy (*B*) of actin-GFP, and f-actin staining with Texas Red-X phalloidin (*C*) in a fixed HEK293 cell. (*D*) Anisotropy in both live (*red*) and fixed (*blue*) cells is spatially heterogeneous with significant decreases in regions known to be f-actin-rich. Scale bar = 10 μm.

homogenous, with an average value of 0.413 ± 0.023 (n = 23), comparable to previously published results (20).

The anisotropy of somatic actin-GFP is comparable to that of GFP alone, indicating no interaction between actin-GFPs and implying that somatic actin-GFP is monomeric. The cell periphery, on the other hand, exhibits significantly reduced anisotropy, as would be expected from actin-GFP that had incorporated into f-actin and was undergoing emFRET. The slightly lower anisotropy in the periphery of live cells compared to fixed cells is possibly due to destabilization of f-actin during fixation. These results are consistent with phalloidin stains (Fig. 3 *C*), which reveal f-actin to be low in the soma but enriched in the growing periphery.

Validation of the theoretical model in cells

Comparing the theoretical and experimental dependence of anisotropy on polymer fraction and expression level

Our theoretical model (Eq. 14) predicts a relationship between actin-GFP anisotropy and polymer fraction with a proportionality term that depends on the expression level. Although the expression level can be treated as a constant for a single cell during most experiments, it will vary from cell to cell. Validating Eq. 14 therefore requires empirically checking the relationship between anisotropy and polymer fraction for a range of expression levels.

We take the actin-GFP expression level to be proportional to the mean actin-GFP fluorescence of the extranuclear soma, i.e., $F_{soma} = \alpha[actin - GFP]$, where α is a constant for a given set of imaging parameters. Combining this with Eqs. 11 and 14, we get

$$r = r_m\left(1 - m_\ell\left(\frac{C_p}{C_T}\right)\frac{\zeta F_{soma}}{\zeta F_{soma} + 1}\right), \qquad (16)$$

where $\zeta = K_{acGFP}/(\alpha[endogenous\ g\text{-}actin])$ is assumed a constant. Equation 16 is simply a restatement of our model that can be more conveniently tested in cells. We measured the anisotropy from two types of intracellular regions in fixed HEK293 cells: lamella/lamellipodia (which are typically f-actin-rich), and actin-hotspot-free regions of the soma (which are typically f-actin-poor). In selecting regions from lamellipodia, care was taken to avoid filopodia and microspikes, as these structures contain compact bundles of f-actin that may exhibit interfilament FRET (see Discussion). For each region of interest, lamellipodium or soma, we recorded the anisotropy, r, and the mean fluorescence from the extranuclear soma of the parent cell as the corresponding measure of expression level F_{soma}. These measurements were made in a large number of cells (Lamellipodia: 138 regions of interest (ROIs) from 75 cells; Somas: 103 ROIs from 103 cells) spanning two orders of magnitude in expression level. The resulting plot of anisotropy versus expression level is shown in Fig. 4 *A* (*data points*). Each data point represents a binning (mean ± SD) of five ROIs of comparable F_{soma} values. We fit this cellular data with Eq. 16 (Fig. 4 *A*, *dashed lines*) using r_m, C_p/C_T, and ζ as fitting parameters and setting $m_\ell = 0.251$, as discussed above.

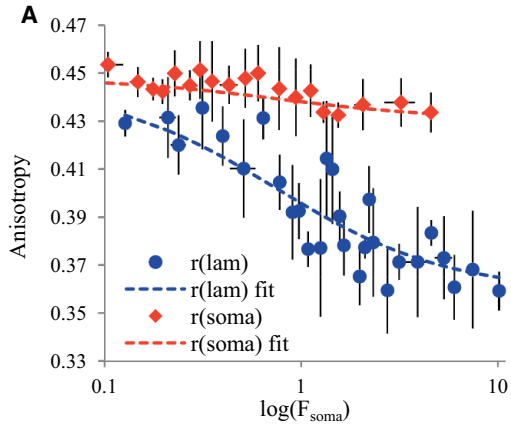

B	C_p/C_T	r_m	ζ	χ_r^2
Lam	0.77 ±0.07	0.445 ±0.010	1.3 ±0.2	1.22
Soma	0.15 ±0.04	0.448 ±0.002	1.3 fixed	0.52

FIGURE 4 Validation of the theoretical model (part 1). (*A*) The dependence of anisotropy on expression level is well fit (*dashed lines*) by our theoretical model in both f-actin-rich lamellipodia (*lam*) and f-actin poor somas (*soma*). Each data point represents a binning (mean ± SD) of 5 ROIs of comparable F_{soma} values. The best-fit values for the fit parameters are summarized in panel *B*.

The model fits the experimental data well over a large range of expression levels. Furthermore, the fit yields a polymer fraction (C_p/C_T) of 0.77 in lamellipodia and 0.15 in somas (Fig. 4 *B*), consistent with the fact that they are f-actin-rich and -poor, respectively. Our value for the polymer fraction in HEK cell lamellipodia is remarkably close to that obtained by Koestler et al. (21) ($C_p/C_T = 0.76$) in the lamellipodia of mouse melanoma cells using a very different experimental approach. Because the soma is very low in polymeric actin, there are few polymers for actin-GFP to incorporate into and hence expression level has little effect on anisotropy (Fig. 4 *A*, *red diamonds*). Conversely, lamellipodia are rich in polymeric actin that incorporates actin-GFPs and hence increasing the expression level can significantly affect the incorporation probability, energy migration, and therefore anisotropy (Fig. 4 *B*, *blue circles*). At low expression levels, actin-GFPs are unlikely to interact even if incorporated into a polymer, and hence the anisotropies from lamellipodia and somas should converge to the same value at zero expression—the anisotropy of the actin-GFP monomer. The estimates of the monomer anisotropy (Fig. 4 *B*) from lamellipodia and soma curves, 0.445 and 0.448, are indeed very close. We take the average value

from these two fits to be the actin-GFP monomer anisotropy r_m: 0.447.

The anisotropy-derived polymer concentration reproduces the phalloidin staining pattern and drug response

Having measured the actin-GFP monomer anisotropy (r_m), we can now use Eq. 15 to calculate, pixel-by-pixel, an image that is proportional to the actin polymer concentration. Furthermore, because the total actin-GFP concentration C_T is proportional to the total fluorescence intensity (F_T), we can rewrite Eq. 15 as

$$C_p(x,y,z) \propto \left(1 - \frac{r(x,y,z)}{r_m}\right) F_T(x,y,z). \qquad (17)$$

As an independent measure of the f-actin distribution, actin-GFP-expressing HEK293 cells were fixed and stained with Texas Red-X phalloidin. The anisotropy-derived actin polymer distribution could then be directly compared to the phalloidin distribution. Fig. 5 shows the calculated total fluorescence intensity, anisotropy-derived actin polymer distribution, and phalloidin stain. The anisotropy-derived polymer distribution and the phalloidin signal (Fig. 5, *B* and *C*) are highly similar, yielding very high correlation (0.89 ± 0.03, $n = 16$) and overlap coefficients (0.92 ± 0.03, $n = 16$). The anisotropy-derived polymer concentration is therefore a good indicator of the f-actin distribution. Furthermore, the near unity of its linear correlation coefficient with the phalloidin stain further validates the use of Eq. 15 and our treatment of $\tau^{-1}\langle(G^{-1})_{00}\rangle$ as a constant for a given expression level.

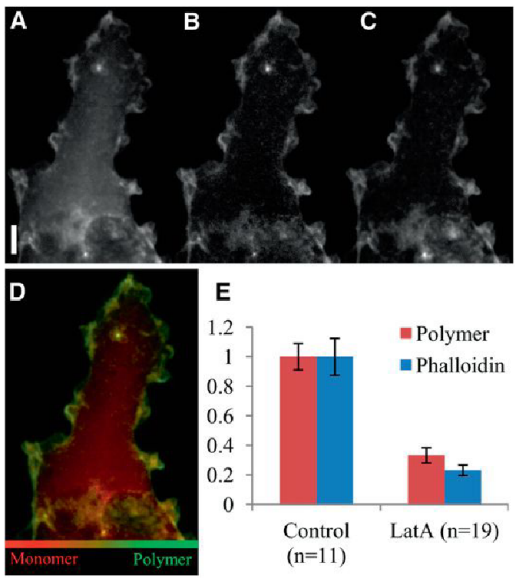

FIGURE 5 Validation of the theoretical model (part 2). Total fluorescence intensity (*A*) and the anisotropy-derived polymer concentration (*B*) of actin-GFP. Scale bar = 10 μm. The derived polymer concentration (*B*) shows a high similarity to the Texas Red-X phalloidin stain (*C*). Panels *A* and *B* can be combined in a red-green image (*D*) to visualize the monomer-polymer continuum. (*E*) Latrunculin A induces a comparable decrease in both the anisotropy-derived polymer concentration and the phalloidin signal (mean ± SD).

To facilitate visualization, we display the anisotropy-derived polymer concentration in green and the total fluorescence intensity in red (Fig. 5 *D*). It follows that a purely red pixel contains only g-actin. Pixels that are increasingly green have proportionally higher concentrations of f-actin.

To ensure that the anisotropy-derived polymer concentration responds correctly to drug-induced perturbations of the f-actin level, actin-GFP-expressing HEK293 cells were treated with the actin-destabilizing drug Latrunculin A (15 min, 1 μM) and then fixed and stained with Texas Red-X phalloidin. The anisotropy-derived polymer fraction and the phalloidin signal were then measured in single z planes near the base of the cell and found to be comparably lower in treated cells (Fig. 5 *E*) compared to control cells. Hence, the anisotropy-derived polymer concentration indicates changes in f-actin that are similar to those calculated from the gold-standard phalloidin stain.

Live imaging of the actin-polymerization state

Because our method is based on two-photon excitation, it can readily be extended to living cells and tissue. We demonstrate here imaging of the anisotropy-derived actin polymerization state in live cell cultures, acute hippocampal slices from mouse, and intact *Drosophila* larvae. To the best of our knowledge, these are the first direct images of the actin polymerization state acquired in acute hippocampal slices and in live animals. We utilize the red-green monomer-polymer display described above.

Cultured cells

In live HEK293 cells (Fig. 6 and Movie S1 in the Supporting Material), as in fixed cells, the soma appears mostly red, indicating monomeric g-actin. Lamellipodia and filopodia (Fig. 6, *B* and *C*) have higher green intensities, indicating larger polymeric f-actin concentrations. In lamellipodia, the actin polymerization state depends on whether the lamellipodium is extending or retracting—as defined by the position of the leading edge with respect to a fixed point near the base (Fig. 6 *D*, *green line*). During extension, the polymer fraction and the total actin concentration (C_T) remain roughly constant (Fig. 6 *D*) throughout the lamellipodium, with a somewhat higher polymer fraction near the leading edge. During this phase, it is common to see filopodia or microspikes that develop into filopodia (Fig. 6 *B*, *blue arrows*). During retraction, the leading edge exhibits a decrease in the polymer fraction (Fig. 6 *D*, *blue line*) but an apparent increase in the total actin concentration (Fig. 6 *D*, *red line*).

The drop in the polymer fraction at the leading edge during retraction indicates an expected destabilization of the actin cytoskeleton. In contrast, the accompanying

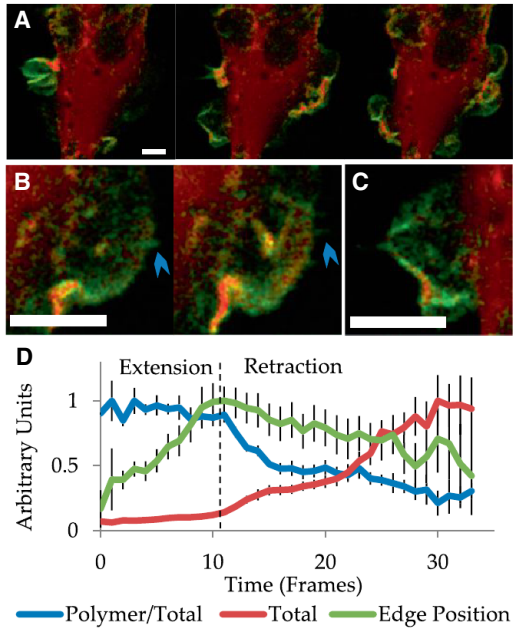

FIGURE 6 Imaging the actin polymerization state in live cells (*A*; select frames from Movie S1 in the Supporting Material). Scale bar = 10 μm. Saturated pixels (bright red) could not be used to calculate a polymer concentration and hence, have an associated green value of zero. Actin dynamics in live lamellipodia (*B* and *C*) show a high f-actin concentration near the leading edge. Actin microspikes (*B*, *blue arrow*) can be seen that develop into filopodia. The polymer fraction near the lamellar leading edge (*D*, *blue line*) is constant during extension (left of *dashed line*) but declines during retraction. The leading-edge total actin concentration (*D*, *red line*) undergoes an apparent increase during retraction. The extension and retraction phases are defined by the position of the leading edge (*D*, *green line*) with respect to a fixed point near the base.

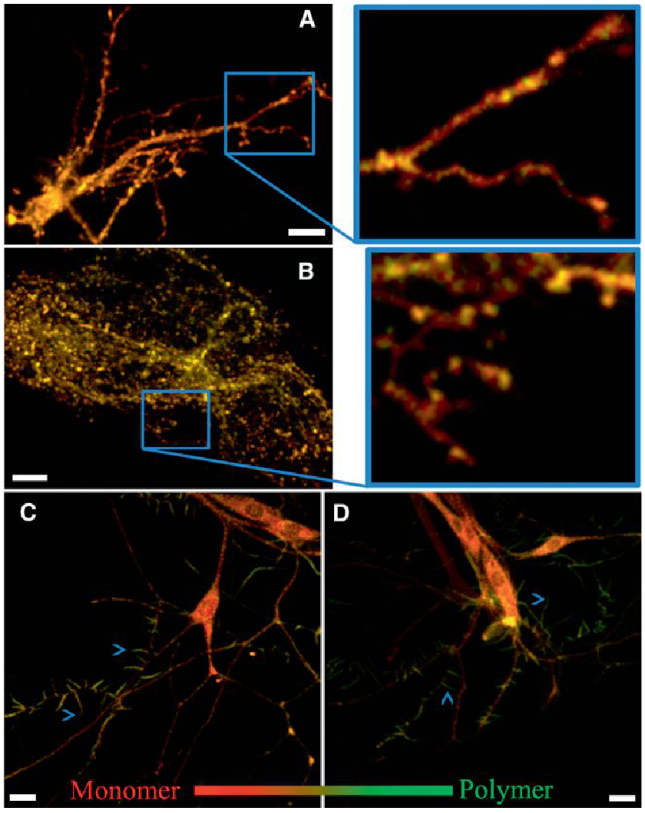

FIGURE 7 Imaging the anisotropy-derived actin polymerization state in vivo. (*A* and *B*) Live acute hippocampal slices expressing virally transduced actin-GFP. Maximal *z* projections of a granule neuron (*A*) in the dentate gyrus, and interneuron (*B*) in the stratum oriens of the CA1 layer. (*Blue highlighted boxes*) Single *z* planes. (*C* and *D*) Peripheral sensory neurons in live, intact, unanesthetized *Drosophila* larvae expressing actin-GFP selectively in peripheral sensory neurons. (*Blue arrows*) Examples of dendritic filopodia. Images are average *z* projections. Scale bars = 10 μm.

increase in the total actin signal is surprising and could be a volumetric effect due to thickening of the lamellipodium edge as it peels back from the substrate. Corrections for volume changes are often necessary in fluorescence microscopy and are typically implemented by normalizing intensity changes to those of a whole cell marker. Fluorescence anisotropy and the calculated actin polymer fraction, being inherently ratios, are immune to volumetric artifact and therefore accurately represent changes in the actin polymer fraction.

Acute hippocampal slices

We virally transduced actin-GFP in the hippocampi of adult mice and prepared acute hippocampal slices from these mice after 2–3 weeks of expression. The slices were perfused with oxygenated artificial cerebro-spinal fluid and imaged while living. We calculated images of the anisotropy-derived polymer fraction for multiple cell types (Fig. 7, *A* and *B*), including granule neurons in the dentate gyrus, and inhibitory interneurons in the CA1 layer. Both these cell types showed relatively high polymer fractions in the soma and larger neurites. Smaller, more distal neurites, however, tended to have a lower polymer fraction, punctuated by more highly polymerized compartments and terminals (Fig. 7, *A* and *B*, *blue boxes*).

Intact Drosophila larvae

We also calculated images of the anisotropy-derived polymer fraction in live, intact *Drosophila* larvae expressing actin-GFP in peripheral sensory neurons (22,23). *Drosophila* dendritic arborization sensory neurons (Fig. 7, *C* and *D*) show relatively low polymer fractions in their somas and primary dendrites. The filamentous projections from these dendrites, known as dendritic filopodia (*blue arrows*), are highly enriched in f-actin. Dendritic filopodia are believed to be the precursors of new dendrites and are common in young larvae with developing dendritic arbors (22).

In highly scattering tissue such as brain, we were practically limited to imaging at depths of $<$70 μm. Light scattering destroys fluorescence polarization and therefore reduces the dynamic range of anisotropy measurements. Because red light scatters less in tissue, we are developing

emFRET-optimized actin fusion proteins with red emissions to facilitate emFRET imaging in tissue.

DISCUSSION

Interfilament FRET in compact f-actin bundles

Actin filaments can be organized into branched networks and bundles (for review, see Revenu et al. (24)). In networks and the bundles mediated by many f-actin bundling proteins, the interfilament distance (axis-to-axis) is substantially larger than a typical Förster radius. For example, α-actinin bundles f-actin with an interfilament distance of 391 Å (25). In contrast, f-actin bundled by the smallest bundling proteins, fascin and fimbrin, has an interfilament distance as short as 120 Å (26,27). This corresponds to a ~50 Å distance of closest approach for the actin N-termini on adjacent filaments—well within FRET range. It is therefore likely that interfilament FRET in these compact bundles is comparable to, or greater than, intrafilament FRET. Fascin/fimbrin-mediated compact bundles are typically found in thin membrane protrusions such as filopodia, stereocilia, and microvilli.

Because the model presented here considers intrafilament FRET to be the sole source of depolarization, any additional depolarization due to interfilament FRET would lead to an overestimate of the true polymer concentration. This source of error is not immediately apparent in our correlations between phalloidin staining and the anisotropy-derived polymer concentration because filopodia represent a very small fraction of the total number of pixels in HEK cells. Nonetheless, an accurate calculation of the f-actin concentration in compact bundle-rich regions such as filopodia requires the development of additional theory that accounts for interfilament FRET.

The advantages of emFRET over heteroFRET

Although interactions between like proteins can be probed with either heteroFRET or emFRET, there are several advantages to using emFRET.

Incorporation probability affects the rate of energy transfer

In heteroFRET, actin-CFP and actin-YFP compete with each other for incorporation into f-actin. As a result, two potentially interacting sites can be occupied by two donors, or two acceptors, precluding FRET and reducing the ensemble average FRET rate. In emFRET, every incorporated fluorophore is both a donor and an acceptor; as a result, there are no pairs that are incapable of FRET.

The comparison becomes more realistic if we impose the constraint that the total amount of expressed actin fusion protein must be the same in both cases. Under such a constraint, a heteroFRET experiment must split the total expressed fusion protein concentration between the donor and the acceptor, effectively reducing the concentrations of both. The net effect of splitting the expressed concentration and the formation of FRET incompetent pairs is that the average FRET rate in emFRET is potentially fourfold larger than in heteroFRET (see Section S6 in the Supporting Material). As a result, emFRET can potentially generate the same rate of energy transfer as heteroFRET with fourfold less total fusion protein expression. This is of great importance given that overexpression of actin can affect cell physiology (28).

Donor/acceptor stoichiometry

Optimizing heteroFRET typically involves expressing the donor and acceptor in a specific stoichiometry. Although an obligate donor/acceptor stoichiometry is possible with specialized constructs, it generally requires optimization of transfection conditions and displays inevitable cell-to-cell variability. This is a tractable problem in cell culture but becomes increasingly difficult in tissue. In emFRET, because every GFP is both a donor and an acceptor, the stoichiometry problem is completely avoided.

Single fluorophore imaging

Using two fluorophores requires corrections for nonselective excitation and emission bleedthrough between the two detection channels (29). Anisotropy imaging utilizes only one fluorophore and hence avoids these problems altogether. Imaging with high numerical aperture objectives does cause polarization mixing; however, the correction for this is straightforward (30,31).

Indirect probes of actin polymerization state

EmFRET carries the limitations common to overexpressing any actin fusion protein. Overexpression can alter cellular actin dynamics, while the presence of a GFP tag can affect native interactions (32). As an alternative to direct probes, a number of live cell indirect probes have been developed (33–36) based on the fluorescent labeling of f-actin binding proteins and short peptides. Although these techniques are promising and increasingly used, they all involve utilizing probes that compete with endogenous f-actin binding proteins, making them sensitive to the f-actin protein binding state. Their dynamics must therefore be interpreted with some care, as their limitations remain to be fully understood (37). Furthermore, as with imaging the actin-GFP total intensity, the unbound pool of probe represents a background signal that limits the dynamic range of f-actin detection. It would be an intriguing possibility to extend anisotropy imaging to probes like Lifeact-GFP in cells and even live transgenic animals (34) to enhance their ability to detect f-actin.

CONCLUSION

The actin polymerization state has drawn intense study for its role in a diverse set of important cellular processes

ranging from cell division and migration to learning and memory. But the lack of a simple, in vivo method for directly imaging the actin polymerization state has been limiting. For example, in the brain, although the actin polymerization state undoubtedly plays a key role in learning (long-term potentiation), there are indications that both polymerization and depolymerization are necessary for long-term potentiation (5,38,39). Do these opposing polymerization dynamics arise from differing experimental conditions such as the system used (intact brain versus cultured neurons) or compartments studied (dendritic spine versus dendritic field)? Or, alternatively, does actin polymerization during synaptic plasticity have genuinely complex spatiotemporal dynamics? We seek to explore these questions by developing a simple, direct, in vivo probe of the actin polymerization state.

Finally, we note that although our method has been developed for quantitatively imaging the polymerization state of actin, it could potentially be readily extended to any polymer (microtubules, intermediate filaments, amyloids, etc.).

SUPPORTING MATERIAL

Supporting sections, two tables, five figures, one movie, and references (40–42) are available at http://www.biophysj.org/biophysj/supplemental/S0006-3495(12)00113-0.

The authors thank Mark Sonders and Jonathan Javitch (Columbia University) for the use of their multiphoton microscope. Actin-GFP adenovirus and Tet-Off virus were provided by Scott Soderling (Duke University). *Drosophila* larvae expressing actin-GFP in sensory neurons were provided by Jay Brenman (University of North Carolina, Chapel Hill) and housed and maintained by Brian McCabe and Ben Jiwon Choi (Columbia University). The polarizing beam splitter was adapted to the Prairie Ultima using a custom design by John Rafter at Prairie Technologies.

This research was supported by the Howard Hughes Medical Institute.

REFERENCES

1. Waterman-Storer, C. M., A. Desai, …, E. D. Salmon. 1998. Fluorescent speckle microscopy, a method to visualize the dynamics of protein assemblies in living cells. *Curr. Biol.* 8:1227–1230.
2. Tatavarty, V., E. J. Kim, …, J. Yu. 2009. Investigating sub-spine actin dynamics in rat hippocampal neurons with super-resolution optical imaging. *PLoS ONE.* 4:e7724.
3. Taylor, D. L., J. Reidler, …, L. Stryer. 1981. Detection of actin assembly by fluorescence energy transfer. *J. Cell Biol.* 89:362–367.
4. Marushchak, D., S. Grenklo, …, L. B. Johansson. 2007. Fluorescence depolarization studies of filamentous actin analyzed with a genetic algorithm. *Biophys. J.* 93:3291–3299.
5. Okamoto, K. I., T. Nagai, …, Y. Hayashi. 2004. Rapid and persistent modulation of actin dynamics regulates postsynaptic reorganization underlying bidirectional plasticity. *Nat. Neurosci.* 7:1104–1112.
6. Clayton, A. H. A., Q. S. Hanley, …, T. M. Jovin. 2002. Dynamic fluorescence anisotropy imaging microscopy in the frequency domain (rFLIM). *Biophys. J.* 83:1631–1649.
7. Lidke, D. S., P. Nagy, …, T. M. Jovin. 2003. Imaging molecular interactions in cells by dynamic and static fluorescence anisotropy (rFLIM and emFRET). *Biochem. Soc. Trans.* 31:1020–1027.
8. Runnels, L. W., and S. F. Scarlata. 1995. Theory and application of fluorescence homotransfer to melittin oligomerization. *Biophys. J.* 69:1569–1583.
9. Gautier, I., M. Tramier, …, M. Coppey-Moisan. 2001. Homo-FRET microscopy in living cells to measure monomer-dimer transition of GFP-tagged proteins. *Biophys. J.* 80:3000–3008.
10. Blackman, S. M., D. W. Piston, and A. H. Beth. 1998. Oligomeric state of human erythrocyte band 3 measured by fluorescence resonance energy homotransfer. *Biophys. J.* 75:1117–1130.
11. Chan, F. T. S., C. F. Kaminski, and G. S. Kaminski Schierle. 2011. HomoFRET fluorescence anisotropy imaging as a tool to study molecular self-assembly in live cells. *ChemPhysChem.* 12:500–509.
12. Varma, R., and S. Mayor. 1998. GPI-anchored proteins are organized in submicron domains at the cell surface. *Nature.* 394:798–801.
13. Blackman, S. M., C. E. Cobb, …, D. W. Piston. 1996. The orientation of eosin-5-maleimide on human erythrocyte band 3 measured by fluorescence polarization microscopy. *Biophys. J.* 71:194–208.
14. Patterson, G. H., D. W. Piston, and B. G. Barisas. 2000. Förster distances between green fluorescent protein pairs. *Anal. Biochem.* 284:438–440.
15. Miki, M., S. I. O'Donoghue, and C. G. Dos Remedios. 1992. Structure of actin observed by fluorescence resonance energy transfer spectroscopy. *J. Muscle Res. Cell Motil.* 13:132–145.
16. Zhou, H. X. 2001. Loops in proteins can be modeled as worm-like chains. *J. Phys. Chem. B.* 105:6763–6766.
17. Craver, F. W., and R. S. Knox. 1971. Theory of polarization quenching by excitation transfer. 2. Anisotropy and second-neighbor considerations. *Mol. Phys.* 22:385–402.
18. Small, J. V., M. Herzog, and K. Anderson. 1995. Actin filament organization in the fish keratocyte lamellipodium. *J. Cell Biol.* 129:1275–1286.
19. Lewis, A. K., and P. C. Bridgman. 1992. Nerve growth cone lamellipodia contain two populations of actin filaments that differ in organization and polarity. *J. Cell Biol.* 119:1219–1243.
20. Tramier, M., and M. Coppey-Moisan. 2008. Fluorescence anisotropy imaging microscopy for homo-FRET in living cells. *In* Fluorescent Proteins, 2nd Ed. Kluwer Academic, New York. 395–414.
21. Koestler, S. A., K. Rottner, …, J. V. Small. 2009. F- and G-actin concentrations in lamellipodia of moving cells. *PLoS ONE.* 4:e4810.
22. Medina, P. M. B., L. L. Swick, …, J. E. Brenman. 2006. A novel forward genetic screen for identifying mutations affecting larval neuronal dendrite development in *Drosophila melanogaster. Genetics.* 172:2325–2335.
23. Andersen, R., Y. M. Li, …, J. E. Brenman. 2005. Calcium/calmodulin-dependent protein kinase II alters structural plasticity and cytoskeletal dynamics in *Drosophila*. *J. Neurosci.* 25:8878–8888.
24. Revenu, C., R. Athman, …, D. Louvard. 2004. The co-workers of actin filaments: from cell structures to signals. *Nat. Rev. Mol. Cell Biol.* 5:635–646.
25. Taylor, K. A., D. W. Taylor, and F. Schachat. 2000. Isoforms of α-actinin from cardiac, smooth, and skeletal muscle form polar arrays of actin filaments. *J. Cell Biol.* 149:635–646.
26. Volkmann, N., D. DeRosier, …, D. Hanein. 2001. An atomic model of actin filaments cross-linked by fimbrin and its implications for bundle assembly and function. *J. Cell Biol.* 153:947–956.
27. Sedeh, R. S., A. A. Fedorov, …, M. Bathe. 2010. Structure, evolutionary conservation, and conformational dynamics of *Homo sapiens* fascin-1, an F-actin crosslinking protein. *J. Mol. Biol.* 400:589–604.
28. Peckham, M., G. Miller, …, G. A. Dunn. 2001. Specific changes to the mechanism of cell locomotion induced by overexpression of β-actin. *J. Cell Sci.* 114:1367–1377.
29. Okamoto, K.-I., and Y. Hayashi. 2006. Visualization of F-actin and G-actin equilibrium using fluorescence resonance energy transfer (FRET) in cultured cells and neurons in slices. *Nat. Protoc.* 1:911–919.

30. Axelrod, D. 1979. Carbocyanine dye orientation in red cell membrane studied by microscopic fluorescence polarization. *Biophys. J.* 26: 557–573.

31. Axelrod, D. 1989. Fluorescence polarization microscopy. *Methods Cell Biol.* 30:333–352.

32. Wu, J.-Q., and T. D. Pollard. 2005. Counting cytokinesis proteins globally and locally in fission yeast. *Science.* 310:310–314.

33. Riedl, J., A. H. Crevenna, …, R. Wedlich-Soldner. 2008. Lifeact: a versatile marker to visualize F-actin. *Nat. Methods.* 5:605–607.

34. Riedl, J., K. C. Flynn, …, R. Wedlich-Söldner. 2010. Lifeact mice for studying F-actin dynamics. *Nat. Methods.* 7:168–169.

35. Burkel, B. M., G. von Dassow, and W. M. Bement. 2007. Versatile fluorescent probes for actin filaments based on the actin-binding domain of utrophin. *Cell Motil. Cytoskeleton.* 64:822–832.

36. Dutta, D., J. W. Bloor, …, D. P. Kiehart. 2002. Real-time imaging of morphogenetic movements in *Drosophila* using Gal4-UAS-driven expression of GFP fused to the actin-binding domain of moesin. *Genesis.* 34:146–151.

37. Munsie, L. N., N. Caron, …, R. Truant. 2009. Lifeact cannot visualize some forms of stress-induced twisted F-actin. *Nat. Methods.* 7:605–607.

38. Ouyang, Y., M. Wong, …, D. W. Choi. 2005. Transient decrease in F-actin may be necessary for translocation of proteins into dendritic spines. *Eur. J. Neurosci.* 22:2995–3005.

39. Kim, C. H., and J. E. Lisman. 1999. A role of actin filament in synaptic transmission and long-term potentiation. *J. Neurosci.* 19:4314–4324.

40. Evers, T. H., E. M. W. M. van Dongen, …, M. Merkx. 2006. Quantitative understanding of the energy transfer between fluorescent proteins connected via flexible peptide linkers. *Biochemistry.* 45:13183–13192.

41. Lepine, Y., and A. Caille. 1978. Configuration of a polymer-chain interacting with a plane interface. *Can. J. Phys.* 56:403–408.

42. Lakowicz, J. R. 1999. Principles of Fluorescence Spectroscopy. Springer, New York.

Crosstalk and Competition in Signaling Networks

Michael A. Rowland,[†] Walter Fontana,[§] and Eric J. Deeds[†‡*]
[†]Center for Bioinformatics and [‡]Department of Molecular Biosciences, University of Kansas, Lawrence, Kansas; and [§]Department of Systems Biology, Harvard Medical School, Boston, Massachusetts

ABSTRACT Signaling networks have evolved to transduce external and internal information into critical cellular decisions such as growth, differentiation, and apoptosis. These networks form highly interconnected systems within cells due to network crosstalk, where an enzyme from one canonical pathway acts on targets from other pathways. It is currently unclear what types of effects these interconnections can have on the response of networks to incoming signals. In this work, we employ mathematical models to characterize the influence that multiple substrates have on one another. These models build off of the atomistic motif of a kinase/phosphatase pair acting on a single substrate. We find that the ultrasensitive, switch-like response these motifs can exhibit becomes transitive: if one substrate saturates the enzymes and responds ultrasensitively, then all substrates will do so regardless of their degree of saturation. We also demonstrate that the phosphatases themselves can induce crosstalk even when the kinases are independent. These findings have strong implications for how we understand and classify crosstalk, as well as for the rational development of kinase inhibitors aimed at pharmaceutically modulating network behavior.

INTRODUCTION

Signal propagation through a network of interacting proteins is central to a cell's ability to process and respond to stimuli. In most cases, these interactions involve an enzyme (e.g., a kinase) that covalently modifies a substrate and changes its functionality (i.e., activates/deactivates it as an enzyme, or causes translocation to a different compartment). To regulate the signal, another enzyme (e.g., a phosphatase) reverses the modification, restoring the original functionality of the substrate in question. The net activity of these enzymes alters the functional state of the proteins in the network in response to inputs, and the overall state of the network ultimately determines the cellular response.

Intracellular signaling networks are extremely complex in metazoans, which makes it difficult to understand their behavior (1,2). A major source of this complexity is network crosstalk, i.e., the sharing of input signals between multiple canonical pathways (3–7). For example, kinases can often transmit signals to a large number of different targets: Akt can act on at least 18 substrates, and the receptor tyrosine kinases in the EGF/ErbB family can interact with >20 substrates (8,9). Because eukaryotic genomes contain fewer distinct phosphatases than distinct kinases, phosphatases are generally considered more promiscuous, and even with adaptor proteins targeting their activity, they often act on multiple substrates (10). Although it is clear that crosstalk is widespread in mammalian signaling networks, we currently do not have a clear conceptual picture of how this highly interconnected architecture might influence the response of a network to incoming signals.

In this work, we seek to understand how the competition and promiscuity induced by crosstalk ultimately influence network behavior. In classic crosstalk, a kinase is shared between two pathways and can transfer signals from one pathway to another (3,5,7,11); for instance, mitogen-activated protein kinase (MAPK) networks often use the same enzymes in multiple cascades (12). Most previous computational studies on this subject have focused on characterizing the spatial or temporal mechanisms for the insulation of MAPK signaling cascades despite the potential for crosstalk (13–15). It has been demonstrated, however, that competition among targets of the same kinase can have profound effects on substrate phosphorylation (16). Here, we extend these previous findings to characterize in detail how crosstalk can actively couple the response of multiple proteins to incoming signals. We developed models that consider a set of general motifs, with the goal of understanding how features such as substrate saturation and phosphatase architecture can influence substrate response.

Our models build off a simple futile cycle in which one enzyme modifies a single substrate and another enzyme removes the modification, which we represent as a kinase and phosphatase pair interacting with a target protein (see Fig. 1 *A*). As first shown by Goldbeter and Koshland (18) over 30 years ago, the fraction of modified substrate for this cycle can be expressed as a function of three parameters:

$$K_K = \frac{K_{m,K}}{[S]_0}, \quad K_P = \frac{K_{m,P}}{[S]_0}, \quad r = \frac{V_{max,K}}{V_{max,P}} \qquad (1)$$

where $[S]_0$ is the total amount of substrate, $K_{m,K}$ and $K_{m,P}$ are the Michaelis constants for the two enzymes, K_K and K_P represent the inverse of the degree of saturation of the enzymes, and r is the ratio of their maximum velocities. Detailed definitions of these constants in terms of the underlying rates of the enzymatic reactions can be found in the context of Eq. 2 below. One can easily solve the underlying

Submitted August 16, 2012, and accepted for publication October 10, 2012.

*Correspondence: deeds@ku.edu

Editor: Dennis Bray.

0006-3495/12/12/2389/10 $2.00

http://dx.doi.org/10.1016/j.bpj.2012.10.006

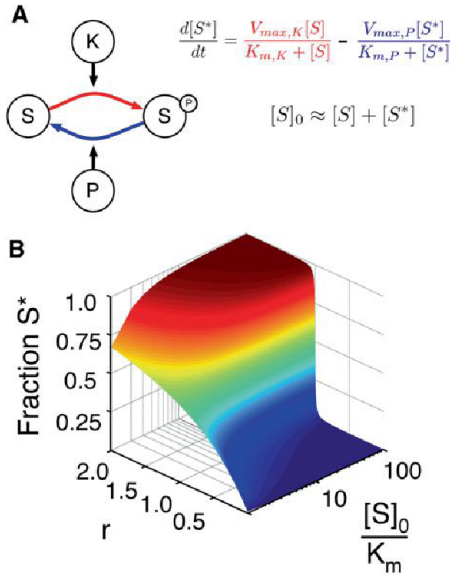

FIGURE 1 The Goldbeter-Koshland loop. (*A*) A pair of enzymes (say, a kinase *K* and a phosphatase *P*) acts on a single substrate. The associated equations show the change in *S** concentration as the difference between the production of *S** by the kinase (in *red*) and the production of *S* by the phosphatase (in *blue*). Here we assume that the concentration of free *S* and *S** is far greater than the concentrations of bound *S* in either form, which is necessary to obtain the standard Michaelis-Menten forms for the enzymatic reaction velocities (18). (*B*) The fraction of phosphorylated *S* (*z* axis) is a function of *r* and $[S]_0$. The total concentration of [*S*] is normalized by its K_m (which is identical for both the kinase and phosphatase) and is plotted on a log scale.

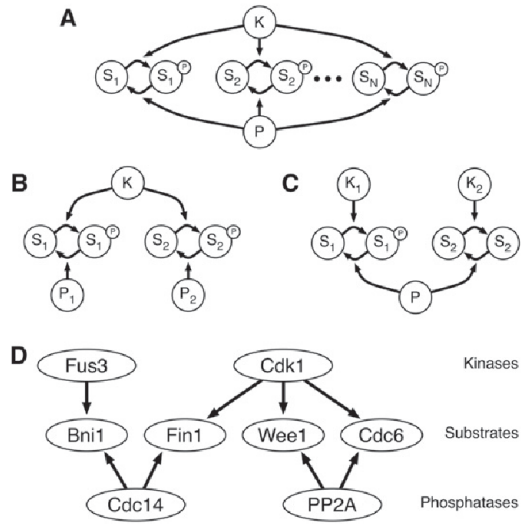

FIGURE 2 Crosstalk schematic. (*A*) A pair of enzymes (a kinase *K* and phosphatase *P*) acting on *N* substrates; we term this the 1K1P loop. (*B*) A kinase that has two substrates, each with its own independent phosphatase (P_1 and P_2); we term this the 1K2P loop. (*C*) Two independent kinases (K_1 and K_2) acting on two substrates that share a single phosphatase *P*; we term this the 2K1P loop. (*D*) A section of the yeast Cdk1 signaling network, including each of these three motifs (16,44–49). Although the interactions shown are specific to yeast, there are human homologs for each of the proteins listed. The full network in this case contains a number of downstream feedback mechanisms that are omitted for clarity. These mechanisms may be abrogated by mutations so that the local influence of competition can be studied experimentally (16). The competition between Wee1 and Cdc6 is an example of the 1K1P loop, whereas Wee1 and Fin1 form a 1K2P loop, and Fin1 and Bni1 form a 2K1P loop.

system of differential equations (see Fig. 1 *A*) at steady state, providing a relationship between overall substrate phosphorylation and the parameters listed in Eq. 1 (see Eq. 3 below, with $\alpha_{K,1} = \alpha_{P,1} = 1$). Because protein levels tend to change slowly (17), we expect that saturation (and thus K_K and K_P) will remain constant on short timescales during the response to signal. On the other hand, *r* changes with the concentration of active kinase and phosphatase. Incoming signals generally modulate active *K* or *P* concentration, thus making *r* the dominant response parameter. When the substrate does not saturate the enzymes, phosphorylation of the substrate increases hyperbolically with *r*. However, when the substrate saturates both enzymes, the loop displays a switch-like behavior in *r*, referred to as 0^{th} order ultrasensitivity (Fig. 1 *B*). In this case, at values of $r < 1$ the fraction of phosphorylated substrate is very low, and at $r > 1$ the system switches to a highly phosphorylated state (18). The ultrasensitive response of a substrate at saturating concentrations has been observed experimentally in a number of systems (16,19–23).

We expanded this model to include competing substrates at either or both enzymes to characterize the influence of multiple targets on signaling (Fig. 2, *A–C*). All three of the motifs we consider are found in well-known signaling systems, such as the Fus3/Cdk1 network in yeast and other eukaryotes (Fig. 2 *D*). We found that shared signaling enzymes can couple the responses of different substrates. For instance, when there is more than one substrate of the same kinase and phosphatase (see Fig. 2 *A*), if one substrate is at sufficient concentration to elicit an ultrasensitive response, then all substrates that share the pair enzymes in the cycle will exhibit ultrasensitivity without necessarily saturating the enzyme themselves. We have shown that in systems in which two substrates share a phosphatase (see Fig. 2 *C*), one substrate saturating the phosphatase can cause the other substrate to ultrasensitively respond to signals from the first kinase. This indicates a novel potential for phosphatases to be involved in network crosstalk.

Kinases are becoming increasingly popular drug targets in the treatment of cancer and other diseases (24). We considered how such inhibitors might influence the behavior of these various crosstalk architectures, and found that these inhibitors can have important consequences that would be difficult to predict in the absence of a detailed understanding of network topology and enzyme saturation.

Overall, our work demonstrates that enzymes with multiple targets can couple signal responses, and that systems considered in a cellular context may exhibit behaviors vastly different from those considered in isolated models. These results have implications for how we understand the role

of crosstalk in signaling, and how we can potentially control the propagation of the effects of enzymatic inhibitors through highly connected networks.

MATERIALS AND METHODS

The behaviors of each model are described by sets of ordinary differential equations (ODEs), which are written explicitly for each system in section 1 of the Supporting Material. The systems of ODEs were numerically integrated using the CVODE package from SUNDIALS (25). We employed the dense linear solver with the backward differentiation formula and a Newton iteration methodology available in that package for all of the dynamics discussed in this work. The values of the parameters used in each case are included in the Supporting Material.

Steady-state measurements were obtained by allowing the system to run until the level of each species of the system stabilized. The actual times at which the measurements were made were chosen heuristically by visual inspection of the trajectories themselves. The surfaces obtained in Figs. 3 and 4 were confirmed analytically by solving for S_1* in the same manner as described by Goldbeter and Koshland (18). The analytical results are derived in sections 2–4 of the Supporting Material.

RESULTS

1-Kinase/1-phosphatase loop with two substrates

We first considered a signaling motif in which a kinase (K) and phosphatase (P) act on multiple substrates, which we term the 1-kinase/1-phosphatase (1K1P) loop. An example of this can be found in yeast, where the proteins Wee1 and Cdc6 compete for both the kinase Cdk1 and phosphatase PP2A (Fig. 2 *D*). In the simplest case, we included two substrates of the kinase and phosphatase, S_1 and S_2, each of which can exist in an unphosphorylated and phosphorylated (e.g., S_1*) form (see Fig. 2 *A*, N = 2). The set of enzymatic reactions is as follows:

$$\begin{aligned}
S_1 + K &\underset{k_{-,K,1}}{\overset{k_{+,K,1}}{\rightleftharpoons}} KS_1 \xrightarrow{k_{cat,K,1}} S_1^* + K \\
S_2 + K &\underset{k_{-,K,2}}{\overset{k_{+,K,2}}{\rightleftharpoons}} KS_2 \xrightarrow{k_{cat,K,2}} S_2^* + K \\
S_1^* + P &\underset{k_{-,P,1}}{\overset{k_{+,P,1}}{\rightleftharpoons}} PS_1^* \xrightarrow{k_{cat,P,1}} S_1 + P \\
S_2^* + P &\underset{k_{-,P,2}}{\overset{k_{+,P,2}}{\rightleftharpoons}} PS_2^* \xrightarrow{k_{cat,P,1}} S_2 + P
\end{aligned} \tag{2}$$

Each of the above reactions involves three elementary rates: the rate of complex formation (k_+), the rate of complex dissociation (k_-), and the enzyme catalytic rate (k_{cat}). From these rates we can obtain the Michaelis constant for both enzymes: $K_{m,K,i} = (k_{-,K,i} + k_{cat,K,i})/k_{+,K,i}$ and $K_{m,P,i} = (k_{-,P,i} + k_{cat,P,i})/k_{+,P,i}$. Additionally, we can define the maximum velocity of each enzymatic reaction as $V_{max,K,i} = [K]_0\, k_{cat,K,i}$ and $V_{max,P,i} = [P]_0\, k_{cat,P,i}$. Each kinase and phosphatase molecule can only bind and act on one substrate at any given moment, and as such, S_2 acts as a competitive inhibitor of the kinase and phosphatase reactions with S_1. This results in a set of inhibitory constants, $\alpha_{K,1} = 1 + [S_2]/K_{m,K,2}$ and $\alpha_{P,1} = 1 + [S_2^*]/K_{m,P,2}$, that capture the effects of S_2 on the S_1 kinase and phosphatase reactions, respectively. S_1 inhibition of the S_2 reactions generates similar constants, $\alpha_{K,2}$ and $\alpha_{P,2}$ (see the Supporting Material). The fact that multiple targets constitute competitive inhibitors of each other has been observed experimentally for both kinases and phosphatases (16,26,27). These α terms are identical to what one would obtain for a generic competitive inhibitor, $\alpha = 1 + [I]/K_I$ (28). Where the activity of a generic inhibitor against its target enzyme depends solely on its concentration, a competitive substrate will inhibit either the kinase or the phosphatase based on the concentrations of its unphosphorylated and phosphorylated forms, respectively. Because these concentrations are controlled by incoming signals, mutual inhibition has the potential to couple substrate responses.

The chemical reactions in Eq. 2 can be readily used to define a system of ODEs in which the binding, dissociation, and catalysis steps are treated explicitly (see the Supporting Material). We numerically integrated these equations and calculated the fraction $S_1^* \equiv [S_1^*]/[S_1]_0$ at steady state at various concentrations of S_2 for a case in which S_1 does not saturate the enzymes. In this work, we consider a case in which the saturation of all enzymes by any given substrate is equal; we leave the case of differential saturation among enzymes (12) to future studies. The response of the system is controlled by two r values, r_1 and r_2, which are the ratios of the maximum velocities of the enzymes with respect to either substrate. The results of these calculations are summarized in Fig. 3 *A*. As expected, when there is no S_2 present to compete with S_1 for the enzymes, S_1* increases as a rectangular hyperbola in r_1. When S_2 saturates the enzymes, however, we find that S_1 displays an ultrasensitive response in r_1 in a fashion similar to the ultrasensitive response obtained by increasing S_1 concentration in Fig. 1 *B*.

These findings can be understood by treating the 1K1P loop analytically. In the limit in which the total concentration of the substrates is much larger than the total concentration of either enzyme (i.e., $[S_i]_0 \approx [S_i] + [S_1^*]$), we can calculate the fraction S_1* as

$$S_1^* = \frac{(r_1 - 1) - (\alpha_{K,1}K_{K,1} + \alpha_{P,1}r_1K_{P,1}) + \sqrt{((r_1 - 1) - (\alpha_{K,1}K_{K,1} + r_1\alpha_{P,1}K_{P,1}))^2 + 4(r_1 - 1)r_1\alpha_{P,1}K_{P,1}}}{2(r_1 - 1)} \tag{3}$$

which is identical to the original result of Goldbeter and Koshland (18) except for the α inhibition terms (see the Supporting Material for details about the solution). Note that S_1* depends on $[S_1]_0$ through the K terms as well as $[S_2]$ and $[S_2$*] through the α terms. The equation for S_2* is identical to Eq. 3 with a change of indices. This result is a generalization of previous findings on multiple substrates in a Goldbeter-Koshland loop, allowing for both kinase saturation and saturation of a shared phosphatase (16). When $[S_1]_0 \ll K_m$, as in Fig. 3 *A*, $\alpha_{K,2} \approx 1$ and $\alpha_{P,2} \approx 1$. In this case, S_2 will behave as an isolated Goldbeter-Koshland loop and as such will display an ultrasensitive response in r_2 when $[S_2]_0 \gg K_m$. Because incoming signals vary r by changing the relative concentrations of active enzymes, $r_1 \propto r_2$ (for purposes of display in Fig. 3 *A*, we assumed $r_1 = r_2$). When $r_2 < 1$, S_2 will be largely unphosphorylated and will inhibit the kinase's action on S_1, causing S_1 to be primarily in its unphosphorylated state. Similarly, when $r_2 > 1$, S_2 will be mostly phosphorylated and will inhibit the S_1 dephosphorylation reaction by saturating the phosphatase. In combination, this coupling transfers the ultrasensitive response of S_2 to the S_1 curve. We have proven mathematically that an increase in S_2 ultrasensitivity (i.e., increasing S_2 concentration) always increases the ultrasensitivity of the response of S_1 in r_2 regardless of the values of the kinetic parameters (see the Supporting Material). The general behavior observed in Fig. 3 *A* is thus a qualitative feature of all 1K1P loops.

It has been shown experimentally that the competition between multiple phosphorylation sites on the protein Wee1 contributes to the ultrasensitivity of Wee1's response to incoming signals (16). Although multisite phosphorylation can have a number of influences on such systems (e.g., by introducing thresholds or bistability (2,29,30)), these findings are consistent with the predictions made by Eq. 3.

1K1P with many substrates

We further developed the 1K1P loop to include $N > 2$ substrates of the kinase and phosphatase (see Fig. 2 *A*). As described above, we numerically integrated the resulting ODEs and calculated the fraction S_1 at steady state in a case in which we include a varying number of substrates, each of which does not saturate the enzymes. The results of these calculations are summarized in Fig. 3 *B*. As expected, S_1* increases as a rectangular hyperbola in r_1 in the absence of other substrates. As new unsaturating substrates are added to the system, we see that S_1* starts to show an ultrasensitive response in r_1, even though none of the substrates are at a concentration that would produce such a response on their own.

Once again, these results can be understood by treating the loop analytically. In this case, the collection of substrates act as competitive inhibitors of the S_1 loop. As such, the inhibitory constants must now account for all competing substrates and can be expressed as $\alpha_{K,1} = 1 + \sum_{i=2}^{N}[S_i]/K_{m,K,i}$ and $\alpha_{P,1} = 1 + \sum_{i=2}^{N}[S_i^*]/K_{m,P,i}$ (see the Supporting Material for the derivation). Considering the case in which $N > 2$ reveals that saturation of the enzymes can be the combined result of many substrates, rather than one substrate saturating the enzymes on its own. When the kinase is saturated by any subset of its targets, S_1's kinase reaction is inhibited, and a similar inhibition occurs with the phosphatase. Thus, given enough substrates, the entire system can show ultrasensitivity in r_1 even when none of the substrates individually saturate the enzymes.

As mentioned in the Introduction, kinases often have multiple targets within cells; for instance, Cdk1 has hundreds of substrates in yeast (2,31,32), and the ErbB receptor tyrosine kinases in humans have between 20 and 40 potential targets. In the latter case, the K_D values measured by Kaushansky et al. (33) indicate that the 1 μM K_M value used in generating Fig. 3 is a reasonable estimate. The collective-saturation mechanism described above may thus represent a common scenario for generating ultrasensitivity in substrate response.

1-Kinase/2-phosphatase loop

Most of our empirical understanding of crosstalk comes from studies that focused on the motif of a kinase with more than one substrate (34). Because the specific phosphatases that act on any given set of targets are often not known, it is not clear that all kinase crosstalk will follow the 1K1P pattern discussed above (Fig. 2 *A*). For instance, Fin1 and Wee1 share the same kinase (Cdk1) but have separate phosphatases (Cdc14 and PP2A, respectively; Fig. 2 *D*). Also, because kinases often have a very large number of targets, systems in which substrates share the same kinase but possess separate phosphatases may be widespread (8,9,31,32). As such, we considered the behavior of the 1-kinase/2-phosphatase (1K2P) loop as diagramed in Fig. 2 *B*. In this case, because the phosphatases are independent, we can separate the r parameters (i.e., $r_2 \not\propto r_1$). At low substrate concentrations, S_1 responds hyperbolically in r_1 and is insensitive to r_2 (Fig. 4 *A*). When $[S_2]_0 \gg K_m$ and $r_2 < 1$, S_1 phosphorylation is greatly reduced (Fig. 4 *B*). In fact, one observes very little S_1 phosphorylation until $r_2 > 1$. In contrast to the 1K1P loop, the response of S_1 to r_2 thus exhibits a threshold: when $r_2 < 1$, S_1 essentially cannot respond to signals. At values of $r_2 > 1$, however, S_1 responds hyperbolically to both r_1 and r_2.

The fraction S_1* for the 1K2P loop also follows Eq. 3, but with $\alpha_{P,1} = 1$ because the phosphatases are independent. The presence of S_2 in the system thus generally decreases the phosphorylation level of S_1 (compare Fig. 4, *A* and *B*). The thresholding behavior seen in Fig. 4 *B* occurs because the concentration of the inhibitor

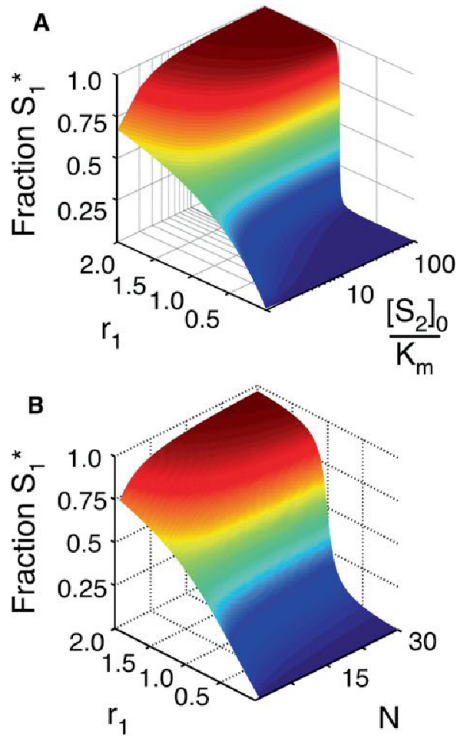

FIGURE 3 Results for the 1K1P loop. (*A*) The fraction of phosphorylated S_1 (z axis) as a function of r_1 and $[S_2]_0$. Note that for the purpose of display, we have set $r_1 = r_2$ in this case. The total concentration of $[S_2]$ is normalized by its K_m (which is identical for both the kinase and phosphatase) and is plotted on a log scale. (*B*) The fraction of phosphorylated S_1 as a function of r_1 and the number of additional substrates in the loop (N, see Fig. 2 *A*). All substrates are below saturating concentrations ($[S_i]_0 = 0.1 \times K_m$). As in *A*, for the purpose of display, the r and K_m parameters have been set to be equal for all substrates. Note that in both panels *A* and *B*, the fraction S_1* responds to r_1 with increasing ultrasensitivity as the total saturation of the enzymes (represented by $[S_2]_0/K_m$ or N, respectively) increases.

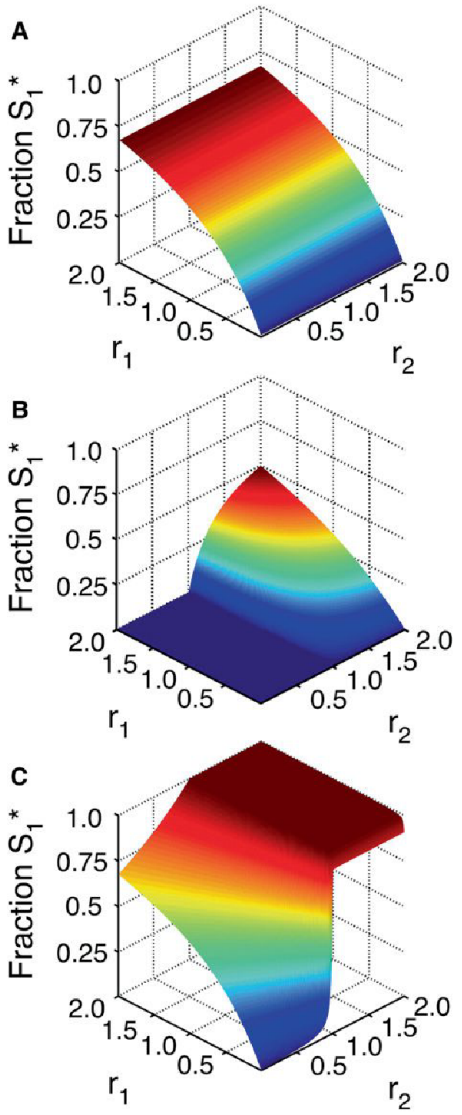

FIGURE 4 Influence of phosphatase architecture on network response. (*A*) The fraction of phosphorylated S_1 as a function of r_1 and r_2 when $[S_2]_0 \ll K_m$ for both the 1K2P and 2K1P loops. In this case, $[S_1]_0 = 0.1 \times K_m$. Note that r_2 has little effect on the response of the S_1 loop. (*B*) The fraction of phosphorylated S_1 as a function of r_1 and r_2 for a 1K2P loop with $[S_2]_0 = 20 \times K_m$. As in *A*, $S_1 = 0.1 \times K_m$. If S_2 saturates the enzymes, it becomes a gatekeeper; when $r_2 < 1$ (i.e., when the S_2 loop is switched to the unphosphorylated state), the S_1 loop essentially cannot respond to incoming signals. When $r_2 > 1$, however, S_1* responds hyperbolically in both r_1 and r_2. (*C*) The fraction of phosphorylated S_1 as a function of r_1 and r_2 for a 2K1P loop. As in *B*, $[S_1]_0 = 0.1 \times K_m$ and $[S_2]_0 = 20 \times K_m$. Saturating concentrations of S_2 generally increase phosphorylation in this case. Note that even when $r_1 \ll 1$, S_1 shows an ultrasensitive response to r_2 (and thus K_2) despite receiving only basal levels of signal from its own kinase. This indicates the potential for significant phosphatase crosstalk in signaling networks.

(i.e., unphosphorylated S_2) responds ultrasensitively to r_2. If $r_2 < 1$, the inhibitor concentration is high, and no phosphorylation of S_1 can take place. At $r_2 > 1$, the inhibitor is largely removed from the system, allowing S_1 to respond to incoming signals. However, it is only in the limit $r_2 \to \infty$ (i.e., $\alpha_{K,1} \to 1$) that S_1 will behave as an isolated futile cycle. As with the 1K1P loop, we have shown mathematically that addition of S_2 always decreases S_1* regardless of the values of the parameters in the limit $S_1^* \ll K_m$ (see the Supporting Material). This indicates that the gatekeeper function played by S_2 is a robust feature of 1K2P loops.

Kim and Ferrell (16) showed experimentally that adding Fin1 and Cdc6 to *Xenopus* cell extracts increases the active kinase concentration (i.e., r) required to induce a Wee1 response. Although the experiment in this case involves both a 1K1P and a 1K2P loop (Fig. 2 *D*), these findings are consistent with our prediction that competitive substrates tend to decrease the phosphorylation levels of other targets when the phosphatase is not shared.

2-Kinase/1-phosphatase loop

The human genome encodes ~150 catalytically active phosphatases and phosphatase domains, and almost 500 kinases (35,36). As such, phosphatases are generally considered

promiscuous; although adaptor proteins help increase phosphatase specificity, these complexes still can target multiple substrates (10). Because of this promiscuity, it is reasonable to imagine that motifs in which two substrates share a single phosphatase but are phosphorylated by independent kinases are relatively common arrangements in signaling networks. There are certainly examples of such situations: for instance, Fin1 and Bni1 in yeast share a phosphatase (Cdc14) but have different kinases (Cdk1 and Fus3, respectively; Fig. 2 *D*). We used the 2-kinase/1-phosphatase (2K1P) loop as modeled in Fig. 2 *C* to characterize the behavior of such systems. As with the 1K2P loop, the distinct kinases in the 2K1P system allow the separation of r parameters so that $r_1 \not\propto r_2$.

At low substrate concentrations, this is essentially the case. As anticipated, S_1 responds hyperbolically in r_1 and is insensitive to r_2 (see Fig. 4 *A*). The situation is very different when $[S_2]_0 \gg K_m$. We see the expected hyperbolic S_1 response in r_1 when r_2 is nearly zero (i.e., when the S_2 loop has not received an activation signal); however, as r_2 increases, the fraction of phosphorylated S_1 molecules increases until it reaches nearly one at $r_2 > 1$ (Fig. 4 *C*). When r_1 is close to zero, S_1 responds ultrasensitively to r_2. This indicates that a signal that switches S_2 to its phosphorylated state can cause a similar switch in S_1 even if very little signal is received via K_1.

As with the 1K1P loop, this behavior can be explained in terms of the inhibition of one loop by another. In this case, the fraction S_1* can be defined as in Eq. 3 with $\alpha_{K,1} = 1$ to account for the independence of the kinases. Adding S_2 to the system thus generally increases phosphorylation of S_1 (compare Fig. 4, *A* and *C*). Because phosphorylated S_2 acts as a phosphatase inhibitor, an incoming signal that increases r_2 to values greater than one introduces high concentrations of the inhibitor in a switch-like manner, inducing a response in S_1. We have shown mathematically that this increase in phosphorylation in response to S_2 competition will always occur regardless of parameters in the limit $S_1^* \ll K_m$ (see the Supporting Material).

Phosphatase tunneling

In the models described above, we focused on crosstalk occurring between substrates on the same level of signaling; the only relationship between the substrates is the shared enzymes. Signaling networks, however, often contain cascades in which a set of proteins activate each other in sequence (37). Although the sharing of phosphatases between different levels of a cascade has been documented (6), the phosphatase architecture in these cases is often poorly understood. Indeed, anonymous and independent phosphatases are often added to mathematical models of MAPK cascades to fill in these gaps (21,38–40). Given this ambiguity, we constructed models of cascades in which each kinase has an independent phosphatase, in addition to a case in which a single phosphatase acts on all of the proteins in the cascade (Fig. 5, *A* and *B*).

Each type of cascade was modeled with depth $N = 2, 3, 4$, or 5 substrates present in saturating ($10 \times K_m$) or unsaturating ($0.1 \times K_m$) concentrations. The input parameter r was defined as the ratio of the maximum velocities of the initial kinase (K) to the phosphatase acting on S_1 (P_1 or P for the independent and shared cases, respectively), and the models were analyzed for the fraction of the final substrate phosphorylated (S_N*) at steady state.

For both classes of cascade, we found that the response of the final substrate becomes exponentially more sensitive to input signals with increasing cascade depth. The $N = 5$ case generally reaches its $r_{1/2}$ (the r-value at which half of S_N is phosphorylated) with 9 orders of magnitude less input

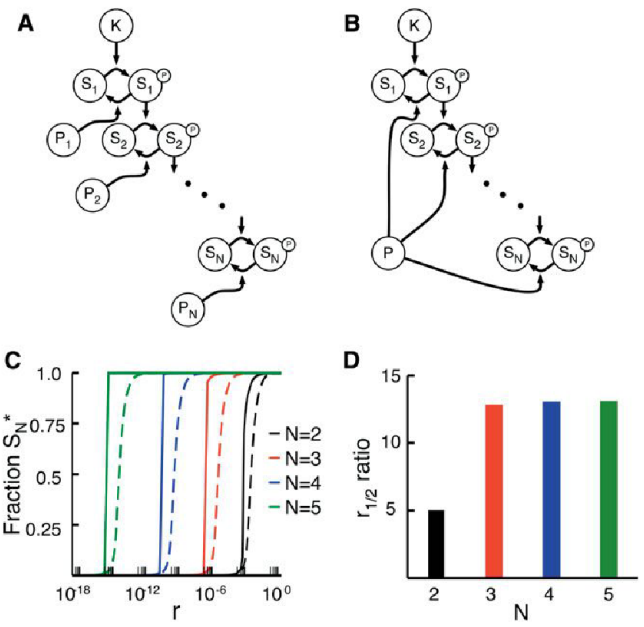

FIGURE 5 Influence of phosphatase tunneling on cascade signals. (*A*) A kinase cascade with N members. The kinase K provides the input signal, and each substrate S_i acts as the kinase for substrate S_{i+1}. In this model, there are N independent phosphatases (P_i). This expands upon systems previously described by Goldbeter and Koshland (18). (*B*) A kinase cascade similar to that in panel *A*, but with a single shared phosphatase *P*. (C) Fractional phosphorylation of the final substrate in the cascade as a function of r for cascades with two to five substrates. In this case, r is defined as the V_{max} of the input kinase (K in *A* and *B*) divided by the V_{max} of the phosphatase for the first substrate in the cascade (P_1 in *A*, and P in *B*). The dashed lines represent cascades with N phosphatases and the solid lines represent cascades with a single shared phosphatase. Note that the responses of cascades become exponentially more sensitive to r with increasing depth N. Cascades with a single shared phosphatase are considerably more sensitive to r compared with those with independent phosphatases. (*D*) In this case, we define a parameter, $r_{1/2}$, as the value of r in panel C at which the response of a cascade is half-maximal. For any given number of substrates, N, the $r_{1/2}$ ratio is the $r_{1/2}$ of the independent case divided by the $r_{1/2}$ of the shared case (i.e., the $r_{1/2}$ of the dashed curve in *C* divided by the $r_{1/2}$ for the solid curve). For $N = 2$, the independent case requires ~5 times as much input signal to achieve a half-maximal response; for $N = 3$, 4, and 5, the independent case requires ~13 times as much input signal.

than $N = 2$ (see Fig. 5 *C*). This increase in sensitivity is an expected outcome of amplification in signaling cascades (18,41). Additionally, models with a single, shared phosphatase show a higher degree in input sensitivity in r compared with models with independent phosphatases, but only when the substrates are present at saturating concentrations.

To quantify the changes in input sensitivity for saturating conditions, we took the ratio of the $r_{1/2}$-values for the two types of cascade at a given value of N (see Fig. 5 *D*). In the most basic cascade, with $N = 2$, the $r_{1/2}$ for the single phosphatase model is ~5 times less than that for the multiple phosphatase model. This ratio increases and plateaus for cascades with depth $N \geq 3$; in these cases, the single phosphatase models require ~13 times less signal. This occurs because the signal is able to tunnel through the shared phosphatase when the substrates are at saturating concentrations. Activation of the upstream kinases not only activates the rest of the cascade but also produces phosphorylated substrate molecules that act as phosphatase inhibitors. This reduces the effective concentration of free phosphatase available for downstream substrates, amplifying the apparent signal strength.

Kinase inhibitors

As mentioned above, there is a growing interest in developing small molecules that target and inhibit kinases as potential therapeutics for a variety of diseases (24). It is unclear, however, what kind of effects these inhibitors will have in loops with significant kinase or phosphatase crosstalk; in these cases, kinase inhibitors not only influence their targets' activity but also the concentration of other inhibitors (namely, S_2 and S_2*) in the system. We considered the impact of two separate types of inhibitors on the loops described above. Type 1 inhibitors, which are currently by far the most commonly used in practice (24), target the ATP-binding site of a specific kinase and disrupt its activity toward all of its targets. Type 2 inhibitors, on the other hand, target and disrupt a specific kinase–target interaction, leaving the kinase free to act on a subset of its other targets. Although the latter is not currently common, peptide inhibitors have been successfully used in this manner (27), and there is increasing interest in developing the capacity to inhibit specific protein-protein interactions within cells (42).

We modeled the potential effects of these inhibitors by including explicit inhibitor molecules in our loops, with I_1 and I_2 representing type 1 and type 2 inhibitors, respectively. We first considered a 1K1P loop with S_2 at saturating concentrations and in the active state ($r_1 = r_2 = 1.5$; see Fig. 2 *A*). As one would expect, adding I_1 significantly decreases S_1*, because a generic inhibitor for the kinase will clearly reduce overall phosphorylation of all targets (Fig. 6 *A*). However, even an inhibitor that is specific to S_2 decreases the phosphorylation of S_1 (Fig. 6 *A*). The specific inhibitor in this case decreases the concentration of S_2*, reducing competition for the phosphatase and thus decreasing S_1*.The effect of I_2 is not as dramatic as that of I_1 for the 1K1P loop, but this nonetheless represents a

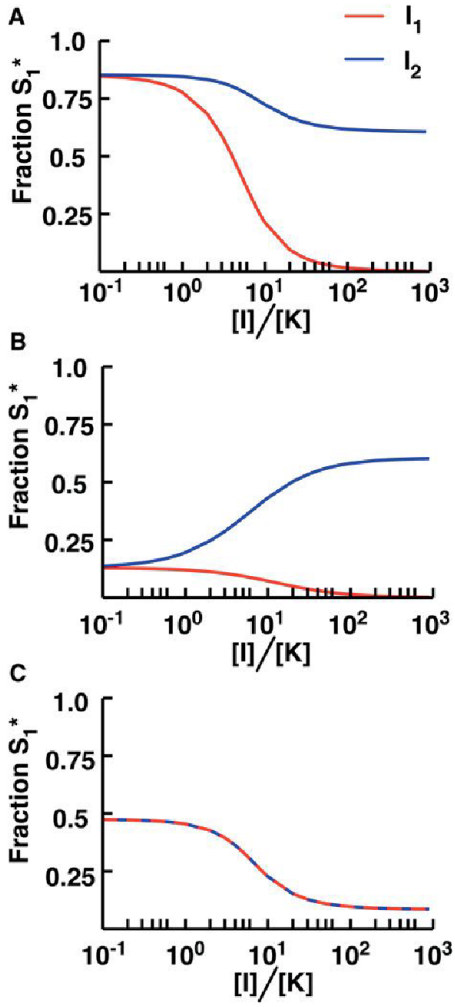

FIGURE 6 Effect of kinase inhibitors in the presence of crosstalk. (*A*) A 1K1P loop with two substrates in the presence of one of two kinase inhibitors: I_1, which prevents reactions with all targets of the kinase (*red*), or I_2, which specifically disrupts K-S_2 interactions (*blue*). We plot the fraction of phosphorylated S_1 against the ratio of $[I_1]$ or $[I_2]$ to $[K]$. In this case, $[S_1]_0 = 0.1 \times K_m$, $[S_2]_0 = 20 \times K_m$ and $r_1 = r_2 = 1.5$. Note that using either inhibitor causes a decrease in the fraction S_1*, although the effect is less pronounced with the S_2-specific inhibitor. In the latter scenario, I_2 reduces the $[S_2$*$]$, which is itself a phosphatase inhibitor for S_1*. The net effect of I_2 is thus to decrease S_1 phosphorylation. (*B*) A 1K2P loop with the same kinase inhibitors as in panel *A*. The fraction of phosphorylated S_1 is plotted against the ratio of $[I_1]$ or $[I_2]$ to $[K]$. In this case, $[S_1]_0 = 0.1 \times K_m$, $[S_2]_0 = 20 \times K_m$, $r_1 = 0.5$ and $r_2 = 1.5$. Although the general inhibitor still reduces S_1*, the specific inhibitor increases S_1*. This is because decreasing the concentration of S_2* reduces competition for the shared kinase. (*C*) A 2K1P loop in the presence of both I_1 and I_2. Note that because the kinases are independent in this case, the effects of both inhibitors are identical. The fraction of phosphorylated S_1 is plotted against the ratio of the concentrations of $[I_2]$ to $[K]$. In this case, $[S_1]_0 = 0.1 \times K_m$, $[S_2]_0 = 20 \times K_m$, $r_1 = 0.01$ and $r_2 = 1.5$. Both inhibitors decrease S_1*, as the reduction in phosphorylated S_2 due to the inhibitors reduces S_2*'s inhibition of the S_1 phosphatase reaction.

potentially unintended consequence of a (putatively) specific inhibitor.

In the 1K2P case, we find exactly the opposite behavior: whereas I_1 decreases S_1* as expected, I_2 increases the phosphorylation of the first substrate (Fig. 6 *B*). This is because the inhibitor reduces S_2 interactions with the kinase, alleviating competition. In this case, the response of the system is perhaps more intuitive: because S_2 is a competitive inhibitor of S_1 phosphorylation, inhibiting its phosphorylation in a specific way increases the capacity of S_1 to respond to signals.

In the 2K1P loop, if the two types of inhibitors are aimed at the second kinase (K_2), they have the same net effect. Because K_2 cannot act on S_1 in this model, there is no difference between an inhibitor that simply targets K_2 and one that specifically targets the K_2-S_2 interaction. When the second loop is activated by a signal and the first loop is not, the K_2 inhibitor completely abolishes S_1 phosphorylation (Fig. 6 *C*). Although the source of this behavior is clear from Fig. 4 *C*, the effect is nonetheless striking. In the absence of knowledge about the shared phosphatase (or the phenomenology of the 2K1P loop), a response like the one shown in Fig. 4 *C* might lead to the erroneous conclusion that K_2 acts directly on S_1, or that the inhibitor in this case is nonspecific.

DISCUSSION

The 1K1P and 1K2P loops discussed above (Fig. 2, *A* and *B)* represent two variations on the classic crosstalk motif, i.e., a kinase that has multiple downstream targets in different pathways. In the traditional view, the coupling between the substrates in these two loops is understood as simply arising from the fact that they will all respond to some of the same upstream signals (34). Our work reveals that a shared enzyme not only modifies each target but also can strongly couple the response of one target to that of another through competitive inhibition at the shared enzyme. For instance, if the targets in question share the same phosphatase, we find that 0^{th}-order ultrasensitivity becomes transitive; all of the targets in this case will respond in a switch-like manner to incoming signals (Fig. 3 *A*). We also find that in situations where there are a large number of substrates (Fig. 3 *B*), the system can respond ultrasensitively even if none of the targets is at a high enough concentration to elicit such a response on its own (Fig. 3 *B*). It has been shown that some kinases do in fact act on many targets (e.g., Akt, the EGF receptors, and Cdk1 (8, 9, 31, 32)), indicating that this collective saturation may represent a common mechanism for inducing ultrasensitivity without having to express any given protein target at saturating levels.

We find that the alternative variation on traditional kinase crosstalk, the 1K2P loop (Fig. 2 *B*), displays a completely different set of behaviors from those observed when the phosphatase is shared. In this case, the saturating substrate acts as a type of gatekeeper for the other substrates in the loop. Below the signal threshold at which this saturating substrate switches into the phosphorylated state, other substrates will simply be unable to respond to incoming signals, whereas above this threshold the unsaturating targets will respond in a hyperbolic manner (Fig. 4 *B*). Although direct experimental tests are currently lacking, our predictions for both 1K1P and 1K2P loops are consistent with available data (16). Overall, these findings indicate that when a particular kinase has multiple targets in multiple pathways, it is difficult to reason in general about the behavior of the system in the absence of detailed information regarding phosphatase architecture and relative saturation levels (Figs. 3 and 4).

To date, nearly all experimental characterizations of crosstalk have focused on kinases, and, to our knowledge, the potential for phosphatases to couple signaling responses on their own has not been previously considered (34). Our analysis of the 2K1P loop (Fig. 2 *C*) demonstrates that such coupling is readily achieved. Indeed, a shared phosphatase can elicit an ultrasensitive response of a target to signals from kinases that do not directly act on the target in question (Fig. 4 *C*). Furthermore, phosphatase architecture plays a role in the sensitivity of a signaling cascade. We found that cascades in which every substrate shares a common phosphatase are more responsive to input signals than cascades with independent phosphatases when the substrates are at saturating levels. Given that phosphatases are generally considered more promiscuous than kinases, this indicates that phosphatase crosstalk may be widespread in biological networks. Because the specific phosphatases that act on many targets in signaling networks are often not known (38–40), it is currently unclear to what extent phosphatase crosstalk can influence global network behavior.

Given the widespread crosstalk present in mammalian signaling networks, our work highlights the inherent difficulty of predicting a priori the effects that kinase inhibitors will have on cells. These effects ultimately will depend not only on the kinase connectivity of the network but also on the degree of saturation in the targets and the phosphatase architecture. In many cases, both of these facts are unknown—even if the intracellular concentrations of the target proteins are known, the K_m-values for kinases and (especially) phosphatases are not known, and for many signaling pathways the relevant phosphatases have not yet been identified. Understanding these details will be a crucial component of any attempt to rationally design a kinase inhibition strategy that can elicit some desired effect on some set of targets without inducing unintended decreases (or increases) in the phosphorylation levels of other proteins in the network (Fig. 6).

Ultimately, our work indicates that studies on signaling and regulatory networks need to be increasingly mindful

of the highly interconnected and interdependent structure of the networks themselves. This is especially true of phosphatases. To understand the real consequences of rampant kinase crosstalk, we clearly must obtain more reliable information about which phosphatases act on which targets, what adaptor domains they employ, etc. The findings described above also highlight the fact that individual elements of signaling networks can exhibit responses that are sensitive to the context in which the element is found. Care must be taken to ensure that this dependence on network architecture informs our interpretation and understanding of how networks function and interact with each other.

SUPPORTING MATERIAL

Additional equations, results, and reference (43) are available at http://www.biophysj.org/biophysj/supplemental/S0006-3495(12)01109-5 .

The authors thank Tom Kolokotrones, Van Savage, Dan Yamins, Javier Apfeld, Catalina Romero, Nick Stroustrup, and Deborah Marks for many helpful discussions. We thank Ryan Suderman, Dustin Maurer, and Zaikun Xu for their comments on the manuscript.

REFERENCES

1. Mayer, B. J., M. L. Blinov, and L. M. Loew. 2009. Molecular machines or pleiomorphic ensembles: signaling complexes revisited. *J. Biol.* 8:81.
2. Thomson, M., and J. Gunawardena. 2009. Unlimited multistability in multisite phosphorylation systems. *Nature.* 460:274–277.
3. Danielpour, D., and K. Song. 2006. Cross-talk between IGF-I and TGF-β signaling pathways. *Cytokine Growth Factor Rev.* 17:59–74.
4. Hill, S. M. 1998. Receptor crosstalk: communication through cell signaling pathways. *Anat. Rec.* 253:42–48.
5. Javelaud, D., and A. Mauviel. 2005. Crosstalk mechanisms between the mitogen-activated protein kinase pathways and Smad signaling downstream of TGF-β: implications for carcinogenesis. *Oncogene.* 24:5742–5750.
6. Junttila, M. R., S. P. Li, and J. Westermarck. 2008. Phosphatase-mediated crosstalk between MAPK signaling pathways in the regulation of cell survival. *FASEB J.* 22:954–965.
7. Liu, Q. H., and P. A. Hofmann. 2004. Protein phosphatase 2A-mediated cross-talk between p38 MAPK and ERK in apoptosis of cardiac myocytes. *Am. J. Physiol. Heart Circ. Physiol.* 286:H2204–H2212.
8. Brazil, D. P., and B. A. Hemmings. 2001. Ten years of protein kinase B signalling: a hard Akt to follow. *Trends Biochem. Sci.* 26:657–664.
9. MacBeath, G. 2002. Protein microarrays and proteomics. *Nat. Genet.* 32 (*Suppl*):526–532.
10. Virshup, D. M., and S. Shenolikar. 2009. From promiscuity to precision: protein phosphatases get a makeover. *Mol. Cell.* 33:537–545.
11. Eliceiri, B. P. 2001. Integrin and growth factor receptor crosstalk. *Circ. Res.* 89:1104–1110.
12. Gomez-Uribe, C., G. C. Verghese, and L. A. Mirny. 2007. Operating regimes of signaling cycles: statics, dynamics, and noise filtering. *PLOS Comput. Biol.* 3:e246.
13. Behar, M., H. G. Dohlman, and T. C. Elston. 2007. Kinetic insulation as an effective mechanism for achieving pathway specificity in intracellular signaling networks. *Proc. Natl. Acad. Sci. USA.* 104:16146–16151.
14. Kim, Y., Z. Paroush, …, S. Y. Shvartsman. 2011. Substrate-dependent control of MAPK phosphorylation in vivo. *Mol. Syst. Biol.* 7:467.
15. McClean, M. N., A. Mody, …, S. Ramanathan. 2007. Cross-talk and decision making in MAP kinase pathways. *Nat. Genet.* 39:409–414.
16. Kim, S. Y., and J. E. Ferrell, Jr. 2007. Substrate competition as a source of ultrasensitivity in the inactivation of Wee1. *Cell.* 128:1133–1145.
17. Belle, A., A. Tanay, …, E. K. O'Shea. 2006. Quantification of protein half-lives in the budding yeast proteome. *Proc. Natl. Acad. Sci. USA.* 103:13004–13009.
18. Goldbeter, A., and D. E. Koshland, Jr. 1981. An amplified sensitivity arising from covalent modification in biological systems. *Proc. Natl. Acad. Sci. USA.* 78:6840–6844.
19. Bagowski, C. P., J. Besser, C. R. Frey, and J. E. Ferrell, Jr. 2003. The JNK cascade as a biochemical switch in mammalian cells: ultrasensitive and all-or-none responses. *Curr. Biol.* 13:315–320.
20. Hardie, D. G., I. P. Salt, …, S. P. Davies. 1999. AMP-activated protein kinase: an ultrasensitive system for monitoring cellular energy charge. *Biochem. J.* 338:717–722.
21. Huang, C. Y., and J. E. Ferrell, Jr. 1996. Ultrasensitivity in the mitogen-activated protein kinase cascade. *Proc. Natl. Acad. Sci. USA.* 93: 10078–10083.
22. LaPorte, D. C., and D. E. Koshland, Jr. 1983. Phosphorylation of isocitrate dehydrogenase as a demonstration of enhanced sensitivity in covalent regulation. *Nature.* 305:286–290.
23. Meinke, M. H., J. S. Bishop, and R. D. Edstrom. 1986. Zero-order ultrasensitivity in the regulation of glycogen phosphorylase. *Proc. Natl. Acad. Sci. USA.* 83:2865–2868.
24. Zhang, J., P. L. Yang, and N. S. Gray. 2009. Targeting cancer with small molecule kinase inhibitors. *Nat. Rev. Cancer.* 9:28–39.
25. Hindmarsh, A. C., P. N. Brown, …, C. S. Woodward. 2005. SUNDIALS: suite of nonlinear and differential/algebraic equation solvers. *ACM Trans. Math. Software.* 31:363–396.
26. Khandelwal, R. L., J. R. Vandenheede, and E. G. Krebs. 1976. Purification, properties, and substrate specificities of phosphoprotein phosphatase(s) from rabbit liver. *J. Biol. Chem.* 251:4850–4858.
27. Radhakrishnan, Y., W. H. Busby, Jr., …, D. R. Clemmons. 2010. Insulin-like growth factor-I-stimulated insulin receptor substrate-1 negatively regulates Src homology 2 domain-containing protein-tyrosine phosphatase substrate-1 function in vascular smooth muscle cells. *J. Biol. Chem.* 285:15682–15695.
28. Voet, D., and J. G. Voet. 2011. Biochemistry. John Wiley & Sons, Hoboken, NJ.
29. Gunawardena, J. 2005. Multisite protein phosphorylation makes a good threshold but can be a poor switch. *Proc. Natl. Acad. Sci. USA.* 102:14617–14622.
30. Markevich, N. I., J. B. Hoek, and B. N. Kholodenko. 2004. Signaling switches and bistability arising from multisite phosphorylation in protein kinase cascades. *J. Cell Biol.* 164:353–359.
31. Ubersax, J. A., E. L. Woodbury, …, D. O. Morgan. 2003. Targets of the cyclin-dependent kinase Cdk1. *Nature.* 425:859–864.
32. Ptacek, J., G. Devgan, …, M. Snyder. 2005. Global analysis of protein phosphorylation in yeast. *Nature.* 438:679–684.
33. Kaushansky, A., A. Gordus, …, G. MacBeath. 2008. System-wide investigation of ErbB4 reveals 19 sites of Tyr phosphorylation that are unusually selective in their recruitment properties. *Chem. Biol.* 15:808–817.
34. Hunter, T. 2007. The age of crosstalk: phosphorylation, ubiquitination, and beyond. *Mol. Cell.* 28:730–738.
35. Arena, S., S. Benvenuti, and A. Bardelli. 2005. Genetic analysis of the kinome and phosphatome in cancer. *Cell. Mol. Life Sci.* 62:2092–2099.
36. Manning, G., D. B. Whyte, …, S. Sudarsanam. 2002. The protein kinase complement of the human genome. *Science.* 298:1912–1934.
37. Walsh, C. 2006. Posttranslational Modification of Proteins: Expanding Nature's Inventory. Roberts and Co. Publishers, Greenwood Village, CO.

38. Kholodenko, B. N. 2000. Negative feedback and ultrasensitivity can bring about oscillations in the mitogen-activated protein kinase cascades. *Eur. J. Biochem.* 267:1583–1588.

39. Schoeberl, B., C. Eichler-Jonsson, …, G. Müller. 2002. Computational modeling of the dynamics of the MAP kinase cascade activated by surface and internalized EGF receptors. *Nat. Biotechnol.* 20: 370–375.

40. Shao, D., W. Zheng, …, C. Tang. 2006. Dynamic studies of scaffold-dependent mating pathway in yeast. *Biophys. J.* 91:3986–4001.

41. Nelson, D. L., A. L. Lehninger, and M. M. Cox. 2008. Lehninger Principles of Biochemistry. W.H. Freeman, New York.

42. Wells, J. A., and C. L. McClendon. 2007. Reaching for high-hanging fruit in drug discovery at protein-protein interfaces. *Nature.* 450: 1001–1009.

43. Wolfram Research. 2010. Mathematica. Wolfram Research, Champaign, IL.

44. Loog, M., and D. O. Morgan. 2005. Cyclin specificity in the phosphorylation of cyclin-dependent kinase substrates. *Nature.* 434:104–108.

45. Yan, Z., S. A. Fedorov, …, R. S. Williams. 2000. PR48, a novel regulatory subunit of protein phosphatase 2A, interacts with Cdc6 and modulates DNA replication in human cells. *Mol. Cell. Biol.* 20: 1021–1029.

46. Woodbury, E. L., and D. O. Morgan. 2007. Cdk and APC activities limit the spindle-stabilizing function of Fin1 to anaphase. *Nat. Cell Biol.* 9:106–112.

47. Bloom, J., I. M. Cristea, …, F. R. Cross. 2011. Global analysis of Cdc14 phosphatase reveals diverse roles in mitotic processes. *J. Biol. Chem.* 286:5434–5445.

48. Matheos, D., M. Metodiev, …, M. D. Rose. 2004. Pheromone-induced polarization is dependent on the Fus3p MAPK acting through the formin Bni1p. *J. Cell Biol.* 165:99–109.

49. Enserink, J. M., and R. D. Kolodner. 2010. An overview of Cdk1-controlled targets and processes. *Cell Div.* 5:11.

Live-Cell Fluorescence Microscopy with Molecular Biosensors: What Are We Really Measuring?

Jason M. Haugh*
Department of Chemical and Biomolecular Engineering, North Carolina State University, Raleigh, North Carolina

ABSTRACT Engineered protein biosensors, such as those based on Förster resonance energy transfer, membrane translocation, or solvatochromic shift, are being used in combination with live-cell fluorescence microscopy to reveal kinetics and spatial localization of intracellular processes as they occur. Progress in the application of this approach has been steady, yet its general suitability for quantitative measurements remains unclear. To address the pitfalls of the biosensor approach in quantitative terms, simple reaction-diffusion models were analyzed. The analysis shows that although high-affinity molecular recognition allows robust detection of the fluorescence readout, either of two detrimental effects is fostered. Binding of an intramolecular biosensor or of a relatively abundant intermolecular biosensor introduces observer effects in which the dynamics of the target molecule under study are significantly perturbed, whereas binding of a sparingly expressed intermolecular biosensor is subject to a saturation effect, where the pool of unbound biosensor is significantly depleted. The analysis explores how these effects are manifest in the kinetics and spatial gradients of the biosensor-target complex. A sobering insight emerges: the observer or saturation effect is always significant; the question is whether or not it can be tolerated or accounted for. The challenge in managing the adverse effects is that specification of the biosensor-target affinity to within a certain order of magnitude is required.

INTRODUCTION

If our mechanistic understanding of cell regulation is to dramatically advance, existing methods for quantifying concentrations and activity states of intracellular molecules will need to be improved, and new ones will need to be developed. Although biochemical assays are commonly used and can be quantitative if performed carefully, these methods offer no direct information about cell-to-cell heterogeneity or subcellular localization. Other methods, such as flow cytometry and immunofluorescence, address one or both of these issues but are nonetheless end-point assays with respect to kinetics. In contrast, live-cell microscopy uniquely elucidates spatiotemporal dynamics of intracellular processes in real-time and at the single-cell level, i.e., in conjunction with observations of cell behavior (1–4).

Two distinct variations of this method have been used extensively:

In the first, a full-length protein or other molecule found in the cell is tagged with a fluorescent protein or dye, and the subcellular localization of the conjugate is monitored by various modes of fluorescence microscopy (5). We may refer to this as the "biomarker approach". This approach has been successfully (and cleverly) applied to elucidate quantitative aspects of cytoskeletal and focal adhesion dynamics (for example, Danuser and Waterman-Storer (6) and Kolin and Wiseman (7)); however, it has certain limitations. Biomarkers indicate dynamic localization of the tagged molecule but not changes in its activity or modification states. Moreover, the subcellular localization of a protein is often affected by multiple factors (protein-protein and protein-lipid interactions and posttranslational modifications), in which case the measurement is challenging to interpret from a molecular standpoint.

The second variation strives to overcome those limitations through the introduction of an engineered fluorescent probe or protein construct that possesses minimal molecular recognition. We refer to this as the "biosensor approach". By engaging in a specific binding interaction to form a noncovalent complex, the biosensor yields a fluorescence readout that is meant to indicate the state or abundance of a particular target. In early applications of the biosensor approach, fluorescent probes were developed to measure intracellular concentrations of small molecules, most notably calcium and cAMP. Protein domains and motifs have since been used to distinguish between activity or modification states of protein and lipid targets (8). Irrespective of the molecular details, intracellular biosensors may be classified as either intramolecular, where the molecular recognition element and its target are contained within the same chain (connected by a flexible linker), or intermolecular, where the recognition module binds to form a bimolecular complex with a target that is endogenous to the cell (Fig. 1) (9,10). Biosensors of the first type include those based on intramolecular Förster resonance energy transfer, with donor and acceptor fluorophores flanking the two ends of the chain; this approach has been applied most prominently to study signaling mediated by small GTPases (11–14) and protein kinases (15–20). Intermolecular biosensors include those based on membrane translocation (21–26) or solvent-sensitive fluorescence (27,28).

The biosensor approach is not without its own limitations. As of this writing, there are only a small number of validated biosensors, as compared with the broad palette of antibodies

Submitted January 3, 2012, and accepted for publication March 23, 2012.

*Correspondence: jason_haugh@ncsu.edu

Editor: David Odde.

0006-3495/12/05/2003/9 $2.00

doi: 10.1016/j.bpj.2012.03.055

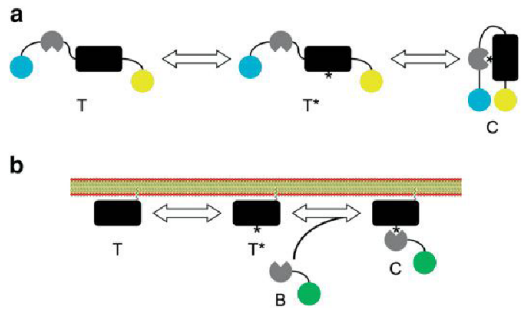

FIGURE 1 Two general classes of molecular biosensors. (*a*) An intramolecular biosensor contains both the target and molecular recognition element, connected by a linker. The inactive target T is activated by an endogenous intracellular process to produce the active, unoccupied target T^*; the activated state is bound by the molecular recognition element to form the complex C, generating the biosensor readout. (*Illustration*) Common scenario where intramolecular binding brings a Förster resonance energy transfer pair into close proximity. (*b*) An intermolecular biosensor, B, contains a molecular recognition element that binds to an endogenous target to form a bimolecular complex, C. (*Illustration*) Common scenario where complex formation results in membrane translocation of the tagged biosensor.

available. More critically, the biosensor readout cannot perfectly report the intracellular process being studied. The ideal condition may be stated thus: the biosensor-based measurement ought to be proportional to the target concentration (at any given time and intracellular location) that would have been present if molecular recognition by the biosensor did not occur. To the uninitiated observer, this might seem to be a reasonable assumption; however, it presents a clear paradox. Without molecular recognition, there is no signal, but formation of the complex masks the active target from deactivating enzymes and endogenous effectors. This issue, an example of the observer effect in physics, is endemic to the biosensor approach.

Although the general nature of the problem is intuitive and has been recognized for some time (29,30), the following questions have not been addressed in detail:

First, in what specific ways does the biosensor readout deviate from the ideal response?

Second, for each of those, how does the severity of the problem depend on the properties of the biosensor and of the system under study?

Finally, how and to what extent might those issues be avoided while also allowing for a reliably detectable signal?

Answers are provided here through the analysis of simple reaction-diffusion models.

MATERIALS AND METHODS

Model equations

It is supposed that the fluorescence readout is directly related to the local concentration (or, in the case of a membrane-associated species, the area density) of a biosensor complex, C. The key assumption is that the complex is sequestered and thus shielded from participating in other reactions. Thus, the conservation of the complex is governed by net diffusion (advective or motor-driven transport could be added if warranted) and binding as follows:

$$\frac{\partial C}{\partial t} = D_C \nabla^2 C + v_{bind}. \tag{1}$$

The rate term v_{bind} accounts for reversible binding, and two scenarios are considered: intramolecular and intermolecular binding (Fig. 1). In the intramolecular case, the target species is fused with the biosensor, and once activated, the biosensor transitions reversibly between activated and unbound (T^*) and bound (C) forms. In the intermolecular case, the T^* species forms a complex with a fluorescent biosensor (local concentration $[B]$) to form C. According to mass action,

$$v_{bind} = \begin{cases} k_{on}T^* - k_{off}C, & \text{intramolecular;} \\ k_{on}[B]T^* - k_{off}C, & \text{intermolecular.} \end{cases} \tag{2}$$

In both cases, the free target becomes available via an activation process, $T \rightarrow T^*$, with local rate v_{act}. Activation is reversed via deactivation with local rate v_{deact}. A more complete model would additionally account for target interactions with endogenous binding partners. With the common assumption of slow synthesis and turnover rates, the balances for the inactive and active target forms are as follows:

$$\frac{\partial T}{\partial t} = D_T \nabla^2 T - v_{act} + v_{deact}, \tag{3}$$

$$\frac{\partial T^*}{\partial t} = D_{T^*} \nabla^2 T^* + v_{act} - v_{deact} - v_{bind}. \tag{4}$$

The simplest plausible rate laws for v_{act} and v_{deact} were assumed as follows:

$$v_{act} = k_{act} S(t,x) T, \tag{5}$$

$$v_{deact} = k_{deact} T^*. \tag{6}$$

Thus, the temporal or spatial dependence of the response is driven by a case-specific signal function, $S(t,x)$.

In the intermolecular case, the conservation of the free biosensor must also be accounted for, and in so doing one would need to consider whether complex formation occurs in the same cellular compartment or involves translocation of the biosensor from the cytosol to a membrane surface (m). The latter is assumed to be the case here; further assuming slow synthesis and turnover of the biosensor,

$$\frac{\partial [B]}{\partial t} = D_B \nabla^2 [B]; \quad D_B (\mathbf{n} \cdot \nabla [B])\big|_m = v_{bind}\big|_m. \tag{7}$$

Note that in Eq. 7 and in Eq. 8 below, conversion between numbers of molecules and moles as needed is implicit.

For analysis, models are often simplified by assuming well-mixed compartments (as in Figs. 2–4). In that case, the diffusion terms in Eqs. 1, 3, and 4 are neglected, and Eq. 7 reduces to

$$\begin{aligned} \frac{d[B]}{dt} &= -\frac{A_{mem}}{V_{cyt}} v_{bind}, \\ [B](t) &= [B]_0 - \frac{A_{mem}}{V_{cyt}} C(t), \end{aligned} \tag{8}$$

where A_{mem}/V_{cyt} is the ratio of the membrane surface area divided by the volume of cytosol, and $[B]_0$ is the free biosensor concentration when no active target is present.

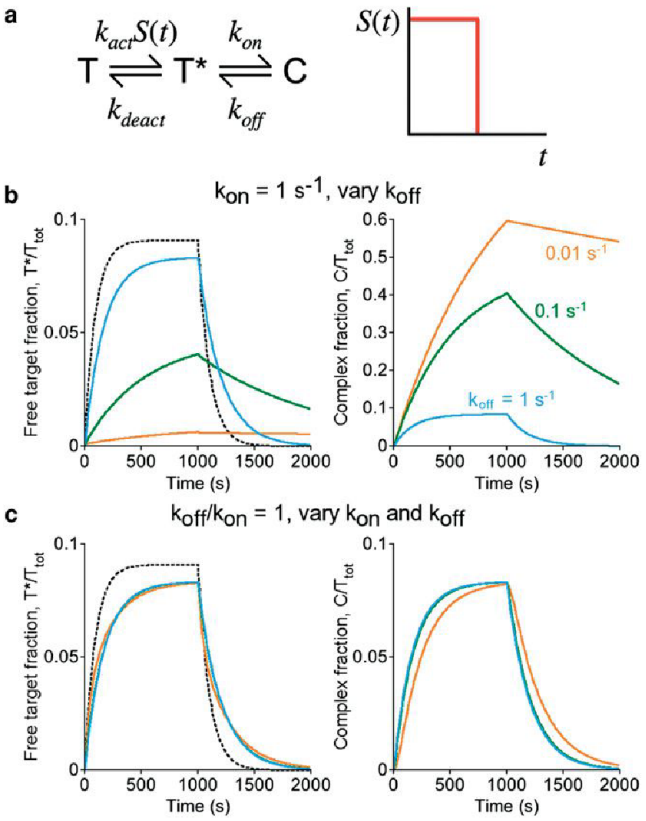

FIGURE 2 Perturbation of active target level and kinetics: intramolecular biosensors, or intermolecular biosensors expressed in stoichiometric excess. (*a*) Kinetic scheme for an intramolecular biosensor, following the nomenclature established in Fig. 1 *a*; the scheme holds equally for an intermolecular biosensor expressed in excess ([*B*] ≈ constant). In the hypothetical scenario, stimulation ($S = 1$) is pulsed for a period of 1000 s. (*b*) The fractions of the total biosensor pool in the free, active target (*T**, *left*) and complexed (*C*, *right*) states are plotted as a function of time. The affinity of the molecular recognition element was adjusted by progressively decreasing the dissociation rate constant k_{off}, as indicated: $k_{off} = 1$ s^{-1}, 0.1 s^{-1}, or 0.01 s^{-1}. (*Dashed curve*) Active target kinetics in the absence of complex formation ($k_{off} = \infty$). Other parameter values were fixed at $k_{on} = 1$ s^{-1}, $k_{act} = 0.001$ s^{-1}, and $k_{deact} = 0.01$ s^{-1}. (*c*) Same as panel *b*, except that the ratio of k_{off}/k_{on} was fixed at 1, with $k_{off} = k_{on} = 1$ s^{-1}, 0.1 s^{-1}, or 0.01 s^{-1}.

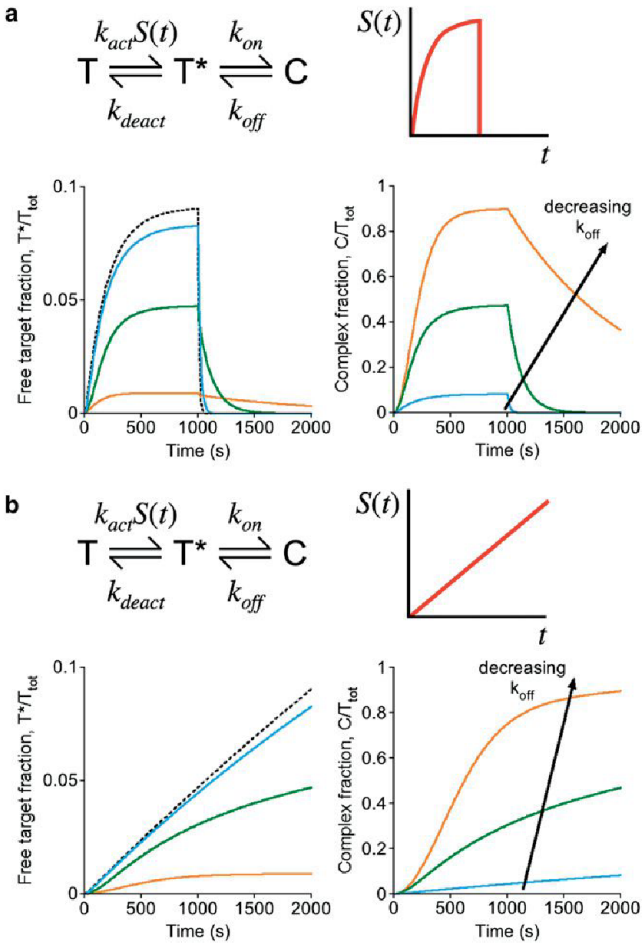

FIGURE 3 Response of an intramolecular biosensor to gradually changing input. (*a*) Assuming the kinetic scheme depicted for an intramolecular biosensor, the scenario presented in Fig. 2 was altered so that the activation of the target during the first 1000 s is more gradual, with $S(t) = 1 - \exp(-0.005t)$ (t in s). The fractions of the total biosensor pool in the free, active target (*T**, *left*) and complexed (*C*, *right*) states are plotted as a function of time. The affinity of the biosensor was adjusted by progressively decreasing the dissociation rate constant k_{off}: $k_{off} = 1$ s^{-1}, 0.1 s^{-1}, or 0.01 s^{-1}. Other parameter values were fixed at $k_{on} = 1$ s^{-1}, $k_{act} = 0.01$ s^{-1}, and $k_{deact} = 0.1$ s^{-1}. (*b*) Same as panel *a*, except that the stimulation was assumed to follow a linear ramp, with $S(t)$ reaching a value of 1 at $t = 2000$ s.

Model implementation

Models were implemented in the Virtual Cell software environment (www.vcell.org) (31) and are publicly accessible under the BioModel "Biosensor simple". For all models, values of the rate constants are specified in the corresponding figure caption. In Figs. 2, 4, and 5, the value of k_{deact} was set at 0.01 s^{-1}, consistent with a signaling state lifetime of ~1 min (e.g., Schneider and Haugh (32)). In Fig. 3, a 10-fold higher value ($k_{deact} = 0.1$ s^{-1}) was considered.

For well-mixed compartmental models (Figs. 2–4), the cytosol was assigned a reasonable volume of 1.667 pL = 1667 μm^3, such that a concentration of 1 μM corresponds to 10^6 molecules in that volume; the plasma membrane was assigned an area of 1000 μm^2.

In models accounting for spatial gradients (Fig. 5), the spatial domain is a thin rectangle with length $L = 100$ μm (typical length scale for a fully spread and polarized fibroblast) and height = 3.4 μm (to approximately match the A_{mem}/V_{cyt} ratio assumed in the compartmental model calculations). A spatially focused stimulus is applied, confined to the small domain $x \in (0,0.01L)$; under these conditions, the problem is effectively one-dimensional with a point source at one end. Typical effective diffusivity values were assigned, with $D_B = 30$ μm^2/s for the biosensor in the cytosol and $D_T = D_{T^*} = D_C = 0.5$ μm^2/s for all membrane species. For numerical implementation, grid spacings of 0.05 and 0.1 μm were used, yielding approximately identical results.

RESULTS AND DISCUSSION

Biosensor binding generally reduces the availability of the active target and slows down its kinetics of accumulation and clearance

We consider the common situation where the active target molecule of interest is not subject to deactivation while it

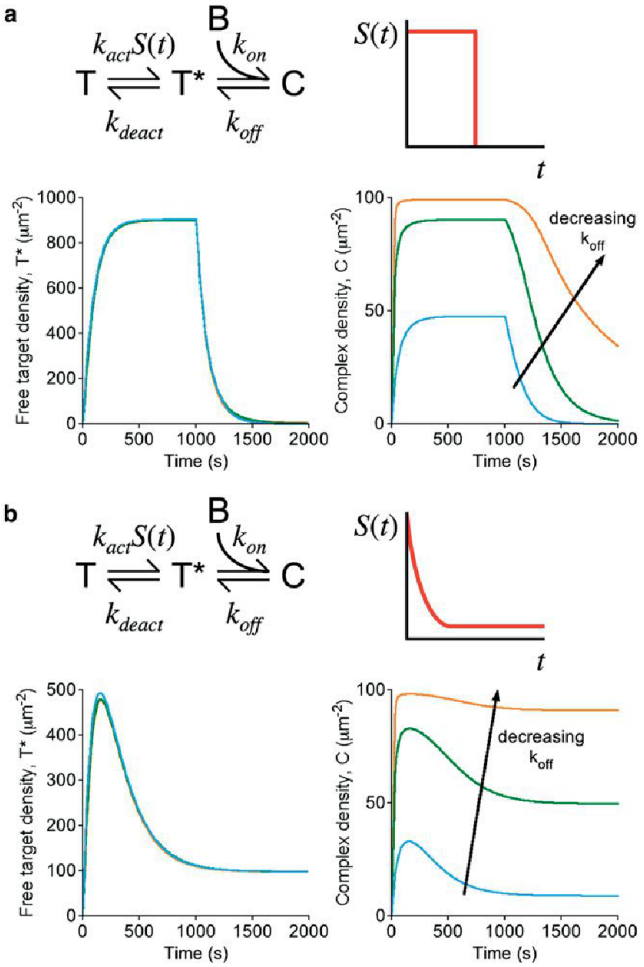

FIGURE 4 Saturation of the biosensor readout: intermolecular biosensors with active target in excess. (*a*) Assuming the kinetic scheme depicted for an intermolecular biosensor, applying the nomenclature established in Fig. 1 *b*, stimulation ($S = 1$) is pulsed for a period of 1000 s. The membrane densities of the free, active target (T^*, *left*) and target-biosensor complexes (C, *right*) are plotted as a function of time. The affinity of the biosensor was adjusted by progressively decreasing the dissociation rate constant k_{off}: $k_{off} = 1\ s^{-1}$, $0.1\ s^{-1}$, or $0.01\ s^{-1}$. Other parameter values were fixed at $T(0) = 10^4\ \mu m^{-2}$, $[B]_0 = 0.1\ \mu M$, $k_{on} = 1\ \mu M^{-1}\ s^{-1}$, $k_{act} = 0.001\ s^{-1}$, and $k_{deact} = 0.01\ s^{-1}$. (*b*) Same as panel *a*, except that the stimulation was assumed to follow incomplete adaptation according to $S(t) = 0.1 + 0.9\exp(-0.005t)$ (t in s).

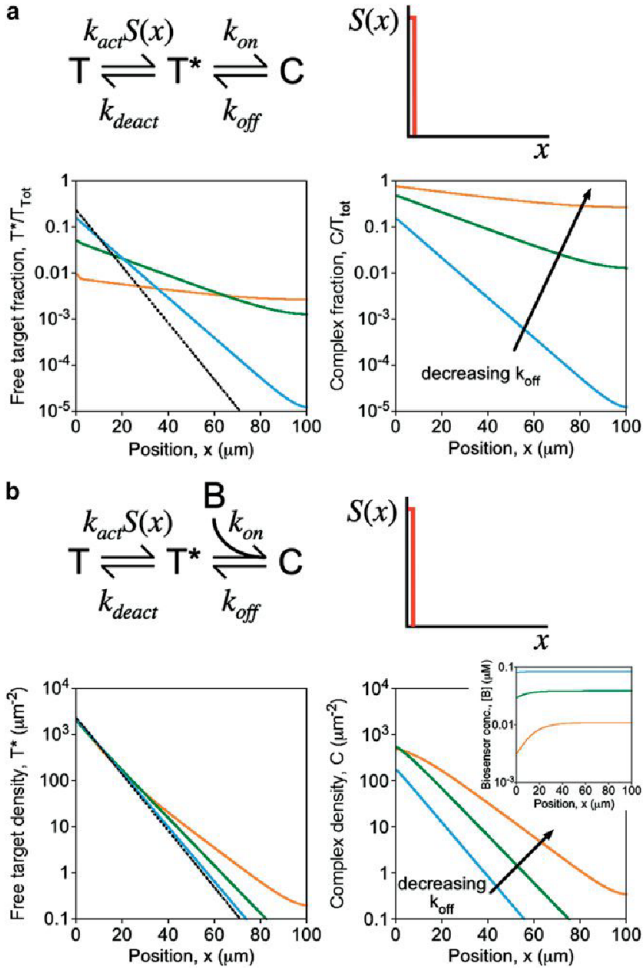

FIGURE 5 Actual or apparent blurring of spatial gradients. Stimulation is focused in a small region at one end of the cell, and concentration profiles were calculated at steady state. To aid in the evaluation of relative gradient steepness, all concentration profiles are presented as semilog plots. (*a*) Assuming the kinetic scheme depicted for an intramolecular biosensor, the steady-state fractions of the total biosensor pool in the free, active target (T^*, *left*) and complexed (C, *right*) states are plotted as a function of position. The affinity of the molecular recognition element was adjusted by progressively decreasing the dissociation rate constant k_{off}: $k_{off} = 1\ s^{-1}$, $0.1\ s^{-1}$, or $0.01\ s^{-1}$. (*Dashed curve*) Active target kinetics in the absence of complex formation ($k_{off} = \infty$). Other parameter values were fixed at $k_{on} = 1\ s^{-1}$ and $k_{deact} = 0.01\ s^{-1}$. (*b*) Same as panel *a*, except that the kinetic scheme depicted for an intermolecular biosensor was assumed, with $T(x,0) = 10^4\ \mu m^{-2}$, $[B]_0 = 0.1\ \mu M$, and $k_{on} = 1\ \mu M^{-1}\ s^{-1}$. (*Inset*) Associated concentration profiles of the free biosensor, $[B](x)$.

is sequestered in the biosensor complex. For example, at least by all contemporary accounts, recognition of phosphorylated molecules precludes access by phosphatases (33), and binding of effectors to active small GTPases hinders GTP hydrolysis (34–36). To illustrate how this impacts the biosensor output, a simple yet reasonable model of target activation and deactivation is imposed (Fig. 2 *a*): a step pulse of an external signal turns activation on and off, and the rates of activation and deactivation are linear with respect to substrate concentrations. For now, the model is further simplified by supposing that complex formation is intramolecular. As shown in Fig. 2 *b*, progressively increasing the affinity of the biosensor complex results in: 1), reduction of the free target concentration at steady state, and 2), increasingly sluggish kinetics relative to the scenario where the complex does not form. The extent of the former effect depends on the extent of activation in the absence of biosensor binding. Thus, for the scenario where as much as half of the active form is in the biosensor complex ($C = T^*$), but most target molecules remain inactive at steady state ($T = 10T^*$; Fig. 2 *b*, *cyan curves*), the steady-state value of T^* is reduced by only a modest percentage. By comparison, the effect on kinetics is more direct; if half of the active

form is sequestered ($k_{on} = k_{off}$), for example, then the characteristic time to reach steady state is prolonged by roughly a factor of two. As shown in Fig. 2 *c* (*orange curves*), additional sluggishness of the biosensor readout begins to appear if the timescales of biosensor complex association and dissociation are not significantly faster than that of target deactivation.

The more intuitive of these effects is the tendency of complex formation to buffer the active target concentration at steady state. The less appreciated but more consistently detrimental effect as shown by the calculations concerns the transient kinetics, as during the response of the system to external stimulation. When the concentration of free target is increasing, the net formation of the complex reduces the rate of free target accumulation (that is, makes it less positive). Conversely, when the concentration of free target is decreasing, the net dissociation of the complex slows the rate of decline (makes it less negative). Thus, complex formation generally causes the system to respond more sluggishly. The adequacy of a biosensor hinges, in part, on the mildness or severity of these effects under various conditions.

The calculations described above effectively assume instantaneous on- and off-states for the upstream signal, $S(t)$. This scenario approximates rapid, receptor-mediated activation followed by rapid, pharmacological inhibition, as considered previously (32,37). In many other situations, the dynamics of $S(t)$ might be relatively slow on the timescale of the mean lifetime of T^*, $1/k_{deact}$, in which case the ideal biosensor would faithfully track the kinetics of $S(t)$. To evaluate this situation, an alternate scenario in which $S(t)$ increases and approaches a plateau gradually, followed by rapid inhibition of S, was considered (Fig. 3 *a*). To ensure that the biosensor could more readily respond to changes in $S(t)$, higher values of k_{act} and k_{deact} were used here. Although the biosensor response, $C(t)$, is predicted to be robust and roughly matches the timescale of $S(t)$, the decay of the system after rapid inhibition is slowed dramatically for $k_{on}/k_{off} >> 1$ (Fig. 3 *a*). This disparity between the kinetics of the stimulation and inhibition phases of the hypothetical experiment is consistent with measured kinetics of the c-Jun N-terminal kinase activation reporter (20).

Whereas the $C(t)$ kinetics in the stimulation phase qualitatively reflect those of $S(t)$, quantitative correspondence between the two was found to suffer when $k_{on}/k_{off} >> 1$. To show this definitively, a different scenario was considered in which $S(t)$ increases as a slow, linear ramp (Fig. 3 *b*). As expected, the biosensor response $C(t)$ deviates perceptibly from linearity for high k_{on}/k_{off}. Analysis of the system shows that two effects influence the fidelity of the biosensor response. At short times, the rate of biosensor response is affected according to how severely complex formation prolongs the mean lifetime of the active target, which is approximately equal to $(1 + k_{on}/k_{off})/k_{deact}$. At long times, fidelity is limited by the availability of the unbound target when most of the biosensor is driven into the bound state.

From a mathematical point of view, these analyses of intramolecular complex formation hold equally for intermolecular complex formation with the biosensor in vast excess (with k_{on} replaced by $k_{on}[B]$, where the free biosensor concentration $[B]$ is approximately constant); however, from a biological point of view, it is important to distinguish the two. In the case of an intramolecular biosensor, the active target is a part of the biosensor itself. Therefore, high-affinity complex formation does not have a direct impact on the endogenous biology (although indirect effects via sequestration of activating/deactivating enzymes and endogenous effectors, beyond the analysis presented here, should be considered). By comparison, an intermolecular biosensor expressed at excessive levels has a buffering effect that not only affects the kinetics of the biosensor readout; more critically, it can act as a dominant negative in terms of biological function.

Suggestive of such a buffering condition, Yip et al. (39) reported that a carcinoma cell line with heterologously expressed Btk pleckstrin homology (PH) domain, which binds to the plasma membrane lipid PtdIns(3,4,5)P_3 with high affinity ($K_D = 80$ nM (38)), showed a dramatic increase in the half-life of PtdIns(3,4,5)P_3 under otherwise rapid turnover conditions (39). Tagged Btk PH domain has been employed as an intermolecular biosensor because of its unique specificity for PtdIns(3,4,5)P_3 relative to PtdIns(3,4)P_2 (30); however, because of its high affinity, the Btk PH domain can be expected to perturb free PtdIns(3,4,5)P_3 levels and kinetics when expressed at excessive levels in cells.

With intermolecular binding, excess biosensor can affect free target kinetics, whereas excess target can result in a saturated readout

In the previous section, we considered situations in which the fluorescent biosensor is not stoichiometrically limiting for complex formation. The opposite situation, which is relevant only to intermolecular binding, arises when the target molecule is in vast excess and the biosensor affinity is sufficiently high (K_D sufficiently low), such that nearly all of the biosensor molecules in the cell are in complex. This scenario is illustrated for two simple models of target activation: 1), a transient pulse (as in Fig. 2), and 2), a decay with incomplete adaptation. Both sets of associated calculations show that as the active target progressively depletes the limiting pool of available biosensor, the free target is not significantly perturbed; however, the biosensor readout does not quantitatively reflect the free target kinetics. The pulsed activation case (Fig. 4 *a*) illustrates that the increase in complex formation after stimulation approaches steady state faster than does the free target, because the concentration of available biosensor is initially much higher than its steady-state value. Conversely, after activation is turned

off, the decay of the complex is relatively sluggish, as the liberation of free biosensor counterbalances the decay of free target concentration. The incomplete adaptation case (Fig. 4 *b*) further illustrates that the change in the abundance of the complex (the apparent degree of adaptation) tends to be more modest than the actual change in free target concentration. In the limit of near-complete depletion of available biosensor (Fig. 4 *b*, *orange curves*), the adaptation kinetics of the target would be missed completely.

These calculations demonstrate that, when an intermolecular biosensor is limiting for complex formation, perturbation of the free target accumulation or clearance kinetics is minimal. Rather, the issue is that formation of the complex is saturated and thus serves as a poor quantitative readout. A prominent example of the saturation effect is the binding of tagged PLCδ PH domain, which binds the plasma membrane lipid PtdIns(4,5)P_2. In many cells at least, PtdIns(4,5)P_2 is quite abundant; its characteristic concentration on a whole-cell basis has been estimated at 10 μM, which is much higher than the measured biosensor K_D of 2 μM (40). Hence, it is widely appreciated that tagged PLCδ PH tends to be mostly in complex with PtdIns(4,5)P_2 (or with the soluble hydrolysis product, Ins(1,4,5)P_3, in the cytosol) (40), and thus the membrane-localized fluorescence in cells is insensitive to treatments that partially reduce the level of PtdIns(4,5)P_2 by inhibition of its resynthesis (24).

A spatial gradient of free target is made (or appears to be made) less steep as a consequence of biosensor complex formation

The spatial range (or dynamic length scale) of an active chemical species is defined by how far it diffuses on average before reverting to the inactive state. If biosensor-target complexes are not subject to deactivation, it follows from the intuition developed above that the spatial range of the active target would be extended when a significant fraction of it is bound. Thus, formation of the complex makes the active target gradient shallower than it would have been in the absence of binding. This effect has been recognized and discussed in the context of fluorescent biosensors (41), and calculations show that it is relevant to the case of an intramolecular biosensor with high-affinity binding (or an intermolecular biosensor with biosensor in excess) (Fig. 5 *a*). In the simplified scenario assumed here, a one-dimensional, steady-state gradient is formed via constant activation within a thin strip located at one end of the spatial domain and deactivation throughout. In the absence of complex formation, the concentration profile of the active target is approximately exponential, with a spatial decay constant that scales as the square root of k_{deact}. Therefore, with an intramolecular biosensor, the steepness of the active target gradient (the negative slope of the gradient on a semi-log plot) is affected according to the fraction of the active form that is sequestered. For example, 50% sequestration ($C = T^*$) increases the spatial range of the target and thus decreases the steepness of its gradient by a factor of roughly square-root of 2 (Fig. 5 *a*; compare the *cyan* and *black curves*). In more extreme cases, the spatial range is comparable to the cell length, and reflection at the distal boundary tempers the gradient even more (Fig. 5 *a*, *orange curves*). Consistent with the analysis presented in Fig. 2 *b*, the other effect is a reduction in free target concentration at the site of its activation.

The alternative scenario, where the biosensor is intermolecular and the endogenous target is in excess, was also investigated (Fig. 5 *b*). In this case, based on the analysis presented in Fig. 4, one might predict that biosensor binding would have no appreciable effect on the active target gradient, but the gradient of biosensor-target complexes would not be a faithful reflection thereof. Indeed, the calculations demonstrate that the free target profile is not significantly perturbed (except in the tail of the profile, where the free target concentration is low), while the gradient of bound complex is rendered progressively more shallow as the affinity and lifetime of the biosensor-target complex are enhanced (Fig. 5 *b*). This effect does not follow directly from the saturation effect illustrated in Fig. 4, however—which is to say that global depletion of the free biosensor does not adequately explain the result. Rather, local depletion of the free biosensor, manifest as an opposing gradient in $[B](x)$, causes the $C(x)$ gradient to be tempered relative to that of $T^*(x)$ (Fig. 5 *b*, *inset*). By manipulating Eqs. 1 and 7 for an effectively one-dimensional system at steady state, it is apparent that

$$V_{cyt}\frac{d[B]}{dx} = -\frac{D_C}{D_B}\left(A_{mem}\frac{dC}{dx}\right). \quad (9)$$

Equation 9 shows that, because diffusion in the cytosol is relatively fast ($D_B >> D_C$), the absolute gradient in the cytosol is always much shallower than that of the membrane-associated complex; however, the relative gradients (fractional changes in $[B]$ and C per unit length) become closer in magnitude with progressively greater binding of the biosensor at that location. Also contributing to the tempering of the observed $C(x)$ gradient is the potential for a long-lived complex (42). This distinct effect is significant when the mean lifetime of the complex ($1/k_{off}$) is comparable to or greater than that of the active target ($1/k_{deact}$) (Fig. 5 *b*, *orange curves*).

Constraints and trade-offs in the practical application of intra- and inter-molecular biosensors for live-cell fluorescence microscopy

The analyses presented above demonstrate the potential pitfalls that might, unbeknownst to the observer, give misleading results in live-cell imaging experiments. Here,

reasonably general guidelines are developed for diagnosing and avoiding such issues, framed in terms of the properties of intra- and intermolecular biosensors that might be introduced into cells. Again, the goal of the experimental design is for the concentration of bound complex to accurately reflect changes in activation status of an endogenous target, as they would normally occur. But this ideal must be balanced against the practical consideration of what can be reliably measured by standard fluorescence microscopy.

Let us first consider the properties of an intramolecular biosensor. In this case, the design space is defined by two dimensionless ratios: the k_{on}/k_{off} (affinity constant) of intramolecular binding and the context-dependent ratio of target activation and deactivation frequencies in the cell (Fig. 6 *a*). Through the analyses described in the previous sections, it was demonstrated that if k_{on}/k_{off} were too high, the apparent kinetics and spatial pattern of the readout would be perturbed relative to those of the endogenous target (the observer effect). On the other hand, if either the k_{on}/k_{off} ratio or the ratio of active/inactive unbound target were too low, there would not be enough of the bound complex C to reliably quantify against the background of fluorescent biosensor molecules in the T and T^* states. These competing considerations together define a region of feasibility, wherein one would hope to operate (Fig. 6 *a*, *shaded region*). The analysis allows as much as half of the active target to be shielded from deactivation ($k_{on}/k_{off} \leq 1$) and considers that the readout could be reliably measured if as little as 5% of the biosensor were in the C form. Still, these considerations impose restrictive constraints on both the complex affinity, which must be of intermediate strength, and the extent of target activation, which must be sufficiently high. Obviously, less generous constraints would shrink or altogether eliminate the region of feasibility. Another caveat is that higher values of k_{on}/k_{off} could be tolerated, up to a point, when the shape of the temporal or spatial response is not sensitive to the rate of target deactivation, i.e., when the upstream signal $S(t,x)$ changes gradually in time or space (as considered in Fig. 3). Higher k_{on}/k_{off} ratios would also be tolerable for biosensors with conformations that breathe enough to allow a nonzero rate of deactivation while in the bound state.

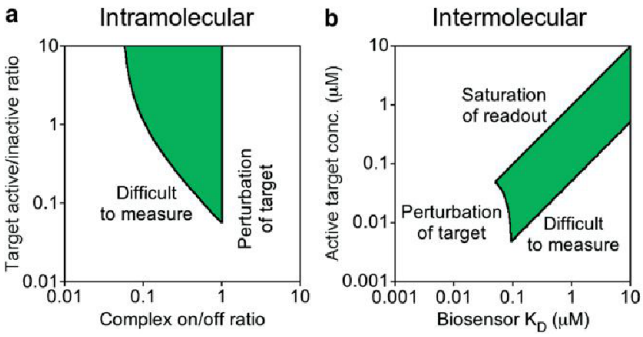

FIGURE 6 Design space for engineering suitable biosensors. In each case, a desirable region of feasibility is defined by the shaded area. (*a*) The design space for an intramolecular biosensor is defined by the affinity of complex formation and the extent of target activation. To the left of the desired region, 5% or less of the biosensor molecules are in complex, resulting in a readout that is difficult to measure. To the right of the desired region, 50% or more of the modified target is bound, resulting in significant perturbation of the observed kinetics. (*b*) The design space for an intermolecular biosensor is defined by the biosensor binding affinity and the concentration of the active target. A moderate biosensor expression level of 0.1 μM is assumed. In addition to the criteria outlined under panel *a*, saturation of complex formation becomes significant when the active target concentration exceeds both the concentration and binding K_D of the biosensor.

In the case of an intermolecular biosensor, the considerations are similar but with the additional constraint that the readout should not be saturated (complex formation should not be limited by the availability of biosensor). Here, the design space is adequately framed in terms of concentrations: those of the biosensor and active target relative to the value of the intermolecular K_D. The total biosensor concentration is fixed here at $[B]_0 = 0.1$ μM, because this is at the lower end of fluorescent protein concentrations that are visible by standard fluorescence microscopy; hence, the design space is defined by variable ranges of the active target concentration (calculated on the basis of the cytosolic volume) and K_D (Fig. 6 *b*). If neither of these values is >0.1 μM, the biosensor concentration is in excess, and the spatiotemporal dynamics of the endogenous target would be significantly perturbed as in the intramolecular case. The other considerations concern the active target concentration in relation to K_D; if it is too low, not enough of the fluorescent biosensor will be in complex, whereas if it is too high, the free biosensor will be significantly depleted, and the measurement will approach saturation. The shaded region of feasibility allows up to 50% depletion of free biosensor and, as before, considers that only 5% of the biosensor needs to be in complex for a reliable measurement (Fig. 6 *b*). It is concluded that for quantitative studies with an intermolecular biosensor, the active target should be present at a high nanomolar concentration or above, and the ideal biosensor would possess a K_D value moderately above that.

Prospects for truly quantitative live-cell imaging of cell biochemistry

As a cell biology workhorse, live-cell fluorescence microscopy is a powerful approach, and the resulting measurements can be reasonably quantitative if great care is taken. Yet, as illustrated in this article, even perfectly measured live-cell biosensor readouts cannot perfectly track the spatiotemporal dynamics of intracellular processes, and in extreme cases, such measurements can be misleading. Two steps may be taken to mitigate the issue.

First, the binding affinity of a biosensor should be characterized and optimized for a particular application.

Practitioners of live-cell microscopy should be aware that high-affinity molecular recognition is not desirable. The traditional approach of using modular-binding domains found in nature is too restrictive in that regard; hence, identifying biosensors using protein-engineering methods (43) presents an attractive alternative. Screening protein variant libraries for desired binding properties is well documented (44).

Second, mathematical models may be used to deconvolute the data so as to account for the deviation from ideality. Provided that the binding affinity and intracellular concentration of the biosensor were known, one could back-calculate the free target concentration or density, $T^*(x,t)$, from the measured $C(x,t)$. Indeed, mathematical recipes for accomplishing this in the context of calcium imaging have been offered (45), and the use of modeling to account for saturable translocation of phosphoinositide biosensors has been demonstrated previously (32,46). This method is complicated, however, when the target perturbation effect is significant; as illustrated in Fig. 2 *b*, the free target kinetics might be markedly altered relative to the unperturbed scenario. Fitting the data to a more complete model, including the parameters characterizing endogenous target dynamics, would allow the unperturbed kinetics or spatial pattern to be reconstructed (47), but formulation of such a model requires advance knowledge or strong assumptions about the mechanisms under study. As with other quantitative approaches in cell biology, analysis of live-cell microscopy data is potentially powerful yet also potentially perilous.

This work was supported by grants (Nos. 0828936 and 1133476) from the National Science Foundation.

REFERENCES

1. Lippincott-Schwartz, J., E. Snapp, and A. Kenworthy. 2001. Studying protein dynamics in living cells. *Nat. Rev. Mol. Cell Biol.* 2:444–456.
2. Meyer, T., and M. N. Teruel. 2003. Fluorescence imaging of signaling networks. *Trends Cell Biol.* 13:101–106.
3. Tsien, R. Y. 2005. Building and breeding molecules to spy on cells and tumors. *FEBS Lett.* 579:927–932.
4. Miyawaki, A. 2011. Proteins on the move: insights gained from fluorescent protein technologies. *Nat. Rev. Mol. Cell Biol.* 12:656–668.
5. Stephens, D. J., and V. J. Allan. 2003. Light microscopy techniques for live cell imaging. *Science.* 300:82–86.
6. Danuser, G., and C. M. Waterman-Storer. 2006. Quantitative fluorescent speckle microscopy of cytoskeleton dynamics. *Annu. Rev. Biophys. Biomol. Struct.* 35:361–387.
7. Kolin, D. L., and P. W. Wiseman. 2007. Advances in image correlation spectroscopy: measuring number densities, aggregation states, and dynamics of fluorescently labeled macromolecules in cells. *Cell Biochem. Biophys.* 49:141–164.
8. Zhang, J., R. E. Campbell, …, R. Y. Tsien. 2002. Creating new fluorescent probes for cell biology. *Nat. Rev. Mol. Cell Biol.* 3:906–918.
9. Miyawaki, A. 2011. Development of probes for cellular functions using fluorescent proteins and fluorescence resonance energy transfer. *Annu. Rev. Biochem.* 80:357–373.
10. Mehta, S., and J. Zhang. 2011. Reporting from the field: genetically encoded fluorescent reporters uncover signaling dynamics in living biological systems. *Annu. Rev. Biochem.* 80:375–401.
11. Mochizuki, N., S. Yamashita, …, M. Matsuda. 2001. Spatio-temporal images of growth-factor-induced activation of Ras and Rap1. *Nature.* 411:1065–1068.
12. Itoh, R. E., K. Kurokawa, …, M. Matsuda. 2002. Activation of Rac and Cdc42 video imaged by fluorescent resonance energy transfer-based single-molecule probes in the membrane of living cells. *Mol. Cell. Biol.* 22:6582–6591.
13. Kalab, P., K. Weis, and R. Heald. 2002. Visualization of a Ran-GTP gradient in interphase and mitotic *Xenopus* egg extracts. *Science.* 295:2452–2456.
14. Pertz, O., L. Hodgson, …, K. M. Hahn. 2006. Spatiotemporal dynamics of RhoA activity in migrating cells. *Nature.* 440:1069–1072.
15. Zhang, J., Y. Ma, …, R. Y. Tsien. 2001. Genetically encoded reporters of protein kinase A activity reveal impact of substrate tethering. *Proc. Natl. Acad. Sci. USA.* 98:14997–15002.
16. Ting, A. Y., K. H. Kain, …, R. Y. Tsien. 2001. Genetically encoded fluorescent reporters of protein tyrosine kinase activities in living cells. *Proc. Natl. Acad. Sci. USA.* 98:15003–15008.
17. Sato, M., Y. Kawai, and Y. Umezawa. 2007. Genetically encoded fluorescent indicators to visualize protein phosphorylation by extracellular signal-regulated kinase in single living cells. *Anal. Chem.* 79:2570–2575.
18. Harvey, C. D., A. G. Ehrhardt, …, K. Svoboda. 2008. A genetically encoded fluorescent sensor of ERK activity. *Proc. Natl. Acad. Sci. USA.* 105:19264–19269.
19. Tomida, T., M. Takekawa, …, H. Saito. 2009. Stimulus-specific distinctions in spatial and temporal dynamics of stress-activated protein kinase kinase kinases revealed by a fluorescence resonance energy transfer biosensor. *Mol. Cell. Biol.* 29:6117–6127.
20. Fosbrink, M., N. N. Aye-Han, …, J. Zhang. 2010. Visualization of JNK activity dynamics with a genetically encoded fluorescent biosensor. *Proc. Natl. Acad. Sci. USA.* 107:5459–5464.
21. Stauffer, T. P., and T. Meyer. 1997. Compartmentalized IgE receptor-mediated signal transduction in living cells. *J. Cell Biol.* 139:1447–1454.
22. Stauffer, T. P., S. Ahn, and T. Meyer. 1998. Receptor-induced transient reduction in plasma membrane PtdIns(4,5)P_2 concentration monitored in living cells. *Curr. Biol.* 8:343–346.
23. Oancea, E., M. N. Teruel, …, T. Meyer. 1998. Green fluorescent protein (GFP)-tagged cysteine-rich domains from protein kinase C as fluorescent indicators for diacylglycerol signaling in living cells. *J. Cell Biol.* 140:485–498.
24. Várnai, P., and T. Balla. 1998. Visualization of phosphoinositides that bind pleckstrin homology domains: calcium- and agonist-induced dynamic changes and relationship to myo-[^{3}H]inositol-labeled phosphoinositide pools. *J. Cell Biol.* 143:501–510.
25. Várnai, P., K. I. Rother, and T. Balla. 1999. Phosphatidylinositol 3-kinase-dependent membrane association of the Bruton's tyrosine kinase pleckstrin homology domain visualized in single living cells. *J. Biol. Chem.* 274:10983–10989.
26. Gray, A., J. Van Der Kaay, and C. P. Downes. 1999. The pleckstrin homology domains of protein kinase B and GRP1 (general receptor for phosphoinositides-1) are sensitive and selective probes for the cellular detection of phosphatidylinositol 3,4-bisphosphate and/or phosphatidylinositol 3,4,5-trisphosphate in vivo. *Biochem. J.* 344: 929–936.
27. Kraynov, V. S., C. Chamberlain, …, K. M. Hahn. 2000. Localized Rac activation dynamics visualized in living cells. *Science.* 290: 333–337.
28. Nalbant, P., L. Hodgson, …, K. M. Hahn. 2004. Activation of endogenous Cdc42 visualized in living cells. *Science.* 305:1615–1619.

29. Teruel, M. N., and T. Meyer. 2000. Translocation and reversible localization of signaling proteins: a dynamic future for signal transduction. *Cell.* 103:181–184.

30. Várnai, P., and T. Balla. 2006. Live cell imaging of phosphoinositide dynamics with fluorescent protein domains. *Biochim. Biophys. Acta.* 1761:957–967.

31. Moraru, I. I., J. C. Schaff, …, L. M. Loew. 2008. Virtual cell modeling and simulation software environment. *IET Syst. Biol.* 2:352–362.

32. Schneider, I. C., and J. M. Haugh. 2004. Spatial analysis of 3′ phosphoinositide signaling in living fibroblasts: II. Parameter estimates for individual cells from experiments. *Biophys. J.* 86:599–608.

33. Rotin, D., B. Margolis, …, J. Schlessinger. 1992. SH2 domains prevent tyrosine dephosphorylation of the EGF receptor: identification of Tyr^{992} as the high-affinity binding site for SH2 domains of phospholipase C γ. *EMBO J.* 11:559–567.

34. Adari, H., D. R. Lowy, …, F. McCormick. 1988. Guanosine triphosphatase activating protein (GAP) interacts with the p21 Ras effector binding domain. *Science.* 240:518–521.

35. Zhang, X. F., J. Settleman, …, J. Avruch. 1993. Normal and oncogenic $p21^{ras}$ proteins bind to the amino-terminal regulatory domain of c-Raf-1. *Nature.* 364:308–313.

36. Zhang, B. L., Z. X. Wang, and Y. Zheng. 1997. Characterization of the interactions between the small GTPase Cdc42 and its GTPase-activating proteins and putative effectors. Comparison of kinetic properties of Cdc42 binding to the Cdc42-interactive domains. *J. Biol. Chem.* 272:21999–22007.

37. Haugh, J. M., and I. C. Schneider. 2004. Spatial analysis of 3′ phosphoinositide signaling in living fibroblasts: I. Uniform stimulation model and bounds on dimensionless groups. *Biophys. J.* 86:589–598.

38. Manna, D., A. Albanese, …, W. Cho. 2007. Mechanistic basis of differential cellular responses of phosphatidylinositol 3,4-bisphosphate- and phosphatidylinositol 3,4,5-trisphosphate-binding pleckstrin homology domains. *J. Biol. Chem.* 282:32093–32105.

39. Yip, S. C., R. J. Eddy, …, J. M. Backer. 2008. Quantification of PtdIns(3,4,5)P(3) dynamics in EGF-stimulated carcinoma cells: a comparison of PH-domain-mediated methods with immunological methods. *Biochem. J.* 411:441–448.

40. McLaughlin, S., J. Y. Wang, …, D. Murray. 2002. PIP_2 and proteins: interactions, organization, and information flow. *Annu. Rev. Biophys. Biomol. Struct.* 31:151–175.

41. Hammond, G. R. V., Y. Sim, …, R. F. Irvine. 2009. Reversible binding and rapid diffusion of proteins in complex with inositol lipids serves to coordinate free movement with spatial information. *J. Cell Biol.* 184:297–308.

42. Caudron, M., G. Bunt, …, E. Karsenti. 2005. Spatial coordination of spindle assembly by chromosome-mediated signaling gradients. *Science.* 309:1373–1376.

43. Gulyani, A., E. Vitriol, …, K. M. Hahn. 2011. A biosensor generated via high-throughput screening quantifies cell edge Src dynamics. *Nat. Chem. Biol.* 7:437–444.

44. Binz, H. K., P. Amstutz, and A. Plückthun. 2005. Engineering novel binding proteins from nonimmunoglobulin domains. *Nat. Biotechnol.* 23:1257–1268.

45. Borst, A., and H. D. I. Abarbanel. 2007. Relating a calcium indicator signal to the unperturbed calcium concentration time-course. *Theor. Biol. Med. Model.* 4:7.

46. Xu, C., J. Watras, and L. M. Loew. 2003. Kinetic analysis of receptor-activated phosphoinositide turnover. *J. Cell Biol.* 161:779–791.

47. Dehmelt, L., and P. I. Bastiaens. 2010. Spatial organization of intracellular communication: insights from imaging. *Nat. Rev. Mol. Cell Biol.* 11:440–452.

Impact of Methylation on the Physical Properties of DNA

Alberto Pérez,[†‡△] Chiara Lara Castellazzi,[‡△] Federica Battistini,[‡] Kathryn Collinet,[‡] Oscar Flores,[‡] Ozgen Deniz,[‡] Maria Luz Ruiz,[‡] David Torrents,[†¶] Ramon Eritja,[§] Montserrat Soler-López,[‡] and Modesto Orozco[†‡‖*]

[†]IRB-BSC Joint Research Program on Computational Biology, Barcelona Supercomputing Center, Barcelona, Spain; [‡]IRB-BSC Joint Research Program on Computational Biology and [§]Chemistry and Molecular Pharmacology Program, Institute for Research in Biomedicine, Barcelona, Spain; [¶]Institució Catalana de Recerca i Estudis Avançats, Barcelona, Spain; and [‖]Departamento de Bioquímica, Facultat de Biología, Barcelona, Spain

ABSTRACT There is increasing evidence for the presence of an alternative code imprinted in the genome that might contribute to gene expression regulation through an indirect reading mechanism. In mammals, components of this coarse-grained regulatory mechanism include chromatin structure and epigenetic signatures, where d(CpG) nucleotide steps are key players. We report a comprehensive experimental and theoretical study of d(CpG) steps that provides a detailed description of their physical characteristics and the impact of cytosine methylation on these properties. We observed that methylation changes the physical properties of d(CpG) steps, having a dramatic effect on enriched CpG segments, such as CpG islands. We demonstrate that methylation reduces the affinity of DNA to assemble into nucleosomes, and can affect nucleosome positioning around transcription start sites. Overall, our results suggest a mechanism by which the basic physical properties of the DNA fiber can explain parts of the cellular epigenetic regulatory mechanisms.

INTRODUCTION

Determining the mechanisms that regulate gene expression in complex organisms is the next frontier of genomics research (1). In the traditional paradigm, specific proteins regulate gene expression through the recognition of certain sequence signals (by means of specific hydrogen-bond interactions) upstream of the transcription start sites (TSSs) (2). Nevertheless, there is increasing evidence about the presence of an alternative code that may contribute to a rough regulation of gene expression through an indirect reading mechanism, probably signaled by chromatin structure and epigenetic marks (3,4). This mechanism is unlikely (even in a synergistic manner) to achieve the fine-tuning and specificity of the direct protein-DNA readout. Conversely, it probably plays a pivotal role in basal gene expression, which requires less regulation and for which the extreme cost of developing a highly specific protein regulation infrastructure seems unjustified. Key players in this regulatory mechanism may be d(CpG) steps, which despite being largely underrepresented in the genome of complex organisms are enriched in nearly 60% of human promoters, where they often define ultrarich CpG segments, the so-called CpG islands (5,6). Even if CpG islands do not contain specific transcription binding motifs, they clearly favor the downstream binding of the transcription machinery (7), particularly for those genes that are usually active. The molecular basis of the d(CpG) effect on gene regulation remains unclear, although it has been suggested to be related to the definition of DNA fiber properties (8).

One of the most intriguing features of the d(CpG) step is its ability to undergo nonmutagenic chemical modifications such as cytosine methylation (9). In mammalian genomes, DNA methyltransferases (DNMTs) can transfer a methyl group from S-adenosylmethionine to cytosine at CpG dinucleotides (10). The bulk of the methylation takes place during DNA replication in the S-phase of the cell cycle (11), and is the most abundant form of post-replicative DNA modification observed in eukaryotic organisms (12). During this process, the cytosine is flipped 180° out of the DNA backbone into an active-site pocket of the enzyme (13) where methylation of cytosine takes place.

Intriguingly, methylation of cytosines seems to be an erroneous decision of evolution because it dramatically increases the chances of C→T mutation, but this seeming disadvantage is compensated for by the gain in regulatory possibilities offered by methylation. Indeed, highly methylated DNA is typically associated with inactive genes, whereas methylation depletion is observed for active genes (14,15). Furthermore, most cytosines in CpG steps, except those in CpG islands, are methylated in vertebrate somatic cells (16,17). The first step of methylation occurs early in mammalian development as a result of de novo DNMTs (Dnmt3a and Dnmt3b) (18) that methylate CpG steps in both DNA strands. The methylation profile is conserved by maintenance DNA methyltransferase (Dnmt1) throughout cell divisions. During replication, daughter strands are nonmethylated, resulting in hemimethylated DNA. Dnmt1 recognizes hemimethylated CpG steps and methylates the daughter strand (19). Recent studies have demonstrated that changes in methylation patterns along CpG islands and CpG shores (methylation

Submitted December 27, 2011, and accepted for publication March 22, 2012.

△Alberto Pérez and Chiara Lara Castellazzi contributed equally to this work.

*Correspondence: modesto@mmb.pcb.ub.es

Editor: Michael Levitt.

0006-3495/12/05/2140/9 $2.00

doi: 10.1016/j.bpj.2012.03.056

hotspots on the outskirts of CpG islands (20)) correlate with tissue differentiation and cancer, proving the role of methylation in cellular reprogramming (20,21,23,24). The regulatory function of methylated cytosines (hereafter referred to as ^{Me}C) was traditionally explained by their interaction with methyl-CpG binding domain proteins (MBDs) (18), but considering the prevalence of cytosine methylation, MBDs alone cannot entirely account for the role of d(CpG) methylation in the cell. An increased level of complexity is provided by the almost nonexistent sequence specificity of the DNMTs, precluding the mechanism underlying the methylation reaction (26).

Here we present a comprehensive theoretical analysis of the d(CpG) properties along with an experimental validation of key theoretical findings. We show that d(CpG) steps display unique physical properties, especially in the context of CpG islands, that severely change upon methylation. Our calculations suggested, and experiments confirmed, that DNA segments containing ^{Me}C are very stiff and hard to bend, and display a lower tendency to circularize or form nucleosomes by wrapping around histones. The latter effect has striking consequences for the organization of nucleosome arrays near TSSs, which in turn modifies the accessibility of regulatory proteins, leading to alterations in the pattern of DNA expression. Overall, without diminishing the role of specific regulatory proteins, basic descriptors of DNA physical properties can help us rationalize several seemingly disconnected pieces of the puzzle of DNA regulation.

METHODS

Molecular-dynamics simulations

We performed molecular-dynamics (MD) simulations on an array of different oligomers containing CpG steps, in both their methylated and nonmethylated forms (see Table S1 in the Supporting Material). We also included in our analysis trajectories of unmethylated CpG step data from the Ascona B-DNA Consortium (ABC) (27) database in all tetramer environments to enrich the dynamics database. All simulations were carried out in duplicates for 100 ns (after equilibration) using explicit solvent, the parmbsc0 refinement of the Amber force field (28), and state-of-the-art simulation conditions (Supporting Material).

Mesoscopic model of DNA flexibility

We derived a flexibility model from different MD equilibrium trajectories using a harmonic model (29–31). Accordingly, we projected the MD trajectories onto a helical reference system to obtain equilibrium values and derive the covariance matrix, which we then inverted to recover the stiffness matrices for each basepair step, from which a mesoscopic estimate of the energy associated to a given deformation can be easily computed (29,32) as

$$E = 0.5\sum_{i=1}^{6}\sum_{j=1}^{6} f_{ij}\Delta X_i \Delta X_j,$$

where ΔX_i is the perturbation from equilibrium geometry (Fig. 1), and f_{ij} are elements of Θ, where Θ is the 6×6 stiffness matrix expressing the stiffness of a given step to deformation in roll, tilt, twist, slide, shift, and rise (see Supporting Material, Fig. 2, and Pérez et al. (33)). Alternatively, global deformation parameters can be derived using a similar approach, but considering global instead of local geometric descriptors (see Fig. S1, Supporting Material, and Lankas et al. (34)). Note that elastic parameters derived from protein-DNA crystal complexes (29,31) or simulation data are in good agreement (33), supporting their use to describe DNA flexibility. Here, we favored the use of MD-derived values for consistency with the newly derived parameters describing ^{Me}CpG steps (which cannot be derived from analysis of crystal structures).

In this work, we used a mesoscopic method to estimate deformation energy related to nucleosome formation and circularization assays. This implies that indirect readout mechanisms prevail over the direct readout for the description of sequence preferences in nucleosome binding. A second implication is that these deformations follow a harmonic behavior. Both of these assumptions represent simplifications, and thus the validity of the method is not always guaranteed (32,35,36).

Circularization assays and modeling

We carried out DNA circularization experiments to validate our theoretical estimations about the impact of methylated cytosines on DNA physical properties. For this purpose, we designed a short polymerizable oligonucleotide (d(GAAAAAACGGGCGAAAAACGG)·d(TCCCGTTTTTCGCCCGTTTTT)) based on a reported sequence favoring the formation of minicircles (37), with the incorporation of a central CpG dinucleotide subject to be methylated and 5′-sticky ends to enable the formation of multimers. Thus, under favorable ligation conditions, the multimers form circles that are as short as allowed by the geometry and flexibility of the DNA (Fig. 3). As a negative control, we selected a previously reported nonbendable oligonucleotide (d(GCAAATATTGAAAAC)·d(GCGTTTTCAATATTT; see Supporting Material for details). The ligation products were analyzed by atomic force microscopy (AFM) and by two-dimensional gel electrophoresis (Fig. 3, Fig. S2, Fig. S3, and Supporting Material).

Circularization efficiency was determined based on the *J*-factor, which defines the ratio of circular and linear DNA species for a given sequence length (37). Experimental *J*-factors were extracted from the linear and circle DNA signal intensities as detected on two-dimensional gels (see Supporting Material and Fig. S3). Although the absolute *J*-factors depend on the experimental setup, the ratio of *J*-factors of methylated versus nonmethylated oligos provide a reliable measure of the impact of methylation on DNA circularization. Accordingly, experimental *J*-factors can validate whether theoretical suggestions regarding physical changes induced by methylation are correct. We derived theoretical *J*-factors from Monte Carlo simulations (Supporting Material) using mesoscopic descriptors derived from MD simulations (see above).

Mesoscopic model of nucleosome deformation energy

We theoretically determined the ability of a 147-mer DNA sequence to wrap around a nucleosome using harmonic deformation energy as described above considering mesoscopic descriptors. To reduce the noise, we determined the deformation vector (ΔX above) using the target geometry obtained by Fourier-averaging all available crystal structures of nucleosome particles. As noted above, our mesoscopic model is useful in so far as histone-bound DNA deforms harmonically and the indirect readout has an important contribution in directing nucleosome formation. Regarding the first point, the rotational degrees of motion in nucleosomes (twist, roll, and tilt) clearly fall within the normal fluctuations of DNA (38,39), and only the translational parameter slide shows slightly more positive values than expected. Clearly, evolution has optimized nucleosome positioning sequences to have flexible steps such as d(CpA) and d(TpA) in crucial positions to accommodate the deformations required for nucleosome binding (see results of SELEX experiments in Thåström et al.

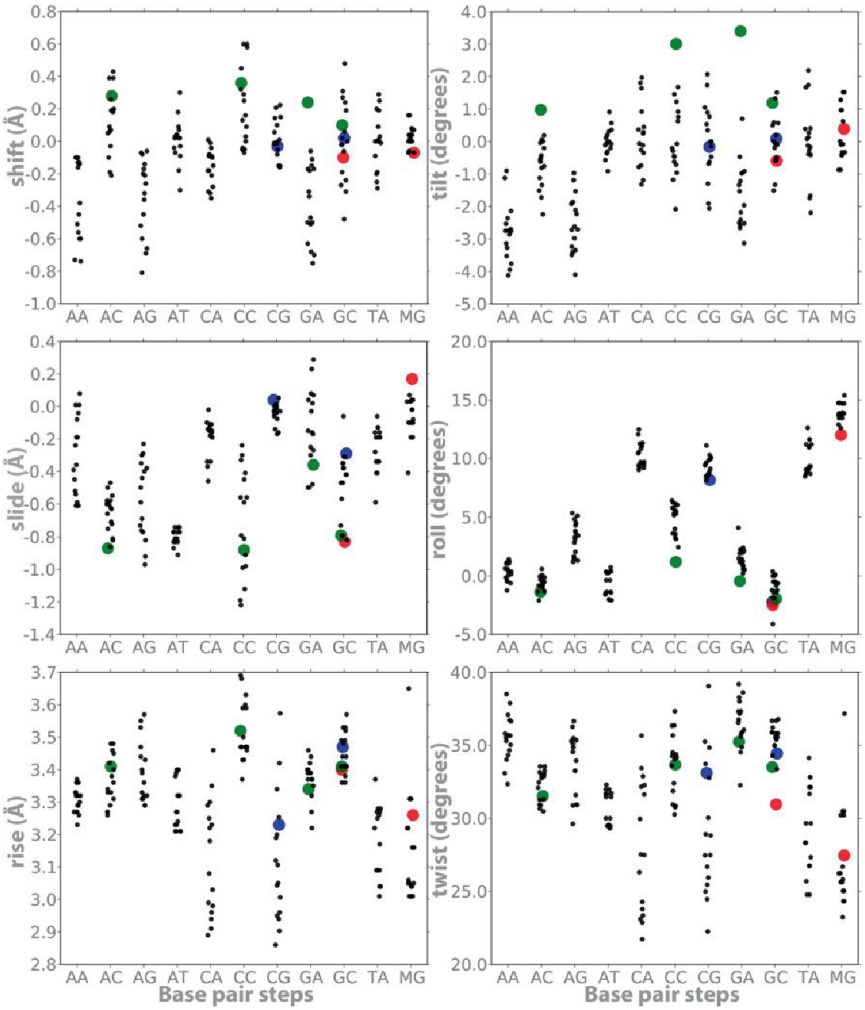

FIGURE 1 Average helical parameters (translations in angstroms and rotations in degrees) derived from MD simulations of the usual 10 dinucleotides plus d(^{Me}CpG; referred to as MG in the figure). The black dots correspond to control simulations (those performed for this work and those obtained from the ABC database (27)) for each central basepair step representing the different tetramer environments; notice the slight displacement from the vertical to avoid stacking of data. Blue dots stand for d(CpG) and d(GpC) steps when embedded in a poly d(CpG) track. Green dots refer to neighboring methylated steps (Xp^{Me}C): d(Ap^{Me}C), d(Tp^{Me}C)=d(GpA), d(Cp^{Me}C), and d(Gp^{Me}C). Finally, red dots stand for d(^{Me}CpG) and d(Gp^{Me}C) in the context of a poly d(CpG) track.

(40)). Note also that by using a single conformation to model all nucleosomes, Tolstorukov et al. (38) and Balasubramanian et al. (39) found a high degree of correlation between the predictions arising from harmonic deformation energies and nucleosome positioning sequences, a result that was consistent with nucleosome location experiments performed by our group (41). Thus, without ignoring its limitations, we believe the model can be useful to rationalize nucleosome positioning.

In vitro nucleosome reconstitution

To assess the effect of methylated DNA on nucleosome assembly, we selected a nucleosome positioning sequence (DNA construct 601.2 in Anderson and Widom (42)) to reconstitute nucleosomes in vitro after incubation with histones, before and after extensive DNA methylation (see Supporting Material). Methylated states were verified by DNA sequencing. The reconstituted nucleosomes were subsequently analyzed by gel shift assays (see Fig. 4).

RESULTS

Physical properties of CpG steps and CpG islands

MD simulations performed here in conjunction with those retrieved from the ABC database (27) revealed that sequence is crucial for defining the DNA equilibrium geometries (Fig. 1). In general, Pyr-Pur steps show a lower rise and twist, as well as higher roll values, than the rest of the dinucleotide steps. Additionally, they display an unusually large dispersion in certain key equilibrium helical parameters (e.g., twist), arising from different tetramer environments. Focusing on the different tetramer environments, we can see that the d(CpG) steps are peculiar in presenting bimodal distributions of some parameters (e.g., twist; see Fig. S4), which confirms previous ABC findings (27). Such bimodality is not an artifact that arises from incomplete sampling, because it is also present in multi-microsecond trajectories (43), and suggests that the d(CpG) step is specially flexible, as confirmed by a stiffness analysis (Fig. 2). It is worth noting that the large deformability in twist and roll, combined with large roll values, suggests that protein-induced curvature may be favored in DNA with CpG steps. Fig. S5 shows that CpG, despite the neighboring basepair, is more curved than most basepair steps (only TA and CA are comparable) and is directed preferentially toward the major groove.

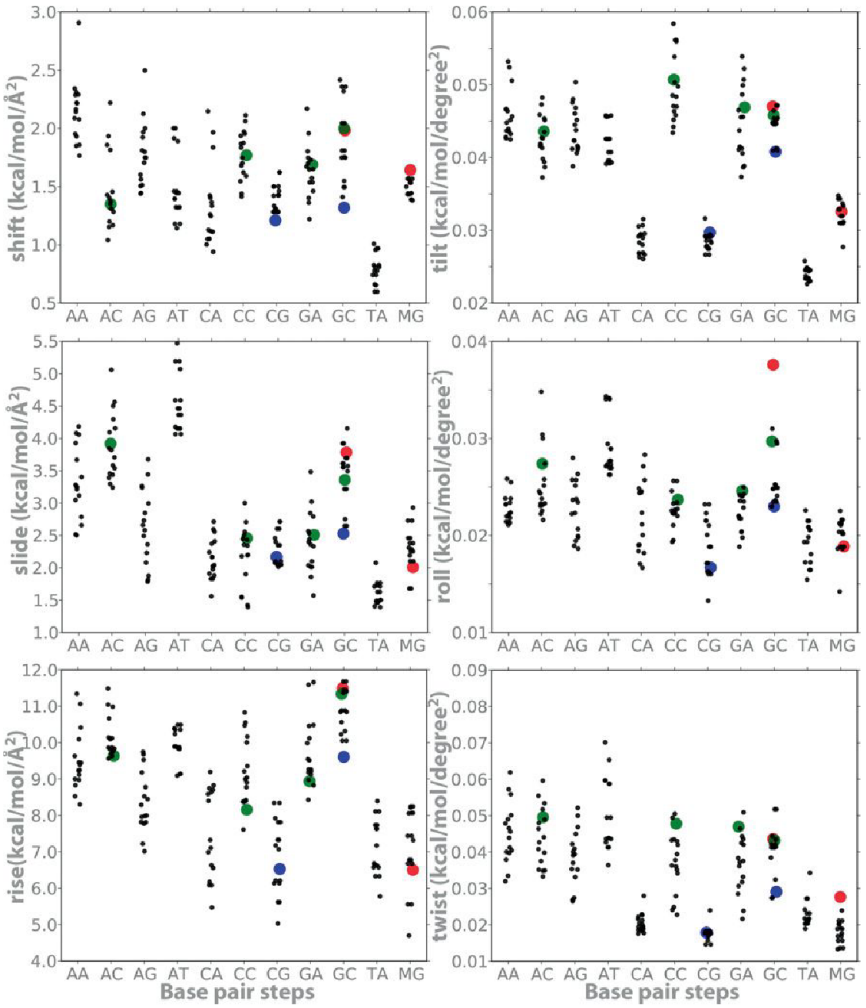

FIGURE 2 Average stiffness helical parameters (translations in kcal/mol Å^2 and rotations in kcal/mol deg^2) derived from MD simulations of the usual 10 dinucleotides plus d(^{Me}CpG; referred to as MG in the figure). Same notation as in Fig. 1.

One might expect the unique physical properties of d(CpG) steps to be amplified in long d(CpG)$_n$ tracks (i.e., CpG islands). Surprisingly, this is not the case, and the global geometrical properties of long d(CpG) segments are different from those expected by extrapolating the individual characteristics of the d(CpG) steps (Fig. S1). Thus, the high flexibility of the d(CpG) steps suggests that poly d(CpG) should be extremely flexible. Conversely, the d(CpG)$_9$ segment studied here is hardly distinguishable from other 18-mer duplexes in terms of global unwinding and isotropic bending. This is hardly surprising when one considers the differences between an individual d(CpG) step and a poly d(CpG). The former has the properties of an individual d(CpG) step, whereas the d(CpG)$_9$ segment has properties due to the alternation of d(CpG) and d(GpC) steps. Thus, the lower flexibility of d(GpC) steps (Fig. S1) makes the whole sequence overall stiffer than a simple extrapolation of d(CpG) properties. Furthermore, whereas the large roll of individual d(CpG) steps would imply a strong curvature of the entire oligonucleotide, the d(CpG)$_9$ curvature is actually very moderate due to the low roll values of d(GpC) steps. In conclusion, the properties of long d(CpG) segments are distinct from the extrapolation of properties of isolated d(CpG) steps, warning against the use of oversimplified rules of DNA flexibility.

Effect of CpG methylation

Early structural experiments suggested that cytosine methylation (Fig. S5) might induce helical transitions from B- to Z-DNA (44). However, a secondary structure analysis of CpG methylated oligonucleotides by circular dichroism spectroscopy (Supporting Material and Fig. S6) revealed that the transition only occurred at nonphysiological salt concentrations (from 1 to 2 M NaCl). This evidence is in agreement with our MD results and previously reported Fourier transform infrared (FTIR) spectroscopy data (45), demonstrating that in vivo DNA remains in the B-form upon methylation, and accordingly, the transition to the Z-form is not the underlying determinant for the physiological role of CpG methylation.

The results of the MD simulations suggest that when methylated, d(CpG) steps increase their average roll value and reduce their twist (Fig. 1), leading to an increase in local

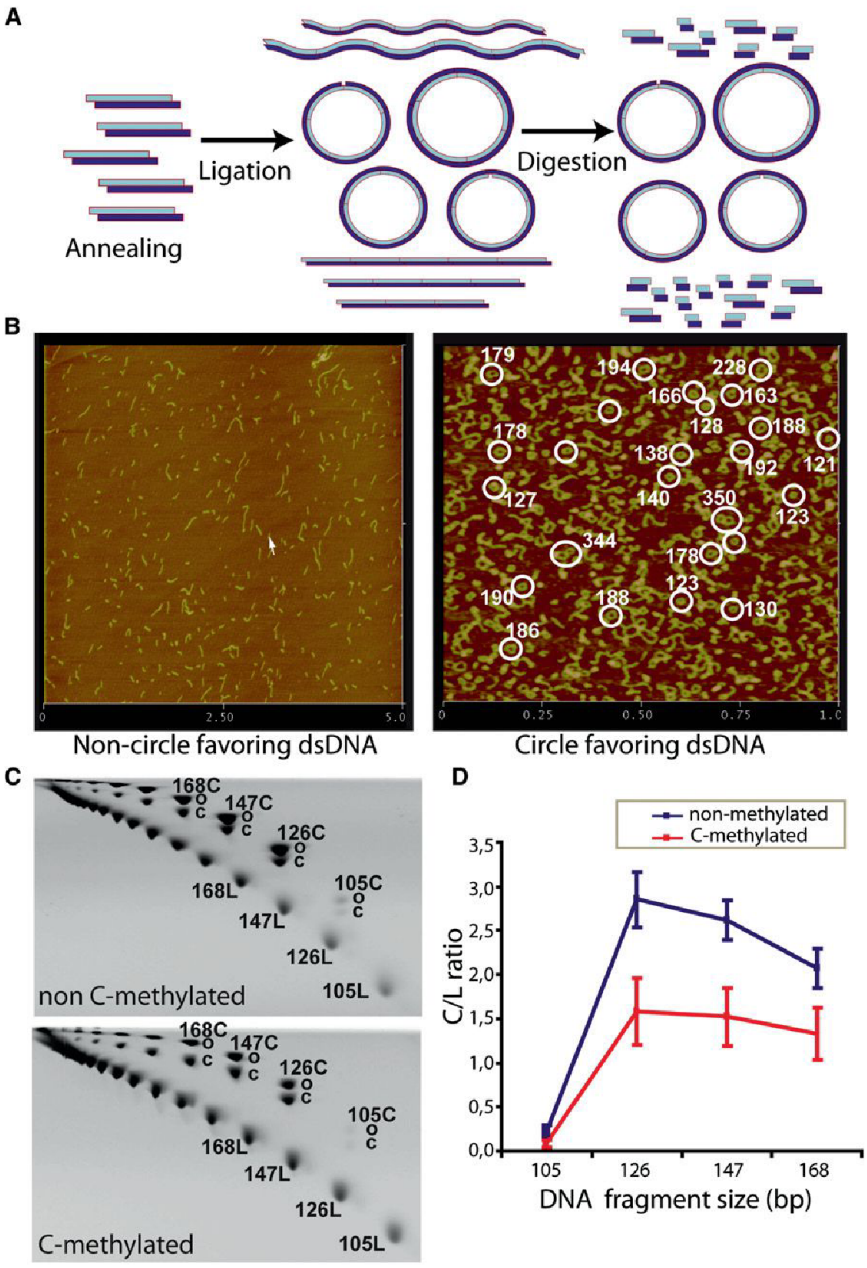

FIGURE 3 Overview of circularization assays. (*A*) Schematic diagram of the underlying principle of circularization assays. A DNA oligonucleotide is first annealed to form duplexes and subsequently is multimerized-circularized by a ligation reaction. Under favorable ligation conditions, DNA forms circles as short as allowed by the geometry and flexibility of the DNA. Only circularized DNA is resistant to an exonuclease digestion; linear multimers will be degraded. (*B*) AFM images of ligation products for 15-bp nonfavoring (*left*) and 21-bp favoring (*right*) circularization oligonucleotides; circle size estimations are highlighted in white. (*C*) 2D polyacrylamide native gels showing different migrations of linear (L) and circular (C) DNA species (which can be either covalently closed (cC) or nicked open (oC)) for nonmethylated and ^{Me}C oligomers of 21 bp, respectively. Linear DNA molecules are positioned on the lower diagonal, and circular DNA molecules are positioned on the upper diagonal. (*D*) The circularization efficiency is expressed as the ratio between C and L molecules of the same size.

curvature. Furthermore, methylation makes d(CpG) steps stiffer, especially in terms of roll and tilt deformations: the ^{Me}CpG step has larger tilt and roll force constants on average than the CpG step (MG and CG, respectively, in Fig. 2). Methylation also alters the geometric properties of the basepair step previous to the d(CpG) site, here denoted as d(XpC), where X = A, C, G, or T (Figs. 1 and 2). In canonical DNA, d(XpC) steps tend to compensate for the geometry and relative stiffness of d(CpG) in twist, tilt, and roll. However, upon methylation, we observed an increase of force constants for rotational parameters in both the ^{Me}CpG and d(Xp^{Me}C) steps (*green dots* in Fig. 2). Hence, the additive effect of methylation leads to significant alterations in the global physical properties of DNA, especially for CpG islands (Figs. 1 and 2, and Fig. S1).

The higher stiffness of the d(^{Me}CpG) steps should lead to a decrease in the DNA circularization efficiency, which must be especially visible for the smallest circles. Indeed, Monte Carlo calculations using the MD-derived stiffness parameters (see Materials and Methods, and Supporting Material) suggested that circularization of 126- to 189-bp-long methylated oligos (one ^{Me}CpG every 21 bp) is more difficult than circularization of unmethylated ones (with a relative *J*-factor of 0.05–0.2). This result was confirmed by circularization experiments on the same sequence with a relative *J*-factor of ~0.5 (see Fig. 3, Materials and Methods, and Supporting Material).

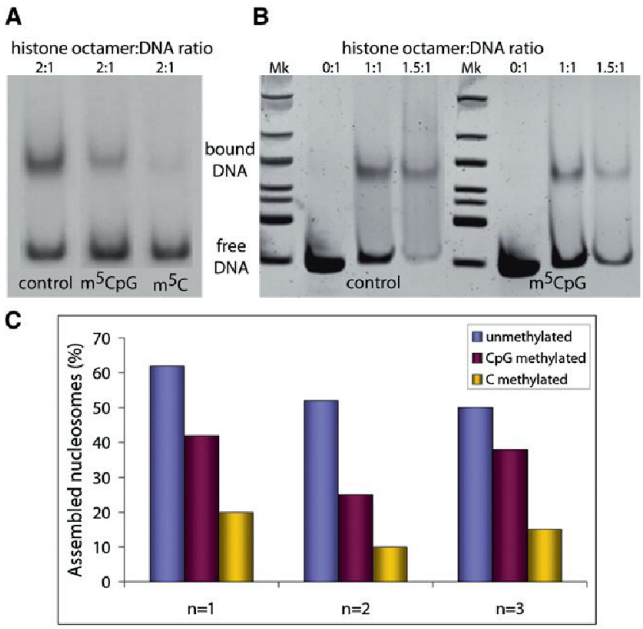

FIGURE 4 In vitro nucleosome core particle reconstitution. Results of gel mobility shift assays of nucleosomes reconstituted in vitro with a 147-bp 601.2 DNA fragment containing either C or ^{Me}C at different histone octamer concentrations are shown. The upper bands correspond to histone core-bound DNA, and lower bands correspond to unbound (or free) DNA. Mk: DNA ladder for size band estimation. (*A*) Radiolabeled DNA bands. (*B*) DNA bands stained with SyBr Safe (Invitrogen) and visualized by ultraviolet light. (*C*) Histograms displaying the percentage of in vitro assembled nucleosomes using the same sequence in different methylation conditions coming from triplicate experiments.

Potential impact on chromatin structure

The sequence-dependent physical properties of DNA play a crucial role in determining nucleosome positioning (46–52) and thus are instrumental in genome regulation (53,54). An analysis of nucleosome distribution in *Saccharomyces cerevisiae* (55,56) revealed that d(CpG)s are enriched in nucleosome-bound regions but depleted in internucleosomal segments, supporting the idea that d(CpG) steps are easily fitted into the nucleosome structure. Protein-DNA interactions are governed by direct and indirect readouts. The former arises from protein-DNA direct interactions, whereas the latter is based on the ability of a DNA sequence to deform into a conformation that makes the interaction happen. Without underestimating the importance of direct readout mechanisms in nucleosome binding, we note that indirect readout models seem to capture well the global positioning profile of nucleosomes (41). Thus, changes in the physical properties of the DNA fiber related to methylation should have a direct impact on nucleosome affinity and positioning. Our models prompted us to hypothesize that in the absence of external factors (e.g., MBD proteins or chromatin remodelers), the increased stiffness due to d(CpG) methylation leads to a higher deformation energy required to wrap DNA around a nucleosome (Fig. 5). We tested this hypothesis by conducting in vitro nucleosome reconstitution experiments (see Materials and Methods, and Supporting Material) with normal and methylated DNAs. The results confirm that the d(^{Me}CpG) DNA has a lower ability to form nucleosomes than the nonmethylated sequence (Fig. 4).

Interestingly, nucleosome formation was further decreased when all cytosines in the DNA were methylated, which confirms that a reduced flexibility is mainly responsible for the lower affinity of methylated DNA for the histones. Other nonmammalian organisms that have alternative cytosine methylation patterns besides the methylation of CpG steps could use this strategy for gene regulation. Tillo and Hughes (57) established that increasing C+G contents correlate well with higher nucleosome formation. Therefore, it is not surprising that a mechanism in which more cytosines are methylated would further rigidify the sequence, further changing the nucleosome positioning preferences (57).

DISCUSSION

d(CpG) steps are statistically underrepresented in the genome, but they appear concentrated in regulatory regions,

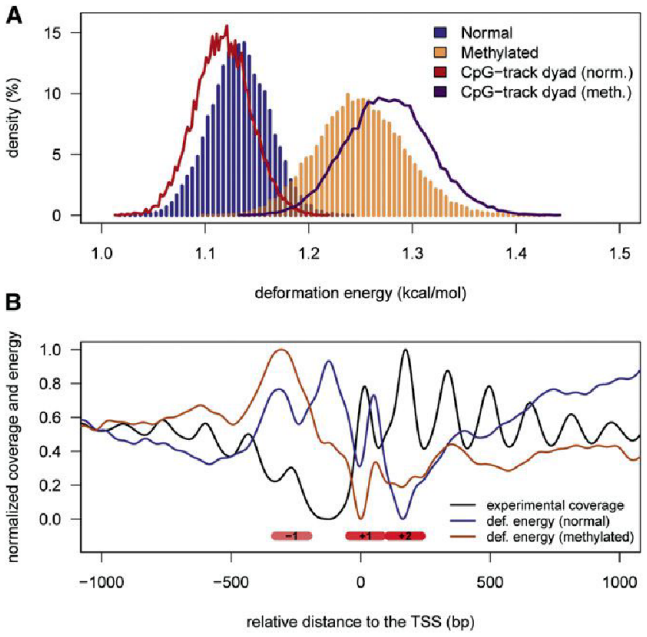

FIGURE 5 Impact of methylation on nucleosome positioning. (*A*) The distribution of predicted energies (per base step) for 147-bp-long random DNAs in normal (*blue histogram*) and methylated (*orange histogram*) forms, respectively. The curves correspond to the predicted energy (per base step) when random oligos contain a poly d(CpG) track at the dyad, in normal (*red*) and methylated (*magenta*) forms. (*B*) The nucleosome distribution surrounding the TSSs of yeast genes determined from MNase digestion experiments (*black line*), compared with the predicted distortion energy to wrap a nucleosome in those sites when genomic DNA is normal (*blue line*) or methylated (*orange line*). All values were normalized to facilitate the interpretation of the plots. Nucleosome positions −1, +1, and +2 are indicated by red boxes for clarity.

which suggests that d(CpG) steps provide the suitable physical properties that enable the DNA to efficiently interact with regulatory proteins (58,59) and help define the correct nucleosome positioning. Indeed, our MD results suggest that isolated d(CpG) steps are curved (see Fig. S5) and particularly flexible, making d(CpG) steps appropriate for those regions in which DNA needs to be locally distorted to facilitate protein binding, in agreement with early NMR measures (60). This hypothesis is supported by an analysis of whole-genome nucleosome positioning in yeast, which revealed a d(CpG) step depletion in internucleosomal segments (41,55,56).

Mesoscopic calculations (Fig. 5 *A*) indicate that a $d(CpG)_5$ segment located at the dyad axis may favor nucleosome formation, and hence very long d(CpG) tracks (CpG islands) are very likely to assemble into nucleosomes. Nucleosomes can easily move along the d(CpG) track, presumably leading to a nucleosome-depleted region at the external borders of the island, and thereby imprinting a distinct nucleosome array organization that would define the accessibility to regulatory regions downstream of the CpG islands, where many promoters are located. This also accords with the fact that high C+G content correlates with nucleosome positioning (57)

Methylation increases the curvature of d(CpG) steps (Fig. S5), although this local geometric effect tends to be compensated for by neighboring steps. In fact, all tested 18-mer methylated oligos (except CpG islands) were less curved and less flexible than their unmethylated counterparts. On the other hand, as previously suggested (61,62), methylation increases d(CpG) stiffness, and this effect propagates to neighboring steps, leading to a global increase in the rigidity of DNA. Our results suggest that this effect alone explains (within the indirect readout model) the limited ability of methylated DNA to interact with certain proteins, such as transcription factors (63–65). Our in silico simulations and in vitro nucleosome reconstitution experiments showed that methylation reduces DNA affinity for nucleosomes, probably due to the increased rigidity of the DNA fiber. Our results are in full agreement with previous findings (66,67), with recent data about the anticorrelation between nucleosome formation and methylation (68), and with physical intuition that suggests that a more flexible fiber should wrap more easily than a rigid one. Additionally, the rigidifying effect of ^{Me}CpG is also observed in recent fluorescence resonance energy transfer (FRET)-derived data (69,70) showing that methylating nucleosome-bound DNA results in nucleosome compaction and rigidity. Taken together, these results indicate that DNA methylation may regulate nucleosome dynamics by increasing the rigidity of DNA either before or during nucleosome assembly.

Our combined theoretical and experimental results demonstrate that methylation decreases nucleosome formation. Nucleosome depletion is usually considered as a signal of gene activity (71,72). At the same time, gene activity correlates with low levels of methylation (73). We postulate that the presence of almost 10^5 ^{Me}CpG steps present in the genome could significantly modify the nucleosome positioning landscape. This hypothesis would explain how the gene expression pattern can change while the number of nucleosomes (but not positions) is kept constant in either methylated or canonical genomes. Hence, we analyzed the nucleosome organization around TSSs on the unmethylated yeast genome and subsequently compared the in silico effects of methylation on nucleosome positioning (Fig. 5 *B*). TSSs are typically characterized by a nucleosome-depleted region and well-positioned -1, $+1$, and $+2$ nucleosomes (55,74). As expected, these positions are clearly marked in the energy profiles: regions with high deformation energy signal nucleosome-depleted areas and vice versa (Fig. 5). These profiles support recent claims about particular nucleosome positioning sites (signaled by large in vitro propensities for nucleosome assembly) anchoring the formation of nucleosomal arrays in vivo (75,76). Methylation of d(CpG) steps modifies the deformation energy profile associated with nucleosome wrapping around the TSS, which ultimately may be reflected by a change in the nucleosome array (Fig. 5 *B*; note that this does not necessarily make the nucleosomes more diffuse) and, accordingly, in gene expression (77). In particular, it seems that upon methylation, the nucleosome-free region is less defined and the nucleosome -1 is moved downstream. Furthermore, our calculations suggest that when CpG islands are methylated, nucleosomes are concentrated at the CpG island edges, leading to a completely different configuration of the nucleosome array around the TSS and consequently to a change in gene activity. Hence, we can partially rationalize the striking effect of methylated CpG islands on the activity of several genes, particularly those involved in cancer (78), by considering the highly unfavorable impact that methylation has on the ability of poly CpG tracks to wrap around nucleosomes (Fig. 5 *A*). Further work is required to shed more light on this interesting hypothesis.

Taken together, our studies show how an apparently minor covalent change such as methylation can alter the physical properties of DNA, and how such a change can modify the ability of DNA to organize the chromatin fiber, which may be reflected by significant alterations in gene regulation, even in the absence of specific MBDs.

CONCLUSIONS

In summary, simple physical properties of DNA (described from calculations based on first principles) can provide a rationale for the seemingly chaotic diversity of gene regulatory signals in developed organisms, particularly epigenetic signatures such as cytosine methylation. Our results support the hypothesis that physical properties define a basal regulatory code that is superposed onto more elaborated

mechanisms involving the action of specific proteins when fine-tuning of gene function is required. Furthermore, our findings suggest that simply by varying the physical properties of some distant regions to a particular gene while keeping the specific protein-binding boxes unaltered, we may be able to modulate that gene's biological functionality. This raises interesting possibilities in the emerging field of synthetic biology. From the results of this study, it follows that methylated DNA is not as likely to form nucleosomes. However, the complete picture is even more complex when one considers that DNMTs have a greater preference to target nucleosome-bound DNA, slightly enriching it (1%) in ^{Me}CpG steps (79).

SUPPORTING MATERIAL

Supplementary materials and methods, seven figures, a table, and references are available at http://www.biophysj.org/biophysj/supplemental/S0006-3495(12)00397-9.

We thank Anna Aviñó for help with the experiments. The authors declare that they have no competing interests and acknowledge no conflict of interest.

This work was supported by the Spanish Ministry of Science and Innovation (BIO2009-10964 and Consolider E-Science, INB-Genoma España, and COMBIOMED RETICS), the European Research Council, and the Fundación Marcelino Botín. A.P. received support from a Juan de la Cierva postdoctoral fellowship.

REFERENCES

1. Collins, F. S., E. D. Green, …, M. S. Guyer, US National Human Genome Research Institute. 2003. A vision for the future of genomics research. *Nature.* 422:835–847.
2. Hélène, C. 1981. Recognition of base sequences by regulatory proteins in procaryotes and eucaryotes. *Biosci. Rep.* 1:477–483.
3. Schueler, M. G., and B. A. Sullivan. 2006. Structural and functional dynamics of human centromeric chromatin. *Annu. Rev. Genomics Hum. Genet.* 7:301–313.
4. Butcher, L. M., and S. Beck. 2008. Future impact of integrated high-throughput methylome analyses on human health and disease. *J. Genet. Genomics.* 35:391–401.
5. Bird, A. P. 1986. CpG-rich islands and the function of DNA methylation. *Nature.* 321:209–213.
6. McClelland, M., and R. Ivarie. 1982. Asymmetrical distribution of CpG in an 'average' mammalian gene. *Nucleic Acids Res.* 10:7865–7877.
7. Elango, N., and S. V. Yi. 2011. Functional relevance of CpG island length for regulation of gene expression. *Genetics.* 187:1077–1083.
8. Kundu, T. K., and M. R. Rao. 1999. CpG islands in chromatin organization and gene expression. *J. Biochem.* 125:217–222.
9. Doerfler, W. 1983. DNA methylation and gene activity. *Annu. Rev. Biochem.* 52:93–124.
10. Goll, M. G., and T. H. Bestor. 2005. Eukaryotic cytosine methyltransferases. *Annu. Rev. Biochem.* 74:481–514.
11. Leonhardt, H., A. W. Page, …, T. H. Bestor. 1992. A targeting sequence directs DNA methyltransferase to sites of DNA replication in mammalian nuclei. *Cell.* 71:865–873.
12. Clark, T. A., I. A. Murray, …, J. Korlach. 2012. Characterization of DNA methyltransferase specificities using single-molecule, real-time DNA sequencing. *Nucleic Acids Res.* 40:e29.
13. Klimasauskas, S., S. Kumar, …, X. Cheng. 1994. HhaI methyltransferase flips its target base out of the DNA helix. *Cell.* 76:357–369.
14. Chandler, L. A., and P. A. Jones. 1988. Hypomethylation of DNA in the regulation of gene expression. *Dev. Biol.* 5(N Y 1985):335–349.
15. Cedar, H., and Y. Bergman. 2009. Linking DNA methylation and histone modification: patterns and paradigms. *Nat. Rev. Genet.* 10: 295–304.
16. Southern, E. M. 1984. DNA sequences and chromosome structure. *J. Cell Sci. Suppl.* 1:31–41.
17. Suzuki, M. M., and A. Bird. 2008. DNA methylation landscapes: provocative insights from epigenomics. *Nat. Rev. Genet.* 9:465–476.
18. Hermann, A., H. Gowher, and A. Jeltsch. 2004. Biochemistry and biology of mammalian DNA methyltransferases. *Cell. Mol. Life Sci.* 61:2571–2587.
19. Hermann, A., R. Goyal, and A. Jeltsch. 2004. The Dnmt1 DNA-(cytosine-C5)-methyltransferase methylates DNA processively with high preference for hemimethylated target sites. *J. Biol. Chem.* 279: 48350–48359.
20. Irizarry, R. A., C. Ladd-Acosta, …, A. P. Feinberg. 2009. The human colon cancer methylome shows similar hypo- and hypermethylation at conserved tissue-specific CpG island shores. *Nat. Genet.* 41: 178–186.
21. Doi, A., I. H. Park, …, A. P. Feinberg. 2009. Differential methylation of tissue- and cancer-specific CpG island shores distinguishes human induced pluripotent stem cells, embryonic stem cells and fibroblasts. *Nat. Genet.* 41:1350–1353.
22. Reference deleted in proof.
23. Lister, R., M. Pelizzola, …, J. R. Ecker. 2009. Human DNA methylomes at base resolution show widespread epigenomic differences. *Nature.* 462:315–322.
24. Bhutani, N., J. J. Brady, …, H. M. Blau. 2010. Reprogramming towards pluripotency requires AID-dependent DNA demethylation. *Nature.* 463:1042–1047.
25. Reference deleted in proof.
26. Choi, S. H., K. Heo, …, A. S. Yang. 2011. Identification of preferential target sites for human DNA methyltransferases. *Nucleic Acids Res.* 39:104–118.
27. Lavery, R., K. Zakrzewska, …, J. Sponer. 2010. A systematic molecular dynamics study of nearest-neighbor effects on base pair and base pair step conformations and fluctuations in B-DNA. *Nucleic Acids Res.* 38:299–313.
28. Pérez, A., I. Marchán, …, M. Orozco. 2007. Refinement of the AMBER force field for nucleic acids: improving the description of α/γ conformers. *Biophys. J.* 92:3817–3829.
29. Olson, W. K., A. A. Gorin, …, V. B. Zhurkin. 1998. DNA sequence-dependent deformability deduced from protein-DNA crystal complexes. *Proc. Natl. Acad. Sci. USA.* 95:11163–11168.
30. Lankas, F., J. Sponer, …, T. E. Cheatham, 3rd. 2003. DNA basepair step deformability inferred from molecular dynamics simulations. *Biophys. J.* 85:2872–2883.
31. Morozov, A. V., K. Fortney, …, E. D. Siggia. 2009. Using DNA mechanics to predict in vitro nucleosome positions and formation energies. *Nucleic Acids Res.* 37:4707–4722.
32. Orozco, M., A. Noy, and A. Pérez. 2008. Recent advances in the study of nucleic acid flexibility by molecular dynamics. *Curr. Opin. Struct. Biol.* 18:185–193.
33. Pérez, A., F. Lankas, …, M. Orozco. 2008. Towards a molecular dynamics consensus view of B-DNA flexibility. *Nucleic Acids Res.* 36:2379–2394.
34. Lankas, F., J. Sponer, …, J. Langowski. 2000. Sequence-dependent elastic properties of DNA. *J. Mol. Biol.* 299:695–709.

35. Paillard, G., and R. Lavery. 2004. Analyzing protein-DNA recognition mechanisms. *Structure.* 12:113–122.

36. Pérez, A., F. J. Luque, and M. Orozco. 2012. Frontiers in molecular dynamics simulations of DNA. *Acc. Chem. Res.* 45:196–205.

37. Podtelezhnikov, A. A., C. Mao, …, A. Vologodskii. 2000. Multimerization-cyclization of DNA fragments as a method of conformational analysis. *Biophys. J.* 79:2692–2704.

38. Tolstorukov, M. Y., A. V. Colasanti, …, V. B. Zhurkin. 2007. A novel roll-and-slide mechanism of DNA folding in chromatin: implications for nucleosome positioning. *J. Mol. Biol.* 371:725–738.

39. Balasubramanian, S., F. Xu, and W. K. Olson. 2009. DNA sequence-directed organization of chromatin: structure-based computational analysis of nucleosome-binding sequences. *Biophys. J.* 96:2245–2260.

40. Thåström, A., P. T. Lowary, …, J. Widom. 1999. Sequence motifs and free energies of selected natural and non-natural nucleosome positioning DNA sequences. *J. Mol. Biol.* 288:213–229.

41. Deniz, O., O. Flores, …, M. Orozco. 2011. Physical properties of naked DNA influence nucleosome positioning and correlate with transcription start and termination sites in yeast. *BMC Genomics.* 12:489.

42. Anderson, J. D., and J. Widom. 2000. Sequence and position-dependence of the equilibrium accessibility of nucleosomal DNA target sites. *J. Mol. Biol.* 296:979–987.

43. Pérez, A., F. J. Luque, and M. Orozco. 2007. Dynamics of B-DNA on the microsecond time scale. *J. Am. Chem. Soc.* 129:14739–14745.

44. Behe, M., and G. Felsenfeld. 1981. Effects of methylation on a synthetic polynucleotide: the B—Z transition in poly(dG-m5dC).poly(dG-m5dC). *Proc. Natl. Acad. Sci. USA.* 78:1619–1623.

45. Banyay, M., and A. Gräslund. 2002. Structural effects of cytosine methylation on DNA sugar pucker studied by FTIR. *J. Mol. Biol.* 324: 667–676.

46. Schones, D. E., K. Cui, …, K. Zhao. 2008. Dynamic regulation of nucleosome positioning in the human genome. *Cell.* 132:887–898.

47. Kaplan, N., I. K. Moore, …, E. Segal. 2009. The DNA-encoded nucleosome organization of a eukaryotic genome. *Nature.* 458:362–366.

48. Chung, H. R., and M. Vingron. 2009. Sequence-dependent nucleosome positioning. *J. Mol. Biol.* 386:1411–1422.

49. Cui, F., and V. B. Zhurkin. 2010. Structure-based analysis of DNA sequence patterns guiding nucleosome positioning in vitro. *J. Biomol. Struct. Dyn.* 27:821–841.

50. Travers, A., E. Hiriart, …, E. Di Mauro. 2010. The DNA sequence-dependence of nucleosome positioning in vivo and in vitro. *J. Biomol. Struct. Dyn.* 27:713–724.

51. Trifonov, E. N. 2010. Nucleosome positioning by sequence, state of the art and apparent finale. *J. Biomol. Struct. Dyn.* 27:741–746.

52. Olson, W. K., and V. B. Zhurkin. 2011. Working the kinks out of nucleosomal DNA. *Curr. Opin. Struct. Biol.* 21:348–357.

53. Field, Y., N. Kaplan, …, E. Segal. 2008. Distinct modes of regulation by chromatin encoded through nucleosome positioning signals. *PLOS Comput. Biol.* 4:e1000216.

54. Bai, L., and A. V. Morozov. 2010. Gene regulation by nucleosome positioning. *Trends Genet.* 26:476–483.

55. Segal, E., Y. Fondufe-Mittendorf, …, J. Widom. 2006. A genomic code for nucleosome positioning. *Nature.* 442:772–778.

56. Lee, W., D. Tillo, …, C. Nislow. 2007. A high-resolution atlas of nucleosome occupancy in yeast. *Nat. Genet.* 39:1235–1244.

57. Tillo, D., and T. R. Hughes. 2009. G+C content dominates intrinsic nucleosome occupancy. *BMC Bioinformatics.* 10:442.

58. Goñi, J. R., C. Fenollosa, …, M. Orozco. 2008. DNAlive: a tool for the physical analysis of DNA at the genomic scale. *Bioinformatics.* 24:1731–1732.

59. Goñi, J. R., A. Pérez, …, M. Orozco. 2007. Determining promoter location based on DNA structure first-principles calculations. *Genome Biol.* 8:R263.

60. Bertrand, H., T. Ha-Duong, …, B. Hartmann. 1998. Flexibility of the B-DNA backbone: effects of local and neighbouring sequences on pyrimidine-purine steps. *Nucleic Acids Res.* 26:1261–1267.

61. Nathan, D., and D. M. Crothers. 2002. Bending and flexibility of methylated and unmethylated EcoRI DNA. *J. Mol. Biol.* 316:7–17.

62. Mirsaidov, U., W. Timp, …, G. Timp. 2009. Nanoelectromechanics of methylated DNA in a synthetic nanopore. *Biophys. J.* 96:L32–L34.

63. Bell, A. C., and G. Felsenfeld. 2000. Methylation of a CTCF-dependent boundary controls imprinted expression of the Igf2 gene. *Nature.* 405:482–485.

64. Clark, S. J., J. Harrison, and P. L. Molloy. 1997. Sp1 binding is inhibited by (m)Cp(m)CpG methylation. *Gene.* 195:67–71.

65. Hark, A. T., C. J. Schoenherr, …, S. M. Tilghman. 2000. CTCF mediates methylation-sensitive enhancer-blocking activity at the H19/Igf2 locus. *Nature.* 405:486–489.

66. Davey, C. S., S. Pennings, …, J. Allan. 2004. A determining influence for CpG dinucleotides on nucleosome positioning in vitro. *Nucleic Acids Res.* 32:4322–4331.

67. Pennings, S., J. Allan, and C. S. Davey. 2005. DNA methylation, nucleosome formation and positioning. *Brief. Funct. Genomics Proteomics.* 3:351–361.

68. Felle, M., H. Hoffmeister, …, G. Längst. 2011. Nucleosomes protect DNA from DNA methylation in vivo and in vitro. *Nucleic Acids Res.* 39:6956–6969.

69. Choy, J. S., S. Wei, …, T. H. Lee. 2010. DNA methylation increases nucleosome compaction and rigidity. *J. Am. Chem. Soc.* 132:1782–1783.

70. Lee, J. Y., and T. H. Lee. 2012. Effects of DNA methylation on the structure of nucleosomes. *J. Am. Chem. Soc.* 134:173–175.

71. Lee, C. K., Y. Shibata, …, J. D. Lieb. 2004. Evidence for nucleosome depletion at active regulatory regions genome-wide. *Nat. Genet.* 36: 900–905.

72. Field, Y., Y. Fondufe-Mittendorf, …, E. Segal. 2009. Gene expression divergence in yeast is coupled to evolution of DNA-encoded nucleosome organization. *Nat. Genet.* 41:438–445.

73. Choi, J. K., J. B. Bae, …, Y. J. Kim. 2009. Nucleosome deposition and DNA methylation at coding region boundaries. *Genome Biol.* 10:R89.

74. Feng, J., X. Dai, …, C. He. 2010. New insights into two distinct nucleosome distributions: comparison of cross-platform positioning datasets in the yeast genome. *BMC Genomics.* 11:33.

75. Kaplan, N., I. Moore, …, E. Segal. 2010. Nucleosome sequence preferences influence in vivo nucleosome organization. *Nat. Struct. Mol. Biol.* 17:918–920, author reply 920–912.

76. Valouev, A., J. Ichikawa, …, S. M. Johnson. 2008. A high-resolution, nucleosome position map of C. elegans reveals a lack of universal sequence-dictated positioning. *Genome Res.* 18:1051–1063.

77. Wang, X., G. O. Bryant, …, M. Ptashne. 2011. An effect of DNA sequence on nucleosome occupancy and removal. *Nat. Struct. Mol. Biol.* 18:507–509.

78. Esteller, M. 2006. Epigenetics provides a new generation of oncogenes and tumour-suppressor genes. *Br. J. Cancer.* 94:179–183.

79. Chodavarapu, R. K., S. Feng, …, M. Pellegrini. 2010. Relationship between nucleosome positioning and DNA methylation. *Nature.* 466:388–392.

Membrane Tension, Myosin Force, and Actin Turnover Maintain Actin Treadmill in the Nerve Growth Cone

Erin M. Craig,[†] David Van Goor,[‡] Paul Forscher,[‡] and Alex Mogilner[†*]
[†]Department of Neurobiology, Physiology and Behavior, and Department of Mathematics, University of California, Davis, California; and [‡]Department of Molecular, Cellular, and Developmental Biology, Yale University, New Haven, Connecticut

ABSTRACT A growth cone is a motile structure at the tips of axons that is driven by the actin network and guides axon extension. Low actin adhesion to the substrate creates a stationary actin treadmill that allows leading-edge protrusion when adhesion increases in response to guidance cues. We use experimental measurements in the *Aplysia* bag growth cone to develop and constrain a simple mechanical model of the actin treadmill. We show that actin retrograde flow is primarily generated by myosin contractile forces, but when myosin is inhibited, leading-edge membrane tension increases and drives the flow. By comparing predictions of the model with previous experimental measurements, we demonstrate that lamellipodial and filopodial filament breaking contribute equally to the resistance to the flow. The fully constrained model clarifies the role of actin turnover in the mechanical balance driving the actin treadmill and reproduces the recent experimental observation that inhibition of actin depolymerization causes retrograde flow to slow exponentially with time. We estimate forces in the actin treadmill, and we demonstrate that measured G-actin distributions are consistent with the existence of a forward-directed fluid flow that transports G-actin to the leading edge.

INTRODUCTION

Cell migration is a ubiquitous process underlying morphogenesis, wound healing, and cancer, among other biological phenomena (1). Leading-edge protrusion on flat surfaces—the first step in cell crawling—relies on continuous remodeling of a cytoskeletal structure called the lamellipodium (2), a broad and flat network of actin filaments. The lamellipodium is several microns in width, but only ~0.1–0.2 μm high (3). The actin network, a polarized dendritic array (Fig. 1 *A*), grows near the lamellipodial leading edge (4). Combined with adhesion to the substrate, this growth moves the leading edge forward in response to guidance cues. Meanwhile, the actin network disassembles throughout the lamellipodium (4), and actin monomer diffusion recycles the monomers to the leading edge (4). Diffusive transport can be assisted by a forward-directed flow of the fluid fraction of the cytoplasm (5). The front-to-rear length of the dynamic lamellipodial network is governed by the dynamics of this biochemical cycle in which actin is being continuously converted from monomer to polymer and back again (6).

Growing actin filaments push forward on the membrane enveloping the leading edge, resulting in membrane tension (7). The membrane tension slows actin polymerization by pushing back on growing filaments (8–10).When adhesion to the substrate is weak or absent, membrane tension pushing back on the filaments also generates retrograde flow of the actin network (11–14). In some cells (including keratocytes and nerve growth cones), myosin II (which we refer to simply as myosin) also contributes to retrograde flow in the lamellipodium by contracting the actin network and disassembling it at the rear (11,15–17). This retrograde flow, balanced by leading-edge actin polymerization (4) and depolymerization throughout the network (18), creates a stationary lamellipodial treadmill. According to the adhesion clutch hypothesis (19–21), increased adhesion attenuates the retrograde flow, so that the leading-edge actin polymerization is not cancelled by the flow anymore, but rather produces net protrusion and resulting cell motility.

Mechanical components of the actin treadmill have been identified and many of their interactions characterized (22). This lays the groundwork for the challenging task of developing a quantitative understanding of the relative contributions of myosin, leading-edge tension, and actin turnover to the balance of forces underlying the treadmill. We seek to address this challenge in the context of the nerve growth cone, a sensory motile structure that guides axon growth (23). A growth cone is composed of two regions (22), a central (C) domain filled with organelles and microtubules and a peripheral (P) domain (Fig. 1 *A*). The P domain is composed of a fine veil network of actin filaments interspersed with tightly packed parallel actin bundles called filopodia (24) (Fig. 1 *A*). The P-domain actin network undergoes dynamic treadmilling, similar to the lamellipodial region of other motile cells. The boundary between the peripheral and central domains of the growth cone is known as the transition (T) zone (Fig. 1 *A*). Retrograde flow of veil and filopodial actin in the P domain slows dramatically when it reaches the T zone (25), perhaps in part because the microtubules and vesicles in the central domain create a physical barrier to continued flow. Although uniform veil F-actin depolymerization throughout the P domain produces a lower network density at the T zone

Submitted October 7, 2011, and accepted for publication March 2, 2012.

*Correspondence: mogilner@math.ucdavis.edu

Editor: Alissa Weaver.

0006-3495/12/04/1503/11 $2.00

doi: 10.1016/j.bpj.2012.03.003

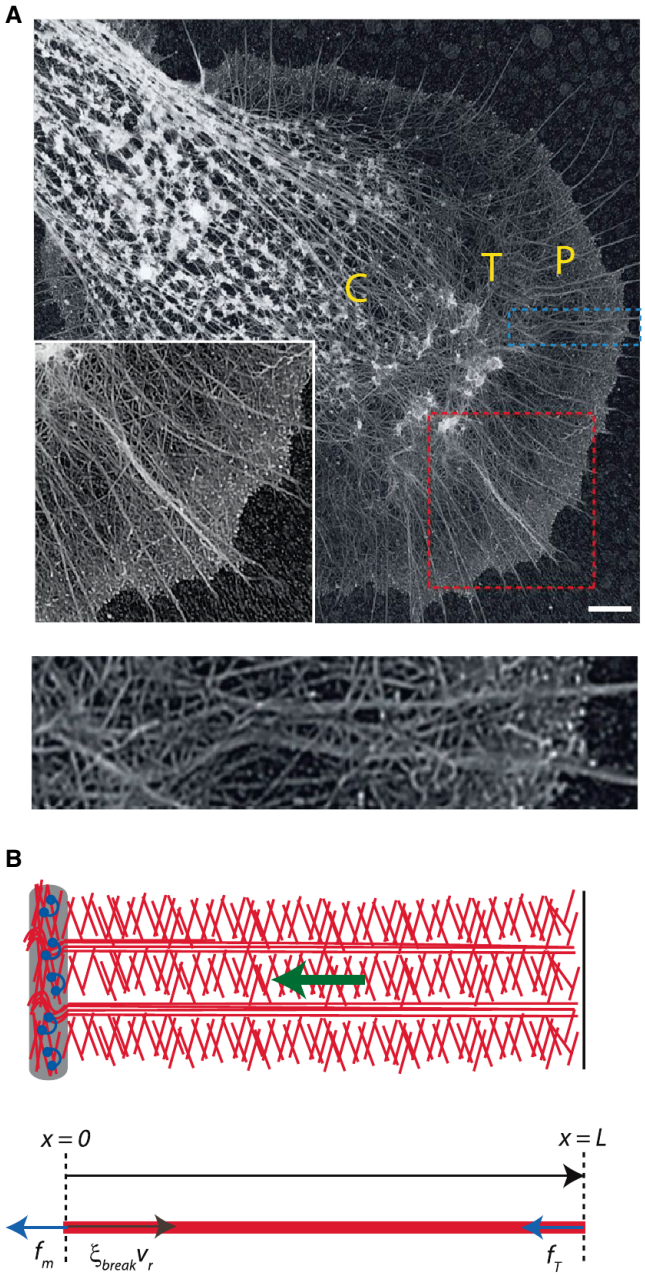

FIGURE 1 Actin treadmill in the nerve growth cone. (*A*) Upper, Electron microscopy image of an *Aplysia* bag cell nerve growth cone, obtained as described in Schaefer et al. (40). (*Inset*) Higher magnification of P domain (*larger box*), showing the dendritic network of veil filaments interspersed with filopodial bundles. The central (C) domain, transition (T) zone, and peripheral (P) domain are labeled. Scale bar, 3.5 μm. Lower, Higher magnitude of quasi-1D slice of P domain (*smaller box* in *upper image*), to illustrate a representative region of interest for the 1D model illustrated in *B*. (*B*) Upper, Schematic of the actin treadmill components: actin filaments (*center*), leading edge (*right*), and T zone and myosin (*left*). The actin network undergoes retrograde flow (*green arrow*). Lower, balance of forces in the 1D model for the P-domain actin network. The coordinate x represents the distance from the boundary between the T zone and P domain, with $x = L$ corresponding to the leading edge. The active forces driving retrograde flow are membrane tension, f_T, and myosin contraction, f_m (*arrows pointing to the left*). The effective drag force opposing retrograde flow (*arrow pointing to the right*) arises from the necessity to disassemble the actin network at the T zone.

than at the leading edge (26), the remaining actin network must be disassembled at the T zone to allow recycling of actin and continuous treadmilling.

Here, we develop a quantitative mechanical model of the actin treadmill in the P domain of nerve growth cones. Aplysia bag cell neurons are a convenient model system for understanding the mechanics of the steady-state lamellipodial treadmill, because when they are plated on poly-L-lysine-coated coverslips (17), adhesion of actin to the substrate is very weak, making the cones stationary with a rapidly treadmilling P domain. It is useful to analyze a system with rapidly treadmilling actin and negligible adhesion, because mechanical properties of adhesions are often complex (14,27) and the treadmill has to be understood and calibrated before attempting to quantify the adhesion clutch coupled with actin dynamics. Another advantage of this model system is the abundance of quantitative data (26,28,29), which offer the rare opportunity not only to fully constrain the model using part of the data but also to test the model predictions against the rest of the data within a single experimental system. The actin network components and characteristics are conserved across various cell types (2), and we expect that a growth cone model will also be relevant to other types of cells. Previous models of growth cone motility have focused primarily on chemical guidance (30–33), and one early model explored the mechanism for traction force generation (34). In contrast, the model presented here is designed to investigate the mechanical properties of the growth-cone lamellipodial treadmill. We model the P-domain actin array and use recent experiments in the growth cone to constrain the model and determine the balance of forces, movements, and actin turnover in the P domain.

A key outcome of the model is that the actin network rapidly adjusts to mechanical perturbations by transitioning into a new steady state with different P-domain width and retrograde flow speed, an adaptability that may contribute to robust growth-cone motility in varying biological conditions. We also determine numerical values for the myosin contractile stress and membrane tension force driving retrograde flow, and suggest that veil and filopodial filament breaking contribute equally to the resistance to retrograde flow. The model predicts exponential slowing of retrograde flow if depolymerization is inhibited, in good numerical agreement with experimental measurements (26). Finally, we use measurements of G-actin spatial profiles in Van Goor et al. (26) to estimate the forward-directed fluid flow in the P domain, and we find that it is on the same order of magnitude as actin retrograde flow.

MATERIALS AND METHODS

One-dimensional model of the actin treadmill

We consider the P-domain actin network, which assembles at the leading edge and disassembles at a constant rate while undergoing retrograde flow. Actin retrograde flow in an *Aplysia* bag growth cone is in the radial

direction (25), and considering a segment of the P domain a few microns wide allows a one-dimensional (1D) description (Fig. 1 *A*). We assume that the flow is driven by myosin motors pulling within the T zone and membrane tension pushing from the leading edge and that it is resisted by an effective drag force that depends on the density of filaments at the T zone. The P-domain width and retrograde flow speed are dynamic variables that depend on the mechanical properties of the growth cone and the balance of forces on the actin network (Fig. 1 *B*).

Below, we outline the biological assumptions and develop the mathematical details of the model.

Kinematics

The speed of protrusion in the lab coordinate system, v_{cell}, is

$$v_{cell} = v_g - v_r, \tag{1}$$

where v_g is the actin growth rate and v_r is the retrograde flow rate. In the stationary P domain, $v_{cell} = 0$ and $v_g = v_r$. The model illustrated in Fig. 1 *B* is based on the following force-speed relations.

Actin growth rate

A few recent studies have reported direct measurements of membrane tension in epithelial (35) and neutrophil (36) motile cells in the tens of pN range, as well as a lower tension in nerve growth cones (37), and have suggested that this tension slows actin growth. We assume that the leading-edge membrane is under tension and that the tension force/μm of the leading edge, f_T, reduces the polymerization speed according to the force-velocity relation

$$v_g = \begin{cases} v_0\left(1 - \left(\dfrac{f_T}{f_s}\right)^{\omega}\right) & \text{if } f_T < f_s, \\ 0 & \text{if } f_T \geq f_s, \end{cases} \tag{2}$$

where f_s is the stall force/μm and v_0 is the free polymerization speed. Measurements (8,10) and theory (9) have confirmed the validity of Eq. 2 and have yielded the parameter $\omega > 1$, such that the velocity is insensitive to tension at low loads. We assume that the membrane tension is proportional to the P-domain width rather than to the whole growth cone area, based on the observations discussed in detail in the Supporting Material.

Retrograde flow rate

Our main hypothesis is that resistance to buckling and breaking filaments in the T zone creates a drag opposing the myosin pulling, f_m, and membrane pushing, f_T, forces on the network. The balance of these three forces determines the retrograde flow. We suggest that the retrograde flow speed is determined by the force balance (Fig. 1 *B*),

$$f_m + f_T = \xi_{break} v_r. \tag{3}$$

Four assumptions underlie Eq. 3: 1), The veil-filopodia network deforms very little, so that no resistance to the retrograde flow comes from compression or shear in the front few microns of the network, and the forces pulling the network at the rear and pushing it at the front simply add. Data and previous modeling indicate that there is a small amount of compression and shear in the lamellipodium of other cells (38,39). However, there is little gradient in the symmetric retrograde flow speed from the growth cone leading edge to the T zone (26), suggesting that compression and shear can be neglected. 2), The adhesion force is negligible, which allows us to isolate the dynamics of the stationary treadmill from potentially complicated adhesion dynamics. 3), We treat myosin contractility as a constant external force, f_m (per unit edge length), acting on the actin network in the P domain, based on the assumption (supported by the observation in Medeiros et al. (28)) that myosin is localized in the T zone and pulls the actin network inward. 4), Electron microscopy shows that the filaments and bundles bend, buckle, and break in the T zone (40) (Fig. 1 *A*), and we assume that this breaking force resisting the network flow is viscous-like in proportion to the flow rate (see Supporting Material for physical reasoning). The parameter ξ_{break} characterizes the resistance to flow associated with breaking actin filaments at the T zone.

We assume, and justify below by comparison with experiment, that ξ_{break} is proportional to the actin-filament density remaining at the T zone after partial network disassembly in the P domain, and that veil and filopodial filaments contribute equally to the force, which leads to the equation

$$\xi_{break} = F_{break}\big(a_f + a_l(x = 0, t)\big). \tag{4}$$

Here the parameter F_{break} is proportional to the breaking force/filament, f_{break}, and a_f and a_l are the filopodial and veil filament densities, respectively, at the boundary between the P domain and the T zone.

Actin disassembly

Based on experimental data (26), we assume a constant net rate, γ, of the veil filament network disassembly, which yields the following equation for the veil actin density:

$$\frac{\partial a_l}{\partial t} = -\gamma a_l + v_r \frac{\partial a_l}{\partial x}. \tag{5}$$

We do not model the underlying molecular mechanism of network disassembly here. The steady-state veil actin distribution for the stationary treadmill is then

$$a_l(x) = a_0 \exp\left(-\frac{\gamma(L - x)}{v_r}\right). \tag{6}$$

Here, x is the anterior-posterior coordinate; $x = 0$ refers to the T zone and $x = L$ corresponds to the leading edge of the P domain (Fig. 1 *B*). In experiments, the observed distance between the T zone and the leading edge, L, depends on mechanical properties of the actin treadmill components; for example, reduced myosin density inhibits actin disassembly, producing a larger P domain (28). Therefore, L is a dynamic variable of our model. Parameter a_0 characterizes a constant density of the veil actin filaments at the leading edge (number/μm). Using the same formulation for the filopodial actin density, $a_{fil}(x)$, the total actin density in the P domain is given by

$$a_l(x) + a_{fil}(x) \approx a_0 \exp\left(-\frac{\gamma(L - x)}{v_r}\right) + a_f, \tag{7}$$

where a_f is the leading-edge filopodial density. Filopodial bundles have significantly slower turnover rates (estimated half-life ~25 min) than veil F-actin (0.5–3 min) (41). The observed actin flow in the growth cone is such that a filament travels from the front to the T zone in just 1–3 min, allowing us to approximate the actin density along filopodia as constant from front to rear. This means that filopodia will not turn over significantly and must be recycled by other means, most likely by being mechanically broken.

G-actin spatial distribution

The G-actin concentration can be found from equations describing the balance of F- and G-actin, governed by disassembly and transport processes. The equation for the veil (lamellipodial) F-actin concentration, F_l, has the same form as Eq. 5, $\partial F_l/\partial t = -\gamma F_l + v_r \partial F_l/\partial x$, and has the same solution as Eq. 6 (a_l and F_l simply have different dimensions). The total F-actin density distribution in the steady state is then given by $F(x) = F_l(x) + F_{fil}(x) \approx F_0 \exp(-\gamma(L - x)/v_r)$. The equation for the G-actin concentration, G, has the form

$$\frac{\partial G}{\partial t} = \gamma F_l(x) - v_f \frac{\partial G}{\partial x} + D \frac{\partial^2 G}{\partial x^2}. \tag{8}$$

Here, the first term on the right-hand side corresponds to the net local source of G-actin due to lamellipodial F-actin disassembly, and we neglect the contribution of the filopodia. The second term describes the hypothetical flow of the fluid fraction of cytoplasm forward with speed v_f. Such flow can be generated by myosin contraction at the rear and membrane permeability at the front, as observed in Keren et al. (5). The third term describes actin monomer diffusion. The boundary conditions at the leading edge ($x = L$) are that there is a finite G-actin concentration there, G_0, necessary to maintain the protrusion with the observed speed, and that the outflux of the G-actin is equal to the influx of the F-actin: $\left(v_f G - D\frac{\partial G}{\partial x}\right)\Big|_{x=L} = v_r F_0$ (all actin monomers assembling onto the filament tips at the front become F-actin), similar to Lan and Papoian (42). In this simple model, we have omitted separation of the G-actin pool into fractions characterized by binding with various proteins. More detailed models have been investigated (7,18), but qualitatively, the result described below regarding the gradient of the total G-actin is insensitive to these details. Model equations were solved as described in the Supporting Material.

Experimental constraints on the model

The actin treadmill model described by Eqs. 1–7 can be fully constrained by comparing model predictions with results from a set of experiments with the *Aplysia* bag nerve growth cone reported in three studies (26,28,29) in which P-domain width and retrograde flow speed were measured under several drug-treatment conditions (Fig. 2 and Table S1): 1), control conditions; 2), actin polymerization inhibited by cytochalasin B; 3), filopodia removed by treatment with low cytochalasin B; 4), myosin inhibited by blebbistatin + actin polymerization inhibited by cytochalasin B; 5), myosin contractile forces inhibited by blebbistatin; 6), actin depolymerization inhibited by jasplakinolide; and 7), actin depolymerization inhibited by jasplakinolide in cones pretreated with blebbistatin. We discuss the respective experimental results in the Supporting Material. Note that all of the experiments we consider were performed on the same experimental system, allowing us to constrain the model in a self-consistent way.

RESULTS

Calibrating the model: roles of filopodia, myosin force, and membrane tension

Veil and filopodial filament breaking provides mechanical resistance to retrograde flow

A major assumption of the model is that there is a certain breaking force per actin filament at the T zone, and that this breaking force is the same for veil and filopodial filaments. We further assume that the effective drag force opposing retrograde actin flow is given by the amount of force required to break all the filaments. We can test these assumptions by comparing the predictions of the model with experimental measurements of the retrograde flow and P-domain width in the control case and when filopodia are absent (29). When filopodia were removed by treating the growth cone with low levels of cytochalasin B, the velocity of retrograde flow was unchanged from the control case, but the P-domain width decreased. Assuming that the myosin force, f_m, does not change after filopodia removal, we can infer that the effective drag, $\xi_{break} = f_m/v_r$, is also unchanged. In other words, the location of the transition zone is determined by the distance from the leading edge at which F-actin density is low enough for myosin contractile forces to effectively break down the network; when filopodia are removed and no longer contribute to the F-actin density distribution, the P domain narrows such that the F-actin density at the T zone remains the same for a fixed myosin density. Setting the expression for ξ_{break} (Eqs. 4 and 7) under control conditions equal to the expression for

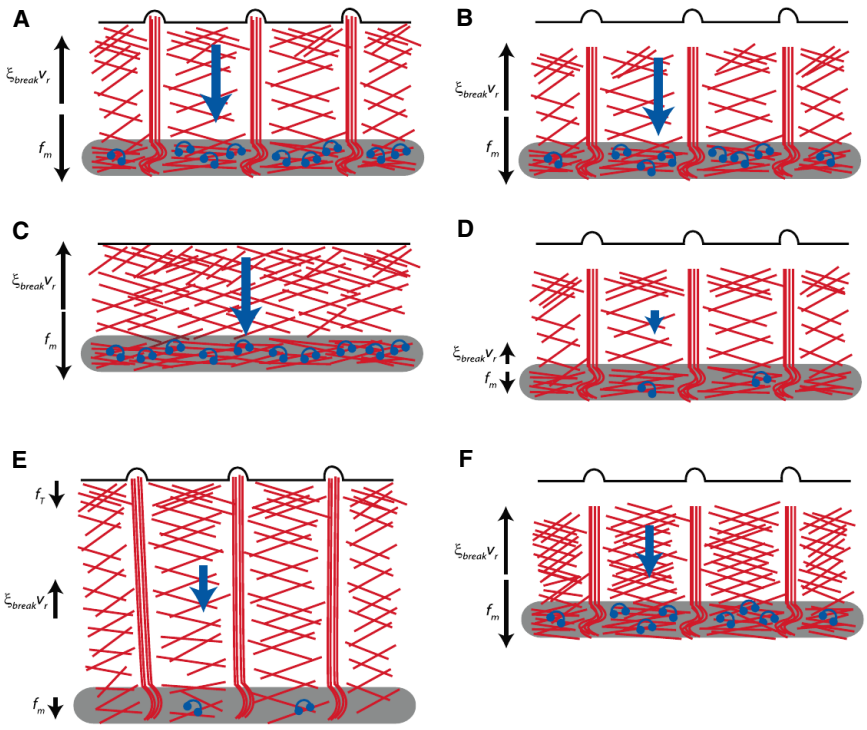

FIGURE 2 Schematics of growth-cone experiments used to constrain and test the model. (*A*) Under control conditions, myosin pulling is balanced by the actin breaking force. (*B*) When the leading-edge polymerization is inhibited by cytochalasin B, the force balance does not change. (*C*) When filopodia are removed with a low concentration of cytochalasin B, the force balance and flow do not change but the P domain shortens. (*D*) Inhibition of both polymerization (by cytochalasin B) and myosin (by blebbistatin) lowers both pulling and resistive forces and actin flow. (*E*) When myosin is inhibited by blebbistatin, the P domain widens and the remaining actin flow is driven by a combination of leading-edge tension and weakened myosin contractile force. (*F*) Inhibition of actin depolymerization by jasplakinolide increases the resistance of the actin network and slows the actin flow.

the case without filopodia, we establish a relationship between the leading-edge veil and filopodial densities:

$$\frac{a_f}{a_0} = \exp\left(\frac{-\gamma L_{nofil}}{v_r}\right) - \exp\left(\frac{-\gamma L}{v_r}\right), \quad (9)$$

where L, v_r, and γ are the control values for the P domain width, retrograde flow, and veil depolymerization rate, and L_{nofil} is the P-domain width after filopodial removal (Fig. S1 *A*). Measured values for these parameters (Table S2) allow us to estimate the right-hand side of Eq. 9, yielding $a_f/a_0 \approx 0.08$.

This prediction is consistent with experimental estimates of veil and filopodial actin filament densities: EM images of a growth-cone P domain show ~20 filopodial bundles for every 30 μm in width along the leading edge (43). If each filopodial bundle is comprised of $\approx$25 individual filaments (44), the filopodial filament density is $a_f \approx 15/\mu$m. Veil filament density is similar to the lamellipodial density of barbed ends at the leading edge of epithelial cells, which is of the order of $a_0 \approx 200/\mu$m (3,7), so $a_f/a_0 \approx 0.075$. The consistency between these measurements and the prediction of Eq. 9 supports the model assumption that filopodial and veil actin contribute equally to retrograde flow resistance.

The myosin contractile force, f_m, exerted on the network is equal to the force/filament, f_{break}, times the actin-filament density at the transition domain. Using experimentally measured values for P-domain width and retrograde flow speed (Table S1) and the leading-edge veil and filopodial densities (Table S2), and a theoretical estimate for f_{break} (Table S2), we calculate $f_m = f_{break}(a_f + a_0\exp(-\gamma L/v_r)) \approx 1$ nN/μm. A single myosin motor domain exerts forces on the order of 1 pN, suggesting that there are ~1000 motors/μm exerting contractile force in the P domain, consistent with other cell data (45,46). According to our assumption that buckled filaments in the T zone exert an equal and opposite effective drag force on the P-domain network, the effective drag coefficient opposing retrograde flow under control conditions is $\xi_{break} = f_m/v_r \approx 170$ pN $\times$ min/μm^2.

P-domain width adapts to mechanical perturbations to maintain a balance of forces

When leading-edge polymerization and myosin forces are both inhibited (after treating growth cones with cytochalasin B and blebbistatin, the P-domain leading edge retreats from the membrane, nullifying potential membrane tension), the remaining retrograde flow is $\approx$20% of the control value (28). This observation suggests that the residual myosin forces under blebbistatin treatment are $\approx$20% of f_m under control conditions, so $f_m^b = 0.2\,f_m$. When growth cones are treated with blebbistatin alone, inhibiting myosin without interfering with actin polymerization, the retrograde flow, v_r^b, is $\approx$50% of the control value and the P-domain width expands by $\approx$80% relative to control (28). In this case, the remaining retrograde flow is higher than what would be predicted if retrograde flow were still driven by myosin forces alone. The additional retrograde flow can be explained by two factors: reduced resistance to flow, because a larger P-domain width decreases the actin density at the boundary between the P domain and the T zone (Eq. 7), and hypothetical leading-edge tension that arises due to the expansion of the P-domain width. Indeed, cell protrusion requires membrane delivery to the front against a tension gradient (47) and is associated with increasing membrane tension (35). Using the P-domain width measurement $L_b \approx 13$ μm under blebbistatin conditions (28), we can estimate the effective drag coefficient for blebbistatin-treated cells, $\xi_{break}^b = \xi_{break}(a_f + a_l(L_b, v_r^b))/(a_f + a_l(L, v_r))$ (Eqs. 4 and 7), and find that the leading-edge tension, f_T^b, in this case is $f_T^b = \xi_{break}^b v_r^b - f_m^b \approx 90$ pN/μm. Using the steady-state condition for the blebbistatin-treated cells ($v_g^b = v_r^b = 0.5v_0$), we can determine the actin-network stall force, f_s. According to the load-velocity relationship for actin-network polymerization (Eq. 2), $f_s = f_T^b/(1 - v_g^b/v_0)^{1/\omega} = f_T^b/0.5^{1/\omega} \approx 100$ pN/μm (Fig. S1 *B*), where we have used $\omega = 6$ based on experimental measurements (10). This stall force is lower than that measured for motile fish keratocyte cells (~400 pN/μm) (8), but the order of magnitude is the same.

These results illustrate a key feature of the actin-network treadmill: the steady-state P-domain width adapts to maintain a balance of active forces (myosin and tension) and passive forces (resistance to filament breaking). Under control conditions, myosin forces alone drive retrograde flow quickly enough to keep up with leading-edge polymerization, thus alleviating leading-edge membrane tension. In this case, the P-domain width is determined by the distance from the leading edge at which the actin-network density provides enough resistance to balance the myosin forces driving the flow. When myosin is inhibited, this initially produces an imbalance between the leading-edge polymerization and the reduced retrograde flow speed. Initial increase of the P-domain width creates membrane tension, which in turn increases retrograde flow speed. The new steady-state treadmill is achieved when the P domain has expanded enough for the combination of membrane tension and remaining myosin forces to balance the passive force associated with filament breaking at the T zone. Our calculations suggest that myosin contractile forces still contribute significantly to the treadmill dynamics after blebbistatin treatment ($f_m^b = 0.2f_m \sim 200$ pN/μm, compared with $f_T^b \sim 100$ pN/μm). This dynamic transition from the control steady-state treadmill to the steady-state treadmill under blebbistatin conditions is illustrated with numerical calculations based on Eqs. 1–7 (Fig. 3). Note that the values of f_s and ω determine how quickly the system evolves to a new steady state, but do not affect the values of the steady-state retrograde flow speed or P-domain width (Fig. S2). The

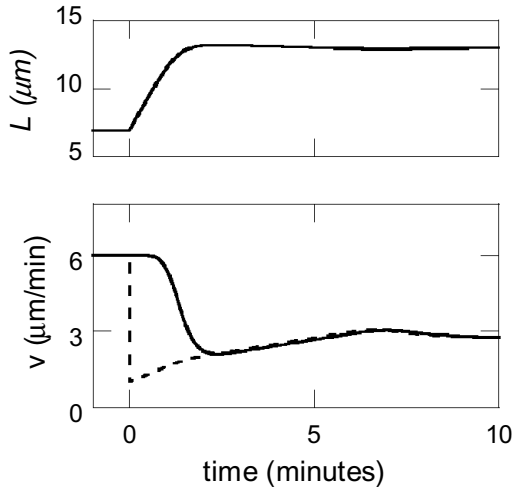

FIGURE 3 P-domain width adapts to mechanical perturbations to maintain treadmill. Numerical calculation of the P-domain width, L (*upper*), polymerization speed, v_g (*lower, solid line*), and retrograde flow speed, v_r (*lower, dashed line*), before and after blebbistatin treatment (at time $t = 0$), illustrating the transition to a new steady-state treadmill. Using calibrated values of the system parameters, the model reproduces experimental measurements of v_r and L after blebbistatin treatment. Note that the steady-state values of L and v_r are independent of the polymerization load-velocity parameter ω (Fig. S2).

constrained values of the model parameters are summarized in Table S2. The model calibration, and the resulting qualitative insights, are relatively robust to variation in the measured values of v_r and L that can be expected from one growth cone to the next (Supporting Material).

Testing the model: role of actin turnover

F-actin disassembly throughout the P domain lowers effective drag force at the transition zone

Now that the F-actin treadmill model is fully constrained, with no remaining free parameters, additional experiments can be used to test the model assumptions. In particular, we consider experiments in which the role of actin turnover in P-domain dynamics was explored (26).

When leading-edge polymerization in the growth cone is inhibited by application of cytochalasin B, ongoing retrograde flow at a constant speed causes the network to retreat from the leading edge (28). We can simulate this experiment using reaction drift (Eq. 5) for veil actin density, $a_l(t)$, in combination with the time-dependent retrograde flow speed, $v_r' = v_r\left(a_f + a_0 e^{-\gamma L/v_r}\right)\Big/\left(a_f + a_l(t)|_{x=0}\right)$ (Eqs. 3 and 4), where v_r and L are the values measured under control conditions. In principle, this expression could predict the retrograde flow rate varying with time, because the veil actin density at the T zone could vary transiently. However, when we begin with the steady-state actin-density distribution in control (Eq. 7) as the initial condition, and then remove the boundary condition of constant leading-edge density, $a_0 + a_f$, allowing the density distribution to evolve, we find that the resulting rate of retrograde flow balances exactly with the rate of depolymerization, such that the actin density at the T domain ($x = 0$) remains constant (Fig. 4 *A*). For this reason, the retrograde flow speed does not change, in agreement with the experimental observation.

On the other hand, when actin depolymerization throughout the P domain is inhibited by treating a growth cone with jasplakinolide (26), the pool of available G-actin is depleted, which essentially freezes the network actin turnover. As a result, the network is cleared from the P domain by continued myosin pulling at a retrograde flow speed that decreases exponentially with time (26). Fluorescent images and electron micrographs illustrate a buildup of actin filaments in the transition zone coincident with retrograde flow deceleration. We simulate this experiment by numerically calculating the time-dependent actin density distribution in the manner described in the previous paragraph, but this time using the smaller depolymerization rate, γ_J, measured under jasplakinolide conditions (Table S2). In this case, the balance between depolymerization and retrograde flow rates is no longer maintained, and the actin density at the T zone increases with time, in agreement with the experimental observation (Fig. 4 *B*). This in turn causes retrograde flow speed to decrease exponentially with time, in good numerical agreement with the experimental data (Fig. 4 *C*). In these two cases, the model with no tunable parameters successfully reproduces experimentally observed behavior and illustrates the role of actin turnover in maintaining the balance of forces in the actin treadmill. This supports the assumption that retrograde flow is opposed by an effective drag force associated with actin filament disassembly at the T zone, and illustrates that constant depolymerization throughout the P domain is necessary to maintain a balance of forces on the actin network.

The decay rate of the retrograde flow speed after jasplakinolide treatment, relative to the initial speed, is only sensitive to the actin depolymerization parameters γ and γ_J and does not depend on the initial values of v_r and L. For instance, a lower initial value of v_r produces a steeper initial actin-density gradient (Eq. 6), which in turn causes the T-domain actin density to increase more quickly after jasplakinolide treatment. However, the retrograde flow balances with the actin gradient so that the T-domain actin density changes by the same ratio for a given time interval. For this reason, $v_r(t)/v_r(t = 0)$ is independent of the initial value of v_r. Indeed, growth cones pretreated with blebbistatin (which alters the steady-state v_r and L but has no significant effect on γ and γ_J (26)) exhibit nearly the same retrograde flow decay rate after jasplakinolide treatment as the control cones (26), in agreement with this model prediction. For the same reason, the model predicts that $v_r(t)/v_r(t = 0)$ is independent of the veil actin filament

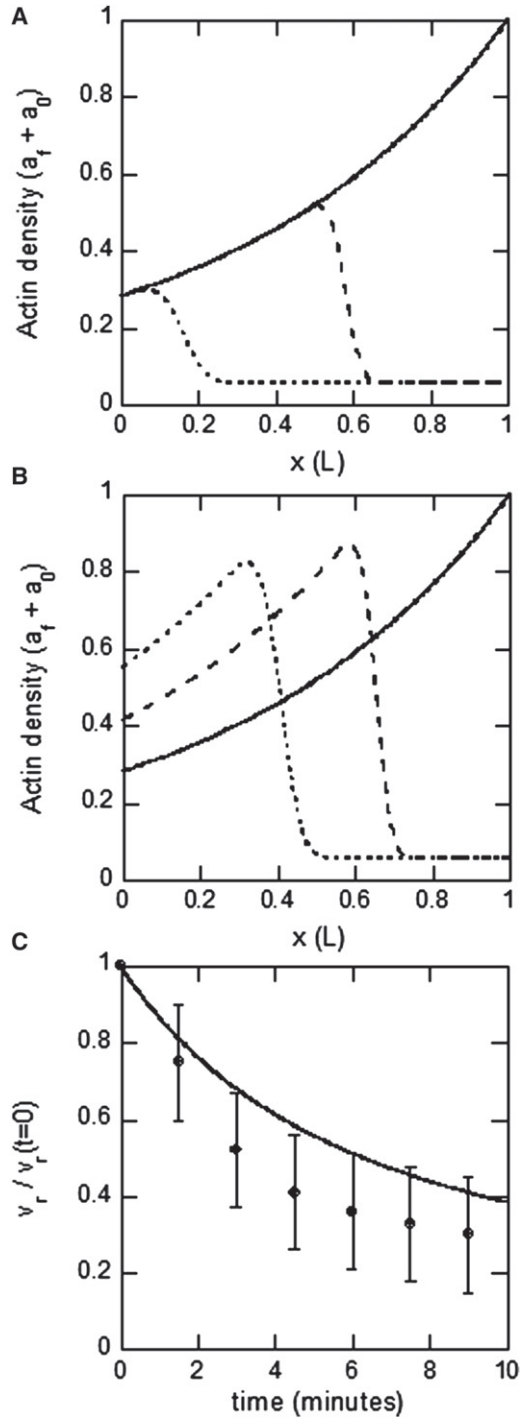

FIGURE 4 Model testing: role of actin turnover. (*A*) Actin density distribution calculated from Eq. 6 at several times after treatment with cytochalasin B, inhibiting leading-edge polymerization ($t = 0$, solid line; $t =$ 3 min, dashed line; $t = 6$ min, *dotted line*). Because the actin density at the transition domain remains constant, the resulting v_r is also constant. (*B*) Same as *A*, but with a lower depolymerization rate, γ_J, corresponding to the case of jasplakinolide-treated growth cones. In this case, the actin density at the transition domain increases with time due to the slower rate of depolymerization in the network as it moves rearward. (*C*) Retrograde flow versus time after jasplakinolide treatment, resulting from the actin density calculations in *B* (*solid line*) and experimental measurements (*data points*).

density at the leading edge, which decreases after jasplakinolide treatment (26).

Model predictions: role of G-actin concentration in treadmill and mechanism of G-actin recycling

P-domain width and retrograde flow are sensitive to leading-edge G-actin concentration

Now that the F-actin treadmill model (Eqs. 1–7) has been constrained and tested by published experimental data, we can use the calibrated model to illuminate the role of the G-actin distribution in the treadmill dynamics, and explore a hypothetical mechanism for recycling of G-actin to the leading edge. Note that our previous calculations of physical parameters for the F-actin treadmill do not depend in a detailed way on the G-actin distribution according to our assumptions that polymerization takes place primarily at the leading edge, and depolymerization is uniform throughout the P domain. However, we expect that the rate of actin polymerization will depend on the pool of available G-actin, and we assume for simplicity that the polymerization rate under zero load, v_0, is directly proportional to the leading-edge G-actin concentration.

To address the question of how the treadmill dynamics depends on the available pool of G-actin, we begin by considering what would happen if the level of G-actin (and thus the unloaded actin polymerization rate v_0) in the stationary growth cone were suddenly increased.

As discussed previously, under control conditions the membrane is not under tension ($f_T = 0$), and thus, we have $v_g = v_0 = v_r = f_m/\xi_{break}$. If the unloaded polymerization speed is suddenly increased by a factor α, the initial imbalance between polymerization speed and retrograde flow speed will cause P-domain expansion, which produces leading-edge membrane tension ($f_T > 0$). The leading-edge tension will increase the retrograde flow and decrease the polymerization speed until a new steady state is reached. In the Supporting Material, we find the relationship between the factor α, by which v_0 was increased, and the resulting steady-state P-domain width L'. Numerical calculations show that if the G-actin concentration is at least doubled, the P-domain width will approximately double to $L' \sim 12 - 14$ μm, producing steady-state membrane tension on the order of $f_T \sim 100$ pN/μm (Fig. 5 *A*). The resulting steady-state retrograde flow is $v_r' \sim 7$–8 μm/min (Fig. 5 *B*), an increase from the control value due to the added tension force on the network and the reduced resistance to flow associated with breaking forces (ξ_{break} decreases with L' because actin has more time to depolymerize before reaching the T zone).

We also consider a second hypothetical experiment in which a blebbistatin-treated growth cone is subjected to a sudden increase in G-actin concentration. The result, in the Supporting Material, shows that in this case, the

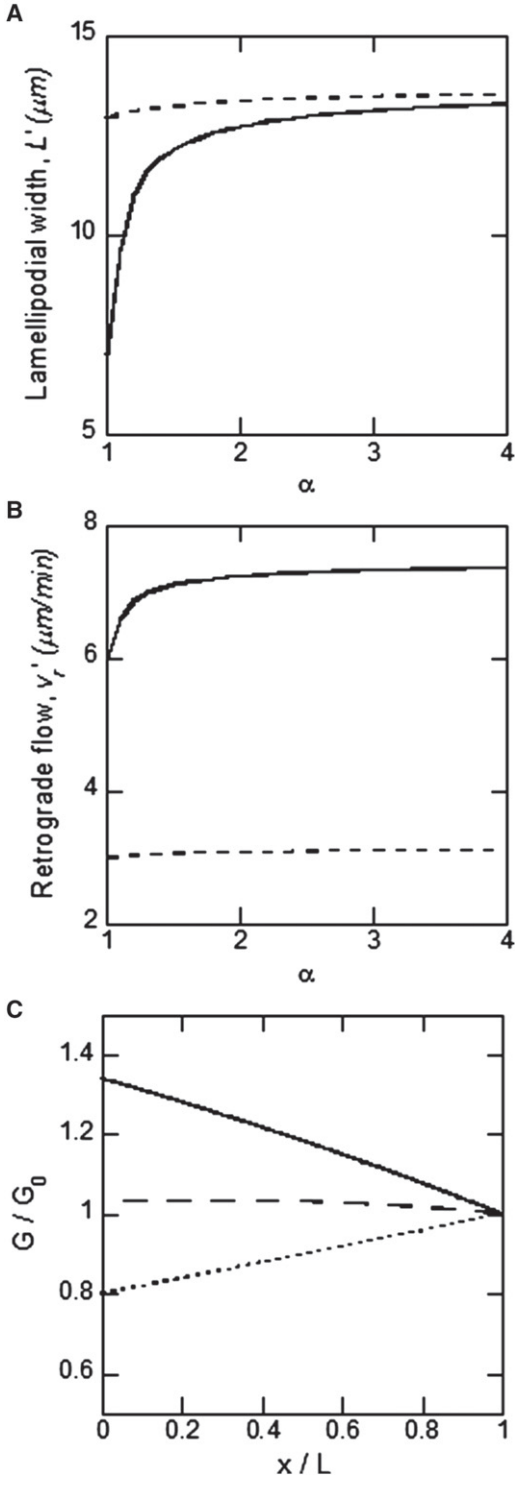

FIGURE 5 Model prediction for G-actin increase. (*A*) P-domain width as a function of G-actin increase factor α for control conditions (*solid line*) and for blebbistatin-treated growth cones (*dashed line*), based on expressions derived in the Supporting Material. (*B*) Retrograde flow rate versus α for the same conditions as in *A*. (*C*) G-actin spatial profiles (normalized by G_0) predicted by Eq. 11 for $v_f = 0$ μm/s (*dotted line*), 0.15 μm/s (*dashed line*), 0.3 μm/s (*solid line*). We used parameters L, γ, and v_r measured in Van Goor et al. (26), $D = 5$ $\mu m^2/s$ (54), and the ratio $F_0/G_0 = 2$ (55).

steady-state P-domain width and retrograde flow speed are relatively insensitive to increase in G-actin concentration (Fig. 5, *A* and *B*). This is because even for control levels of G-actin (i.e., with $\alpha = 1$), the blebbistatin-treated growth cone has leading-edge tension on the same order as the stall force (Table S2), such that only a small amount of actin-network expansion with increasing G-actin is possible. For saturating levels of G-actin, the retrograde flow speed is sensitive to myosin concentration, while the P-domain width is not.

Forward-directed fluid flow can account for observed distributions of G-actin

As discussed above, the actin dynamics in the P domain are sensitive to leading-edge G-actin concentration, and newly recycled G-actin must be delivered to the leading edge quickly enough to maintain the rapid treadmill. A recent experiment using DNaseI labeling to track G-actin monomers demonstrated that the G-actin distribution in the P domain usually has a positive gradient, with G-actin concentration highest at the leading edge (26). Given that F-actin is disassembled and recycled to G-actin uniformly throughout the P domain, we now turn to the question of how G-actin is transported to the leading edge: Can the observed distributions be explained by diffusion alone, or is active transport in the form of forward-directed fluid flow necessary to achieve a positive gradient in the G-actin distribution?

We use the mechanical parameters determined from the calibration of the F-actin treadmill to predict the form of the G-actin distribution as a function of the hypothetical forward fluid flow, v_f. The equation governing the G-actin distribution (Eq. 8) in the steady state has the form

$$D\frac{\partial^2 G}{\partial x^2} - v_f\frac{\partial G}{\partial x} + \gamma F_0 \exp\left(\frac{-\gamma(L-x)}{v_r}\right) = 0, \qquad (10)$$

which has the analytical solution (using the boundary conditions discussed for Eq. 8)

$$G(x) = G_0 \exp\left(-\frac{v_f(L-x)}{D}\right) + \frac{F_0 v_r^2}{v_f v_r - D\gamma} \times \left[\exp\left(-\frac{\gamma(L-x)}{v_r}\right) - \exp\left(-\frac{v_f(L-x)}{D}\right)\right]. \qquad (11)$$

In the absence of forward-directed fluid flow, the predicted G-actin concentration decreases toward the leading edge (Fig. 5 *C*), in contrast to the experimentally observed positive G-actin gradient. On the other hand, in the presence of forward fluid flow of greater than $v_f \sim 0.15$ μm/s, the distribution increases toward the leading edge, and it compares well quantitatively with the experimentally measured G-actin distribution for $v_f \sim 0.3$ μm/s (Fig. 5 *C*) (26). Thus, we conclude that forward-directed fluid flow of

magnitude 0–0.3 μm/s may actively transport G-actin toward the leading edge in the P domain of the growth cone. Such flow was observed and measured in other cells (5,48); here, for the first time to our knowledge we suggest its existence in the nerve growth cone. Flow of this magnitude can increase the G-actin concentration at the leading edge twofold compared to diffusion-based transport, which would significantly accelerate the actin treadmill.

DISCUSSION

Using a model for the actin network in the peripheral region of stationary nerve growth cones, we have calibrated the balance of forces on the actin treadmill, demonstrating that retrograde actin flow under control conditions is driven primarily by myosin contractile forces. Our results support the assumption that the effective drag force resisting retrograde flow is proportional to filopodial and veil (lamellipodial) actin density at the transition domain, because filaments must be severed to maintain actin turnover. We show that when myosin contractile forces are inhibited, the system transitions to a new steady state in which retrograde flow is driven by membrane tension. Simulations of the model illustrate that a constant rate of actin depolymerization throughout the lamellipodial network is essential for maintaining a balance of forces with a constant rate of retrograde flow. Available experimental data allow estimates of all relevant forces.

After constraining and testing the F-actin treadmill model with published experimental data, we make a testable prediction that increasing the G-actin concentration would alter the force balance, increasing the contribution of leading-edge tension to the retrograde flow. This transition would be characterized by an increase in P-domain width and retrograde flow, a prediction that could in principle be tested experimentally by using drugs that alter the G-actin/F-actin balance. We also predict that the P-domain dynamics will be less sensitive to G-actin concentration in blebbistatin-treated cells, where myosin inhibition has already led to an increase in leading-edge tension.

We demonstrate that the experimentally observed positive G-actin gradient (increasing toward the leading edge) in the P domain can be maintained if rapid forward-directed fluid flow of the cytoplasm on the order of 10–20 μm/min exists in the P domain. This predicted flow would significantly increase the G-actin concentration at the leading edge, accelerating the actin treadmill. Forward-directed fluid flow has been directly observed in keratocytes (5). Further research will be needed to observe and measure fluid flow directly in growth cones. More detailed future models could also help distinguish the potential roles of forward-directed fluid flow and other hypothetical forms of active transport of G-actin, such as myosin transport along filopodia (49).

Another future extension for our model is to predict the behavior of the system when substrate adhesion increases in response to external guidance cues. A careful treatment of the question will require a submodel for adhesion dynamics, similar to that in Chan and Odde (27), but we can make some simple initial predictions based on the conclusions of the study described here. Assuming, according to previous modeling (10,11) and observations (12), that adhesion to the substrate generates viscous-like friction, Eq. 3, which describes the force balance on the P domain, can be rewritten as $f_m + f_T = (\xi_{break} + \xi_{adh})v_r$, where ξ_{adh} is the effective adhesion drag coefficient. When adhesion increases drastically, this equation says that the retrograde flow is almost canceled. In the treadmill stage, the polymerization rate at the front is balanced by the speed of the retrograde actin flow. This means that when the flow is canceled by the adhesion, the protrusion speed will be equal to the polymerization rate, and thus to the retrograde flow speed when the cell was stationary. The P-domain width after the adhesion increase, according to the model, will not change. Expanded to 2D, this model predicts that the cone can turn by establishing an asymmetric adhesion pattern, in which case asymmetric retrograde flow and protrusions will emerge, as suggested in Danuser and Oldenbourg (50). Note, however, that another study (51) proposes that the retrograde flow is symmetric, and instead, variations of the polymerization rate govern the turning behavior.

The importance of the nerve growth-cone mechanics in motility (52) and of mechanical cues in its guidance (53) is well established. Thus, the quantitative description of the growth-cone mechanics resulting from our study is an important step toward a more complete understanding of nervous system development. In the future, a more detailed mechanical model should incorporate the effects of compression and shear in the lamellipodium (52). Another future application of the model could be to analyze the role of microtubules and microtubule-based motors in the actin treadmill and growth-cone turning (54,55).

SUPPORTING MATERIAL

More observations discussed in detail, physical reasoning, model equations, experimental results, references, two tables, and two figures are available at http://www.biophysj.org/biophysj/supplemental/S0006-3495(12)00283-4.

We thank C. Hyland for critical reading of the manuscript.

This work was supported by National Institutes of Health grants GM068952 to A.M. and NS28695 and NS51786 to P.F. and the Nikon Partners-in-Research Program.

REFERENCES

1. Bray, D. 2002. Cell Movements. Garland, New York.
2. Pollard, T. D., and G. G. Borisy. 2003. Cellular motility driven by assembly and disassembly of actin filaments. *Cell.* 112:453–465.
3. Abraham, V. C., V. Krishnamurthi, …, F. Lanni. 1999. The actin-based nanomachine at the leading edge of migrating cells. *Biophys. J.* 77:1721–1732.

4. Borisy, G. G., and T. M. Svitkina. 2000. Actin machinery: pushing the envelope. *Curr. Opin. Cell Biol.* 12:104–112.
5. Keren, K., P. T. Yam, …, J. A. Theriot. 2009. Intracellular fluid flow in rapidly moving cells. *Nat. Cell Biol.* 11:1219–1224.
6. Bindschadler, M., and J. L. McGrath. 2007. Relationships between actin regulatory mechanisms and measurable state variables. *Ann. Biomed. Eng.* 35:995–1011.
7. Mogilner, A., and L. Edelstein-Keshet. 2002. Regulation of actin dynamics in rapidly moving cells: a quantitative analysis. *Biophys. J.* 83:1237–1258.
8. Prass, M., K. Jacobson, …, M. Radmacher. 2006. Direct measurement of the lamellipodial protrusive force in a migrating cell. *J. Cell Biol.* 174:767–772.
9. Keren, K., Z. Pincus, …, J. A. Theriot. 2008. Mechanism of shape determination in motile cells. *Nature.* 453:475–480.
10. Heinemann, F., H. Doschke, and M. Radmacher. 2011. Keratocyte lamellipodial protrusion is characterized by a concave force-velocity relation. *Biophys. J.* 100:1420–1427.
11. Lin, C. H., E. M. Espreafico, …, P. Forscher. 1996. Myosin drives retrograde F-actin flow in neuronal growth cones. *Neuron.* 16:769–782.
12. Vallotton, P., S. L. Gupton, …, G. Danuser. 2004. Simultaneous mapping of filamentous actin flow and turnover in migrating cells by quantitative fluorescent speckle microscopy. *Proc. Natl. Acad. Sci. USA.* 101:9660–9665.
13. Renkawitz, J., K. Schumann, …, M. Sixt. 2009. Adaptive force transmission in amoeboid cell migration. *Nat. Cell Biol.* 11:1438–1443.
14. Gardel, M. L., B. Sabass, …, C. M. Waterman. 2008. Traction stress in focal adhesions correlates biphasically with actin retrograde flow speed. *J. Cell Biol.* 183:999–1005.
15. Schaub, S., S. Bohnet, …, A. B. Verkhovsky. 2007. Comparative maps of motion and assembly of filamentous actin and myosin II in migrating cells. *Mol. Biol. Cell.* 18:3723–3732.
16. Wilson, C. A., M. A. Tsuchida, …, J. A. Theriot. 2010. Myosin II contributes to cell-scale actin network treadmilling through network disassembly. *Nature.* 465:373–377.
17. Forscher, P., and S. J. Smith. 1988. Actions of cytochalasins on the organization of actin filaments and microtubules in a neuronal growth cone. *J. Cell Biol.* 107:1505–1516.
18. Huber, F., J. Käs, and B. Stuhrmann. 2008. Growing actin networks form lamellipodium and lamellum by self-assembly. *Biophys. J.* 95:5508–5523.
19. Mitchison, T., and M. Kirschner. 1988. Cytoskeletal dynamics and nerve growth. *Neuron.* 1:761–772.
20. Lin, C. H., and P. Forscher. 1995. Growth cone advance is inversely proportional to retrograde F-actin flow. *Neuron.* 14:763–771.
21. Jay, D. G. 2000. The clutch hypothesis revisited: ascribing the roles of actin-associated proteins in filopodial protrusion in the nerve growth cone. *J. Neurobiol.* 44:114–125.
22. Lowery, L. A., and D. Van Vactor. 2009. The trip of the tip: understanding the growth cone machinery. *Nat. Rev. Mol. Cell Biol.* 10:332–343.
23. Tessier-Lavigne, M., and C. S. Goodman. 1996. The molecular biology of axon guidance. *Science.* 274:1123–1133.
24. Lewis, A. K., and P. C. Bridgman. 1992. Nerve growth cone lamellipodia contain two populations of actin filaments that differ in organization and polarity. *J. Cell Biol.* 119:1219–1243.
25. Schaefer, A. W., V. Th. G. Schoonderwoert, …, P. Forscher. 2008. Coordination of actin filament and microtubule dynamics during neurite outgrowth. *Dev. Cell.* 15:146–162.
26. Van Goor, D., C. Hyland, …, P. Forscher. 2012. The role of actin turnover in retrograde actin network flow in neuronal growth cones. *PLoS ONE.* 7:e30959.
27. Chan, C. E., and D. J. Odde. 2008. Traction dynamics of filopodia on compliant substrates. *Science.* 322:1687–1691.
28. Medeiros, N. A., D. T. Burnette, and P. Forscher. 2006. Myosin II functions in actin-bundle turnover in neuronal growth cones. *Nat. Cell Biol.* 8:215–226.
29. Burnette, D. T., A. W. Schaefer, …, P. Forscher. 2007. Filopodial actin bundles are not necessary for microtubule advance into the peripheral domain of Aplysia neuronal growth cones. *Nat. Cell Biol.* 9:1360–1369.
30. Odde, D. J., and H. M. Buettner. 1998. Autocorrelation function and power spectrum of two-state random processes used in neurite guidance. *Biophys. J.* 75:1189–1196.
31. Wang, F. S., C.-W. Liu, …, D. G. Jay. 2003. Modeling the role of myosin 1c in neuronal growth cone turning. *Biophys. J.* 85:3319–3328.
32. Maskery, S., and T. Shinbrot. 2005. Deterministic and stochastic elements of axonal guidance. *Annu. Rev. Biomed. Eng.* 7:187–221.
33. Mortimer, D., J. Feldner, …, G. J. Goodhill. 2009. Bayesian model predicts the response of axons to molecular gradients. *Proc. Natl. Acad. Sci. USA.* 106:10296–10301.
34. Li, G. H., C. D. Qin, and M. H. Li. 1994. On the mechanisms of growth cone locomotion: modeling and computer simulation. *J. Theor. Biol.* 169:355–362.
35. Gauthier, N. C., M. A. Fardin, …, M. P. Sheetz. 2011. Temporary increase in plasma membrane tension coordinates the activation of exocytosis and contraction during cell spreading. *Proc. Natl. Acad. Sci. USA.* 108:14467–14472.
36. Houk, A. R., V. Risca, …, O. Weiner. 2012. Mechanical tension spatially restricts signals to the leading edge during neutrophil migration. *Cell.* 148:175–188.
37. Hochmuth, F. M., J. Y. Shao, …, M. P. Sheetz. 1996. Deformation and flow of membrane into tethers extracted from neuronal growth cones. *Biophys. J.* 70:358–369.
38. Kruse, K., J. F. Joanny, …, J. Prost. 2006. Contractility and retrograde flow in lamellipodium motion. *Phys. Biol.* 3:130–137.
39. Rubinstein, B., M. F. Fournier, …, A. Mogilner. 2009. Actin-myosin viscoelastic flow in the keratocyte lamellipod. *Biophys. J.* 97:1853–1863.
40. Schaefer, A. W., N. Kabir, and P. Forscher. 2002. Filopodia and actin arcs guide the assembly and transport of two populations of microtubules with unique dynamic parameters in neuronal growth cones. *J. Cell Biol.* 158:139–152.
41. Mallavarapu, A., and T. Mitchison. 1999. Regulated actin cytoskeleton assembly at filopodium tips controls their extension and retraction. *J. Cell Biol.* 146:1097–1106.
42. Lan, Y., and G. A. Papoian. 2008. The stochastic dynamics of filopodial growth. *Biophys. J.* 94:3839–3852.
43. Burnette, D. T., L. Ji, …, P. Forscher. 2008. Myosin II activity facilitates microtubule bundling in the neuronal growth cone neck. *Dev. Cell.* 15:163–169.
44. Sheetz, M. P., D. B. Wayne, and A. L. Pearlman. 1992. Extension of filopodia by motor-dependent actin assembly. *Cell Motil. Cytoskeleton.* 22:160–169.
45. Oliver, T., M. Dembo, and K. Jacobson. 1999. Separation of propulsive and adhesive traction stresses in locomoting keratocytes. *J. Cell Biol.* 145:589–604.
46. Galbraith, C. G., and M. P. Sheetz. 1999. Keratocytes pull with similar forces on their dorsal and ventral surfaces. *J. Cell Biol.* 147:1313–1324.
47. Dai, J., and M. P. Sheetz. 1995. Axon membrane flows from the growth cone to the cell body. *Cell.* 83:693–701.
48. Zicha, D., I. M. Dobbie, …, G. A. Dunn. 2003. Rapid actin transport during cell protrusion. *Science.* 300:142–145.
49. Zhuravlev, P. I., and G. A. Papoian. 2011. Protein fluxes along the filopodium as a framework for understanding the growth-retraction dynamics: the interplay between diffusion and active transport. *Cell Adhes. Migr.* 5:448–456.

50. Danuser, G., and R. Oldenbourg. 2000. Probing f-actin flow by tracking shape fluctuations of radial bundles in lamellipodia of motile cells. *Biophys. J.* 79:191–201.

51. Betz, T., D. Koch, …, J. A. Käs. 2009. Stochastic actin polymerization and steady retrograde flow determine growth cone advancement. *Biophys. J.* 96:5130–5138.

52. Betz, T., D. Koch, …, J. A. Käs. 2011. Growth cones as soft and weak force generators. *Proc. Natl. Acad. Sci. USA.* 108:13420–13425.

53. Franze, K., J. Gerdelmann, …, J. Käs. 2009. Neurite branch retraction is caused by a threshold-dependent mechanical impact. *Biophys. J.* 97:1883–1890.

54. Myers, K. A., I. Tint, …, P. W. Baas. 2006. Antagonistic forces generated by cytoplasmic dynein and myosin-II during growth cone turning and axonal retraction. *Traffic.* 7:1333–1351.

55. Nadar, V. C., A. Ketschek, …, P. W. Baas. 2008. Kinesin-5 is essential for growth-cone turning. *Curr. Biol.* 18:1972–1977.

Fluorescence Fluctuation Spectroscopy Enables Quantitative Imaging of Single mRNAs in Living Cells

Bin Wu, Jeffrey A. Chao, and Robert H. Singer*
Department of Anatomy and Structural Biology, Albert Einstein College of Medicine, Bronx, New York

ABSTRACT Imaging mRNA with single-molecule sensitivity in live cells has become an indispensable tool for quantitatively studying RNA biology. The MS2 system has been extensively used due to its unique simplicity and sensitivity. However, the levels of the coat protein needed for consistent labeling of mRNAs limits the sensitivity and quantitation of this technology. Here, we applied fluorescence fluctuation spectroscopy to quantitatively characterize and enhance the MS2 system. Surprisingly, we found that a high fluorescence background resulted from inefficient dimerization of fluorescent protein (FP)-labeled MS2 coat protein (MCP). To mitigate this problem, we used a single-chain tandem dimer of MCP (tdMCP) that significantly increased the uniformity and sensitivity of mRNA labeling. Furthermore, we characterized the PP7 coat protein and the binding to its respective RNA stem loop. We conclude that the PP7 system performs better for RNA labeling. Finally, we used these improvements to study endogenous β-actin mRNA, which has 24xMS2 binding sites inserted into the 3′ untranslated region. The tdMCP-FP allowed uniform RNA labeling and provided quantitative measurements of endogenous mRNA concentration and diffusion. This work provides a foundation for quantitative spectroscopy and imaging of single mRNAs directly in live cells.

INTRODUCTION

Imaging mRNAs in single living cells allows the dynamics of mRNA transcription, transport, and localization to be studied with greater spatiotemporal resolution compared with traditional approaches. Several techniques have been developed to visualize mRNA with single transcript sensitivity in live cells (1,2). One can directly inject or transfect fluorescently labeled mRNA into cells that can be imaged with excellent signal/noise ratio (SNR) (3,4). A drawback of this approach is that these RNAs are not synthesized and processed normally by the cell, and consequently may lack certain *trans*-acting protein factors that influence RNA metabolism. To image endogenous mRNA, investigators have used different fluorogenic probes, such as molecular beacons. These probes produce fluorescence signal only when they hybridize to their target RNAs (5). However, this technology is limited by complicated hybridization kinetics and the reduced stability of hybridized mRNA. Recently, RNA aptamers that bind to small molecules that resemble GFP-like fluorophores have been developed (6). The small molecule becomes fluorescent only when the reporter RNA containing the aptamer sequence binds to it. This is a promising technique to image RNA; however, the sensitivity needs to be improved to detect single transcripts. In the last approach, an RNA-binding protein fused to a fluorescent protein (FP) is co-expressed with a reporter mRNA containing the RNA sequence that the RNA-binding protein recognizes. The MS2 system is the first and most widely used technique utilizing this strategy (7). A drawback of this system, however, is the background fluorescence generated from free coat proteins, which decreases the SNR and labeling efficiency. In this work, we developed a technology to address this problem by engineering coat proteins so that very low background levels and high SNR can be obtained.

In the MS2 labeling method, a genetically encoded sequence derived from the bacteriophage MS2 is inserted into the gene of interest. The sequence folds into a unique stem-loop structure that forms the MS2-binding site (MBS) for the MS2 coat protein (MCP) (8). When cells that express the gene carrying MBS also express MCP fused to an FP (MCP-FP), the mRNA of interest is fluorescently labeled by MCP-FP. Because both the MCP-FP and the reporter mRNA are genetically encoded, it is possible to make stable cell lines or even transgenic animals. This technique was first employed to image *ASH1* mRNA in yeast (7). Since then it has been used to image transcription, transport, and localization of mRNA in various cell types and organisms (9–13). Recently, a transgenic mouse model (the MBS mouse) was established in which the 24xMBS cassette is inserted into the 3′ untranslated region (UTR) of the β-actin gene (15). With the MBS mouse, it is possible to image an endogenous mRNA in isolated cells, tissue, or even a living animal. For example, visualization of the endogenous β-actin mRNA moving through the nuclear pore complex has been achieved in a cell line derived from the MBS mouse (11). To image multiple mRNAs in the same cell, other RNA-binding proteins and their cognate RNAs have been engineered in a similar manner as the MS2 system (16–19). PP7 bacteriophage coat protein binds to its own stem-loop RNA primer-binding site (PBS) with high affinity ($K_d = 1.6$ nM (18)) but only weakly interacts with the MBS ($K_d > 1$ μM). Because both MCP

Submitted January 27, 2012, and accepted for publication May 7, 2012.

*Correspondence: robert.singer@einstein.yu.edu

Editor: Xiaowei Zhuang.

0006-3495/12/06/2936/9 $2.00

doi: 10.1016/j.bpj.2012.05.017

and PCP recognize unique RNA stem loops, this allows both systems to be used in the same cell to visualize distinct mRNA populations. Recently, the PP7 system was used to image real-time transcription dynamics in live yeast cells (20).

One of the limitations of MS2-like systems is the high fluorescent background due to the unbound MCP-FP signal. To detect single mRNA molecules, it is necessary to incorporate multiple binding sites into the mRNA to increase the signal of the mRNA over the background of MCP-FP. It was previously observed that not all MBSs are completely bound by MCP-FP (21). In addition, it is often found that the mRNAs are not uniformly labeled in different cells, which complicates quantitative analysis. For example, to quantify the number of nascent transcripts at the transcription site, one must know the number of MCP-GFPs per mRNA to correctly calibrate the measurement. It is accepted that both MCP and PCP bind to their target RNA stem loops as dimers. However, the extent of dimerization of the CP-FP fusions in the cell is not known. Therefore, to fully utilize these labeling techniques to obtain quantitative information about mRNA dynamics in living cells, one must ensure that the dimerization of CP-FP is thoroughly calibrated and carefully optimized. In this work, we constructed single-chain tandem dimers of the MS2 and PP7 coat proteins (termed tdMCP and tdPCP, respectively), which eliminated the additional dimerization step and allowed us to achieve uniform labeling and quantitative imaging of RNA with substantially increased SNR.

We used fluorescence fluctuation spectroscopy (FFS) to quantify the MS2 and PP7 labeling systems. FFS utilizes the fluctuating fluorescence signal when fluorescently labeled molecules move through a subfemtoliter observation volume, allowing various physical and biological systems to be studied at the single-molecule level. Fluorescence correlation spectroscopy (FCS) (22–24), a well-known FFS technique, uses the autocorrelation function to measure concentration, diffusion, transport, and interactions both in vitro and in vivo. FCS distinguishes species based on their diffusion coefficients, which ultimately depend on molecular weights (25). The mRNA diffuses much more slowly than the free CP-FP, which allows the diffusion constant of mRNA to be specifically measured with FCS. Another important FFS tool is brightness analysis. Brightness characterizes the average fluorescence intensity of a single particle. Because brightness depends on the number of fluorophores in a particle, it reveals the oligomerization state of a molecule (26–28). For example, if two fluorescently labeled monomers form a dimer, the brightness of the dimer will be twice that of the monomer (27). Brightness analysis has been used to measure stoichiometry and binding curves of proteins directly in live cells (29,30). The mRNA molecule, bound by multiple CP-FPs, has a brightness value much higher than that of free CP-FP. Therefore, both the brightness and the diffusion coefficient can be used to resolve mRNA from the background of free CP-FPs. Time-integrated fluorescence cumulant analysis (TIFCA) (31), which was developed to unify the brightness and diffusion coefficient into a same analytical model, is an ideal tool for extracting quantitative information from the data.

In this study, we first used an FFS brightness analysis to measure the dimerization of both MCP-FP and PCP-FP. We then generated single-chain tandem dimers of both coat protein (tdMCP and tdPCP) that significantly improved the labeling efficiency and uniformity. Subsequently, we measured the copy number of the CP-FPs (or tdCP-FPs) on an mRNA and compared the MS2 and PP7 systems quantitatively. Finally, we demonstrated the biological value of this approach by applying FFS to measure the diffusion constants and concentration of endogenous β-actin mRNA. The concentration of β-actin transcripts in the nucleus during serum stimulation was measured quantitatively.

MATERIALS AND METHODS

FFS and data analysis

The FFS experiments were performed on an in-house-built, dual-channel, two-photon fluorescence fluctuation microscope. The instrument consists of an Olympus IX-71 and a mode-locked Ti:Sapphire laser (Chameleon Ultra; Coherent, Santa Clara, CA). A 60× Plan-Apo oil immersion objective (NA=1.4; Olympus, Center Valley, PA) is used to focus the laser and collect the fluorescence. The scattered laser light is eliminated by two short-pass filters (ET680sp-2p8; Chroma, Rockingham, VT). The fluorescence is separated into two different detection channels with a dichroic mirror (565DCXR; Chroma). The green channel is equipped with a band-pass emission filter (FF01-525/50-01; Semrock, Rochester, NY) to eliminate the reflected fluorescence from red channel. Two avalanche photodiodes (APD) (SPCM-AQR-14; PerkinElmer, Waltham, MA) detect photons in each channel. The output of the APD, which produces TTL pulses, is directly connected to a two-channel data acquisition card (FLEX02; Correlator.com). The recorded photon counts were stored and later analyzed with programs written in IDL (ITT Exelis, McLean, VA).

The normalized brightness b (27) is defined as $b = \lambda_{app}/\lambda_{EGFP}$. The sample apparent brightness λ_{app} is measured via generalized Mandel's Q parameter analysis (32). The brightness λ_{EGFP} is obtained in a calibration experiment by measuring cells transfected with enhanced green fluorescent protein (EGFP). For a mixture of different homo-oligomers, the normalized brightness depends on the dissociation constant and the degree of oligomerization. For a monomer/dimer equilibrium $A_2 \overset{K_d}{\longleftrightarrow} 2A$ with dissociation constant K_d, the normalized brightness b is

$$b = \frac{K_d + 8A_t - \sqrt{K_d(K_d + 8A_t)}}{4A_t}, \qquad (1)$$

where A_t is the total concentration of A, $A_t = 2A_2 + A$. In the FFS experiment, A_t is readily measured by the total intensity divided by the monomer brightness. Therefore, the dissociation constant K_d is determined by fitting b as a function of A_t.

We performed a single-color TIFCA analysis as described previously (31). Basically, we rebinned the raw photon counts to calculate the factorial

cumulants for different sampling times. We then fit the experimental cumulants to a theoretical model:

$$\kappa_{[n]}(T) = \sum_i \gamma_n N_i \lambda_i^n B_n(T; \tau_{di}, r), \quad (2)$$

where N_i, λ_i, and τ_{di} are respectively the number of molecules, brightness, and diffusion time of the i^{th} species. The function $B_n(T; \tau_{di}, r)$ is the n^{th} order binning function as defined previously (31). The summation is over the number of species. The parameter γ_n is the n^{th} order γ-factors, and r is the squared beam waist ratio that describes the excitation laser profile (31).

The autocorrelation curves were fit to a simple diffusion model:

$$G(t) = \sum_i \frac{G0_i}{\left(1 + t/\tau_{di}\right)\sqrt{1 + t/r\tau_{di}}}, \quad (3)$$

where the parameter $G0_i = \gamma_2 f_i^2 / N_i$. Note that $G0_i$ depends not only on the number of molecules but also on the fractional intensities $f_i = N_i\lambda_i / \Sigma_j N_j \lambda_j$. Without knowledge of brightness, the autocorrelation function is not able to recover the number of molecules. Thus, we used it only to obtain the diffusion time of molecules.

Fluorescence imaging and analysis

Images were taken with a 150× 1.45 NA oil immersion objective (Olympus) and 488-nm excitation laser, and recorded with an EMCCD camera (model DU897 BI; Andor iXon, South Windsor, CT). The microscope was controlled with MetaMorph imaging software. A time-lapse movie of a single *Z*-plane was recorded with a 50-ms exposure time. To count mRNA in a single plane, we used a spot detection algorithm based on a two-dimensional Gaussian mask as described previously (33) and implemented in MATLAB (The MathWorks, Natick, MA).

Plasmid construction

To create single-chain tandem dimeric coat proteins, we used polymerase chain reaction (PCR) to produce two coat protein gene sequences with appropriate restriction sites. The linker region between the two MCPs is ATCTACGCCATGGCTTCT, and that between the two PCPs is CGTGCGGATCCGCTAGCCTCC. A nuclear localization signal (NLS) and hemagglutinin (HA) tag were also added to the constructs. We created NLS-PCP-EGFP (P000234), NLS-tdPCP-EGFP (P000233), NLS-MCP-EGFP (P000109), and NLS-tdMCP-EGFP (P000143) genes by PCR (Fig. 1 *A*). The NLS sequence was added to sequester the coat protein in the nucleus and keep the unbound coat protein in the cytoplasm at a minimum. All coat protein constructs used in this work have an NLS signal, so the NLS is omitted for simplicity when we refer to a coat protein. We cloned these genes into a phage-ubc-RIG lentiviral backbone from which the DsRed-IRES-GFP fragments had been excised using NotI and ClaI. We also further modified the lentiviral backbone to replace the human ubiquitin C (UBC) promoter with the cytomegalovirus (CMV) promoter. Using PCR, we generated the sequence coding for cyan fluorescent protein (CFP). After the stop codon, we inserted 24xMBS (24xPBS) sites. Finally, we combined phage-CMV backbone and CFP-24xMBS (P000169) (or CFP-24xPBS (P000179)) into a complete plasmid, yielding mRNA with a CFP open reading frame and 24xMBS (or 24xPBS) in the 3′ UTR.

Cell culture and sample preparation

We used a mouse with 24xMBS sites knocked into the 3′ UTR of the *Actb* gene (MBS mouse) and isolated the E14 mouse embryonic fibroblast (MEF) line as described elsewhere (15). To stably express MCP-EGFP and tdMCP-EGFP, we created recombinant lentiviral particles using the phage UBC plasmid (described above) and used them to infect the MBS-MEF. After several passages, the cells were sorted for positive EGFP fluorescence by flow cytometry. U2OS cells were obtained from American Type Culture Collection. Both cells were maintained in Dulbecco's modified Eagle's medium (10-013; Cellgro, Manassa, VA) supplemented with 10% fetal bovine serum (FBS, F4135; Sigma-Aldrich, St. Louis, MO) and 1% penicillin and streptomycin (15140-122; Invitrogen). Transient transfection was performed with Fugene 6 (11814443001; Roche, Indianapolis, IN) according to the manufacturer's instructions. Cells were subcultured in a Delta-T coverglass-bottomed imaging dish (Bioptechs, Butler, PA). Before measurements, the growth medium was removed and replaced with Leibovitz L15 medium (21083-027; Invitrogen, Grand Island, NY) with 10% FBS unless explicitly indicated. For MEFs, the dish was also coated with 10 μg/ml human fibronectin (F2006; Sigma-Aldrich) for 30 min before the cells were plated. During the course of the experiment, the Delta-T dish was kept at 37°C.

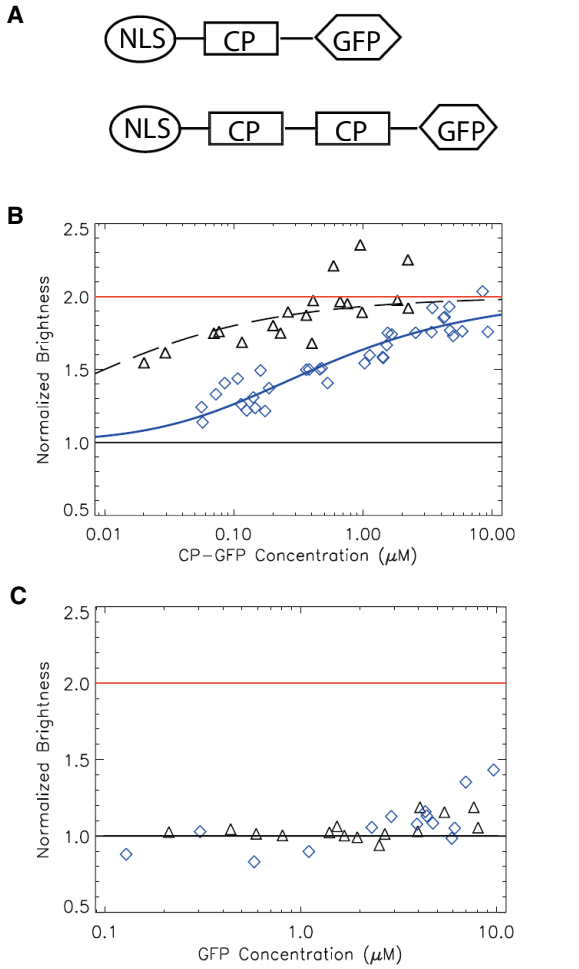

FIGURE 1 Normalized brightness of coat proteins. (*A*) Schematic of the coat protein constructs. (*B*) The brightness of CP-EGFP measured in U2OS cells is plotted as a function of CP concentration. From the data, it is clear that PCP-EGFP (*triangles*) dimerizes at a much lower concentration than MCP-EGFP (*diamonds*) does . The data were fit to Eq. 1 to obtain the dissociation constant of the coat protein (410 nM for MCP-EGFP and <20 nM for PCP-EGFP). (*C*) The normalized brightness of tdCP-EGFP stays at unity at different concentrations, indicating that the tandem dimers are behaving as monomers.

RESULTS

Brightness analysis of the CP-FP and tdCP-FP fusion proteins

Previous studies showed that MCPs and PCPs bind to their target stem loops as dimers (18,34,35). We used FFS brightness analysis to characterize the oligomerization state of MCP-FP and PCP-FP in living cells. We constructed coat proteins fused to EGFP that also contained an N-terminal NLS (Fig. 1 *A*). The NLS was used to concentrate the free CP-FPs in the nucleus and thus achieve a higher SNR of mRNA in the cytoplasm. We expressed CP-EGFP in U2OS cells and conducted FFS measurements in the nucleus. The brightness of the sample was calculated via a generalized Mandel's Q parameter analysis (32). In Fig. 1 *B*, the normalized brightness values are plotted as a function of the concentration of CP-EGFP. Each point represents a measurement in a different cell. The normalized brightness b, determined by the ratio between the brightness of CP-EGFP and EGFP monomer (27), provides a direct measure of the average oligomeric states of the labeled proteins. For instance, a normalized brightness of $b = 2$ indicates that the protein is a dimer. When the concentration of the protein is varied, the normalized brightness will increase from 1 to 2, depending on the proportions of the monomer and dimer. Therefore, a titration curve of brightness versus concentration gives rise to the apparent K_d of the dimerization interaction. The normalized brightness of PCP in Fig. 1 *B* (*triangle*) lies between 1 and 2 and saturates at 2 at high concentrations. The titration curve indicates that the $K_{d,app}$ of PCP-EGFP is $<$20 nM (due to the lack of data at very low concentration, we extrapolated the data using Eq. 1; *dashed line*). Surprisingly, for the MCP (Fig. 1 *B*, *diamond*), the situation is very different. MCP-EGFP reaches a dimer fraction at a much higher concentration than PCP-EGFP does, indicating that the former is a much weaker dimer. Fitting the data to Eq. 1 yields $K_{d,\ app} = 410$ nM, which is considerably weaker than the dimerization estimated by biochemical experiments (8). Although biochemical experiments show similar K_d-values for PCP and MCP in vitro, the live-cell FFS experiment shows that MCP-EGFP is a weaker dimer than PCP-EGFP. Further experiments showed that the NLS signal, the linker length between MCP and EGFP, and the identity of the FP do not affect the dimerization affinity of MCP. The reason for the reduced dimerization affinity for MCP-FP is still under investigation.

Free CP-FPs that do not bind to mRNA increase the background fluorescence, so the concentration of CP should be maintained as low as possible. However, because only the dimeric CP can bind to the stem loop, it is imperative to have the CP concentration high enough to maintain sufficient dimer concentration. This is particularly important for the MS2 system because our data suggest that significant amounts of monomeric MCP-EGFP exist under most experimental conditions. In the crystal structures of both MCP and PCP dimers, the N-terminus of one protomer is in close vicinity to the C-terminus of the other protomer (18,35). Due to this structural arrangement, a single-chain tandem dimer of the coat proteins (tdMCP and tdPCP) can be constructed that enables an intramolecular dimer to be formed. The tdMCP has been shown to bind to the MBS with the same affinity as the intermolecular MCP dimer, and has been used to image single molecules of RNA in bacteria (36,37). Based upon these experiments, we generated tdMCP-EGFP and tdPCP-EGFP and determined that they both had a brightness of one (Fig. 1 *C*), which was, as expected, independent of concentration. The fact that tdCP-FP has a single brightness value is particularly advantageous for FFS brightness analysis, because the apparent brightness of CP-FP depends on its concentration.

tdCP-FP-labeled mRNA has uniform brightness

Quantitative fluorescence imaging and spectroscopy require knowledge of the labeling efficiency of mRNA. Uniform labeling of the mRNA facilitates a quantitative interpretation of experimental results. FFS offers a simple method to measure the number of CP-FPs bound to an mRNA by the normalized brightness of an mRNA. Usually the mRNA has multiple MBSs (or PBSs) and therefore binds to many CP-FPs. The brightness of the mRNA is much higher than that of the free CP-FP. Furthermore, the mRNA is significantly larger than the free CP-FP and diffuses much more slowly. Therefore, one can distinguish them by both brightness and diffusion time. TIFCA (31) is ideal for such an analysis because it incorporates both brightness and diffusion time into the same analysis model.

We constructed plasmids coding for CFP with 24xPBS or 24xMBS inserted after the stop codon in the 3′ UTR (Fig. 2 *A*). The plasmid was transiently transfected together with the appropriate CP-EGFP in U2OS cells. The experiment was done at a two-photon laser wavelength of 1010 nm so that the CFP would not be excited. To aid the focus of the laser in the cell, mCherry was also cotransfected. The fluorescence was split into two channels by a dichroic mirror and detected by two APDs. We focused the two-photon laser spot at the mid-section in the perinuclear region of a cell by monitoring the red channel signal. The fluorescence intensity trace of the red channel and green channel are plotted in Fig. S1 *A* of the Supporting Material. From the figure, it is clear that the green fluorescence intensity has a much higher level of fluctuations than that of the red channel, emphasizing the value of the red channel for defining the focal point of the laser. We analyzed the data in the green channel using TIFCA. A one-species model was not able to fit the data, which was expected because of the presence of two components (the mRNA and the free CP-FPs). We fit the data with a two-species model, which more accurately described the data. An example of the fit is

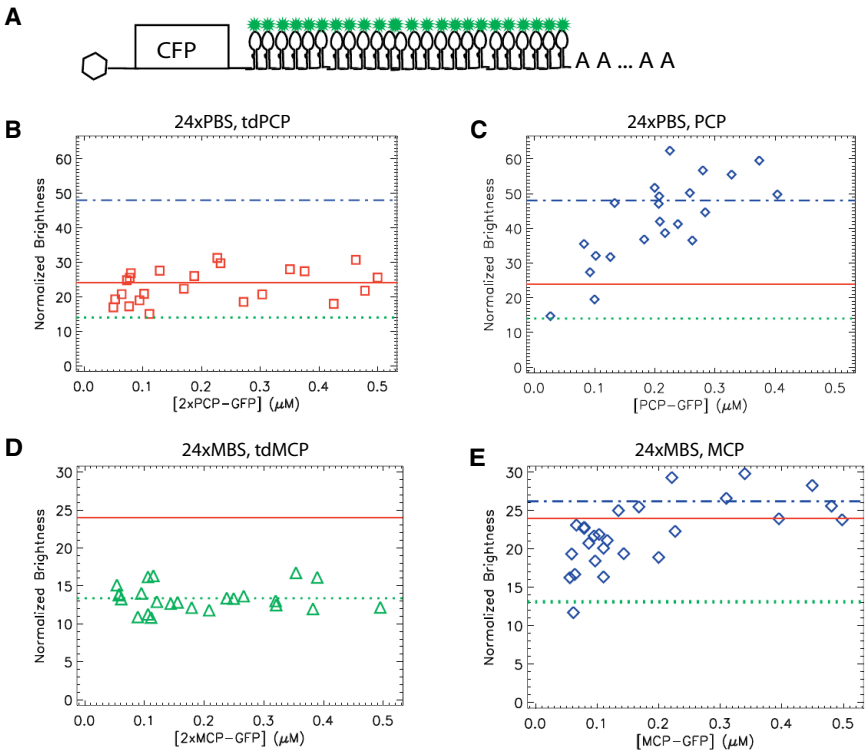

FIGURE 2 Normalized brightness of mRNA. (*A*) mRNA constructs used in the experiment. The mRNAs have a CFP open reading frame. After the stop codon, 24xPBS or 24xMBS is inserted into the 3′ UTR. (*B*) CFP-24xPBS is cotransfected with tdPCP-EGFP and mCherry in U2OS cells and measured for 3 min at a wavelength of 1010 nm. The two-species fit of the data reports the brightness of the mRNA. The normalized mRNA brightness, which measures the number of EGFPs on the mRNA, is plotted as a function of the total concentration of EGFP, determined by dividing the total fluorescence intensity by the EGFP brightness. The data indicate that the average number of EGFP on mRNA is 23 ± 5, implying that 24 PBS are fully occupied. (*C*) The same experiments were performed as in *B* except that tdPCP-EGFP was substituted by PCP-EGFP. The normalized brightness of mRNA saturates at 48 at high PCP concentration, but at low concentration the PP7 stem loops are not fully occupied. (*D* and *E*) The same experiments were performed on CFP-24xMBS cotransfected with tdMCP-EGFP (*D*) or MCP-EGFP (*E*). The normalized brightness of mRNA does not change with concentration for tdMCP-EGFP (the average is 13 ± 2), but it is approximately half of the expected full occupation number, 24. For MCP-EGFP, the mRNA brightness increases with the concentration of MCP and saturates at 26 ± 3.

presented in Fig. S1 *B*. From this fit, we measured the brightness of the mRNA. In Fig. 2 *B*, we plot the normalized brightness of the CFP-24xPBS mRNA labeled by tdPCP-EGFP as a function of total EGFP concentration. Each symbol represents a measurement of a single cell. Even though there were different concentrations of mRNA and tdPCP among the cells, the brightness and the number of coat proteins that bound to the mRNA were relatively constant. The average number of tdPCP-EGFP was 23 ± 5, that is, within error, equal to the expected maximum occupancy of the 24xPBS. We also measured the CFP-24xPBS mRNA cotransfected with PCP-EGFP. The normalized molecular brightness of mRNA is shown in Fig. 2 *C*. At high concentrations of PCP-EGFP, the normalized brightness saturated at 49 ± 9. This is also equal to the expected maximum occupancy number, 48 (represented as the *dash-dotted line*), because each stem loop binds to a dimer of PCP-EGFP. In addition, we notice that the mRNA brightness was reduced at low concentrations of PCP-EGFP, where the dimer was not sufficient to saturate all stem loops on the mRNA.

We performed the same experiment using the MS2 system. We cotransfected the CFP-24xMBS mRNA with tdMCP-EGFP and mCherry. The measured mRNA brightness is shown in Fig. 2 *D*. It is apparent that the normalized brightness stays constant, but at a lower value than the expected number of 24. In fact, the average is only 13 ± 2 (shown as *dotted lines*). Similarly, we cotransfected the CFP-24xMBS mRNA and MCP-EGFP together to assess the binding of MCP dimer to mRNA. Not surprisingly, the brightness of the MCP-EGFP-labeled mRNA depended on the concentration of MCP-FP, as shown in Fig. 2 *E*. The brightness increased with the concentration of MCP-GFP. At the saturation level, the average brightness of mRNA is 26 ± 3, twice that of tdMCP-EGFP, as expected. It was previously reported that the average number of MCP-EGFPs on an mRNA that contains 24xMBS is 33 (21), also indicating an incomplete occupancy. The reason for incomplete binding is further discussed below, but a direct consequence of differences in CP-FP occupancy is that the mRNAs labeled using the PP7 system were brighter, and hence had better SNR than those labeled with the MS2 system in live-cell imaging.

Imaging endogenous β-actin mRNA

As mentioned above, we constructed an MBS mouse in which the 3′ UTR of β-actin gene has 24xMBS knocked in (15). It is possible to image the endogenous β-actin in any cell type from this mouse. We isolated E14 mouse embryonic fibroblasts (MBS-MEF) and made a stable MEF cell line with SV40 T antigen (15). To compare the performance of tdMCP with that of MCP, we made MBS-MEF cell lines that stably express tdMCP-EGFP and MCP-EGFP, respectively, via lentiviral infection, as described in Materials and Methods. The cells were then imaged on a fluorescence microscope. As shown in

Fig. 3 *A*, MCP-EGFP did not label the cells uniformly. The cell in the upper-left corner had higher fluorescence intensity in the nucleus and the mRNA was brightly labeled. However, the mRNAs at the lower right of the image were only faintly labeled. The densities of labeled mRNA were also significantly different between the two cells. This is clearly demonstrated in Movie S1. On the other hand, the cell labeled with tdMCP-EGFP had more uniform labeling, as shown in Fig. 3 *B* and Movie S2. Although the fluorescence intensity in the nucleus was similar to that of the dimmer cell in Fig. 3 *A*, the mRNA was brightly labeled. In fact, in some cells, the tdMCP-EGFP concentration was so low that the nuclei looked dark, but the mRNAs were still brightly labeled. To evaluate the labeling efficiency of MCP and tdMCP quantitatively, we counted the number of β-actin mRNAs in the cytoplasm. We used an automated computer program as described in Materials and Methods (Airlocalize) to localize the diffraction-limited fluorescence spots. The cytoplasm was segmented manually, and spots inside the cytoplasmic area were counted as mRNAs. The average fluorescence intensity inside the nucleus was measured to indicate the expression level of the coat proteins. As shown in Fig. 3 *C*, the detected mRNA number (normalized by the cytoplasm size) stayed constant for various expression levels of tdMCP (*triangle*), whereas for MCP (*diamond*) it depended on the concentration of the coat protein in the nucleus. Only at high concentration did it saturate at the level detected by tdMCP.

FFS of endogenous β-actin mRNA

Finally, we applied FFS to study endogenous β-actin mRNA in MBS-MEF. We stably expressed tdMCP-EGFP in the MBS-MEF as described in the Materials and Methods section and in (15). The two-photon laser was focused in the cytoplasm near the nucleus and measured for 3 min. An example of a fluorescence intensity trace is plotted in Fig. S2 *A*. The autocorrelation function was calculated from the data and fit with a two-species diffusion model (Fig. S2 *B*). From the fit, we obtained two diffusion times. One is close to that of free tdMCP-EGFP and the other is much longer (100 $\pm$ 30 ms), which is identified as the mRNA. From the diffusion time, we can infer the diffusion constant based on the calibration of the laser beam waist. A scatter plot of the diffusion constant of mRNA in the cytoplasm is shown in Fig. 4 *A*. The diffusion constants of mRNA ranged from 0.15 to 0.74 $\mu m^2/s$, with an average of 0.35 $\mu m^2/s$. The same data were also subjected to TIFCA fitting, which provided the molecular brightness and the concentration of mRNA. The histogram of mRNA concentration is plotted in Fig. 4 *B*. The β-actin mRNA concentration ranged from 1 to 30 nM, with an average of 11 nM.

The transcription of β-actin responds to serum starvation and stimulation (38), and the transcription dynamics can be followed by fluorescence in situ hybridization to monitor the

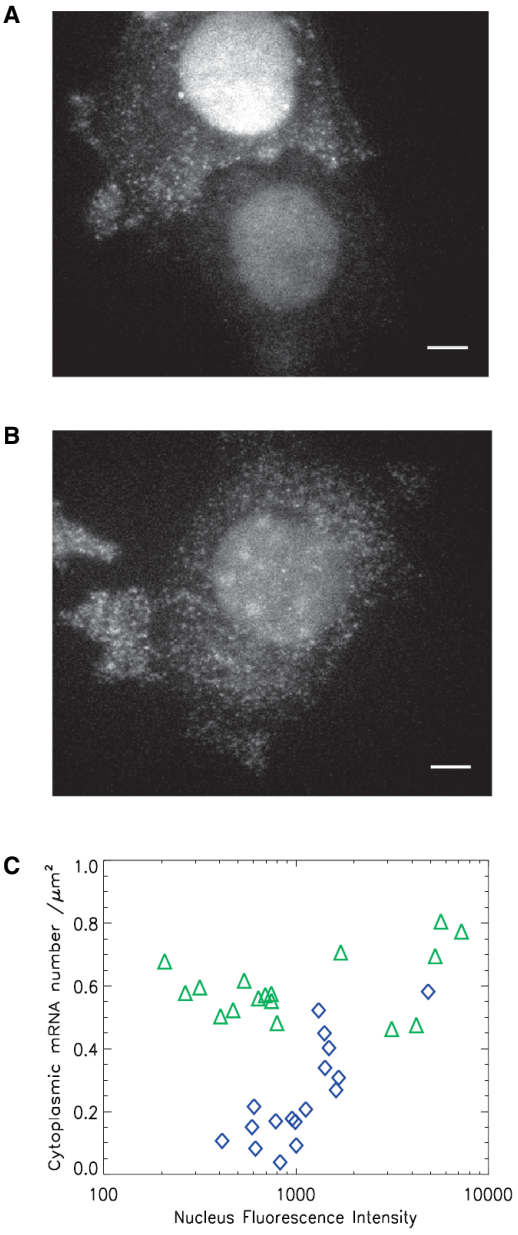

FIGURE 3 MBS-MEF cells stably expressing (*A*) MCP-EGFP or (*B*) tdMCP-EGFP are imaged on an epifluorescence microscope with an excitation wavelength of 488 nm. To assist the comparison, both images are scaled with the same black/white levels. (*A*) The signal of MCP-EGFP-labeled mRNA depends on the concentration of MCP. The upper-left cell has higher fluorescence intensity in the nucleus and more detectable mRNA than the lower-right cell. These two cells are in the same imaging field. (*B*) mRNA is uniformly labeled with tdMCP-EGFP. The cell has similar fluorescence intensity in the nucleus as the dimmer cell in panel *A*, but mRNA molecules are brightly and uniformly labeled. The scale bar is 5 μm. (*C*) The detected mRNA number in the cytoplasm (normalized by the size of the cytoplasm) is plotted as a function of fluorescence intensity in the nucleus. Each symbol is a measurement of a single cell. To facilitate comparison, the same criterion for spot detection was used for all images. With tdMCP labeling, the detected mRNA number does not depend on the expression level of tdMCP (*triangles*). However, for MCP-labeled mRNA (*diamonds*), the detected mRNAs increase with the concentration of MCP and only reach the tdMCP-detected mRNA level at high concentration.

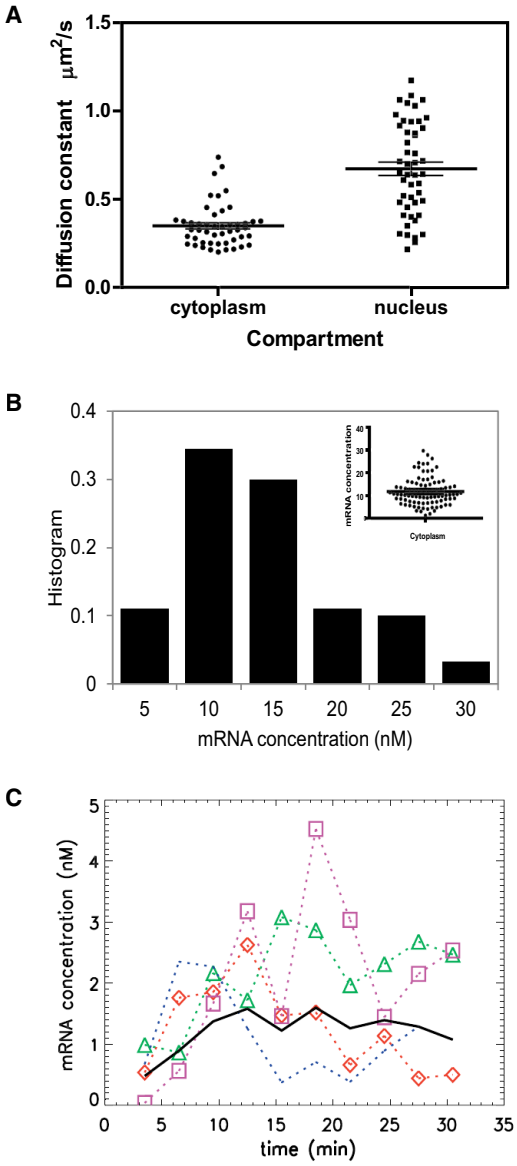

FIGURE 4 FFS measurements of endogenous β-actin mRNA. (*A*) Diffusion constant of β-actin mRNA in the cytoplasm and nucleus. MBS-MEF was infected with lentivirus to stably express tdMCP-EGFP. First, the MBS-MEF cell was measured in cytoplasm for 3 min. The autocorrelation function was fit with a two-species diffusion model (Eq. 3; see Fig. S2 for fit) and the mRNA diffusion constant was measured. Second, to measure the diffusion property of mRNA in the nucleus, MBS-MEF cells were stimulated with 20% serum after serum starvation overnight. FFS measurements were conducted in the nucleus immediately after serum stimulation. The photon counting traces were split into 5-min segments. The autocorrelation curves were calculated from the segments and fit to Eq. 3 to obtain the diffusion constant of mRNA. The scatter plot of the diffusion constants of β-actin mRNA is shown. In the cytoplasm, the diffusion constant of β-actin mRNA ranges from 0.15 to 0.74 $\mu m^2/s$, with an average of 0.35 $\mu m^2/s$. The diffusion constant of mRNA in the nucleus is larger than in cytoplasm, with an average of 0.72 $\mu m^2/s$. (*B*) Concentration of β-actin in cytoplasm. The MBS-MEF cell was measured for 3 min in cytoplasm. The data are fit by a two-species TIFCA model, which provides the concentration of β-actin mRNA. The histogram of mRNA concentration is plotted. In the inset, the scatterplot of the concentration is also shown. The concentration ranges from 1 to 30 nM, with an average of 11 nM. (*C*) The MBS-MEF was serum-stimulated as described for panel *A*. The data were subjected to a two-species TIFCA fit, and the concentration of β-actin mRNA is plotted as a function of time. Each dotted curve represents a measurement of a single cell. The average response of these cells is plotted as solid lines.

transcript level. We studied the serum stimulation kinetics by measuring mRNA concentration in the nucleus with FFS. The MBS-MEF cells were serum-starved overnight before they were subjected to 20% serum. We then took FFS measurements in the nucleus for 30 min. We divided the data into 3-min segments and fit all segments globally by linking the brightness parameters together while allowing the concentration of species to vary. As a result, the concentration of mRNA during the serum stimulation was obtained. The concentration is plotted in Fig. 4 *C*. From the plot, there is essentially no mRNA in the nucleus due to the serum starvation. The concentration of mRNA increases after serum stimulation and reaches a maximum after 10 min and then decreases slowly to a steady-state value. There is a large variation among the cells in terms of kinetic response. In Fig. 4 *A*, we show the scatter plot of the diffusion constant of mRNA in the nucleus compared with that in the cytoplasm. The diffusion constant is larger in the nucleus than in the cytoplasm, possibly due to factors (e.g., ribosomes) binding to the mRNA. The average diffusion constant in the nucleus is 0.72 $\mu m^2/s$.

DISCUSSION

When imaging mRNA with single-transcript sensitivity, the SNR is the limiting factor. The MS2 technology amplifies the signal of mRNA by multimerizing the MS2-binding sites and increasing the number of FPs bound to an individual mRNA. Another way to increase the SNR is to reduce the background. The background, besides the cellular autofluorescence, results from the free unbound CP-FP. It is known that coat proteins must dimerize before they can bind to their respective RNA stem loops. At a certain concentration of coat protein, the fraction of dimer depends on the dissociation constant K_d. By creating an intramolecular dimer, we eliminate the intermolecular dimerization process and enable all tdCPs to bind directly to their targets. As a result, we can express the tdCP-FP at low concentrations and still label the mRNA efficiently. For example, if the total MCP-FP concentration is 50 nM, the concentration of the dimer would be 4 nM, assuming that the dimerization $K_d = 410$ nM. If we further assume that the dimer binds to the stem loop with $K_d = 5$ nM in cells (39), only 40% of the stem loops will be occupied and the SNR of mRNA will be 1.4. However, if a cell has 50 nM tdMCP-FP, 90% of the stem loops will be labeled and the SNR of mRNA will be 3. If we have two EGFPs linked to the tandem dimer (tdMCP-tdFP), the SNR will increase to 4.2, a threefold increase. Experimentally, if the SNR of a particle is too low, it will not be detected. As demonstrated in Fig. 3 *C*,

with tdMCP-FP labeling, the total number of mRNAs detected does not depend on the expression of coat proteins. However, MCP-FP-labeled mRNA depends on the concentration of coat proteins. Therefore, tdCP is more suitable for quantitative counting experiments. Furthermore, tdCP readily saturated the binding sites on an mRNA and resulted in a uniform mRNA brightness, as demonstrated in Fig. 2. This is particularly advantageous for quantifying the number of transcripts at the transcription site.

Combining two coat proteins into a single peptide provides additional advantages. For example, in some applications the coat protein is used to tether the target protein onto RNA (40). The dimerization of coat protein forces the dimerization of the target protein, which might introduce undesirable side effects. The pseudo tandem dimer is a single peptide and effectively behaves as a monomer, which will not cause an undesired oligomerization of the fusion protein. There is, however, a potential drawback of the tandem dimer. Because each tandem dimer is fused to one FP, the maximum number of FPs labeling one mRNA will be reduced to half that of the true dimer. Nevertheless, there is an easy solution for this problem: one can fuse two FPs to the tandem dimer. Preliminary data show that the construct tdMCP-tdEGFP labels mRNA as efficiently as tdMCP-EGFP, but with the additional advantage of being brighter.

Quantitative and sensitive fluorescence fluctuation spectroscopy combined with specific labeling of mRNA provides unique information that is unattainable otherwise. By performing an FFS brightness analysis, we determined the number of CP dimers on the mRNA. For mRNA labeled with 24xPBS, we recovered the expected maximum occupancy number for both tdPCP and PCP. Previously, brightness has been used to measure unknown supramolecular complexes, such as the copy number of the coat protein in viral-like particles (41). Our results provide the first measurement, to our knowledge, of experimentally controlled copy number, which further establishes the validity of the brightness analysis for supramolecular complexes. For mRNA labeled with 24xMBS, our data show that the maximum occupancy number is far below 24. This is consistent with the fluorescence imaging data. The PP7-labeled mRNA is much brighter and has a better SNR than MS2 mRNA. We constructed different MBS constructs by varying the stem length and the linker between the stem loops. The occupation numbers of these mRNAs did not change substantially within experimental error.

We applied FFS to study endogenous β-actin mRNA. As a result, the concentration of β-actin mRNA was measured to be ~10 nM and varied between 1 and 30 nM. Another metric that we are able to determine is the diffusion constant in both cytoplasm and nucleoplasm. The average value of the diffusion constant in cytoplasm and nucleoplasm is 0.35 $\mu m^2/s$ and 0.72 $\mu m^2/s$, respectively. Previous studies obtained mRNA diffusion constants between 0.04 $\mu m^2/s$ (42) and 1.3 $\mu m^2/s$ (11) in nucleoplasm by single-particle tracking, depending on the exposure time and tracking algorithm used. FCS effectively measures an average diffusion constant of many mRNAs and is closer to the recent measurements obtained with single-particle tracking (11). To further investigate the diffusion property of mRNA in the cytoplasm, we constructed mRNAs with different lengths, as shown in Fig. S3 *A*. All three mRNAs have the same coding region of CFP. In the 3′ UTR, 24xPP7, 24xPP7-24xMS2, or 6xPP7 were inserted. Each of these mRNAs was expressed in U2OS cells together with tdPCP-EGFP. The diffusion constants of the mRNAs were measured by FCS and plotted in Fig. S3 *B*. Although CFP-24xPP7-24xMS2 has 1000 more nucleotides than CFP-24xPP7, their diffusion times are the same within experimental error. The diffusion constant of CFP-6xPP7 is slightly larger than that of CFP-24xPP7.

To summarize, we have established methods for obtaining absolute measurements of specifically labeled endogenous and exogenous mRNAs using FFS. We created a single-chain tandem coat protein dimer that labels mRNA uniformly with increased SNR. Such a careful analysis of the kinetics of the two aptamers binding to their respective coat proteins is a requisite for developing a two-color intra- or intermolecular labeling scheme for RNA. This will prove to be an important technology for measuring the single-molecule kinetics of mRNA metabolism, including synthesis, processing, export, translation, and degradation. Another powerful extension of this study is dual-color FFS. Once we have the ability to label an RNA-binding protein of interest with a different color, dual-color FFS promises to provide information about the interaction between protein and mRNA in precise cellular locations.

SUPPORTING MATERIAL

Three figures and two movies are available at http://www.biophysj.org/biophysj/supplemental/S0006-3495(12)00570-X.

We thank Timothée Lionnet for sharing the MATLAB program (Airlocalize) for image analysis, and Xiuhua Meng for cloning some of the plasmids.

This work was supported by grants from the National Institutes of Health (GM84364 and GM86217).

REFERENCES

1. Tyagi, S. 2009. Imaging intracellular RNA distribution and dynamics in living cells. *Nat. Methods.* 6:331–338.
2. Rodriguez, A. J., J. Condeelis, …, J. B. Dictenberg. 2007. Imaging mRNA movement from transcription sites to translation sites. *Semin. Cell Dev. Biol.* 18:202–208.
3. Cha, B. J., B. S. Koppetsch, and W. E. Theurkauf. 2001. In vivo analysis of *Drosophila* bicoid mRNA localization reveals a novel microtubule-dependent axis specification pathway. *Cell.* 106:35–46.
4. Ainger, K., D. Avossa, …, J. H. Carson. 1993. Transport and localization of exogenous myelin basic protein mRNA microinjected into oligodendrocytes. *J. Cell Biol.* 123:431–441.

5. Bratu, D. P., B. J. Cha, …, S. Tyagi. 2003. Visualizing the distribution and transport of mRNAs in living cells. *Proc. Natl. Acad. Sci. USA.* 100:13308–13313.
6. Paige, J. S., K. Y. Wu, and S. R. Jaffrey. 2011. RNA mimics of green fluorescent protein. *Science.* 333:642–646.
7. Bertrand, E., P. Chartrand, …, R. M. Long. 1998. Localization of ASH1 mRNA particles in living yeast. *Mol. Cell.* 2:437–445.
8. Lim, F., M. Spingola, and D. S. Peabody. 1994. Altering the RNA binding specificity of a translational repressor. *J. Biol. Chem.* 269:9006–9010.
9. Zimyanin, V. L., K. Belaya, …, D. St Johnston. 2008. In vivo imaging of oskar mRNA transport reveals the mechanism of posterior localization. *Cell.* 134:843–853.
10. Dynes, J. L., and O. Steward. 2007. Dynamics of bidirectional transport of Arc mRNA in neuronal dendrites. *J. Comp. Neurol.* 500:433–447.
11. Grünwald, D., and R. H. Singer. 2010. In vivo imaging of labelled endogenous β-actin mRNA during nucleocytoplasmic transport. *Nature.* 467:604–607.
12. Chubb, J. R., T. Trcek, …, R. H. Singer. 2006. Transcriptional pulsing of a developmental gene. *Curr. Biol.* 16:1018–1025.
13. Golding, I., J. Paulsson, …, E. C. Cox. 2005. Real-time kinetics of gene activity in individual bacteria. *Cell.* 123:1025–1036.
14. Reference deleted in proof.
15. Lionnet, T., K. Czaplinski, …, R. H. Singer. 2011. A transgenic mouse for in vivo detection of endogenous labeled mRNA. *Nat. Methods.* 8:165–170.
16. Brodsky, A. S., and P. A. Silver. 2000. Pre-mRNA processing factors are required for nuclear export. *RNA.* 6:1737–1749.
17. Lange, S., Y. Katayama, …, R. P. Jansen. 2008. Simultaneous transport of different localized mRNA species revealed by live-cell imaging. *Traffic.* 9:1256–1267.
18. Chao, J. A., Y. Patskovsky, …, R. H. Singer. 2008. Structural basis for the coevolution of a viral RNA-protein complex. *Nat. Struct. Mol. Biol.* 15:103–105.
19. Daigle, N., and J. Ellenberg. 2007. λN-GFP: an RNA reporter system for live-cell imaging. *Nat. Methods.* 4:633–636.
20. Larson, D. R., D. Zenklusen, …, R. H. Singer. 2011. Real-time observation of transcription initiation and elongation on an endogenous yeast gene. *Science.* 332:475–478.
21. Fusco, D., N. Accornero, …, E. Bertrand. 2003. Single mRNA molecules demonstrate probabilistic movement in living mammalian cells. *Curr. Biol.* 13:161–167.
22. Magde, D., E. Elson, and W. W. Webb. 1972. Thermodynamics fluctuations in a reacting system: measurement by fluorescence correlation spectroscopy. *Phys. Rev. Lett.* 29:705–708.
23. Berland, K. M., P. T. So, and E. Gratton. 1995. Two-photon fluorescence correlation spectroscopy: method and application to the intracellular environment. *Biophys. J.* 68:694–701.
24. Dittrich, P., F. Malvezzi-Campeggi, …, P. Schwille. 2001. Accessing molecular dynamics in cells by fluorescence correlation spectroscopy. *Biol. Chem.* 382:491–494.
25. Meseth, U., T. Wohland, …, H. Vogel. 1999. Resolution of fluorescence correlation measurements. *Biophys. J.* 76:1619–1631.
26. Digman, M. A., P. W. Wiseman, …, E. Gratton. 2009. Stoichiometry of molecular complexes at adhesions in living cells. *Proc. Natl. Acad. Sci. USA.* 106:2170–2175.
27. Chen, Y., L. N. Wei, and J. D. Müller. 2003. Probing protein oligomerization in living cells with fluorescence fluctuation spectroscopy. *Proc. Natl. Acad. Sci. USA.* 100:15492–15497.
28. Saffarian, S., Y. Li, …, L. J. Pike. 2007. Oligomerization of the EGF receptor investigated by live cell fluorescence intensity distribution analysis. *Biophys. J.* 93:1021–1031.
29. Wu, B., Y. Chen, and J. D. Müller. 2010. Heterospecies partition analysis reveals binding curve and stoichiometry of protein interactions in living cells. *Proc. Natl. Acad. Sci. USA.* 107:4117–4122.
30. Chen, Y., and J. D. Müller. 2007. Determining the stoichiometry of protein heterocomplexes in living cells with fluorescence fluctuation spectroscopy. *Proc. Natl. Acad. Sci. USA.* 104:3147–3152.
31. Wu, B., and J. D. Müller. 2005. Time-integrated fluorescence cumulant analysis in fluorescence fluctuation spectroscopy. *Biophys. J.* 89:2721–2735.
32. Sanchez-Andres, A., Y. Chen, and J. D. Müller. 2005. Molecular brightness determined from a generalized form of Mandel's Q-parameter. *Biophys. J.* 89:3531–3547.
33. Thompson, R. E., D. R. Larson, and W. W. Webb. 2002. Precise nanometer localization analysis for individual fluorescent probes. *Biophys. J.* 82:2775–2783.
34. Valegård, K., L. Liljas, …, T. Unge. 1990. The three-dimensional structure of the bacterial virus MS2. *Nature.* 345:36–41.
35. Ni, C. Z., R. Syed, …, K. R. Ely. 1995. Crystal structure of the MS2 coat protein dimer: implications for RNA binding and virus assembly. *Structure.* 3:255–263.
36. Peabody, D. S., and F. Lim. 1996. Complementation of RNA binding site mutations in MS2 coat protein heterodimers. *Nucleic Acids Res.* 24:2352–2359.
37. Golding, I., and E. C. Cox. 2004. RNA dynamics in live *Escherichia coli* cells. *Proc. Natl. Acad. Sci. USA.* 101:11310–11315.
38. Levsky, J. M., S. M. Shenoy, …, R. H. Singer. 2002. Single-cell gene expression profiling. *Science.* 297:836–840.
39. Schneider, D., C. Tuerk, and L. Gold. 1992. Selection of high affinity RNA ligands to the bacteriophage R17 coat protein. *J. Mol. Biol.* 228:862–869.
40. Rackham, O., and C. M. Brown. 2004. Visualization of RNA-protein interactions in living cells: FMRP and IMP1 interact on mRNAs. *EMBO J.* 23:3346–3355.
41. Chen, Y., B. Wu, …, J. D. Mueller. 2009. Fluorescence fluctuation spectroscopy on viral-like particles reveals variable gag stoichiometry. *Biophys. J.* 96:1961–1969.
42. Shav-Tal, Y., X. Darzacq, …, R. H. Singer. 2004. Dynamics of single mRNPs in nuclei of living cells. *Science.* 304:1797–1800.

Protein Folding Is Mechanistically Robust

Jeffrey K. Weber and Vijay S. Pande*
Department of Chemistry, Stanford University, Stanford, California

ABSTRACT Markov state models (MSMs) have proven to be useful tools in simulating large and slowly-relaxing biological systems like proteins. MSMs model proteins through dynamics on a discrete-state energy landscape, allowing molecules to effectively sample large regions of phase space. In this work, we use aspects of MSMs to ask: is protein folding mechanistically robust? We first provide a definition of mechanism in the context of Markovian models, and we later use perturbation theory and the concept of parametric sloppiness to show that parts of the MSM eigenspectrum are resistant to perturbation. We introduce a new, to our knowledge, Bayesian metric by which eigenspectrum robustness can be evaluated, and we discuss the implications of mechanistic robustness and possible new applications of MSMs to understanding biophysical phenomena.

INTRODUCTION

Simulations have reached a level at which one can target molecular phenomena on timescales from microseconds to milliseconds (1,2) with atomistically detailed models. However, how accurate are the predictions that come from these models? As any model used is an approximation to reality, a key question must always be addressed: how robust are model properties to errors in the model, and how can one predict what properties might be robust in a given system?

To address these questions in the context of biomolecular simulation, we propose to harness efforts directed at deriving meaningful many-state models of protein folding dynamics. Advances in computational models have made folding simulations possible at vastly longer timescales than were previously reasonable (3–6). Discrete-time, discrete-space Markov state models (MSMs), which propagate a probability distribution using left multiplication on a transition matrix, have shown particular promise for simulating protein folding processes.

After grouping structures into metastable microstates, MSMs capture the rare transitions between a protein's local free energy wells. MSMs offer a statistical approach to simulation: instead of relying on single trajectories, MSMs simulate ensemble dynamics with a state population probability vector (7,8). Recent millisecond-timescale simulations of the 39-residue protein NTL9 (1) and an 80-residue fragment of the λ-repressor protein (2) demonstrate the ability of MSMs to model the large, slowly relaxing systems that are present targets in protein folding research.

Although protein folding mechanisms are intellectually interesting in their own right, the ability to understand folding mechanisms also has implications for studying processes like catalysis, inhibition, and allostery. A number of recent examples in the literature show that folding mechanism (through transitions to intermediate states) can play an important role in mediating biological processes (9,10).

Proteins are good examples of biological systems that demand robustness to changes in environmental parameters. Robustness in folding mechanism modulates the kinetically dependent processes in catalysis, inhibition, and regulation, which proceed in ordered steps, and moderates harmful phenomena like misfolding and aggregation (11). Aspects of this robustness have been well studied and are substantiated by experiments. A protein can reach its native state under a range of physical and chemical conditions, and systematic point mutations often have little impact on a protein's ability to find its final, functional structure (12–14). However, it is unclear where this robustness ends: which properties are most robust to perturbations, and which are the most vulnerable?

Beyond general questions concerning the robustness of protein folding mechanisms, we also aim to gauge the accuracy of MSMs constructed from simulated folding trajectories. Given the general robustness seen in real protein ensembles, we would hope to observe similar properties in the data derived from molecular dynamics (MD) simulations. However, errors due to discretization (in space and time) and finite sampling are inevitable and difficult to quantify (11). As a telling example, one might need to minimize the uncertainties of 100,000,000 parameters to create an informative model for a 10,000 state system (15). If the robustness of protein folding is any indicator, though, optimization of model parameters may be less important than previously thought.

To investigate the possibility of this robust behavior, we use a Hessian-based theory called parametric sloppiness (16–18). In general, biological systems have demonstrated a tendency to show a particular sloppy behavior in the face of parametric perturbation. Here, sloppiness describes the global behavior of a biological system with respect to local changes in environment. A sloppy system is insensitive to (perhaps even drastic) perturbations in the majority of its

Submitted July 27, 2011, and accepted for publication January 12, 2012.

*Correspondence: pande@stanford.edu

Editor: Gerhard Hummer.

0006-3495/12/02/0859/9 $2.00

doi: 10.1016/j.bpj.2012.01.028

defining parameters, varying only with changes on a few stiff coordinates (16,17). This concept of sloppiness is related to system robustness: systems with sloppy sensitivities are invariant to many permutations in environmental conditions.

Sloppy behavior is particularly prominent in complex biological systems, where the accuracy of an ultimate result is crucial, but associated kinetic pathways can be flexible. Previous work in this area has shown sloppy behavior in processes ranging from the *Drosophila* circadian rhythm to rat growth-factor signaling (16–18). For proteins, changes in sequence and environment that are inconsequential can be related to sloppy deviations in parameter space. As events that induce phenomena such as protein misfolding are few and difficult to detect, these processes can be associated with changes in stiff parameters under this framework.

Although this theory of sloppiness is useful, it is not intuitive from a physical standpoint. Accordingly, we preface our study with a discussion of eigenspectrum perturbation theory and its relation to sloppiness and sensitivity. We then use this perturbation theory and sloppiness theory to investigate MSM observable robustness to transition probability perturbation. We also develop a quantitative Bayesian metric by which robustness can be evaluated, and we discuss implications such robustness holds for applications of MSMs to biophysical phenomena.

METHODOLOGY

Exploring mechanism in an MSM context

A great challenge in the field of protein folding lies in understanding holistic folding mechanisms. Although determination of properties like folding rates and native-state structures has become common practice in both experiment and simulation, studies of mechanism are less established. Phi-value analysis, which extracts kinetic information using site-specific mutagenesis, is often used by experimentalists to study folding mechanisms. Although phi-value analysis has provided great insight into many systems, it still suffers from the imprecise meaning of intermediate phi-values and the obvious limitation of trying to extract kinetic information from thermodynamic data (19–21). Deriving mechanistic information from pure MD simulations also presents challenges due to difficulties in analysis and the existence of heterogenous folding pathways. In the case of simulation, however, one might look for MSMs to provide a means for extracting mechanistic information from MD simulations.

If we want to explore robustness in mechanistic properties derived from simulation, we first need to consider how mechanism should be defined in an MSM context. On first thought, one might determine that a protein's folding trajectory as seen in MD simulations represents its folding mechanism. However, we argue that this view of mechanism is overly restrictive: individuals within an ensemble experience different state-to-state transition sequences in the folding process. Although the MSM transition matrix defines which trajectories are possible, it also does not provide a clear picture of which pathways the ensemble prefers over short and long periods of time.

The eigenspectrum of the MSM transition matrix, however, provides both kinetic and thermodynamic information about the ensemble. With units of probability density, the transition matrix eigenvectors represent the normal modes of time evolution in the system. The stationary distribution, the eigenvector with unit eigenvalue, describes the equilibrium populations in the ensemble. The other eigenvectors, with subunit eigenvalues, describe changes in the system's population distribution at timescales set by their respective eigenvalues.

An MSMs probability distribution vector at any given timestep n has the nice property of being propagated by transition matrix eigenvalues and eigenvectors. This relationship is described by a simple equation involving the initial distribution vector $\boldsymbol{\pi}^{(0)}$:

$$\boldsymbol{\pi}^{(n)} \propto \sum_{i=1}^{M} \lambda_i^n \left\langle \boldsymbol{\pi}^{(0)}, \mathbf{g}_i \right\rangle \mathbf{e}_i, \tag{1}$$

where $\boldsymbol{\pi}^{(n)}$ represents the system's nth probability distribution vector, λ_i denotes an eigenvalue of the $M \times M$ transition matrix, and $\mathbf{g}$ and $\mathbf{e}$ are the corresponding right and left eigenvectors of the transition matrix, respectively (11). The parenthetical (n) is used to denote a discrete time index, whereas an n without parentheses indicates an exponent (as in the case of λ_i^n). Here, and below, the angle brackets are used to designate a dot product between the enclosed vectors: $\langle u, v \rangle = \sum_i u_i v_i$.

The previous expression describes how an arbitrary population distribution converges to the equilibrium distribution over time. As the number of timesteps n becomes large, all subunit eigenvalues (through the term λ^n) and their eigenvectors decay to zero, and eventually only the stationary distribution multiplied by the unit eigenvalue remains.

Relating mechanism to an MSM eigenspectrum offers advantages over the alternatives that were previously discussed. The eigenvector decomposition method provides details about how entire probability distributions change, allowing for an idea of mechanism on an ensemble level. Large eigenvector entries represent states that are important to density transfer on the relaxation timescale of an associated eigenvalue. One can inspect the set of eigenvectors to find which individual states are mechanistically relevant at both fast and slow timescales. Information about trajectory (which folding pathways are most probable) and end result (how the state probability distribution converges to a stationary distribution) are intrinsic to the eigenspectrum.

Together, we extend, trajectory and end result define the essential parts of a folding mechanism. As such, we suggest that an MSM mechanism be defined in the context of eigenvector decompositions. To investigate mechanistic properties of MSMs, one should inspect the signs and magnitudes of transition matrix eigenvector elements for the eigenvalues that describe a given process. Furthermore, when one considers a folding mechanism, one is most interested in learning the important long timescale pathways between unfolded states and the native state. In MSMs, these slow processes are described by the eigenvectors with the largest eigenvalues. Therefore, the most salient information about folding mechanism can be extracted from eigenvectors that describe the system's long timescales.

To provide the reader with some intuition about how eigenvalues and eigenvectors can be related to mechanism, we provide a toy MSM example illustrated in Fig. 1 and Fig. 2. Fig. 1 shows a simple one-dimensional potential energy surface and its corresponding continuous probability distribution. To build an MSM on the toy surface, we discretize the potential in a natural manner wherein state boundaries are placed on the barriers between the wells in the surface. We also assume the potential is truly one-dimensional, i.e., transitions can only occur between neighboring wells.

Fig. 2 shows the transition matrix eigenvalue spectrum and selected eigenvectors for the nine-state MSM constructed on our toy potential. State assignments map directly onto the partition: the eigenvector components at left correspond to the states on the left side of the potential, etc. To make mechanistic assertions about dynamics on the surface, we simply need to inspect the magnitudes of eigenvector components. Each eigenvector component represents the relative flux into (if the component is positive) or out of (if the component is negative) the given state at the eigenvalue's timescale.

As seen in the top eigenvector ($\lambda = 0.988$), the system's slowest mode describes the transfer of the population from the right side of the surface

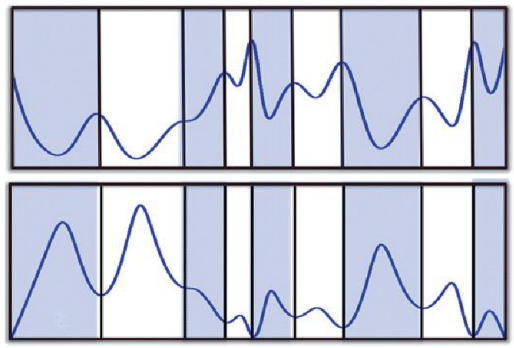

FIGURE 1 Top: Toy one-dimensional potential energy surface used to illustrate the role transition matrix eigenvectors play in describing mechanism. Vertical lines and shading indicate a natural partitioning of space wherein barriers divide states. Bottom: Probability distribution corresponding the toy potential energy surface with discretization.

to the left side. In the system's second slowest mode ($\lambda = 0.875$, middle eigenvector), probability density moves between the wells on the left side of the potential. In the third, high frequency eigenvector ($\lambda = 0.385$, near the lag time rate), probability density is transferred from the shallow wells on the barrier to the system's most populated state.

When considering a folding mechanism, the system's two slowest modes provide the richest mechanistic insight. In an analogy to protein folding, the wells on the right side of the potential might represent the unfolded basin, whereas the state furthest left might represent a native-side intermediate. As such, the first eigenvector shows how population is transferred from the unfolded basin to the native basin at the folding timescale, and which states are important in that transfer; the second eigenvector shows how folding might proceed from a highly populated intermediate and the native state on a relatively slow timescale.

Although the fast eigenvector does provide information about how population descends the native-side barrier, one is presumably less interested in the dynamics between the highly transient states that eigenvector describes. We thus argue that when studying folding mechanism, the slow eigenvectors of an MSM are of fundamental interest.

Perturbation theory framework

With a working definition of folding mechanism now in hand, we can now explore whether or not these mechanisms are robust to perturbation. Before we introduce the Hessian-based method used for the bulk of this study, we will first lay out a simpler method for robustness evaluation that has roots in physics. This formalism is similar to the more statistically rigorous treatment used in later sections and can be used to draw parallels between physical and statistical methods.

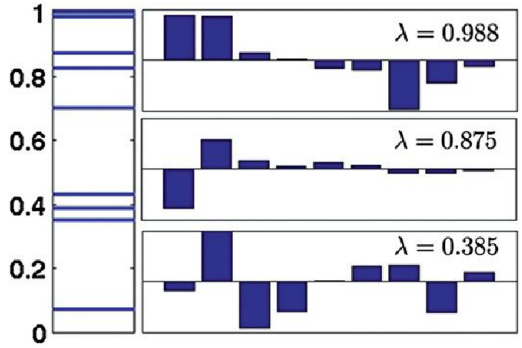

FIGURE 2 Eigenvalue spectrum and selected eigenvectors from the MSM built on the toy potential seen in Fig. 1.

We have already noted that perturbing the interactions of a protein is not new to the field of protein folding. Phi-value analysis (19–21) examines the rates of protein folding and unfolding when minor perturbations (e.g., point mutatations) are made to the protein experimentally. The fundamental assumption of this procedure is that minimal perturbations can probe the folding mechanism without altering it. However, it is natural to ask: what size of perturbation is small enough, and how can one build a framework for understanding these perturbations?

Below, we present a simple framework for understanding perturbations, building upon previous work in examining perturbations to a Hamiltonian in quantum mechanics. A popular method for approximating solutions to the Schrodinger equation involves splitting the system Hamiltonian into zeroth- and higher-order parts with expansion parameter ξ:

$$\mathcal{H} = \mathcal{H}^0 + \xi\mathcal{H}' + \xi^2\mathcal{H}'' \ldots. \tag{2}$$

If the eigenvalue problem for the zeroth-order Hamiltonian can be solved exactly, corrections to the eigenvalues and eigenvectors based on the perturbed Hamiltonian can be calculated with the well-known eigenspectrum perturbation theory (22).

As in the quantum mechanical problem, an MSM transition matrix could also be augmented by a perturbation operator. Suppose we would like to calculate the impact of a random perturbation on the eigenspectrum of the transition matrix. We could define a perturbed transition matrix $\mathbb{T}$ (to first order) such that

$$\mathbb{T} \approx \mathbb{T}^0 + \xi\mathbb{T}', \tag{3}$$

where $\mathbb{T}^0$ is the original transition matrix and $\mathbb{T}'$ is a matrix of random noise under the constraint that the sum $\mathbb{T}^0 + \xi\mathbb{T}'$ is row normalized. The first-order correction due to noise, λ'_m, for each eigenvalue λ^0_m of the transition matrix is given by the dot product

$$\lambda'_m = \left\langle e^0_m, e^0_m \mathbb{T}' \right\rangle, \tag{4}$$

where $\boldsymbol{e}^0_m$ is the mth left eigenvector of the zeroth-order transition matrix (22). Corrected left eigenvectors are given by the formula

$$e_m = e^0_m + \sum_{j \neq m} \frac{\left\langle e^0_j, e^0_m \mathbb{T}' \right\rangle}{\lambda^0_m - \lambda^0_j} e^0_j. \tag{5}$$

Using these corrections due to perturbation, one could gauge the impact of a random noise (or a more systematic) change in a transition matrix on its eigenspectrum. We later apply this perturbation theory to analyze the robustness of eigenvalues for a villin transition matrix. Fig. 3 shows the eigenvalue spectrum for this system. As with the toy model, the villin model has a few slow eigenvalues (above 0.5) that should be important in analyzing folding mechanism.

In performing perturbation theory, we carry out a procedure that is conceptually not unlike that of phi-value analysis. We perform a small perturbation on the system (with added noise to the transition matrix analogous to a point mutation), and we analyze the impact that perturbation has on the mechanism (with differences in the eigenvalue spectrum analogous to free energy differences). Noise-like perturbations, of course, are unrelated to point mutations, but the two methods share many of the same ideas for investigating mechanistic properties. As in phi-value analysis, which elements of an MSM can we change without fundamentally altering the dynamics?

Need for a new framework

The method more extensively used in this study is similar to a classical perturbation theory. We perturb a transition matrix with noise, calculate

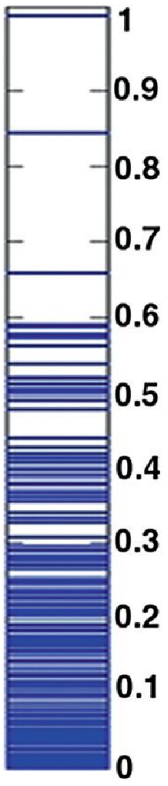

FIGURE 3 Transition matrix eigenvalue spectrum for an MSM of the villin headpiece domain in explicit solvent. This eigenvalue spectrum is analyzed in the Perturbation theory section of this work.

the corrected eigenspectrum, and compare that eigenspectrum to the original. We decide to use an alternative method for two reasons. First, we would like to gauge the rate of change (called the sensitivity) in an eigenvalue or eigenvector with respect to the magnitude of perturbation. Furthermore, we would like to know this eigenspectrum sensitivity for each individual parameter in the model. These desires are not easily fulfilled with analytical perturbation theory. This work's method, drawn from the literature and tested on biological models, is designed to estimate such a rate of change (16–18).

Second, sophisticated theory for error propagation in MSMs has been developed using a sensitivity-based analysis (23,24). These methods use Bayesian schemes to estimate uncertainty based on the available data. The nature of the sensitivities used to estimate such errors, however, has never been well characterized, and it would be useful to gain intuition about the relative magnitudes of these eigenspectrum sensitivities in recently constructed MSMs. Sloppiness-based techniques, as discussed below, provide an avenue to do so.

Sloppiness framework

In developing this more rigorous method for sensitivity analysis, we draw inspiration from theories first used in statistics and computer science. Hessian-based sensitivity studies are common in the statistical literature (25,26). These methods share the characteristic of calculating the Hessian (second-derivative) matrix of a particular function that gauges a model's dependence on a set of parameters. The eigenvalues of this Hessian matrix can then be used to estimate an observable's sensitivity to perturbation. Here, we adopt the notation and language of sloppiness used in recent Hessian-based sensitivity studies on systems biology models (16–18).

To investigate sloppiness in MSM transition probabilities, we start with the so-called model parameter cost function on the transition probability matrix. Given the perturbation of a certain system parameter, the cost function returns the induced sum-squared deviation in a dependent observable. In our case, we define a parameter to be a transition matrix element and an observable to be an eigenvalue or eigenvector. Adapted from the literature (16–18), the cost function $C(\mathbb{T})$ is defined as

$$C(\mathbb{T}) = \frac{1}{N^2}\sum_i \sum_j \left(\sum_{k=1}^{N} \left(e_k\left(p_{ij}^*\right) - e_k\left(p_{ij}\right)\right)^2 \right), \qquad (6)$$

where $\mathbb{T}$ is the $N \times N$ transition matrix, $\boldsymbol{e}$ is a left eigenvector of that matrix, p_{ij} is an individual transition probability defined by the model, p_{ij}^* is a continuous variable representing a perturbation of p_{ij}, and $e_k(p_{ij}^*)$ represents an eigenvector entry as a function of p_{ij}^* (16–18). To quantify the sensitivity of a model to changes in individual parameters, we use the concept of the sensitivity eigenvalue, λ_{sens}, of the cost function Hessian. For simplicity, the Hessian of $C(\mathbb{T})$ is constructed as a diagonal matrix. Accordingly, each sensitivity eigenvalue is merely a Hessian matrix element evaluated at its corresponding parameter p_{ij}:

$$\lambda_{sens}\left(p_{ij=t}\right) = \mathcal{H}_{tt}(p_t) = \frac{\partial^2 C(\mathbb{T})}{\partial p_t^2}(p_t). \qquad (7)$$

The sensitivity spectrum of the transition matrix, generated by plotting the sensitivities of all transition probabilities, gives a qualitative estimate of sloppy behavior, wherein a sensitivity spectrum that spans many orders of magnitude is said to indicate sloppiness (16). We should note that the functions $e_k(p_{ij}^*)$ lack an easily derived analytical form. In this study, such relations were determined by calculating eigenvectors at increments of p_{ij}^* and fitting the numerical relationships $e_k(p_{ij}^*)$ to quartic polynomials.

Although the range of a sensitivity spectrum provides an intuitive estimate of sloppiness, a more quantitative metric would allow for better comparison of robustness within a given set of observables. A useful metric can be developed from individual terms in the cost function. We use a Bayesian approach to define, for a small perturbation, the expected deviation for an observable $\boldsymbol{e}$:

$$\langle \delta(e) \rangle = N^2(\Delta p)^2 \sum_i \sum_j \left(\frac{U_i}{\sum_m (U_m)} \right) \lambda_{sens}\left(p_{ij}\right), \qquad (8)$$

where Δp represents the magnitude of a small transition probability perturbation and each U_i represents the relative uncertainty in a row of the transition matrix. A derivation for this equation is included in the Supporting Material (23,24).

The expected deviation quantifies robustness via a direct cost function variation estimate: for an observable $\boldsymbol{e}$, $\langle \delta(e) \rangle$ represents a weighted average deviation due to perturbation over all components of the cost function $C(\mathbb{T})$.

Before moving on to our results, we should note that under both perturbation schemes the perturbed transition matrix will violate the detailed balance condition $p_{ij}\pi_i = p_{ji}\pi_j$. Such matrices thus describe only near-equilibrium steady states of the perturbed system. As a physical analogy, our perturbation schemes do not represent reversible changes in activation barrier heights, but rather correspond to nonequilibrium experiments in which energy is added to break detailed balance. These nonequilibrium results are then compared among our observables of interest.

RESULTS AND DISCUSSION

Perturbation theory framework

As an instructive example, we first use classical perturbation theory to gauge robustness in eigenvalues of the villin

MSM transition matrix. The stationary eigenvalue will not change with any transition matrix perturbation, because the unit eigenvalue is a property of all regular stochastic matrices. All other eigenvalues, however, do depend on the particular values of transition matrix elements. To measure how much these kinetic eigenvalues change upon perturbation, we perturb the transition matrix and calculate the first-order eigenvalue correction using Eq. 4. Note that, in this case, calculated eigenvalue corrections are exact, as the perturbed transition matrix is itself exactly first order in nature.

In this case, the villin count matrix was perturbed by additive Gaussian noise ($\mu = 5$, $\sigma = 3$) to 1% of matrix elements, constrained to positivity, and then renormalized to yield a perturbed transition matrix. To find the matrix $\mathbb{T}'$ in Eq. 4, we subtract the perturbed matrix from the original matrix. Mean eigenvalue corrections were computed over 1000 random perturbations of the kind just described. Fig. S1 illustrates the relationship between mean eigenvalue correction and eigenvalue relaxation timescale. The eigenvalues at long timescales (i.e., eigenvalues with large magnitudes) require quite small corrections due to the random perturbation, whereas the eigenvalues at shorter timescales (corresponding to high frequency modes in the system) change to a greater extent when the transition matrix is perturbed.

We should note that while large eigenvalues change less when perturbed than their small counterparts, the relaxation timescales derived from these eigenvalues exhibit the opposite trend. The reason for this discrepancy arises from the nonlinear way in which physical timescales are calculated: a relaxation timescale is proportional to one over the logarithm of its corresponding eigenvalue (see Fig. S1 *caption*). Because the system's largest eigenvalues are near a singularity in the timescale function, even modest changes in those eigenvalues translate to large changes in timescale. Thus, whereas the largest eigenvalues (≈ 0.99) change only by a few parts per thousand upon perturbation, their timescales still change by ~25% (≈ 150 ns). Fig. S2 shows the mapping between fractional timescale correction and relaxation timescale for all eigenvalues being considered.

Because slow timescales are often those most important for model interpretation, this intrinsic deficit in slow timescale robustness should be considered in future MSM analyses. However, we maintain that the relatively small deviations in large eigenvalues still allow for meaningful analysis. A 25% change in timescale, while significant, does not drastically alter the physical interpretation of a relaxation process. If the largest eigenvalues changed to the extent that many smaller eigenvalues change, the longest timescales could deviate by an order of magnitude or more, and any conclusions based on those data would be suspect. The fact that the slow timescales do not change so dramatically is comforting from the standpoint of ongoing Markov state modeling.

Sloppiness framework

Having demonstrated the use of perturbation theory in analysis of transition matrix eigenvalues, we now apply the more sophisticated sloppiness theory in analyzing the eigenvectors of MSMs. Transition matrix eigenvector sensitivities were analyzed for MSMs of Fs-peptide (in explicit solvent, lumped to 19 macrostates) and the villin headpiece domain (in both explicit and implicit solvent, lumped to 500 macrostates) (24,27,28).

For a preliminary illustration of sensitivity eigenvalues, Fig. 4 shows stationary distribution sensitivities for all transition probability parameters of the Fs-peptide MSM. Clearly, the magnitudes of sensitivities vary greatly from state to state, suggesting that the stationary eigenvector is much more sensitive to some states than it is to others. The largest sensitivities often, though not always, correspond to parameters leading to the model's most populated states (States 13 and 14) and those along the matrix diagonal. In this case, no sensitivities are particularly large (at most ~1×10^{-3}), indicating the distribution will not change drastically upon perturbation.

The biophysical meaning of the transition matrix perturbations carried out in this work requires some thought. Given that transition probabilities are held constant over the course of a simulation, these perturbations are unlike the thermal fluctuations that cause Brownian motion, because such fluctuations occur on ultrashort timescales. Rather, time-independent perturbations are more like probes present in a nonequilibrium experiment, or, with the enforcement of detailed balance, equilibrium phenomena like interactions with ligands or denaturant. Systematic perturbations, and an analysis of how eigenvectors are affected by these perturbations, might thus provide a means of simulating such interesting processes.

The main purpose of this study, however, is to investigate general mechanistic properties of MSMs. We first look to eigenvector sensitivity spectra to provide a qualitative picture of mechanistic robustness to perturbation: Fig. S3 shows the sensitivity spectra for three selected eigenvectors of the villin implicit solvent model. Because the sensitivities in each spectrum are spread quite evenly over many orders of magnitude, the spectra meet our qualitative criterion for sloppiness. It should be observed that sensitivities near the maximum sensitivity eigenvalue are related to stiff directions in parameter space, as changes in those parameters cause the greatest relative changes in model behavior. For the most part (as seen in all three spectra in Fig. S3), sensitivity values are sparse near the maximum sensitivity eigenvalue, suggesting that stiff parameters are few in number.

Notably, the sensitivity spectrum for the stationary distribution of the villin implicit solvent model (shown in Fig. S3) spans nearly six more orders of magnitude than do the spectra related to other eigenvectors. For the following analysis, suppose 10% of rows in villin's transition matrix are

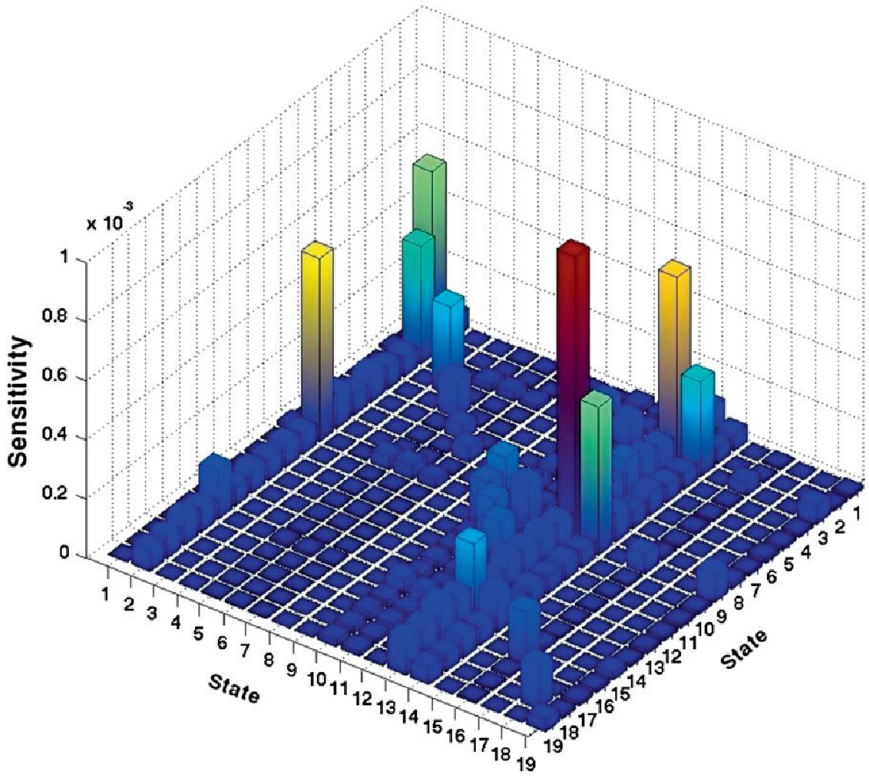

FIGURE 4 Sensitivity eigenvalue matrix for the stationary distribution of the Fs-peptide transition matrix. Indices on the right of the plot indicate states from which a transition originates, whereas indices on the left indicate where a transition terminates. Though all sensitivities are relatively small ($\leq 1 \times 10^{-3}$), the largest sensitivities often correspond to parameters that describe transitions into highly populated states (i.e., States 13 and 14) and self-transition probabilities.

perturbed by noise. Evaluating the stationary distribution under our Bayesian robustness scheme ($\Delta p = 0.01$, $N = 50$), we see that the stationary distribution is three orders of magnitude more robust to perturbation than the rate eigenvectors: $\langle \delta(\boldsymbol{\pi}) \rangle = 4.96 \times 10^{-4}, \langle \delta(\boldsymbol{e}, \lambda = .729) \rangle = 0.10$, $\langle \delta(\boldsymbol{e}, \lambda = .510) \rangle = 0.12$. A similar gap between stationary and rate eigenvectors was seen in both of the other models analyzed. However, the slow rate eigenvectors are still robust under our metric: expected deviations on the order of 0.1 are quite small in eigenvectors over all 500 components. It should also be noted that a transition probability perturbation of 0.01 is not insignificant: transition matrix elements in these models often fall in the range of 0.001–0.05. As discussed below, the so-called slow eigenvectors of all three models were observed to be similarly robust. We observe in general that the thermodynamic observables of MSMs are much more robust to perturbation than their kinetic counterparts. These data help to justify previous observations that equilibrium properties converge more quickly than dynamical ones under rapid conformational sampling (27).

In Fig. 5 and Fig. 6, we use our Bayesian metric on a variety of spectra (again, with $\Delta p = 0.01$) to compare eigenvector robustness as a function of rate within the three systems. Rate is defined as the inverse of an eigenvector's relaxation timescale at the model lag time τ_{lag} ($\tau_{lag} = 10$ ns for villin, 2 ns for Fs-peptide), with $\tau_{relax} = -\tau_{lag}/\ln \lambda$. In each case, λ is the eigenvalue of the transition matrix corresponding to the eigenvector being analyzed (8).

All three plots show a similar increase in expected deviation as eigenvector frequency increases up to (and in the case of Fs-peptide, beyond) the relaxation timescale rate $k = 1/\tau_{relax}$ ns^{-1}. In general, eigenvectors at each system's slowest timescales are 1.5 to 2 times more robust than those near the lag time rate. Absolute robustness, as measured here, appears to be roughly independent of system size: although the villin MSM contains many more states than does the model for Fs-peptide, the magnitudes of deviations seen in Fig. 5 and Fig. 6 are comparable.

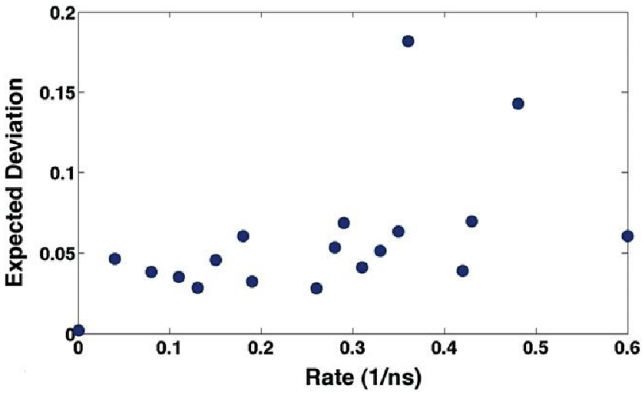

FIGURE 5 Expected deviation, $\langle \delta(\boldsymbol{e}) \rangle$ ($N = 2$, $\Delta p = 0.01$), versus rate for eigenvectors of Fs-peptide. The expected deviation for the stationary distribution corresponds to the point at zero rate, and $N = 2$ was chosen to represent 10% of states. For Fs-peptide, expected deviations in eigenvectors increase loosely with increasing rate.

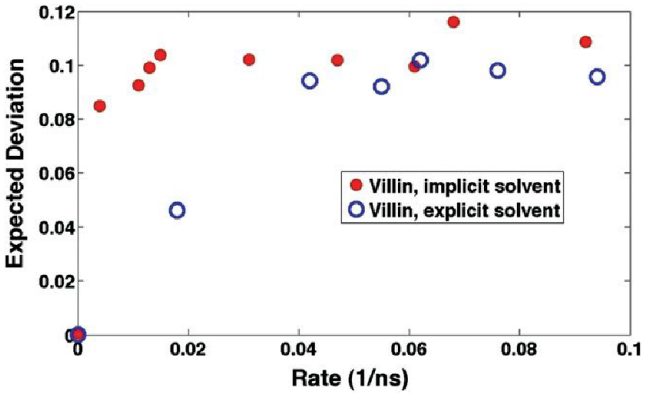

FIGURE 6 Expected deviation, $\langle \delta(\boldsymbol{e}) \rangle$ ($N = 50$, $\Delta p = 0.01$), versus rate for eigenvectors of villin in explicit (*open circles*) and implicit (*solid circles*) solvent. Again, the expected deviations for the stationary distribution are represented at zero rate. In both cases, expected deviation appears to increase with increasing rate; the explicit model seems to be slightly more robust at rates near the lag time rate of 0.1 ns.

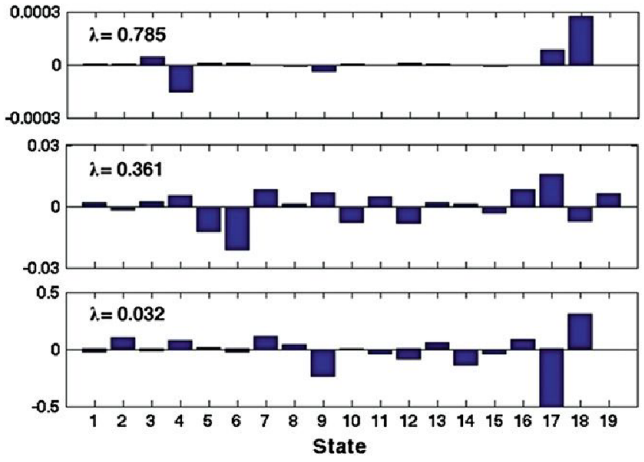

FIGURE 7 Left eigenvector difference maps for a perturbed model of the Fs-peptide. Quantities on the vertical axes are unitless and describe the difference in flux into a state in the perturbed model relative to the original model. As the maps indicate, the fluxes at long timescales are less affected by perturbation. Dynamics into and out of states with low populations (e.g., State 9 and State 17) fluctuate largely at short timescales but are stable in the slowest eigenvectors.

This trend in robustness versus rate is pleasing from a physical point of view. Changes in the transition matrix divert the ensemble's walk to pathways not described by the original model. These diversions, one would expect, might have a large impact on ensemble dynamics at a system's shortest timescales. We see that the transfer of density between states at quite long timescales, however, is less dependent on these high frequency trajectory diversions. Indeed, in processes like protein self-assembly that occur with continual environmental fluctuation, adaptivity over long timescales is needed to ensure reproducible results. Our data show that many protein folding MSM eigenvectors exhibit a similar resistance to parametric perturbation.

To provide a specific example of mechanistic changes at short and long timescales, Fig. 7 contains difference maps for various left eigenvectors of a perturbed Fs-peptide model. The Fs-peptide transition matrix was perturbed in a similar fashion to that used for villin: counts were added to ~5% of count matrix elements using Gaussian noise ($\mu = 5$, $\sigma = 3$). The matrix was then constrained to positivity and renormalized to yield a perturbed model. The difference maps in Fig. 7 simply represent the difference between left eigenvectors of the perturbed model and those of the original model with the indicated eigenvalues λ (after perturbation).

A first observation drawn from Fig. 7 lies in the relative magnitudes of eigenvector deviations: in agreement with Fig. 5, the sum-squared deviations for faster eigenvectors are much larger than those seen for slower eigenvectors. With respect to gaining specific mechanistic insight, changes in the slowest eigenvector ($\lambda = 0.785$, $\tau_{relax} \approx 8$ ns) are relatively uniform, with the exception of a small increase of flux into State 18 and a small increase in flux out of State 4, both intermediate states connected directly to the folded helix.

In the two eigenvectors at fast timescales, however, significant changes in flux occur for a large percentage of the states in the model. In the case of the intermediate eigenvector ($\lambda = 0.361$, $\tau_{relax} \approx 2$ ns), States 5 and 6 (both intermediates connected to the native state) lose the most population flux, whereas many other intermediate (directly connected to the native state) and unfolded (not directly connected with the native state) states gain flux. For the fastest eigenvector ($\lambda = 0.032$, $\tau_{relax} \approx 0.6$ ns), large losses in flux occur for States 9 and 17, which are sparsely populated unfolded states not connected to the native state.

These observations together support our conclusions about mechanistic robustness versus rate. The mechanistic characteristics described by the slow eigenvectors change very little, while fluxes in the faster eigenvectors change drastically. Particularly, fluxes in and out of lowly populated states (like State 17), which one would expect to have little impact on the overall folding mechanism, can change considerably at fast timescales but are damped out once the longest timescale is reached.

CONCLUSION

We have shown that three representative protein folding MSMs exhibit sloppy behavior with respect to their transition probability parameters. In general, the stationary and slow components of the eigenspectrum incurred only small deviations upon perturbation, whereas the high-frequency eigenvalues and eigenvectors were less robust under our framework. Especially near the lag time rate, eigenvalues and eigenvectors experienced deviations more than twice as large as those seen in slowly relaxing kinetic components.

With these conclusions about robustness in mind, we would like to discuss the new implications for MSMs that sloppiness holds.

Implications for models derived from simulation

Every MSM eigenvector analyzed in this study demonstrated sloppy characteristics. Although the degree of sloppiness varied from vector to vector, sensitivities of every observable spanned at least two orders of magnitude with reasonable uniformity.

We would like to reiterate that the robust behavior we report is not necessarily unique to models of protein folding. Topologically, protein folding MSMs are networks that contain many kinetically relevant but few thermodynamically relevant states. It is likely that the reported eigenvector robustness would be observed in any network sharing these characteristics. The important conclusion here, however, is that protein folding MSMs do exhibit this robustness to perturbation. This means that parts of MSM transition matrix eigenspectra (and observables that can be calculated from them) are not highly sensitive to uncertainties in many of the transition matrix elements themselves.

Although improvement in MSM accuracy is an ongoing task, we can thus be comforted that even moderate uncertainties in transition probabilities will have little impact on parts of the transition matrix eigenspectrum. Such confidence, however, comes with a few caveats. First, we have emphasized that the slowly relaxing aspects of mechanism are more robust to perturbation than the quickly relaxing ones. Observations that are contingent on high-frequency eigenvectors should be more closely scrutinized. Second, it is clear the number of parameters with large uncertainties still needs to be limited. Because transition probabilities are coupled together, too many successive errors in transition matrix elements could have drastic effects on the quantitative predictions of a MSM. In particular, if perturbations are large enough to substantially change the slow eigenvalues (i.e., the important timescales) of the model, a breakdown in mechanism will follow. Needless to say, methods for reducing transition probability uncertainties in MSMs remain intensely interesting subjects for investigation.

One area in which perturbation might change mechanistic properties resides in the choice of force field to be used in MD simulation. Shaw et. al. (29) have shown that folding mechanism can vary greatly depending on the force field used: in particular, whereas variants of the AMBER force field performed relatively consistently, discrepancies between variants of the CHARMM force field were large. Work on simulating the Fip35 WW domain has also raised questions regarding the mechanistic predictions made with the CHARMM force field (30).

Implications for interpreting biophysical experiments

The perturbation of model parameters has connections to concepts in protein folding biology that would be of general interest to an experimentalist. In particular, are experimental observations about protein folding robust? Although experiments, of course, are not concerned with simulation-specific perturbations like force field and space discretization errors, analogous perturbations in environmental conditions (temperature, pH, salt conditions, sequence mutations, presence of other proteins, etc.) as well as statistical uncertainty need to be considered in an experimental setting. The robustness seen in protein folding simulations predicts a similar robustness in the interpretation of protein folding experiments, with analogous caveats as discussed previously in the context of simulations. This is important for the comparison of simulation to experiment, comparison between experiments, and also for the interpretation of the experimental data, because less robust aspects of the system are most susceptible to small variations in experimental conditions.

Our analysis can shed light on which elements one would expect to be most robust. For instance, measurements of equilibrium properties (e.g., through thermal or chemical melting studies) are subject to perturbations in temperature and salt conditions. Nevertheless, because the properties of interest in these cases are stationary, an experimentalist should be relatively confident that such perturbations have little impact. In experiments that are time-resolved (from nanoseconds to milliseconds) and at the single molecule level, however, conclusions about kinetics and mechanism should be tempered with considerations of perturbative robustness. Elements of mechanism that occur on relatively slow timescales might be trusted with some surety, but, as with MSMs, conclusions based on high-frequency processes must be more closely scrutinized.

Why can one say that protein folding is mechanistically robust?

The title of this work is Protein Folding Is Mechanistically Robust. One might ask the question, given that some parts of the MSM eigenspectrum are not robust: is the title's statement justified?

Not all MSM observables are robust to perturbation. We should note again, however, that the nonrobust elements of MSM observables belong to fast parts of the transition matrix eigenspectrum. As indicated earlier, one's primary interest in studying folding protein mechanisms resides in understanding the important pathways that occur on the folding timescale. The slow eigenvectors contain this long timescale information and thus contain the most important mechanistic information. Because the slow eigenvectors changed very little upon perturbation, we conclude that protein folding mechanisms, in the context of MSMs, are robust.

Even though folding robustness is an important concept for experimentalists to consider, it has few applications to actually solving problems in biology. Rather, it is

nonrobustness in systems that fundamentally gives rise to interesting behavior. The rare events that induce significant conformational changes (related, using a sloppiness framework, to the stiff parameters of a model) are the particular focus of many biologists. The question as to which parameters in a model are the stiffest, thus, may prove to be much more interesting than previously thought. Determining which parameters are stiff enough to change a low-frequency eigenvector in an MSM, for instance, could indicate which states are important in inducing a particular population shift. Therefore, changes in these parameters could simulate the binding of a ligand or substrate or some perturbation in the cellular environment. This analysis could have applications in conducting in-depth mechanistic simulations of concepts like allostery, calalysis, and inhibition, topics that truly define contemporary biology.

SUPPORTING MATERIAL

Derivation of Eq. 8, references, and three figures are available at http://www.biophysj.org/biophysj/supplemental/S0006-3495(12)00110-5.

We thank Sergio Bacallado and Kyle Beauchamp for providing data to facilitate this study.

We thank National Science Foundation (MCB-0954714) and National Institutes of Health (R01-GM062868) for their support of this work. J.K.W. was supported by the Fannie and John Hertz Foundation on the Professor Yaser S. Abu-Mostafa Fellowship.

REFERENCES

1. Voelz, V. A., G. R. Bowman, …, V. S. Pande. 2010. Molecular simulation of ab initio protein folding for a millisecond folder NTL9(1–39). *J. Am. Chem. Soc.* 132:1526–1528.
2. Bowman, G. R., V. A. Voelz, and V. S. Pande. 2011. Atomistic folding simulations of the five-helix bundle protein $\lambda(6-85)$. *J. Am. Chem. Soc.* 133:664–667.
3. Noé, F. 2008. Probability distributions of molecular observables computed from Markov models. *J. Chem. Phys.* 128:244103.
4. Berezhkovskii, A., G. Hummer, and A. Szabo. 2009. Reactive flux and folding pathways in network models of coarse-grained protein dynamics. *J. Chem. Phys.* 130:205102.
5. Yang, S., N. K. Banavali, and B. Roux. 2009. Mapping the conformational transition in Src activation by cumulating the information from multiple molecular dynamics trajectories. *Proc. Natl. Acad. Sci. USA.* 106:3776–3781.
6. Chodera, J. D., W. C. Swope, …, K. A. Dill. 2006. Longtime protein folding dynamics from short-time molecular dynamics simulations. *Multiscale. Model. Simul.* 5:1214–1226.
7. Schutte, C. 1999. Conformational dynamics: modeling, theory, algorithm, and application to biomolecules. Habilitation thesis. Freie Universitat Berlin, Germany.
8. Swope, W. C., J. W. Pitera, and F. Suits. 2004. Describing protein folding kinetics by molecular dynamics simulations. *J. Phys. Chem. B.* 108:6571–6581.
9. Boehr, D. D., D. McElheny, …, P. E. Wright. 2006. The dynamic energy landscape of dihydrofolate reductase catalysis. *Science.* 313: 1638–1642.
10. Volkman, B. F., D. Lipson, …, D. Kern. 2001. Two-state allosteric behavior in a single-domain signaling protein. *Science.* 23:2429–2433.
11. Prinz, J. H., H. Wu, …, F. Noé. 2011. Markov models of molecular kinetics: generation and validation. *J. Chem. Phys.* 134:174105.
12. Karanicolas, J., and C. L. Brooks, 3rd. 2003. Improved Gō-like models demonstrate the robustness of protein folding mechanisms towards non-native interactions. *J. Mol. Biol.* 334:309–325.
13. Gu, H., N. Doshi, …, D. Baker. 1999. Robustness of protein folding kinetics to surface hydrophobic substitutions. *Protein Sci.* 8:2734–2741.
14. Dobson, C. M. 2004. Principles of protein folding, misfolding and aggregation. *Semin. Cell Dev. Biol.* 15:3–16.
15. Pande, V. S., K. Beauchamp, and G. R. Bowman. 2010. Everything you wanted to know about Markov State Models but were afraid to ask. *Methods.* 52:99–105.
16. Gutenkunst, R. N., J. J. Waterfall, …, J. P. Sethna. 2007. Universal sloppy parameter sensitivities in systems biology models. *PLoS Comput. Biol.* 3:e189.
17. Daniels, B. C., Y. J. Chen, …, C. R. Myers. 2008. Sloppiness, robustness, and evolvability in systems biology. *Curr. Opin. Biotechnol.* 19:389–395.
18. Waterfall, J. J., F. P. Casey, …, J. P. Sethna. 2006. Sloppy-model universality class and the Vandermonde matrix. *Phys. Rev. Lett.* 97:150601.
19. Fowler, S. B., and J. Clarke. 2001. Mapping the folding pathway of an immunoglobulin domain: structural detail from Phi value analysis and movement of the transition state. *Structure.* 9:355–366.
20. Scott, K. A., L. G. Randles, and J. Clarke. 2004. The folding of spectrin domains II: phi-value analysis of R16. *J. Mol. Biol.* 344:207–221.
21. Matthews, J. M., and A. R. Fersht. 1995. Exploring the energy surface of protein folding by structure-reactivity relationships and engineered proteins: observation of Hammond behavior for the gross structure of the transition state and anti-Hammond behavior for structural elements for unfolding/folding of barnase. *Biochemistry.* 34:6805–6814.
22. Fayer, M. D. 2001. Elements of Quantum Mechanics. Oxford University Press.
23. Singhal, N., and V. S. Pande. 2005. Error analysis in Markovian State Models for protein folding. *J. Chem. Phys.* 123:204909.
24. Hinrichs, N. S. 2007. Algorithms for building models of molecular motion from simulations. Ph.D. dissertation, Stanford University, CA.
25. Gupta, N., and R. K. Mehra. 1974. Computational aspects of maximum likelihood estimation and reduction in sensitivity function calculations. *IEEE Trans. Automat. Contr.* 19:774–783.
26. Lue, H. 2004. Principal Hessian directions for regression with measurement error. *Biometrika.* 91:409–423.
27. Huang, X., G. R. Bowman, …, V. S. Pande. 2009. Rapid equilibrium sampling initiated from nonequilibrium data. *Proc. Natl. Acad. Sci. USA.* 106:19765–19769.
28. Bowman, G. R., and V. S. Pande. 2010. Protein folded states are kinetic hubs. *Proc. Natl. Acad. Sci. USA.* 107:10890–10895.
29. Piana, S., K. Lindorff-Larsen, and D. E. Shaw. 2011. How robust are protein folding simulations with respect to force field parameterization? *Biophys. J.* 100:L47–L49.
30. Freddolino, P. L., F. Liu, …, K. Schulten. 2008. Ten-microsecond molecular dynamics simulation of a fast-folding WW domain. *Biophys. J.* 94:L75–L77.

Determination of Membrane-Insertion Free Energies by Molecular Dynamics Simulations

James Gumbart[†*] and Benoît Roux[†‡]
[†]Biosciences Division, Argonne National Laboratory, Argonne, Illinois; and [‡]Department of Biochemistry and Molecular Biology and Gordon Center for Integrative Science, The University of Chicago, Chicago, Illinois

ABSTRACT The accurate prediction of membrane-insertion probability for arbitrary protein sequences is a critical challenge to identifying membrane proteins and determining their folded structures. Although algorithms based on sequence statistics have had moderate success, a complete understanding of the energetic factors that drive the insertion of membrane proteins is essential to thoroughly meeting this challenge. In the last few years, numerous attempts to define a free-energy scale for amino-acid insertion have been made, yet disagreement between most experimental and theoretical scales persists. However, for a recently resolved water-to-bilayer scale, it is found that molecular dynamics simulations that carefully mimic the conditions of the experiment can reproduce experimental free energies, even when using the same force field as previous computational studies that were cited as evidence of this disagreement. Therefore, it is suggested that experimental and simulation-based scales can both be accurate and that discrepancies stem from disparities in the microscopic processes being considered rather than methodological errors. Furthermore, these disparities make the development of a single universally applicable membrane-insertion free energy scale difficult.

INTRODUCTION

The spontaneous partitioning of some amino acids into lipid bilayers underlies the folding and function of all membrane proteins. Knowledge of the energetics of this process is expected to provide the fundamental physico-chemical basis for understanding numerous structural and functional aspects of membrane proteins. However, although it has long been accepted that the residues of membrane proteins loosely follow some hydrophobicity pattern (1), attempts at establishing a definitive free energy scale for the membrane insertion of amino acids have met with varied success. Choosing the optimal membrane-mimicking bulk solvent to measure transfer free energies is one part of the problem. For example, empirical scales based on transfer free energies of side-chain analogs between, e.g., water and octanol (2) or water and cyclohexane (3), disagreed with one another in magnitude, and which scale is best remains unclear. More recently, a biological hydrophobicity scale was determined using a cotranslational system. A putative transmembrane (TM) segment was inserted into the protein-conducting channel, the SecY/Sec61 translocon, concomitant with the nascent protein's synthesis, and glycosylation was used to monitor the state of the system quantitatively (4,5). Perhaps most surprising was the observation of a low free energy cost associated with the presence of a charged residue in the TM helix; according to the translocon experiments, the free energy cost to add one arginine in a TM helix is ~2–3 kcal/mol (4,5). In contrast, molecular dynamics (MD) computations predict free energies of ~14–17 kcal/mol for arginine (6–8). Such a large and mostly unexplained disagreement created much confusion and contributed to doubts regarding the accuracy of the force field used in MD computations.

Despite the aforementioned doubts, it should be noted that solvation free energies calculated from simulation are generally in very good agreement with experimental values for well-defined liquid phases (9–12). Therefore, it is unlikely that errors in methodology or force field are solely responsible for the large discrepancy between simulations and experiments for membrane insertion (13). Rather, at least in part, the large mismatch in free energies resulted from comparing disparate processes. The majority of simulation studies examining the free energy of membrane insertion were predicated on the assumption of two idealized end-states, in which the TM helix was either fully hydrated or fully inserted into the bilayer. Although the translocon measurements are clearly indicative of a thermodynamic partitioning between two microscopic environments of different polarity, it is unlikely that they actually report on the transfer free energy between such idealized end-states (14). The reality of membrane-protein insertion is far more complex, with a variety of states of intermediate solvation also possible (14). Reconsidering the molecular context in which the translocon-assisted transfer free energies were measured led to a more complete resolution of this problem (15,16). Membrane insertion of a TM segment in the cotranslational system is believed to occur via a two-stage process, the first being insertion from ribosome into the channel and the second from the channel laterally into the membrane (15,17). The first stage is extremely slow (~1 residue/s) and irreversibly driven by the nascent chain's elongation for both membrane and secreted proteins.

Submitted November 30, 2011, and accepted for publication January 17, 2012.

*Correspondence: gumbart@mcs.anl.gov

Editor: Scott Feller.

0006-3495/12/02/0795/7 $2.00

doi: 10.1016/j.bpj.2012.01.021

The second stage, however, has no energetic input and, therefore, may represent the equilibrium process measured experimentally. Free-energy perturbation (FEP) calculations measuring the free energy for this process, transfer from channel to membrane, demonstrated a notably improved agreement with the experimental translocon scale compared with prior computational investigations (15).

The ribosome-translocon-membrane system is exceedingly complex, however, and is far from a simple testing ground for force-field validation. Presumably, comparison with a simpler water-to-bilayer (WTB) hydrophobicity scale would yield a clearer view of the issues at hand. Such a scale has been proposed recently by measuring the spontaneous membrane insertion of the outer membrane phospholipase A (OmpLA) under different conditions (18). Specifically, a residue predicted to localize to the membrane's center, Ala^{210}, was mutated to other amino acids, and the corresponding change in free energy of insertion was determined. Surprisingly, even for direct insertion from water to membrane, the cost of placing one arginine inside the membrane turned out to be quite low, at only 3.71 kcal/mol relative to wild-type OmpLA (18), a value fairly similar to that observed in the experimental translocon scale. Thus, the OmpLA-scale measurements seem to indicate that the WTB transfer of one arginine is actually much smaller than predicted by atomic force fields, leading one to, once again, question the accuracy of MD computations (18). However, many of the specific microscopic factors underlying the OmpLA experiments have not yet been considered and it is difficult to ascertain the origin of the observed transfer free energies. The relative simplicity of the OmpLA measurements compared to the translocon-based ones offers a new opportunity to examine the ability of simulations to quantitatively predict membrane-insertion free energies, albeit with some details about the end states still unknown.

To clarify the molecular origins of the free energies in the WTB scale, the insertion of OmpLA mutants into the membrane was mimicked as closely as possible through the use of FEP simulations (19). Among the aspects unique to the OmpLA measurements, it is important to take into consideration the use of the short lipid DLPC, which has only 12 aliphatic carbons in each tail, and a pH of 3.8 (18). In the FEP simulations, the insertion-free-energy difference between Ala^{210} and a given residue is determined by carrying out the mutation in one direction in the membrane and the opposite direction in water. Three representative residues, a charged arginine (Arg), a hydrophobic leucine (Leu), and a hydrophilic serine (Ser), are chosen for comparison, each requiring 240 ns for a reliable determination of its insertion free energy. Close agreement between the simulations and the experimental values for the first two, Arg and Leu, is found, whereas the cost for Ser insertion is slightly higher in simulation. Additional calculations reveal the predominant contributor to the relatively low free energies in the WTB scale is the extraordinarily thin DLPC membrane.

METHODS

System construction

Simulations of OmpLA began from the crystallographic structure of OmpLA (PDB code 1QD5) (20). Protonation states for titratable residues were assigned according to a pH of 3.8, matching experimental conditions, using PropKa (21,22). Specifically, glutamate residues 25, 51, 60, 104, 105, 111, and 165 along with aspartate residues 125, 143, and 205, all solvent exposed, were neutralized. The DLPC bilayer was constructed using the CHARMM GUI Membrane Builder (http://www.charmm-gui.org/) (23–25). Protein and membrane were combined using the visualization and analysis program VMD (26), leaving the membrane with 100 lipids in the upper leaflet and 95 in the lower leaflet. The resulting system was solvated above and below and ionized with Na^+ and Cl^- ions to a concentration of 308 mM. The final system size for OmpLA in the membrane is 63,000 atoms.

The system used for simulations of the pseudo-infinite poly-leucine helix in a DLPC bilayer was prepared in a manner identical to that in Gumbart et al. (15). Briefly, the helix contains 73 amino acids and was placed in a solvated bilayer with K^+ and Cl^- ions at a concentration of 1.0 M surrounding it. The size for this system is 48,500 atoms. All C_α atoms of the helix were restrained, thus maintaining the helix's orientation and structure. To prevent shifting of the membrane relative to the helix, the center-of-mass of all phosphorus atoms in the membrane was restrained along the z axis to the origin.

Simulation protocols

All equilibrium simulations were carried out in the *NPT* ensemble and production simulations in the $NP_z\mathcal{A}T$ ensemble, where N denotes the number of particles, P_z is the normal pressure, $\mathcal{A}$ is the surface area, and T is the temperature. Simulations were run using the molecular dynamics program NAMD 2.8 (27) and the CHARMM force field (28–30). The normal pressure and the temperature were fixed at 1 bar and 310 K, respectively, employing the Langevin piston algorithm (31) and Langevin dynamics with damping coefficient 1 ps^{-1}. Periodic boundary conditions were applied in all dimensions. Short-range Lennard-Jones and Coulombic interactions were truncated smoothly by means of a 12 Å spherical cutoff with a switching function applied beyond 10 Å. The particle-mesh Ewald method (32) was employed to compute long-range electrostatic interactions. A timestep of 2 fs was employed, with bonded interactions and short-range forces calculated every timestep and long-range forces every three timesteps. Covalent bonds involving hydrogen atoms were constrained to their equilibrium values.

Free-energy calculations

In a simulated alchemical transformation, the free energy separating two states is calculated by slowly converting from one to the other through creation and/or annihilation of specific components of the system, controlled by a parameter λ that runs from 0 to 1 (33). To prevent the occurrence of singularities at small values of λ, a scaled-shifted soft-core potential was used for van der Waals interactions (34). For calculating $\Delta\Delta G$ of insertion of the residue-210 mutants of OmpLA relative to the Ala^{210} wild-type, FEP simulations were undertaken in which Ala^{210} is transformed into an alternative residue in the two environments, water and membrane. Similarly, for the transfer free energy of Arg on a polyL helix from water to membrane, an Arg residue distant from the membrane was transformed into Ala while concomitantly an Ala residue in the membrane center was transformed into Arg. Each of the transformations was run in both the forward (λ from 0 to 1) and backward (λ from 1 to 0) directions. The transformations were subdivided into 50 windows and each was run for 0.6 ns of equilibration and 0.6 ns of data collection, giving 60 ns for the full transformation. Thus, for the three residues on OmpLA and the polyL

helix, along with initial equilibration simulations, a total of ~1 μs of simulations were carried out. FEP simulations of the isolated residue and of the seven-residue peptide in water were run for 4.5 ns in each direction. Statistical analysis of the two directions for each FEP calculation was performed by using the Bennett acceptance ratio (35) via the ParseFEP plugin in VMD (26).

Membrane area

Because the packing of lipids may have a nonnegligible effect on the free energy of insertion, the membrane area was carefully monitored. The initially constructed OmpLA-DLPC system was equilibrated in stages (36). Unrestrained equilibration of the membrane-protein system in the *NPT* ensemble for 6 ns produced an area of ~83.5 × 83.5 Å^2. With the protein area estimated at 850 Å^2, the area/lipid is 62.8 Å^2 on average. This is smaller than that from experimental measurements, which give, after accounting for the difference in temperatures (310 K in simulation and 303 K in experiment), 65.1 Å^2 (37). To correct for the slight underestimation in area/lipid, the system's area was increased to 85 × 85 Å^2 and then fixed for subsequent simulations, giving an area/lipid of ~65.4 Å^2.

Corrections to the calculated free energy

For nonneutral systems using PME electrostatics, a self-interaction term arises that must be accounted for in the free energy calculations. For two systems of different charges, q_1 and q_0, the correction takes the form

$$\Delta u = \frac{1}{2}\xi_{\mathrm{EW}}\left(q_1^2 - q_0^2\right), \quad (1)$$

where $\xi = -2.837297/L$ for a cubic lattice (38). For simulations involving mutation of an Ala residue to Arg, $q_1 = 1$ and $q_0 = 0$. Corrections to the free energy in four systems were determined and are detailed in Table S1 in the Supporting Material.

An additional spurious self-interaction between the charged Arg residue and its images in neighboring periodic cells also arises in the simulations (6,39,40). However, because either water or, when in the membrane, the water-filled OmpLA barrel, effectively shields the Arg's charge over the simulation box width, this term is expected to be negligible, and therefore was ignored.

RESULTS

To determine the WTB insertion free energies computationally, a thermodynamic cycle was first constructed, shown in Fig. 1. This cycle connects the unassisted membrane insertion of OmpLA to more computationally tractable alchemical transformations, similar to one used previously (15). By closure of the cycle, the free-energy difference between insertion of the wild-type OmpLA and of the Ala^{210} mutants is given by

$$\Delta\Delta G^{\mathrm{OmpLA}}_{\mathrm{aq.}\rightarrow\mathrm{DPLC}}(Res) = \Delta G^{\mathrm{OmpLA}}_{\mathrm{DLPC}}\left(\mathrm{Ala}^{210}\rightarrow Res\right) - \Delta G^{\mathrm{OmpLA}}_{\mathrm{aq.}}\left(\mathrm{Ala}^{210}\rightarrow Res\right), \quad (2)$$

where *Res* indicates the residue 210 point mutation. Thus, two FEP calculations, one of the free-energy change of Ala^{210} to *Res* in water and one in membrane, suffice to determine the insertion cost of OmpLA mutants relative to wild-type.

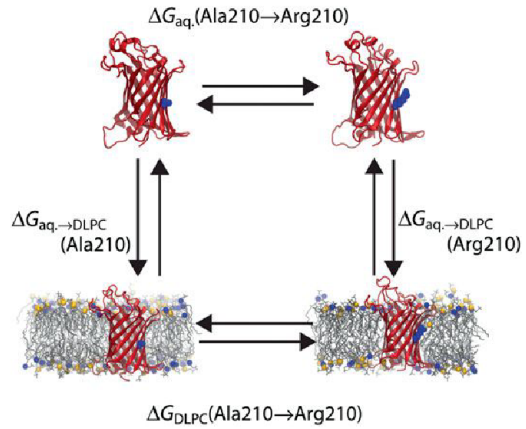

FIGURE 1 Thermodynamic cycle relating membrane-insertion (*vertical legs*) with FEP calculations (*horizontal legs*) for arginine. OmpLA is shown as ribbons and Ala/Arg^{210} is indicated at its center in a space-filling representation. The membrane is displayed as thin gray lines with phosphorus atoms of the headgroups as spheres.

Insertion free-energies for Arg, Leu, and Ser

FEP simulations, each 60 ns, were carried out in both forward (Ala → *Res*) and reverse (*Res* → Ala) directions to improve statistical reliability (15,33); see Table S2 for a full list of the simulations performed. Simulation conditions were chosen to best mimic those in experiment, including using an equilibrated DLPC bilayer (see Methods). One factor, which was not explicitly controlled, however, is the structure of OmpLA before membrane insertion. Whether it is folded, unfolded, or somewhere in between in water is unknown, and may be dependent on the sequence. Therefore, three contexts for the purely aqueous state of residue 210 of OmpLA are considered: as part of the fully folded protein; as part of a seven-residue strand, i.e., residues 207–213 of OmpLA; and as a single isolated amino acid, thereby neglecting completely any role of the rest of the protein (see Fig. S1 in the Supporting Material). All insertion free energies, therefore, are given as a range encompassing the three contexts; see Table 1 for a complete list of values.

In the first tested case, Ala^{210} was mutated to Arg, a residue with one of the most discrepant free energies between computationally and experimentally determined scales. Based on the FEP simulations and the cycle in Fig. 1, along with a correction for the self-energy of nonneutral systems using PME (see Methods), $\Delta\Delta G^{\mathrm{OmpLA}}_{\mathrm{aq.}\rightarrow\mathrm{DLPC}}$ (Arg) is equal to 1.05–3.76 kcal/mol. The upper value, derived from a fully folded aqueous state for OmpLA, is in excellent agreement with the experimental value, denoted in Moon and Fleming (18) as $\Delta\Delta G^{\mathrm{o}}_{w,l}$ = 3.71 kcal/mol. It is also much lower than other direct water-to-membrane free-energy costs determined from simulations, which range from 10 to 17 kcal/mol (6–8,41). The insertion free energy calculated from the other two aqueous states of Ala/Arg^{210} considered are even lower, suggesting that the relatively low

TABLE 1 Relative free energies of membrane insertion for OmpLA mutants

		Aqueous reference state		
Residue	WTB scale (kcal/mol)	Folded	Seven-residue strand	Isolated
$\Delta\Delta G^{\text{OmpLA}}_{\text{aq.}\rightarrow\text{DLPC}}$ (Arg)	3.71 ± 0.13	3.76 ± 0.27	1.06 ± 0.22	2.65 ± 0.20
$\Delta\Delta G^{\text{OmpLA}}_{\text{aq.}\rightarrow\text{DLPC}}$ (Leu)	−1.81 ± 0.13	−0.91 ± 0.06	−2.64 ± 0.08	−2.06 ± 0.07
$\Delta\Delta G^{\text{OmpLA}}_{\text{aq.}\rightarrow\text{DLPC}}$ (Ser)	1.83 ± 0.22	4.08 ± 0.05	3.52 ± 0.06	5.24 ± 0.06

value is not particular to the chosen structure in water but rather to other environmental conditions.

Although proposals addressing the lower free energy for Arg insertion in experiments compared to simulations have been put forth (42,43), a similar reduction in magnitude for hydrophobic residues such as Leu remained elusive. Calculation of translocon-assisted insertion free energies, however, showed lower free energies for both Arg and Leu when compared to other computationally resolved scales (15). The insertion free energy for Leu in the WTB scale, −1.81 kcal/mol (18), lies between that in the biological hydrophobicity scale (−0.6 kcal/mol (4)) and most computational values (−4 kcal/mol (7,8,41,42)). In the second tested case, the insertion free-energy of Leu relative to Ala on OmpLA was computed, employing FEP simulations identical to those carried out for Arg. From these simulations, the free energy $\Delta\Delta G^{\text{OmpLA}}_{\text{aq.}\rightarrow\text{DLPC}}$ (Leu) is found to be between −2.64 and −0.91 kcal/mol. As found for Arg, in all contexts, the free energy of insertion is lower than that measured in previous simulations, and encompasses the experimental value. As opposed to Arg, for Leu the optimal agreement with experiment is found for an isolated Leu in the aqueous environment ($\Delta\Delta G = -2.06$ kcal/mol), although the range overall is quite small.

Finally, the insertion free energy for a hydrophilic residue, Ser, was determined. For this residue, the WTB insertion free energy (1.83 kcal/mol) lies slightly below the range of free-energy values determined from the thermodynamic cycle in Fig. 1, i.e., 3.52–5.24 kcal/mol. The solvation free energy for a serine side-chain analog in the CHARMM force field is in good agreement with experiments (9), suggesting that the difference here results from limited system-specific issues. Ser is accommodated in the membrane core primarily through hydrogen bonding to the backbone carbonyl of Glu^{224}, disturbing a β-strand of the OmpLA barrel, as opposed to the Arg residue, which quickly induces the formation of a stable water defect in the membrane (see Fig. 2). The slow process of attracting one water molecule to coordinate the serine residue in the membrane core, which was observed during extended equilibration but not during FEP simulations, may bias the calculated insertion free energy cost. Indeed, a subsequent FEP calculation in which the initial state included a water molecule interacting with the membrane-inserted Ser^{210} displayed a reduction in the insertion free energy of 1.21 kcal/mol (see the Supporting Material). Additionally, it is known that the distribution of hydrogen-bond geometries in MD simulations differs from that observed in crystallographic structures, due in part to the lack of polarizability in most force fields (44,45). Comparison between quantum chemical and molecular mechanical interaction energies for observed Ser^{210}-β-barrel interactions, described in the Supporting Material, illustrates that the CHARMM force field undervalues the interaction by an average of 0.46 kcal/mol, and, thus, also may contribute to a reduction in the insertion free energy for Ser. A combination of the two effects, namely the slow diffusion of water to the embedded Ser^{210} and the slight difference in hydrogen-bonding energies, would be sufficient to bring the simulated free energy cost in line with the experimental one.

Contributions to the determined insertion free energies

Although the FEP simulations provide the free energies of insertion for the OmpLA mutants, they do not reveal their origins unambiguously. This ambiguity is especially pertinent for Arg, which deviates the most from previously determined computational scales. Comparing the membrane insertion of Arg on OmpLA to simulated insertion of Arg on a background poly-leucine helix (6,15) suggests three possible sources. The most obvious source is the difference in membrane composition, the former being carried out with DLPC lipids (12-carbon tails) and the latter with DPPC (16-carbon tails). The resulting difference in membrane thickness is ~4–5 Å, shown in Fig. 3. In another MD study, a similar lipid-tail-length change, i.e., DOPC → DMPC, accounted for a decrease of ~5 kcal/mol for insertion of an arginine side-chain analog (46). Alternatively, differences in the local protein environment of the Arg residue, namely the OmpLA β-barrel or the polyL α-helix, may play a role. A final possibility is shifting of the protein in the membrane such that the Arg residue is no longer centrally located. During a 10-ns equilibration, the distance between the C_α of Arg^{210} and the membrane center is 1.67 ± 0.67 Å (see Fig. S2), which is estimated from the potential of mean force for a related system to reduce the insertion free energy by ~3 kcal/mol (6). For comparison, local thinning of the DLPC bilayer within 15 Å of Arg^{210} amounts to 1.61 ± 0.74 Å (see Fig. S3).

To separate the contribution of the variance in bilayer thickness from the other two possible factors, FEP

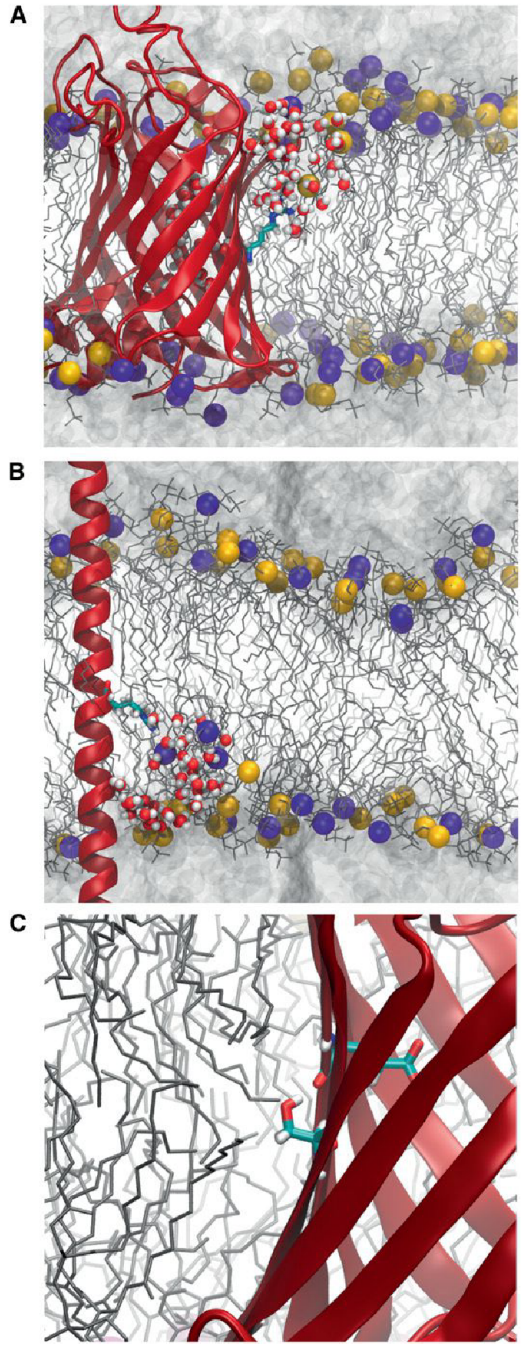

FIGURE 2 Interactions that stabilize residues in the membrane. (*A* and *B*) Membrane deformation induced by the presence of arginine at the center for (*A*) OmpLA:Arg^{210} and (*B*) PolyL:Arg. The protein is colored as in Fig. 1 with arginine shown in a stick representation colored by atom type. The DLPC bilayer is drawn as in Fig. 1. Water is shown as a continuous gray surface above and below the membrane, while water molecules that penetrate the bilayer are shown in a licorice representation. (*C*) Hydrogen-bonding of Ser^{210} to the OmpLA β-barrel backbone.

simulations examining the transfer of an arginine residue borne by an extended polyL α-helix from the aqueous phase to the center of a DLPC bilayer were carried out. The C_α of Arg/Ala was restrained to the bilayer's center to prevent

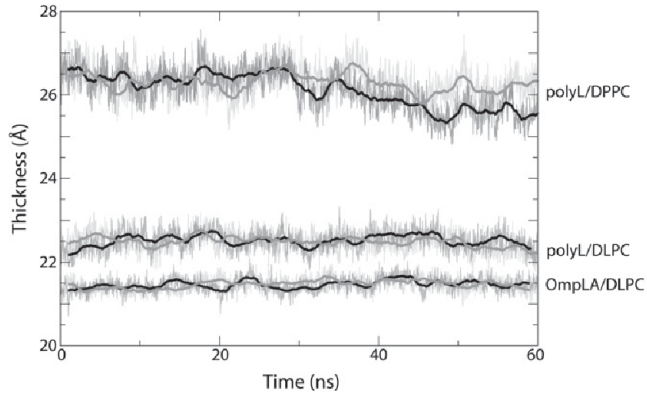

FIGURE 3 Membrane hydrophobic thickness over the course of the Ala → Arg FEP simulations. Thickness was measured as the separation between the average positions of the carbonyl carbon atoms in the lipid tails of each leaflet (denoted C21 and C31 in the force field); this thickness is nearly identical to the experimental value for DLPC, namely $2z_{CG}$ = 21.8 Å (37). The black and gray curves represent the forward and reverse trajectories for each protein-membrane combination indicated in the plot.

sliding of the helix, as done previously (15). The resulting free-energy change, i.e., $\Delta G^{polyL}_{aq.\rightarrow DLPC}(Arg) - \Delta G^{polyL}_{aq.\rightarrow DLPC}(Ala)$, was found to be 6.09 kcal/mol. When the nearly identical transfer process was carried out in a DPPC membrane, the free-energy change was much higher, $\Delta G^{polyL}_{aq.\rightarrow DPPC}(Arg) - \Delta G^{polyL}_{aq.\rightarrow DPPC}(Leu) = 16.9$ kcal/mol (6,15). The difference in the two protocols, namely the use of Ala versus Leu as the Arg counterpart, is expected to contribute up to 1.81 kcal/mol according to other hydrophobicity scales (4,7,8,18). This would make the net $\Delta\Delta G$ for the DLPC membrane 7.9 kcal/mol, at most—still almost 10 kcal/mol less than that for DPPC. Therefore, the membrane thickness is the principal contributor to the relatively low free energies measured in the WTB hydrophobicity scale, with shifting of OmpLA in the membrane also playing a role.

CONCLUSION

Numerous free-energy scales for the partitioning of proteins into membranes have been defined based on different experimental approaches and biophysical circumstances (13). Most recently, a water-to-bilayer (WTB) scale was determined for the direct insertion of each residue centrally located on the β-barrel of OmpLA (18). Although simpler in principle than, e.g., cotranslational insertion through the translocon (5,15,43), many of the molecular details of the OmpLA-mediated insertion process remain unknown. By reproducing here the free energies for Arg, Leu, and Ser insertion computationally, these details become partially revealed. Most notably, the thickness of the membrane is found to be primarily responsible for the relatively compressed free energies measured in the WTB scale, with shifting of the protein off-center in the membrane and interactions within the protein itself affecting them as well.

Because the folding and insertion pathway for OmpLA into the membrane is unknown, and may even be sequence-dependent, three different contexts for the mutated residue outside the membrane were considered: on a fully folded OmpLA; in the center of a seven-residue oligopeptide; and as a completely isolated amino acid. The range of free energies calculated for these contexts is small, but not negligible, at 2.7 kcal/mol for Arg and 1.7 kcal/mol for both Ser and Leu. Furthermore, the ideal agreement between experiment and simulation was found in a different context for each of the three tested residues. The distinct, context-dependent free energies expose the complexity of the OmpLA insertion process, which cannot be assumed to be identical for every residue.

It has become increasingly evident that charged amino acids can be stable in the membrane, at least marginally, albeit only under certain conditions. One example is a high protein content in the bilayer (42). Another such condition was illustrated here, namely an abnormally thin membrane, which, among other things, reduces the deformation required to accommodate snorkeling of an Arg residue to the membrane-water interface (see Fig. 2). These conditions are both distinct from and independent of the typical biological membrane-insertion process, which makes use of the translocon (15,16). Insertion through the translocon can give an apparently low free-energy cost, but does not guarantee thermodynamic stability once in the membrane. Tests on isolated transmembrane segments that can distinguish between stable, membrane-inserted states and initially inserted, but ultimately unstable and/or expelled states, are required to further probe the distinction between translocon-assisted insertion and water-to-bilayer insertion.

The diversity of paths to the membrane for proteins and contributors to their stability therein limits the universality of a single free-energy scale for identifying and characterizing membrane proteins. Indeed, insertion propensity is not even a localized property, with residues on neighboring TM segments being able to affect it (43,47,48). Additionally, insertion free energies for multiple residues on a single TM segment are not uniformly additive (13), requiring the inclusion of multiresidue corrections to any prediction method. Simulations can play a role in the determination of these nonlocal and nonadditive effects, provided they are sufficiently accurate. Although much discussion has arisen as a result of the apparent disparity between computational and experimental membrane-insertion free energies (16,49–51), this disparity is likely due to a comparison of nonequivalent systems, e.g., membranes with different thicknesses or different end-points of the process under study (14). As demonstrated here, simulations and experiments can achieve quantitative agreement provided the specific conditions in each are carefully identified and matched. The addition of polarizability to classical simulations is expected to enhance this agreement further (52,53).

SUPPORTING MATERIAL

Details of corrections to the insertion free energy for Ser, two tables, three figures, and references (54,55) are available at http://www.biophysj.org/biophysj/supplemental/S0006-3495(12)00094-X.

J.G. sincerely thanks Peter Freddolino, Chris Chipot, and Klaus Schulten for helpful discussions and comments on this work.

This work was supported by grants from the National Institutes of Health (R01 GM067887 and U54 GM087519) and the National Science Foundation (MCB-0920261). J.G. is supported by a Director's Postdoctoral Fellowship from the Argonne National Laboratory. Simulations were carried out with resources provided by the Computation Institute and the Biological Sciences Division of the University of Chicago and Argonne National Laboratory, under grant S10 RR029030-01.

REFERENCES

1. Kyte, J., and R. F. Doolittle. 1982. A simple method for displaying the hydropathic character of a protein. *J. Mol. Biol.* 157:105–132.
2. Wimley, W. C., T. P. Creamer, and S. H. White. 1996. Solvation energies of amino acid side chains and backbone in a family of host-guest pentapeptides. *Biochemistry.* 35:5109–5124.
3. Radzicka, A., and R. Wolfenden. 1988. Comparing the polarities of the amino acids: side chain distribution coefficients between the vapor phase, cyclohexane, 1-octanol, and neutral aqueous solution. *Biochemistry.* 27:1664–1670.
4. Hessa, T., H. Kim, …, G. von Heijne. 2005. Recognition of transmembrane helices by the endoplasmic reticulum translocon. *Nature.* 433:377–381.
5. Hessa, T., N. M. Meindl-Beinker, …, G. von Heijne. 2007. Molecular code for transmembrane-helix recognition by the Sec61 translocon. *Nature.* 450:1026–1030.
6. Dorairaj, S., and T. W. Allen. 2007. On the thermodynamic stability of a charged arginine side chain in a transmembrane helix. *Proc. Natl. Acad. Sci. USA.* 104:4943–4948.
7. MacCallum, J. L., W. F. D. Bennett, and D. P. Tieleman. 2007. Partitioning of amino acid side chains into lipid bilayers: results from computer simulations and comparison to experiment. *J. Gen. Physiol.* 129:371–377.
8. Johansson, A. C. V., and E. Lindahl. 2008. Position-resolved free energy of solvation for amino acids in lipid membranes from molecular dynamics simulations. *Proteins: Struct., Funct. Bioinf.* 70:1332–1344.
9. Deng, Y., and B. Roux. 2004. Hydration of amino acid side chains: nonpolar and electrostatic contributions calculated from staged molecular dynamics free energy simulations with explicit water molecules. *J. Phys. Chem. B.* 108:16567–16576.
10. Shirts, M. R., and V. S. Pande. 2005. Solvation free energies of amino acid side chain analogs for common molecular mechanics water models. *J. Chem. Phys.* 122:134508.
11. Shivakumar, D., Y. Deng, and B. Roux. 2009. Computations of absolute solvation free energies of small molecules using explicit and implicit solvent model. *J. Chem. Theory Comput.* 5:919–930.
12. Shivakumar, D., J. Williams, …, W. Sherman. 2010. Prediction of absolute solvation free energies using molecular dynamics free energy perturbation and the OPLS force field. *J. Chem. Theory Comput.* 6:1509–1519.
13. MacCallum, J. L., and D. P. Tieleman. 2011. Hydrophobicity scales: a thermodynamic looking glass into lipid-protein interactions. *Trends Biochem. Sci.* 36:653–662.
14. Roux, B. 2007. Lonely arginine seeks friendly environment. *J. Gen. Physiol.* 130:233–236.
15. Gumbart, J., C. Chipot, and K. Schulten. 2011. Free-energy cost for translocon-assisted insertion of membrane proteins. *Proc. Natl. Acad. Sci. USA.* 108:3596–3601.

16. Schow, E. V., J. A. Freites, …, D. J. Tobias. 2011. Arginine in membranes: the connection between molecular dynamics simulations and translocon-mediated insertion experiments. *J. Membr. Biol.* 239:35–48.

17. Frauenfeld, J., J. Gumbart, …, R. Beckmann. 2011. Cryo-EM structure of the ribosome-SecYE complex in the membrane environment. *Nat. Struct. Mol. Biol.* 18:614–621.

18. Moon, C. P., and K. G. Fleming. 2011. Side-chain hydrophobicity scale derived from transmembrane protein folding into lipid bilayers. *Proc. Natl. Acad. Sci. USA.* 108:10174–10177.

19. Zwanzig, R. W. 1954. High-temperature equation of state by a perturbation method. I. Nonpolar gases. *J. Chem. Phys.* 22:1420–1426.

20. Snijder, H. J., I. Ubarretxena-Belandia, …, B. W. Dijkstra. 1999. Structural evidence for dimerization-regulated activation of an integral membrane phospholipase. *Nature.* 401:717–721.

21. Li, H., A. D. Robertson, and J. H. Jensen. 2005. Very fast empirical prediction and interpretation of protein pK_a values. *Proteins: Struct., Funct. Bioinf.* 61:704–721.

22. Bas, D. C., D. M. Rogers, and J. H. Jensen. 2008. Very fast prediction and rationalization of pK_a values for protein-ligand complexes. *Proteins: Struct., Funct. Bioinf.* 73:765–783.

23. Woolf, T. B., and B. Roux. 1996. Structure, energetics, and dynamics of lipid-protein interactions: a molecular dynamics study of the gramicidin A channel in a DMPC bilayer. *Proteins: Struct., Funct. Gen.* 24:92–114.

24. Jo, S., T. Kim, and W. Im. 2007. Automated builder and database of protein/membrane complexes for molecular dynamics simulations. *PLoS ONE.* 2:e880.

25. Jo, S., J. B. Lim, …, W. Im. 2009. CHARMM-GUI Membrane Builder for mixed bilayers and its application to yeast membranes. *Biophys. J.* 97:50–58.

26. Humphrey, W., A. Dalke, and K. Schulten. 1996. VMD: visual molecular dynamics. *J. Mol. Graph.* 14:33–38, 27–28.

27. Phillips, J. C., R. Braun, …, K. Schulten. 2005. Scalable molecular dynamics with NAMD. *J. Comput. Chem.* 26:1781–1802.

28. MacKerell, Jr., A. D., D. Bashford, …, M. Karplus. 1998. All-atom empirical potential for molecular modeling and dynamics studies of proteins. *J. Phys. Chem. B.* 102:3586–3616.

29. MacKerell, Jr., A. D., M. Feig, and C. L. Brooks, 3rd. 2004. Extending the treatment of backbone energetics in protein force fields: limitations of gas-phase quantum mechanics in reproducing protein conformational distributions in molecular dynamics simulations. *J. Comput. Chem.* 25:1400–1415.

30. Klauda, J. B., R. M. Venable, …, R. W. Pastor. 2010. Update of the CHARMM all-atom additive force field for lipids: validation on six lipid types. *J. Phys. Chem. B.* 114:7830–7843.

31. Feller, S. E., Y. Zhang, …, B. R. Brooks. 1995. Constant pressure molecular dynamics simulation: the Langevin piston method. *J. Chem. Phys.* 103:4613–4621.

32. Darden, T., D. York, and L. G. Pedersen. 1993. Particle mesh Ewald: an $N\cdot\log(N)$ method for Ewald sums in large systems. *J. Chem. Phys.* 98:10089–10092.

33. Pohorille, A., C. Jarzynski, and C. Chipot. 2010. Good practices in free-energy calculations. *J. Phys. Chem. B.* 114:10235–10253.

34. Zacharias, M., T. P. Straatsma, and J. A. McCammon. 1994. Separation-shifted scaling, a new scaling method for Lennard-Jones interactions in thermodynamic integration. *J. Chem. Phys.* 100:9025–9031.

35. Bennett, C. H. 1976. Efficient estimation of free energy differences from Monte Carlo data. *J. Comput. Phys.* 22:245–268.

36. Gumbart, J., and K. Schulten. 2006. Molecular dynamics studies of the archaeal translocon. *Biophys. J.* 90:2356–2367.

37. Kučerka, N., Y. Liu, …, J. F. Nagle. 2005. Structure of fully hydrated fluid phase DMPC and DLPC lipid bilayers using x-ray scattering from oriented multilamellar arrays and from unilamellar vesicles. *Biophys. J.* 88:2626–2637.

38. Hummer, G., L. R. Pratt, and A. E. Garcia. 1996. Free energy of ionic hydration. *J. Phys. Chem.* 100:1206–1215.

39. Allen, T. W., O. S. Andersen, and B. Roux. 2004. Energetics of ion conduction through the gramicidin channel. *Proc. Natl. Acad. Sci. USA.* 101:117–122.

40. Allen, T. W., O. S. Andersen, and B. Roux. 2006. Ion permeation through a narrow channel: using gramicidin to ascertain all-atom molecular dynamics potential of mean force methodology and biomolecular force fields. *Biophys. J.* 90:3447–3468.

41. Choe, S., K. A. Hecht, and M. Grabe. 2008. A continuum method for determining membrane protein insertion energies and the problem of charged residues. *J. Gen. Physiol.* 131:563–573.

42. Johansson, A. C. V., and E. Lindahl. 2009. Protein contents in biological membranes can explain abnormal solvation of charged and polar residues. *Proc. Natl. Acad. Sci. USA.* 106:15684–15689.

43. Rychkova, A., S. Vicatos, and A. Warshel. 2010. On the energetics of translocon-assisted insertion of charged transmembrane helices into membranes. *Proc. Natl. Acad. Sci. USA.* 107:17598–17603.

44. Kortemme, T., A. V. Morozov, and D. Baker. 2003. An orientation-dependent hydrogen bonding potential improves prediction of specificity and structure for proteins and protein-protein complexes. *J. Mol. Biol.* 326:1239–1259.

45. Freddolino, P. L., S. Park, …, K. Schulten. 2009. Force field bias in protein folding simulations. *Biophys. J.* 96:3772–3780.

46. Johansson, A. C. V., and E. Lindahl. 2009. The role of lipid composition for insertion and stabilization of amino acids in membranes. *J. Chem. Phys.* 130:185101.

47. Heinrich, S. U., and T. A. Rapoport. 2003. Cooperation of transmembrane segments during the integration of a double-spanning protein into the ER membrane. *EMBO J.* 22:3654–3663.

48. Hedin, L. E., K. Öjemalm, …, A. Elofsson. 2010. Membrane insertion of marginally hydrophobic transmembrane helices depends on sequence context. *J. Mol. Biol.* 396:221–229.

49. White, S. H. 2007. Membrane protein insertion: the biology-physics nexus. *J. Gen. Physiol.* 129:363–369.

50. Hristova, K., and W. C. Wimley. 2011. A look at arginine in membranes. *J. Membr. Biol.* 239:49–56.

51. Ulmschneider, J. P., J. C. Smith, …, M. B. Ulmschneider. 2011. In silico partitioning and transmembrane insertion of hydrophobic peptides under equilibrium conditions. *J. Am. Chem. Soc.* 133:15487–15495.

52. Harder, E., A. D. Mackerell, Jr., and B. Roux. 2009. Many-body polarization effects and the membrane dipole potential. *J. Am. Chem. Soc.* 131:2760–2761. 10.1021/ja806825g.

53. Jiang, W., D. J. Hardy, …, B. Roux. 2011. High-performance scalable molecular dynamics simulations of a polarizable force field based on classical Drude oscillators in NAMD. *J. Phys. Chem. Lett.* 2:87–92.

54. Kofke, D. A., and P. T. Cummings. 1998. Precision and accuracy of staged free-energy perturbation methods for computing the chemical potential by molecular simulation. *Fluid Phase Equilib.* 150:41–49.

55. Frisch, M. J., G. W. Trucks, …, D. J. Fox. 2009. Gaussian 09, Rev. A.1. Gaussian Inc., Wallingford, CT.

Cell Career Network just got better!

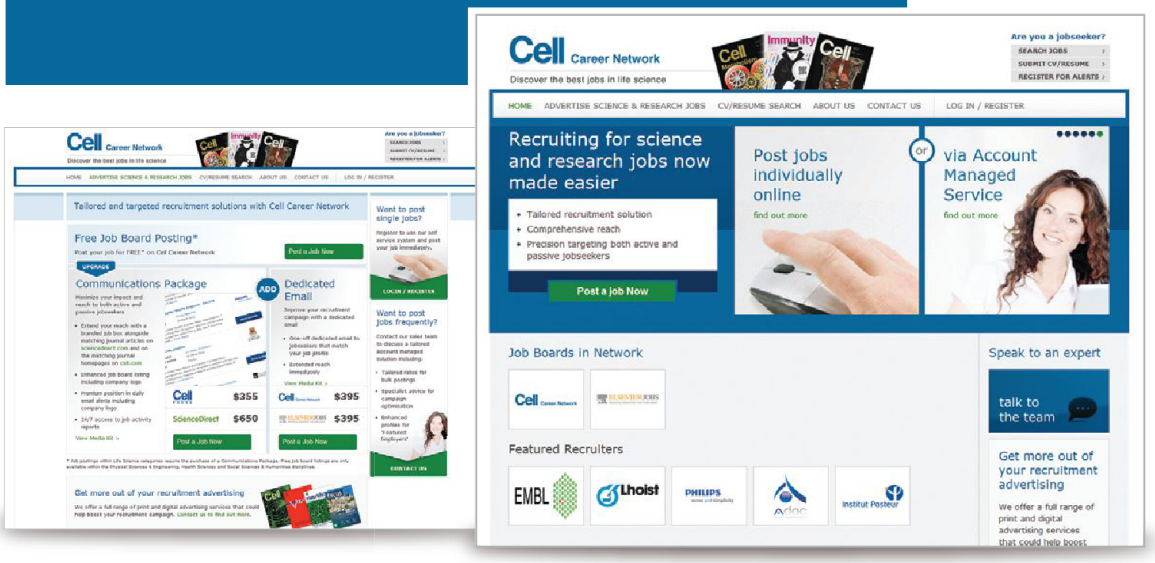

- Additional reach via extended network
- Post a job within 5 minutes via self service
- More intuitive feel and easier navigation
- New vacancy packages and pricing

Your recruitment process just became even easier.
Get started today!

careers.cell.com/recruiters

Cell PRESS

2013 Preview

Cell Press is pleased to announce the schedule for the 2013 Best of Series. In 2012, we published Best of editions for 10 journals, highlighting top research and reviews. In 2013, we plan to expand on the series, offering readers of 12 of our journals the chance to engage with the most popular and impactful papers of the past year. We encourage our readers to examine the content from the full Best of Cell Press collection (www.cell.com/bestof) and gain insight into what the respective scientific communities find the most interesting. We look forward to seeing what research our readers will find most interesting and valuable in the coming year and beyond.

Best Of Edition	Tentative Conference Distribution Includes	Rough Digital Circulation*	Tentative Deadline*
Biophysical Journal	Biophysical Society, SLAS	13,000	Jan 20
Cancer Cell	AACR, Cell Symposia: Cancer Epigenomics	21,000	Mar 10
Immunity	AAI, Cell Symposia: Immunometabolism	17,000	Apr 15
Cell Metabolism	Cell Symposia: Mitochondria, ENDO	11,000	Apr 15
Structure – 20th Anniversary	Experimental Biology	9,000	Apr 1
Cell Host and Microbe	ASM, Cell Symposia: Microbiome and Host Health	7,000	May 1
Stem Cell	ISSCR, Cell Symposia: Stem Cells	14,000	May 25
Molecular Cell	ASBMB, Ubiquitin Drug Discovery and Delivery	31,000	May 1
American Journal of Human Genetics	ASHG, Cell Symposia: Human Evolution	10,156	Sep 25
Neuron	SfN	21,000	Oct 15
Cell	ASCB	51,000	Nov 15
Cell Reports	ASCB	6,000	Nov 15

For more details on Cell Symposia, please visit www.cell.com/symposia. *This information is intended for potential sponsors/advertisers.

For information for the Best of Series, please contact:
Jonathan Christison
Program Director, Best of Cell Press
jchristison@cell.com
617-397-2893

Discover
the
New

NANO ITC & DSC

Powerful new tools for:

- Small-molecule–protein interactions
- Protein-protein interactions
- Drug-target binding
- Biomolecular structure and stability

TA

www.tainstruments.com